Appendix 1

Cationic dyes as morphology-guiding agents for one-dimensional polypyrrole with improved conductivity

Polymer 174 (2019) 11–17

Contents lists available at ScienceDirect

Polymer

journal homepage: www.elsevier.com/locate/polymer

Cationic dyes as morphology-guiding agents for one-dimensional polypyrrole with improved conductivity

Islam M. Minisy[a,b], Patrycja Bober[a,*], Udit Acharya[a,c], Miroslava Trchová[a], Jiřina Hromádková[a], Jiří Pfleger[a], Jaroslav Stejskal[a]

[a] Institute of Macromolecular Chemistry, Academy of Sciences of the Czech Republic, 162 06 Prague 6, Czech Republic
[b] Faculty of Science, Charles University, 128 43 Prague 2, Czech Republic
[c] Faculty of Mathematics and Physics, Charles University, 182 00 Prague 8, Czech Republic

HIGHLIGHTS

- 1D polypyrrole was prepared in the presence of two cationic dyes.
- Conductivity and morphology of polypyrrole was significantly affected by the dyes.
- Conductivity was enhanced to 35 S cm^{-1} in the presence of safranin.

ARTICLE INFO

Keywords:
Polypyrrole
Safranin
Phenosafranin
Nanofibers
Nanotubes
Conductivity

ABSTRACT

Polypyrrole was prepared in the presence of cationic dyes, safranin and phenosafranin. The safranin supported the one-dimensional growth of polypyrrole, converting globules to nanorods and later also to nanotubes, particularly at higher dye concentrations. In the case of phenosafranin, the produced nanotubes were considerably thicker and were always accompanied by globules. Upon oxidation both dyes are expected to generate insoluble oligomeric templates that serve as loci for the deposition of polypyrrole. The formation of globular morphology takes place when the dye becomes depleted, due to its low concentration for safranin, or because of robust templates produced by phenosafranin. In addition to scanning and transmission electron microscopies, the resultant polypyrroles were characterized by FTIR and Raman spectroscopies, and DC conductivity measurements. The conversion of globular morphology to nanotubes/nanofibers was accompanied by the increase in conductivity from 5 to 35 S cm^{-1}, which was explained by the improved ordering of polypyrrole chains more preferable for charge transport. The series of syntheses at varying oxidant-to-pyrrole mole ratios confirmed the stoichiometric ratio 2.5 to be the best for pyrrole oxidation but a good stability of polypyrrole was demonstrated even at extremely high stoichiometric ratio 15.

1. Introduction

Conducting polymers with tunable morphology and electroactivity can be easily synthesized by oxidative polymerization of corresponding monomers [1]. They can be obtained with conventional globular morphology or as various nanostructures, such as nanorods [2], nanowires [3], nanofibers [4,5] or nanotubes [6–8]. Among them, polypyrrole (PPy) is one of the most promising conducting polymers due to its unique physical and electrochemical properties. Its processability can be improved by the formation of various morphologies [9], composites [10], colloids [11,12] or hydrogels [13]. Different additives in the polymerization medium can affect the morphology and conductivity as well; they could be used as morphology directing agents which work as templates to produce polymers with different nanomorphologies. Basically, two main types of structure-directing agents have been used: soft templates represented by micellar aggregates [14] and hard templates, such as porous membranes [15] or *in-situ*-generated solid dye templates. Anionic dyes, such as methyl orange [6], Acid Red 1 [16], Acid Red B [17], and Acid Blue 25 [4], have been reported as templates guiding one-dimensional growth of polypyrrole. Cationic dyes, such as rhodamine B [18,19] and methylene blue complex with heparin [2], have been applied only exceptionally. It has recently been observed that also another cationic dye, safranin, promotes the formation of one-dimensional PPy [20].

* Corresponding author.
E-mail address: bober@imc.cas.cz (P. Bober).

https://doi.org/10.1016/j.polymer.2019.04.045
Received 7 January 2019; Received in revised form 16 April 2019; Accepted 18 April 2019
Available online 23 April 2019
0032-3861/

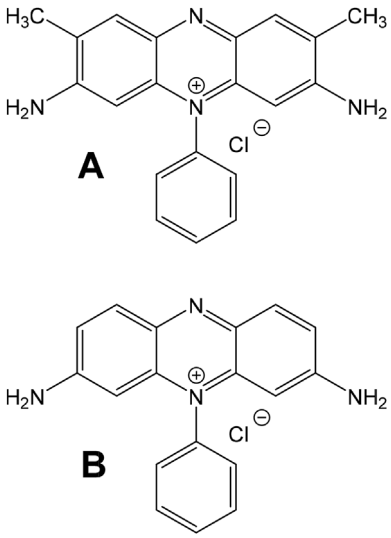

Scheme 1. Chemical formulae of (A) safranin and (B) phenosafranin.

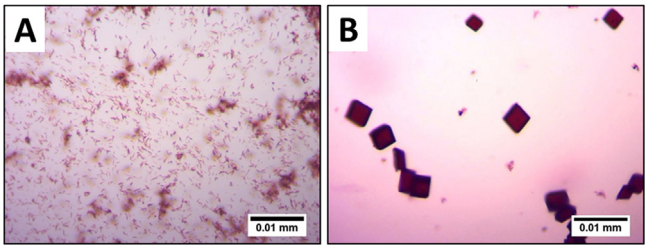

Fig. 1. Optical microscope images of formed templates by mixing (A) 4 mM of safranin and (B) 4 mM of phenosafranin with 0.25 M iron(III) chloride.

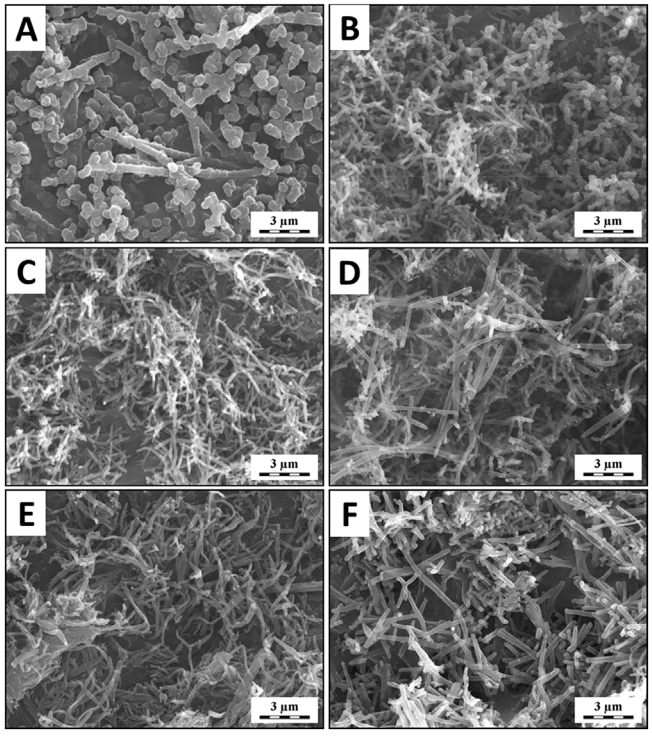

Fig. 2. SEM micrographs of polypyrrole prepared in the presence of safranin with different concentrations: (A) 0.5 mM, (B) 2 mM, (C) 4 mM, (D) 10 mM, (E) 20 mM, and (F) 40 mM.

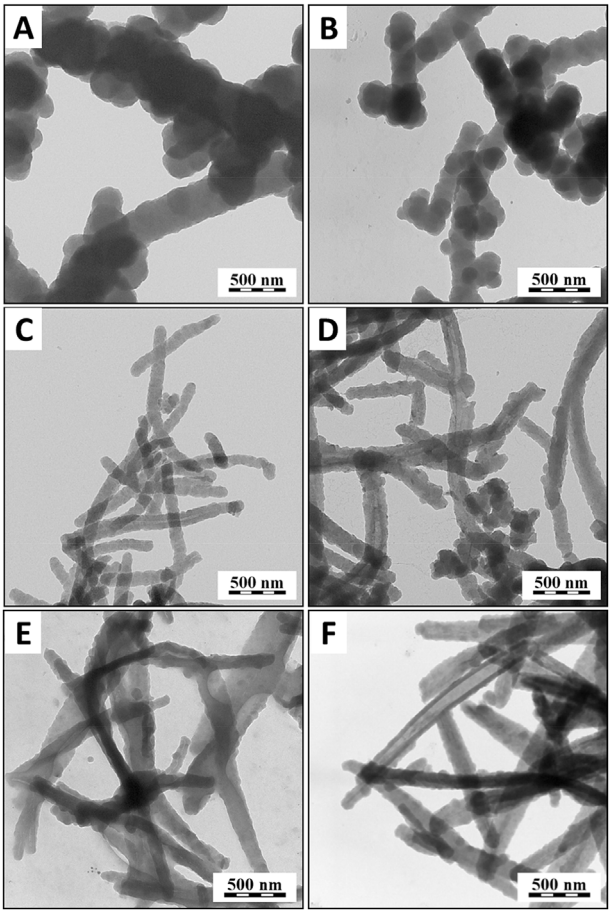

Fig. 3. TEM micrographs of polypyrrole prepared in the presence of safranin with different concentrations: (A) 0.5 mM, (B) 2 mM, (C) 4 mM, (D) 10 mM, (E) 20 mM, and (F) 40 mM.

Among reported PPy morphology modifications, nanotubes have the highest conductivity reaching $\approx 100\ S\ cm^{-1}$ [21]. Moreover, they were found to retain most of their conductivity under the neutral or even alkaline conditions [22] which cannot be achieved in the case of globular PPy.

Various PPy nanostructures have been used in many applications in variety of fields extending from adsorbents [23], chemical sensors [24], biosensors [25], actuators [26], drug delivery systems [27], electrocatalysis [28], supercapacitors [29] to electrode material for batteries [30].

In the present work, PPy nanofibers or nanotubes have been synthesized by the oxidation of pyrrole with iron chloride in the presence of a cationic dye, safranin or chemically similar phenosafranin, (Scheme 1). The influences of the dye chemical structure, dyes concentration, and oxidant-to-monomer mole ratio on morphology and conductivity have been studied to elucidate the role of the dye in the pyrrole polymerization.

2. Experimental section

2.1. Chemicals and reagents

Pyrrole (≥98%), iron(III) chloride hexahydrate, safranin (3,7-diamino-2,8-dimethyl-5-phenylphenazinium chloride; Safranin T, Basic Red 2) and phenosafranine (3,7-diamino-5-phenylphenazinium chloride) were purchased from Sigma-Aldrich. All chemicals were used as received without any further purification.

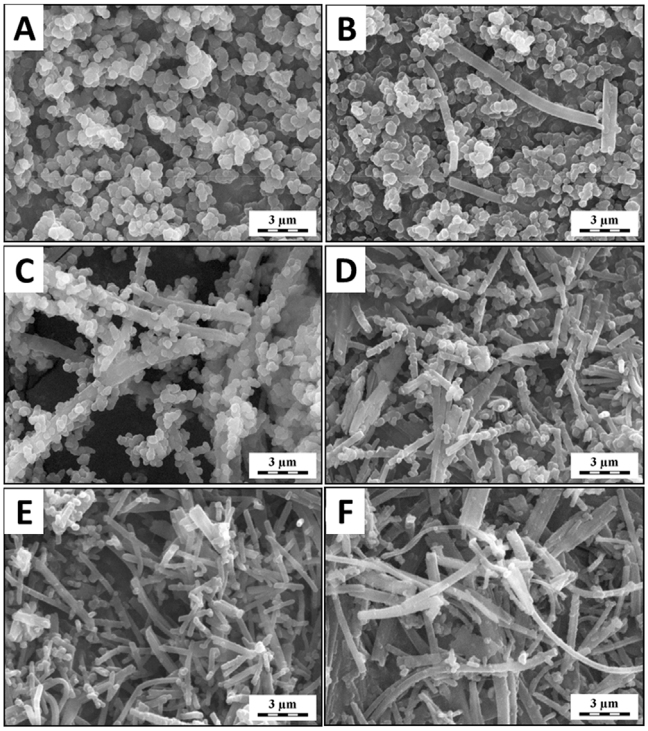

Fig. 4. SEM micrographs of polypyrrole prepared in the presence of different concentrations of phenosafranin: (A) 0.5 mM, (B) 2 mM, (C) 4 mM, (D) 10 mM, (E) 20 mM, and (F) 40 mM.

2.2. Synthesis of PPy in the presence of safranin or phenosafranin

Polypyrrole was prepared by mixing 50 mL of 0.4 M pyrrole (1.34 g of monomer) solution with safranin or phenosafranin (a series of dye concentrations from 0 to 40 mM), then a separately prepared 50 mL aqueous solution of 1 M iron(III) chloride hexahydrate (13.52 g of oxidant) was added. The resulting reaction mixture thus contained 0.2 M pyrrole and 0.5 M iron(III) chloride, i.e. the oxidant/pyrrole mole ratio ([Ox]/[Py]) was 2.5, and a selected concentration of a dye. The polymerization mixtures were stirred for a few seconds and kept for 24 h at room temperature (20 ± 2 °C) without disturbance. The precipitates were collected by vacuum filtration, washed with an excess of 0.2 M hydrochloric acid, followed by ethanol, left to dry in air, and then transferred into desiccators with silica gel until constant weight was achieved.

In order to study the effect of [Ox]/[Py] ratio on the conductivity and morphology of PPy, another series of samples was prepared in the presence of fixed 4 mM safranin and 0.2 M pyrrole concentrations. Iron (III) chloride concentration was varied to obtain [Ox]/[Py] ratios from 1 up to 15.

2.3. Characterization

The morphology of powders was characterized using a VEGATescan scanning electron microscope (SEM) and TECNAI G2 SPIRIT transmission electron microscope (TEM).

PPy pellets with a 13 mm diameter and 1 ± 0.05 mm thickness were compressed with a manual hydraulic press (Trystom H-62) for the conductivity measurements using van der Pauw method. A Keithley 230 Programmable Voltage Source in serial connection with a Keithley 196 System DMM, and a Keithley 181 Nanovoltmeter (Keithley, USA) were used for current and potential drop measurement, respectively. The conductivity value was obtained as an average value from the measurements in two perpendicular directions measured under constant environmental conditions at 23 ± 1 °C and relative humidity

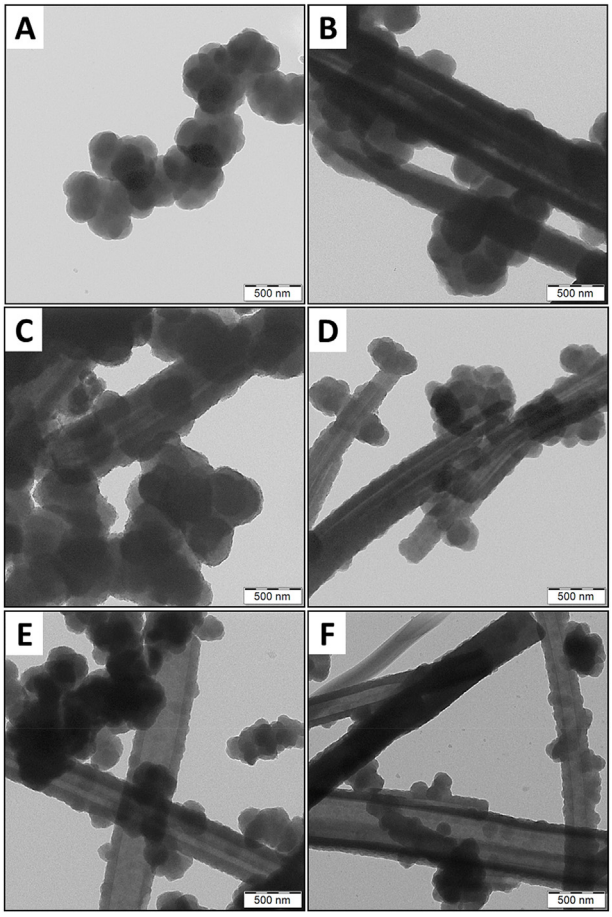

Fig. 5. TEM micrographs of polypyrrole prepared in the presence of different concentrations of phenosafranin: (A) 0.5 mM, (B) 2 mM, (C) 4 mM, (D) 10 mM, (E) 20 mM and (F) 40 mM.

35 ± 5%. The current was kept below 1 mA to avoid heat dissipation in the sample.

Fourier-transform infrared (FTIR) spectra of the powders dispersed in potassium bromide pellets have been registered using a Thermo Nicolet NEXUS 870 FTIR Spectrometer with a DTGS TEC detector in 400–4000 cm^{-1} wavenumber region. Raman spectra were recorded with a Renishaw InVia Reflex Raman microspectrometer. The spectra were obtained using excitation by an argon-ion laser line at 514 nm and analyzed with a spectrograph equipped with a holographic grating 2400 lines mm^{-1}. A research-grade Leica DM LM microscope was used to focus the laser beam. A Peltier-cooled CCD (Charge-coupled device) detector (576 × 384 pixels) registered the dispersed light.

3. Results and discussion

3.1. Template formation

Polypyrrole (Scheme SA) is prepared by the oxidation of pyrrole with a suitable oxidant, such as iron(III) chloride and obtained as a powder with distinct globular morphology. When the oxidation takes place in the presence of suitable organic dyes, one-dimensional morphologies, such as nanotubes or nanofibers, may be obtained [20]. This happens if an organized phase involving a dye is generated in the course of pyrrole oxidation and serves as a template for the surface deposition of PPy [6,31]. The organic dyes have been reported to produce one-dimensional J-aggregates [32] of stacked molecules stabilized by π–π interactions that could serve as templates. Safranin and phenosafranin alone, however, were reported to produce only dimeric

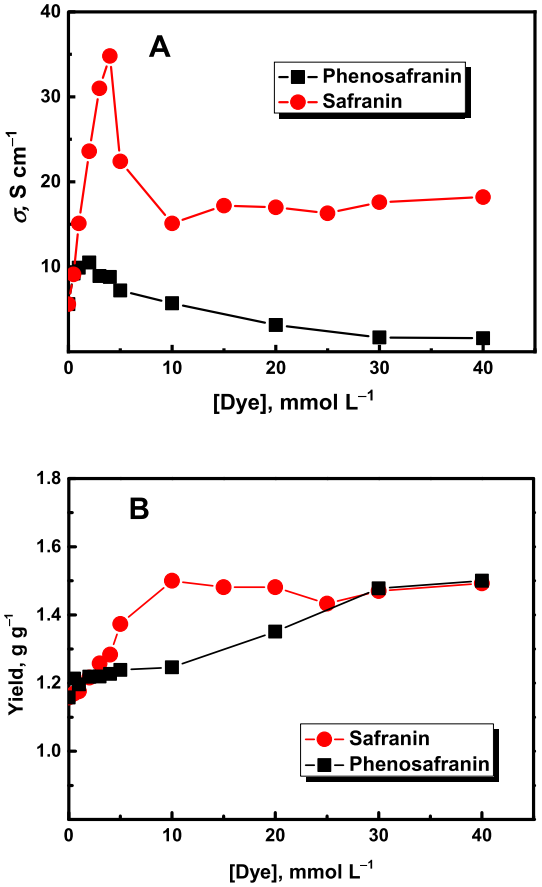

Fig. 6. The dependence of (A) conductivity and (B) yield per gram of pyrrole on molar concentration of safranin or phenosafranin used in the synthesis.

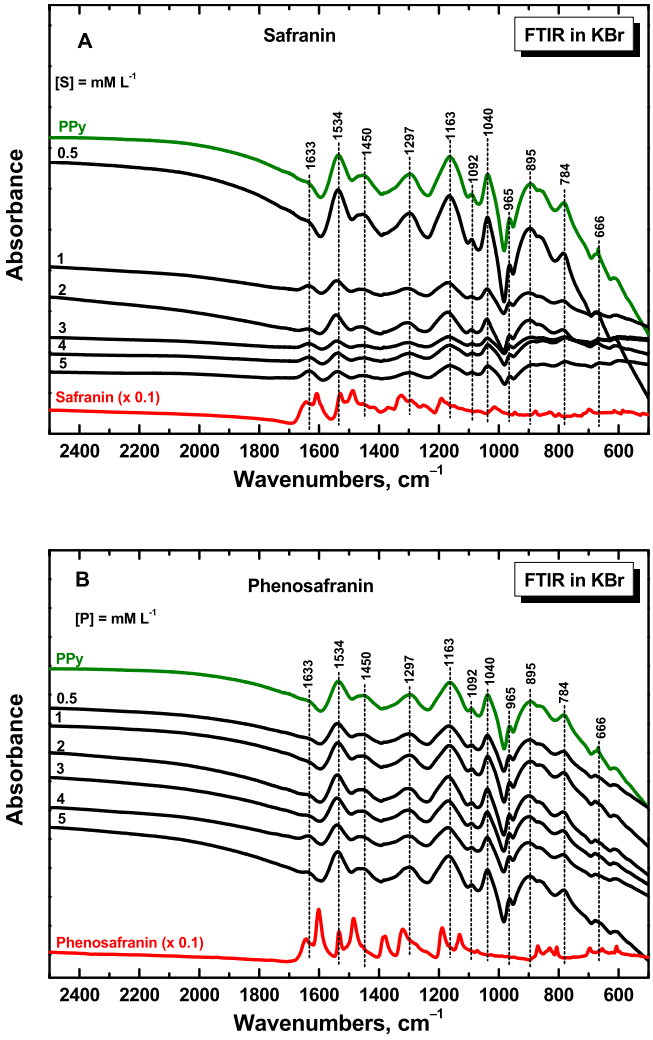

Fig. 7. FTIR spectra of polypyrrole prepared at various concentrations 0.5–5 mM of (A) safranin and (B) phenosafranin.

aggregates [33] that could hardly fulfill such a role.

Turbid solutions have been formed after mixing aqueous solutions of safranin or phenosafranin with iron(III) chloride before addition of pyrrole. Optical microscopic images show the formation of two different types of insoluble solids (Fig. 1). Small fibrillar particles were observed in the case of safranin (Fig. 1A), while phenosafranin produced relatively large microcubes (Fig. 1B). This experiment illustrates the generation of solid phase in the reaction mixture. During the oxidation of pyrrole, such solid objects are prevented to grow to macroscopic dimensions, when pyrrole oligomers adsorb on the surface of emerging solids, now templates, and stimulate following growth of polypyrrole chains [31]. The template formation could be a result of the complex between a dye and iron(III) chloride [34] but the oligomerization of phenosafranin [35] (Scheme SB) or its polymerization [36] yielding insoluble products would be more likely explanation.

To sum up, there are two processes that produce the insoluble solids: (1) the oxidation of pyrrole to polypyrrole (Scheme SA), and (2) the oxidation of phenosafranin or safranin dye to corresponding oligomers (Scheme SB). Depending on the reaction conditions, both reactions proceed simultaneously or in succession as discussed below.

3.2. Effect of dyes concentration on morphology

The conventional PPy obtained with the absence of any dyes has the well-known globular morphology (Fig. S1). The SEM analysis of a series of PPy prepared in the presence of various safranin concentrations shows the significant effect of the safranin, even at very low concentration, on the PPy morphology. At the lowest concentration, 0.5 mM of safranin, the mixture of globules and nanorods is found (Fig. 2A). This might happen if the generation of PPy preceded the formation of a template or if all template dye molecules were depleted in the course of nanorod formation and remaining PPy was therefore produced in globular form. The second explanation is more plausible.

By increasing the safranin concentration nanofibers with different dimensions were obtained (Fig. 2B–F). TEM analysis (Fig. 3) was used to distinguish between fibers and tubes; the results demonstrate the formation of a mixture of nanotubes and nanofibers but no exclusive nanotubes have been observed even at high safranin concentration. At low safranin concentrations (Fig. 3A and B) no tubes cavity was observed while the cavity of the PPy nanotubes increased by increasing the safranin concentration. We can speculate that thicker templates were available for deposition of PPy when the concentration of a dye was higher.

On the other side, SEM micrographs of PPy prepared in the presence of phenosafranin suggest that any fibers have been accompanied with globules (Fig. 4). Moreover, the aspect ratio of the formed fibers is smaller compared to fibers prepared with safranin. By increasing the phenosafranin concentration, the tubular morphology became prominent. TEM analysis (Fig. 5) confirms the formation of nanotubes with rough surfaces and bigger size compared to PPy with safranin. It is worth to mention that the dimensions of the formed nanotubes, about 500 nm in diameter, did not significantly change with the phenosafranin concentration. All these facts indicate that, due to the tendency of phenosafranin to produce larger template compared with safranin (Fig. 1), the phenosafranin dye becomes soon unavailable for the

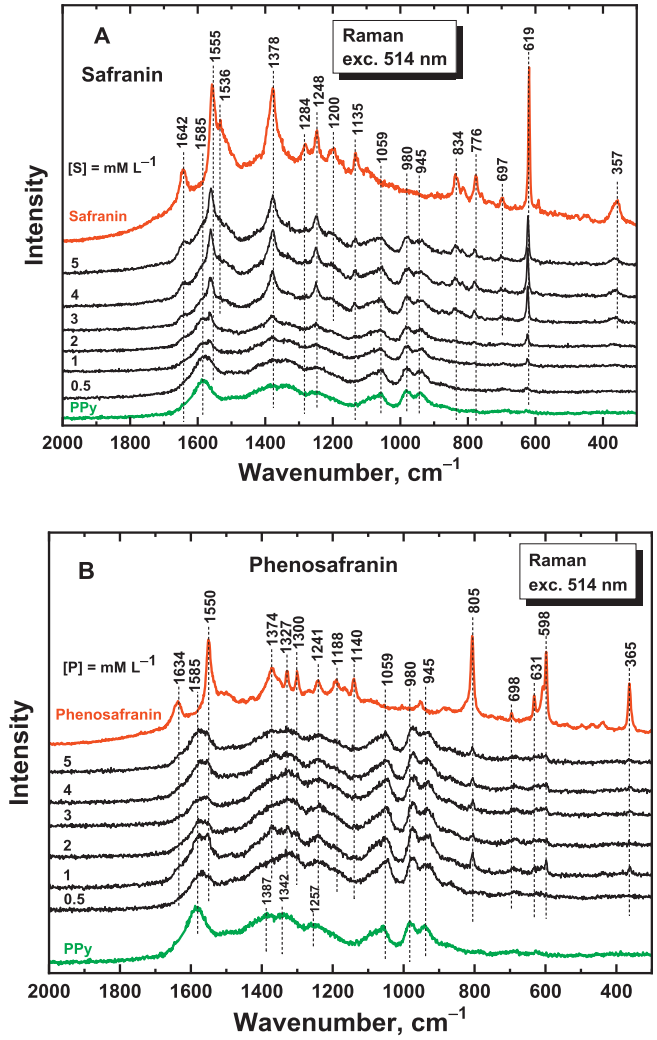

Fig. 8. Raman spectra of polypyrrole prepared in the presence of safranin (A) and phenosafranin (B) at various dye concentrations, 0.5–5 mM.

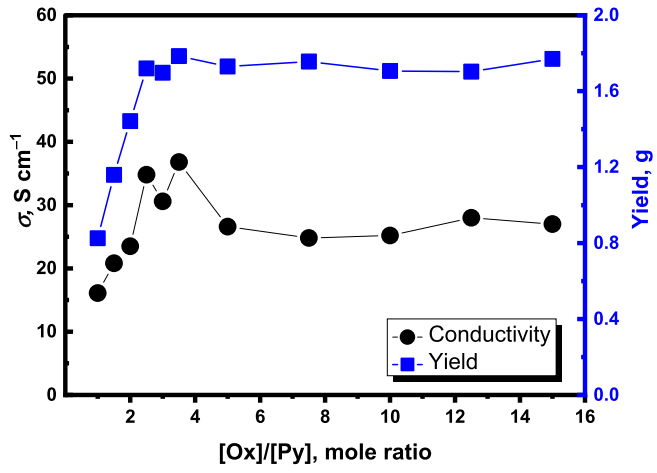

Fig. 9. Dependence of the conductivity and yield of polypyrrole per gram of pyrrole on the iron(III) chloride to pyrrole mole ratio, [Ox]/[Py]. Safranin concentration was 4 mM.

generation of new nanotubes and separate or adhering PPy globules are therefore produced as the polymerization of pyrrole proceeds.

3.3. Conductivity and yield

The DC conductivity of two series of PPy prepared with varied concentrations of safranin or phenosafranin were determined. It is known from the literature that the conductivity of templates composed of oligomeric dyes is low, $\sigma \sim 10^{-9}$ S cm^{-1} [35], and it cannot contribute to the overall conductivity of PPy/dye nanostructured system. PPy prepared in the presence of safranin or phenosafranin has higher conductivity than the conventional globular PPy, $\sigma \sim 5$ S cm^{-1}, prepared in the dye absence. With increasing the safranin concentration, the conductivity increased steadily, reaching a maximum 35 S cm^{-1} at 4 mM dye concentration (Fig. 6A), then the conductivity decreased. The similar trend was found in the case of phenosafranin, where conductivity reached the maximum value 10.5 S cm^{-1} at the concentration 2 mM (Fig. 6B). Compared to our previous results on PPy chains grown at the template surface [37], the increase in the conductivity has been assigned to a better organization of PPy in nanotubular structures compared to the reduced chain-ordering in the globules. Nanotubular structure is also more favorable for the dopant distribution in the bulk of the sample which also leads to the conductivity enhancement. The correlation between conductivity and specific surface areas reported in the literature [38] also points in this direction. By increasing the concentration of dyes and, consequently, the fraction of non-conducting oxidation products [35], the conductivity of composites decreased.

The yield in both cases of dye template used, safranin or phenosafranin, slightly increased with dye concentration (Fig. 6B) as expected. Theoretically 1 g of pyrrole produces 1.3 g of PPy hydrochloride and, as the yield of oxidation product per 1 g of pyrrole is much higher than the theoretical value, the dyes oxidized to insoluble oligomers have to be present as a substantial part of the products. To address this issue, the products have been analyzed with spectroscopic methods.

3.4. FTIR spectroscopy

The infrared spectra of PPy prepared in the presence of various concentrations of safranin (Fig. 7A) and phenosafranin (Fig. 7B) confirm the PPy structure. In the case of safranin the samples prepared with higher dye concentrations were difficult to disperse in potassium bromide pellets. For that reason, infrared absorption spectra were very poorly resolved, and only the bands of stretching and bending vibrations of water molecules at about 3436 cm^{-1} (not shown in Figure) and 1633 cm^{-1} were detected in the spectra. Only low concentrations of dyes from 0.5 mM to 5 mM are presented. For phenosafranin, the samples were better dispersed and the spectra were of good quality. In both cases, we detect the main bands of PPy [20] with maxima at 1534 cm^{-1} (C–C stretching vibrations in the pyrrole ring), at 1450 cm^{-1} (C–N stretching vibrations in the ring), the broad band with maximum at about 1297 cm^{-1} (C–H or C–N in-plane deformation modes), and a local absorption maximum located at 1163 cm^{-1} (breathing vibrations of the pyrrole rings). The band at 1040 cm^{-1} corresponds to the C–H and N–H in-plane deformation vibrations and the peaks at lowest part of the spectrum to the C–H out of plane deformation vibrations of the ring. The peaks typical for safranin or phenosafranin (their spectra are shown in Fig. 7 for comparison) have not been detected in the PPy spectra. This may be due to their low concentrations.

3.5. Raman spectra

The presence of safranin and phenosafranin, however, is well documented by the Raman spectra recorded with a 514 nm excitation wavelength, which is close to the absorbance maximum at 538 nm in UV–visible spectra of these dyes [35] and hence the Raman spectra are

resonantly enhanced (Fig. 8). The spectral features are more pronounced in the case of safranin at 1642, 1555, 1536, 1378, 1284, 1248, 1200, 1135, 834, 776, 697, 619 and 357 cm^{-1}. They are slightly detectable for phenosafranin at 1634, 1550, 1374, 1327, 1300, 1188, 1140, 805, 698, 631, and 365 cm^{-1} at higher dye concentrations. The bands of PPy with maxima at 1585 cm^{-1} (C = C stretching vibrations of PPy backbone), 1387 and 1342 cm^{-1} (bands of ring-stretching vibrations), 1257 cm^{-1} (antisymmetric C–H deformation vibrations), 1059 cm^{-1} (C − H out-of-plane deformation vibrations) and double peak at 980 and 945 cm^{-1} (ring-deformation vibrations of neutral polypyrrole and ring-deformation vibrations in bipolaron units) have also been detected in the spectra. They correspond to the protonated form of PPy [20].

We can conclude from the infrared spectra that PPy was produced in its salt form (Scheme SA), and Raman spectra confirm the presence of dyes in the samples. The spectroscopy, however, is not able to discriminate between the dyes and oligomers produced from these dyes upon oxidation. It is not possible to decide within the present study if the dyes are located inside of the PPy nanostructure or at its surface [38].

3.6. Effect of oxidant/monomer mole ratio

In order to get additional insight into the generation and properties of PPy nanostructures, a series of syntheses with variable oxidant-to-monomer mole ratios, [Ox]/[Py], at fixed 0.2 M pyrrole and 4 mM dye concentrations were carried out. The stoichiometric ratio [Ox]/[Py] = 2.5 was used in experiments discussed in the preceding section. At the ratio reduced to 1, the morphology of PPy was a mixture of fibers and globular particles (Fig. S2). With increasing [Ox]/[Py] ratio up to 3.5, the nanofibers became prominent up to mole ratio equal to 3 (Fig. S2). By further increasing of [Ox]/[Py] mole ratio a mixture of globular and fibrillar morphology with a shape of coral reefs is formed due to the high rate of polymerization at high oxidant concentrations.

The yield as well as the conductivity was found to increase linearly by increasing the oxidant concentration up to [Ox]/[Py] = 2.5 which supplies sufficient amount of oxidant to oxidize all available pyrrole monomers in the reaction mixture. The plateau in the yield is reached at higher ratios (Fig. 9) indicating good stability with respect to over-oxidation. On the other hand, after reaching the maximum value at the concentration [Ox]/[Py] = 3.5 the conductivity decreased to nearly constant 25 S cm^{-1} even at extremely high [Ox]/[Py] ratios. The current use of stoichiometric ratio 2.5 is thus substantiated.

4. Conclusions

Organic cationic dyes, safranin and phenosafranin, have been used in the chemical oxidation of pyrrole for the enhancement of conductivity of polypyrrole and conversion of its globular morphology to nanofibers/nanotubes. Oxidation products of both dyes, i.e. their insoluble oligomers, play a major role as hard templates in directing the morphology of PPy and its aspect ratio. Two processes, (1) the polymerization of pyrrole and (2) the oxidation of dyes to insoluble oligomers proceed simultaneously, and their interplay are responsible for the produced morphology. The highest conductivity of PPy σ = 35 S cm^{-1} and 10 S cm^{-1} were found at 4 mM safranin and 2 mM phenosafranin, respectively, compared with 5 S cm^{-1} of standard globular PPy. Even low concentrations of safranin, 0.5 mM were found to be sufficient to stimulate the growth of one-dimensional morphologies. It is proposed that the PPy chains are better organized in thin one-dimensional structures than in globules and thus nanotubes are more conducting than their globular counterpart. [Ox]/[Py] mole ratio has also significant effect on the conductivity, yield and the morphology of PPy but the currently used value 2.5 affords the products with the best conductivity. The produced PPy can be potentially used in various applications as electrodes materials in supercapacitors, electroactive membranes, etc.

Acknowledgment

The authors wish to thank the Czech Science Foundation (18-04669S) for the financial support.

Appendix A. Supplementary data

Supplementary data to this article can be found online at https://doi.org/10.1016/j.polymer.2019.04.045.

References

[1] A. Malinauskas, Chemical deposition of conducting polymers, Polymer 42 (2001) 3957–3972.
[2] M. Wei, T.Y. Dai, Y. Lu, Controlled fabrication of nanostructured polypyrrole on ion association template: tubes, rods and networks, Synth. Met. 160 (2010) 849–854.
[3] C. Yang, S. Zhang, C. Guan, Polypyrrole nanowires coated with a hollow shell for enhanced electrochemical performance, Mater. Res. Bull. 100 (2018) 116–119.
[4] P. Bober, Y. Li, U. Acharya, Y. Panthi, J. Pfleger, P. Humpolíček, M. Trchová, J. Stejskal, Acid Blue dyes in polypyrrole synthesis: the control of polymer morphology at nanoscale in the promotion of high conductivity and the reduction of cytotoxicity, Synth. Met. 237 (2018) 40–49.
[5] H.D. Tran, K. Shin, W.G. Hong, J.M. D'Arcy, R.W. Kojima, B.H. Weiller, R.B. Kaner, A template-free route to polypyrrole nanofibers, Macromol. Rapid Commun. 28 (2007) 2289–2293.
[6] J. Kopecká, D. Kopecký, M. Vrňata, P. Fitl, J. Stejskal, M. Trchová, P. Bober, Z. Morávková, J. Prokeš, I. Sapurina, Polypyrrole nanotubes: mechanism of formation, RSC Adv. 4 (2014) 1551–1558.
[7] I. Sapurina, Y. Li, E. Alekseeva, P. Bober, M. Trchová, Z. Morávková, J. Stejskal, Polypyrrole nanotubes: the tuning of morphology and conductivity, Polymer 113 (2017) 247–258.
[8] J. Stejskal, I. Sapurina, M. Trchová, E.N. Konyushenko, Oxidation of aniline: polyaniline granules, nanotubes, and oligoaniline microspheres, Macromolecules 41 (2008) 3530–3536.
[9] X.G. Li, A. Li, M.R. Huang, Y. Liao, Y.G. Lu, Efficient and scalable synthesis of pure polypyrrole nanoparticles applicable for advanced nanocomposites and carbon nanoparticles, J. Phys. Chem. C 114 (2010) 19244–19255.
[10] P. Bober, J. Stejskal, I. Šeděnková, M. Trchová, L. Martinková, J. Marek, The deposition of globular polypyrrole and polypyrrole nanotubes on cotton textile, Appl. Surf. Sci. 356 (2015) 737–741.
[11] Y. Li, P. Bober, D.H. Apaydin, T. Syrový, S. Sariciftci, J. Hromádková, I. Sapurina, M. Trchová, J. Stejskal, Colloids of polypyrrole nanotubes/nanorods: a promising conducting ink, Synth. Met. 221 (2016) 67–74.
[12] M. Omastová, P. Bober, Z. Morávková, N. Peřinka, M. Kaplanová, T. Syrový, J. Hromádková, M. Trchová, J. Stejskal, Towards conducting inks: polypyrrole–silver colloids, Electrochim. Acta 122 (2014) 296–302.
[13] S. Ying, W.Q. Zheng, B.R. Li, X. She, H.B. Huang, L. Li, Z.L. Huang, Y.N. Huang, Z.T. Liu, X.H. Yu, Facile fabrication of elastic conducting polypyrrole nanotube aerogels, Synth. Met. 218 (2016) 50–55.
[14] J.S. Jang, H.S. Yoon, Facile fabrication of polypyrrole nanotubes using reverse microemulsion polymerization, Chem. Commun. 6 (2003) 720–721.
[15] M.Q. Xue, F.W. Li, D. Chen, Z.H. Yang, X.W. Wang, J.H. Ji, High-oriented polypyrrole nanotubes for next-generation gas sensor, Adv. Mater. 28 (2016) 8265–8270.
[16] W. Yan, J. Han, Synthesis and formation mechanism study of rectangular-sectioned polypyrrole micro/nanotubules, Polymer 48 (2007) 6782–6790.
[17] J.T. Feng, W. Yan, L.Z. Zhang, Synthesis of polypyrrole micro/nanofibers via a self-assembly process, Microchim. Acta 166 (2009) 261–267.
[18] Y.P. Xue, X.F. Lu, Y. Xu, X.J. Bian, L.R. Kong, C. Wang, Controlled fabrication of polypyrrole capsules and nanotubes in the presence of rhodamine B, Polym. Chem. 1 (2010) 1602–1605.
[19] Y.J. Wang, P. Liu, C. Yang, B. Mu, A.Q. Wang, Improving capacitance performance of attapulgite/polypyrrole composites by introducing rhodamine B, Electrochim, Acta 89 (2013) 422–428.
[20] J. Stejskal, M. Trchová, Conducting polypyrrole nanotubes: a review, Chem. Pap. 72 (2018) 1563–1595.
[21] Y. Li, P. Bober, M. Trchová, J. Stejskal, Polypyrrole prepared in the presence of methyl orange and ethyl orange: nanotubes versus globules in conductivity enhancement, J. Mater. Chem. C 5 (2017) 4236–4245.
[22] J. Stejskal, M. Trchová, P. Bober, Z. Morávková, D. Kopecký, M. Vrňata, J. Prokeš, M. Varga, E. Watzlová, Polypyrrole salts and bases: superior conductivity of nanotubes and their stability towards the loss of conductivity by deprotonation, RSC Adv. 6 (2016) 88382–88391.
[23] B. Boukoussa, A. Hakiki, S. Moulai, K. Chikh, D.E. Kherroub, L. Bouhadjar, D. Guedal, K. Messaoudi, F. Mokhtar, R. Hamacha, Adsorption behaviors of cationic and anionic dyes from aqueous solution on nanocomposite polypyrrole/SBA-15, J. Mater. Sci. 53 (2018) 7372–7386.
[24] A. Karimi, S.W. Husain, M. Hosseini, P.A. Azar, M.R. Ganjali, Rapid, sensitive detection of hydrogen peroxide in milk by enzyme-free electrochemiluminescence

sensor based on a polypyrrole-cerium oxide nanocomposite, Sens. Actuator B 271 (2018) 90–96.
[25] D.M.G. Preethichandra, E.M.I. Mala Ekanayake, M. Onoda, K. Kaneto, Performance enhancement of polypyrrole based nano-biosensors by different enzyme deposition techniques, in: S. Mukhopadhyay, K. Jayasundera, O. Postolache (Eds.), Modern Sensing Technologies. Smart Sensors, Measurement and Instrumentation, vol. 29, Springer, Cham, 2019.
[26] J.R. Hagler, B.N. Peterson, A.R. Murphy, J.M. Leger, Performance of biocompatible silk-polypyrrole actuators under biologically relevant conditions, J. Appl. Polym. Sci. 136 (2019) 46922.
[27] M. Sharma, G.I. Waterhouse, S.W. Loader, S. Garg, D. Svirskis, High surface area polypyrrole scaffolds for tunable drug delivery, Int. J. Pharm. 443 (2013) 163–168.
[28] K. Bouzek, K.M. Mangold, K. Jüttner, Electrocatalytic activity of platinum modified polypyrrole films for the methanol oxidation reaction, J. Appl. Electrochem. 31 (2001) 501–507.
[29] K. Jurewicz, S. Delpeux, V. Bertagna, F. Beguin, E. Frackowiak, Supercapacitors from nanotubes/polypyrrole composites, Chem. Phys. Lett. 347 (2001) 36–40.
[30] H.K. Song, G.T.R. Palmore, Redox-active polypyrrole: toward polymer-based batteries, Adv. Mater. 18 (2006) 1764–1768.
[31] J. Stejskal, Strategies towards the control of one-dimensional polypyrrole nanomorphology and conductivity, Polym. Int. 67 (2018) 1461–1469.
[32] F. Würthner, T.E. Kaiser, C.R. Saha-Möller, J-aggregates: from serendipitous discovery to supramolecular engineering of functional dye materials, Angew. Chem. Int. Ed. 50 (2011) 3376–3410.
[33] R. Pauliukaite, A. Selskiene, A. Malinauskas, C.M.A. Brett, Electrosynthesis and characterisation of poly (safranine T) electroactive polymer films, Thin Solid Films 517 (2009) 5435–5441.
[34] X.M. Yang, Z.X. Zhu, T.Y. Dai, Y. Lu, Facile fabrication of functional polypyrrole nanotubes via a reactive self-degraded template, Macromol. Rapid Commun. 26 (2005) 1736–1740.
[35] G. Ćirić-Marjanović, N.V. Blinova, M. Trchová, J. Stejskal, Chemical oxidative polymerization of safranines, J. Phys. Chem. 111 (2007) 2188–2199.
[36] D. Sarkar, P. Das, A. Girigoswami, N. Chattopadhyay, Spectroscopic characterization of phenazinium dye aggregates in water and acetonitrile media: effect of methyl substitution on the aggregation phenomenon, J. Phys. Chem. A 112 (2008) 9684–9691.
[37] U. Acharaya, P. Bober, M. Trchová, A. Zhigunov, J. Stejskal, J. Pfleger, Synergistic conductivity increase in polypyrrole/molybdenum disulfide composite, Polymer 150 (2018) 130–137.
[38] M. Trchová, J. Stejskal, Resonance Raman spectroscopy of conducting polypyrrole nanotubes: disordered surface versus ordered body, J. Phys. Chem. A 122 (2018) 9298–9306.

Supporting Information for:

Cationic dyes as morphology-guiding agents for one-dimensional polypyrrole with improved conductivity

Islam M. Minisy[a,b], Patrycja Bober[a,*], Udit Acharya[a,c], Miroslava Trchová[a], Jiřina Hromádková[a], Jiří Pfleger[a] and Jaroslav Stejskal[a]

[a]*Institute of Macromolecular Chemistry, Academy of Sciences of the Czech Republic, 162 06 Prague 6, Czech Republic*

[b]*Faculty of Science, Charles University, 128 43 Prague 2, Czech Republic*

[c]*Faculty of Mathematics and Physics, Charles University, 182 00 Prague 8, Czech Republic*

[*] Corresponding author. E-mail address: bober@imc.cas.cz (P. Bober).

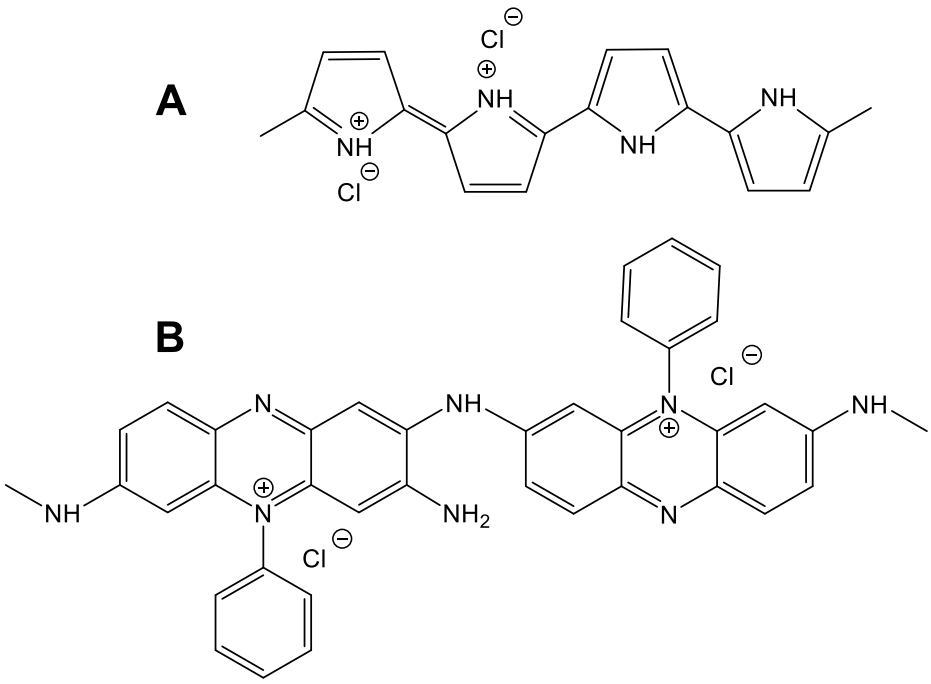

Scheme S. (A) Polypyrrole salt and (B) the hypothetical structure of phenosafranin oligomers proposed in the literature [33,35].

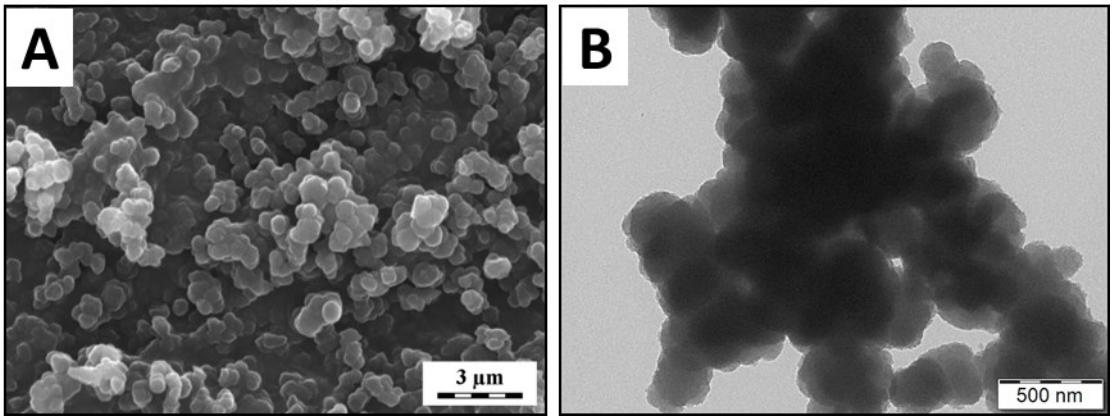

Fig. S1. (A) Scanning and (B) transmission electron micrographs of standard globular polypyrrole.

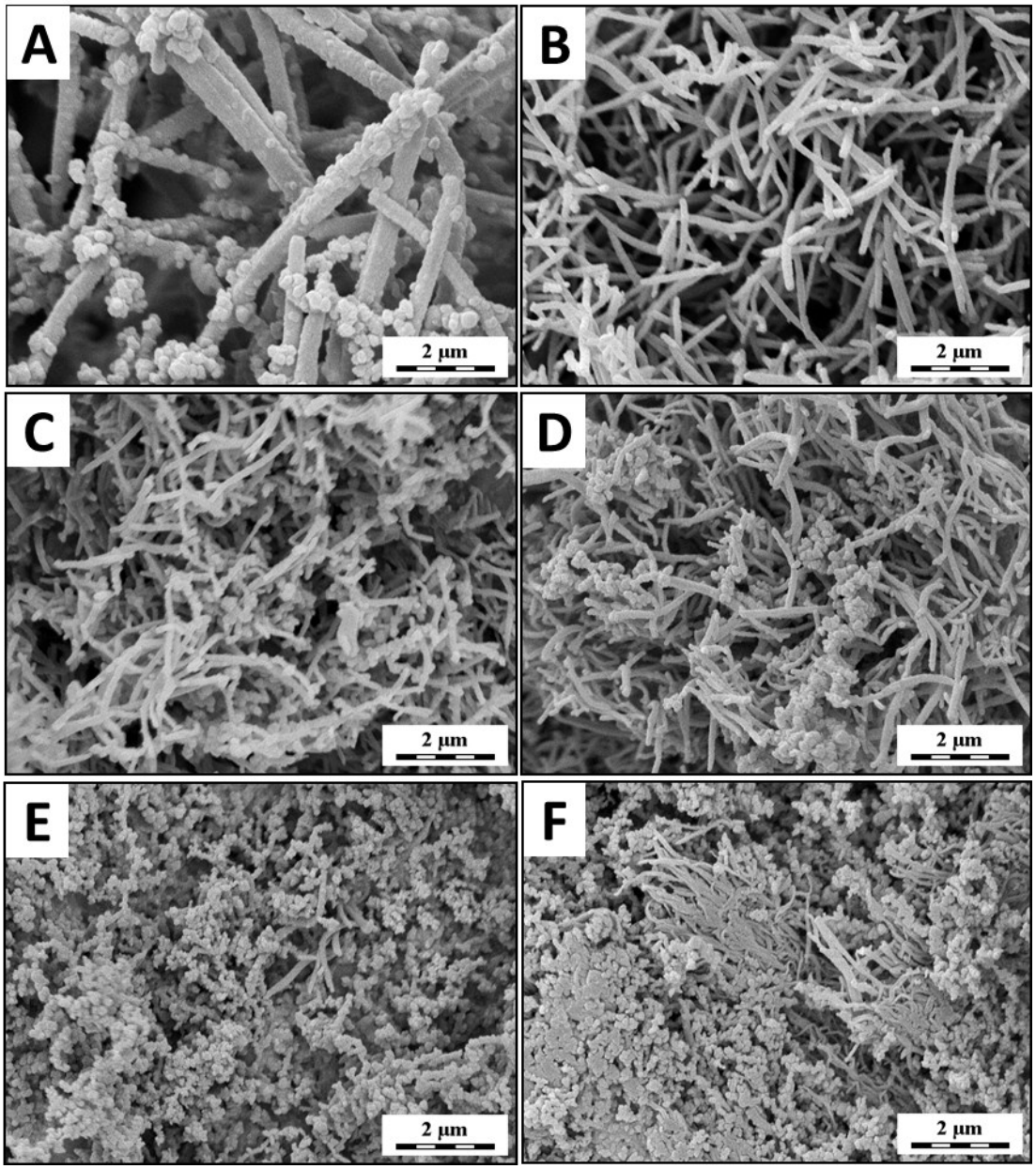

Fig. S2. Polypyrrole prepared with different mole ratios [oxidant]/[pyrrole] (A) 1, (B) 2, (C) 3.5,(D) 5, (E) 10 and (F) 15; 0.2 M pyrrole and 4 mM safranin.

Appendix 2

Methyl red dye in the tuning of polypyrrole conductivity

Polymer 207 (2020) 122854

Contents lists available at ScienceDirect

Polymer

journal homepage: http://www.elsevier.com/locate/polymer

Methyl red dye in the tuning of polypyrrole conductivity

Islam M. Minisy [a,b], Patrycja Bober [a], Ivana Šeděnková [a], Jaroslav Stejskal [a,*]

[a] Institute of Macromolecular Chemistry, Academy of Sciences of the Czech Republic, 162 06 Prague 6, Czech Republic
[b] Faculty of Science, Charles University, 128 43 Prague 2, Czech Republic

ARTICLE INFO

Keywords:
Conducting polymers
Methyl red
Polypyrrole

ABSTRACT

Polypyrrole was prepared by the oxidation of pyrrole with iron(III) chloride in aqueous medium in the presence of methyl red dye. While the acid form of dye had no effect on the polypyrrole synthesis, the presence of its sodium salt increased the conductivity from 1–5 S cm^{-1} up to 84 S cm^{-1} for the polymerizations carried out with variable dye concentration at 20 °C. When the reaction temperature was reduced to −50 °C, the conductivity increased up to 104 S cm^{-1}. At temperatures below −20 °C, the polymerization took place in frozen reaction medium, in ice. The morphology of polypyrrole was mainly globular and often converted to particles of irregular size and shape. It was concluded that one-dimensional morphology, nanotubes or nanofibers characteristic of polypyrrole, is not an automatic prerequisite for the high conductivity of this polymer.

1. Introduction

Conducting polymers represent a special category of macromolecular compounds endowed with conductivity at semiconductor level as a fundamental property. The enhancement of conductivity of probably the most important representative, polypyrrole, became the topical issue in recent years [1–7]. Polypyrrole is prepared as a rule by the oxidation of pyrrole with iron(III) chloride in aqueous medium (Fig. 1). The introduction of organic dyes into the reaction mixture has often been observed to affect the conductivity in positive manner [1–5,8–10]. While the typical conductivity of pyrrole is of the order of 1 S cm^{-1}, it can be enhanced above 50 S cm^{-1} by the addition of methyl orange dye during the polymerization [1,8,9].

Many applications, however, do not rely on the conductivity, and the adsorption of organic dyes or their photocatalytic decomposition in water-pollution treatment comes to the forefront [11]. The morphology of conducting polymers and associated specific surface area become of importance in these cases. Here again, organic dyes may be helpful as the presence of some of them converts the classical globular morphology of polypyrrole to nanotubes or nanofibers with enhanced specific surface area [4,10]. Methyl orange is again the classical example of a dye widely used in the literature for the preparation of polypyrrole nanotubes [1,2,8–10,12–17].

Especially the carbonization of one-dimensional polypyrrole nanotubes became of additional interest for the design of new nitrogen-containing carbons [12,13,18–22] applicable as dye adsorbents, electrodes of supercapacitors, and supports for electrocatalysts or catalysts [22–26]. In these cases, the specific surface area of polypyrrole precursor becomes an important parameter in addition to the conductivity.

Conducting polymers and many organic dyes share some features in common [11]. Both species have conjugated molecular structure incorporating aromatic rings that is responsible for their colour, they are both ionic compounds. For that reason, they may interact by ionic bonding, π–π attractions, hydrogen bonds and other interactions may also be involved. Thanks to these interactions the organic dyes may affect the morphology and properties of polypyrrole during the synthesis, however, usually in unpredictable manner [10]. Being inspired by the success of methyl orange in the control of polypyrrole conductivity and morphology, closely related azo dyes have been tested, Orange I [27] or ethyl orange being examples [1] (Fig. 2). The conductivity was indeed improved when ethyl orange was added during the preparation of polypyrrole, but the polymer morphology remained strictly globular. During the screening of the effect of various dyes [10], methyl red also provided the best results in the conductivity enhancement for polypyrrole. Methyl red was used as a *p*-type dopant for another conducting polymer when forming charge-transfer complex [28]. For that reason, the influence of this dye on the properties of resulting polypyrrole has been investigated in more detail and the results are reported in the present communication.

* Corresponding author.
E-mail address: stejskal@imc.cas.cz (J. Stejskal).

https://doi.org/10.1016/j.polymer.2020.122854
Received 15 May 2020; Received in revised form 15 July 2020; Accepted 25 July 2020
Available online 27 July 2020

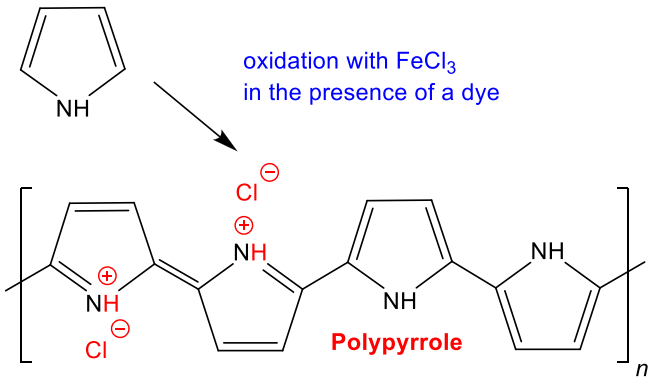

Fig. 1. Pyrrole is oxidized with iron(III) chloride to polypyrrole hydrochloride. An organic dye may be used to modify this process.

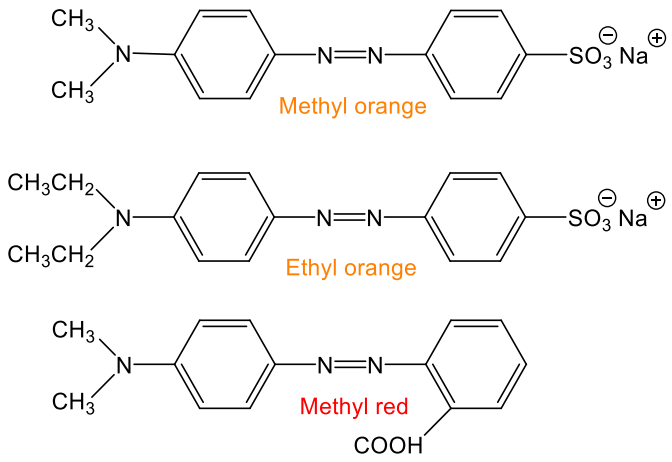

Fig. 2. Methyl orange, ethyl orange sodium salts and methyl red acid. (For interpretation of the references to colour in this figure legend, the reader is referred to the Web version of this article.)

2. Experimental

2.1. Preparation

A series of polypyrroles was prepared by the polymerization of pyrrole (0.2 M, 1.34 g per 100 mL; Sigma-Aldrich) containing methyl red sodium salt (Sigma-Aldrich) in the concentration range 0–0.01 M. Iron(III) chloride hexahydrate (0.5 M, 13.5 g per 100 mL; Sigma-Aldrich) was used as an oxidant. The polymerization mixtures were stirred for a few seconds then kept for 24 h at room temperature (20 ± 2 °C) without disturbance. Dark precipitates were then collected by filtration, washed with 0.2 M hydrochloric acid, followed by ethanol, and then left to dry in open air until constant weight was achieved.

Another series of polypyrrole was prepared at various temperatures in the range −50 to 50 °C following the same procedure mentioned above at fixed methyl red concentration (0.006 M, 0.174 g per 100 mL) corresponding to the maximum conductivity of polypyrrole prepared at room temperature. When needed, solutions were precooled in water/ethylene glycol bath adjusted to the sub-zero temperature. The mixtures were left to polymerize for 24 h at the selected temperatures. For the preparation of polypyrrole at −24 °C and −50 °C, these were immediately frozen in solid carbon dioxide/ethanol bath at −78 °C then transferred to freezers set at −24 °C for 1 day or −50 °C for 10 days until reaction mixture turned black since decreasing the polymerization temperature is reducing the polymerization rate. Polypyrrole powders were collected by filtration after thawing, then washed and dried as mentioned above.

2.2. Characterization

Morphology of prepared polypyrrole powders was characterized by using a MAIA3 TESCAN scanning electron microscope (SEM) and TECNAI G2 SPIRIT transmission electron microscope (TEM). Conductivity of samples were determined at room temperature using van der Pauw method with pellets of 13 mm diameter and 1 ± 0.05 mm thickness. A manual hydraulic press (Trystom H-62) operating at 540 MPa was used for pellet preparation. Fourier-transform infrared spectra (FTIR) of the powders dispersed in the potassium bromide pellet spectra were recorded in the range 400–4000 cm^{-1} using a Thermo Nicolet NEXUS

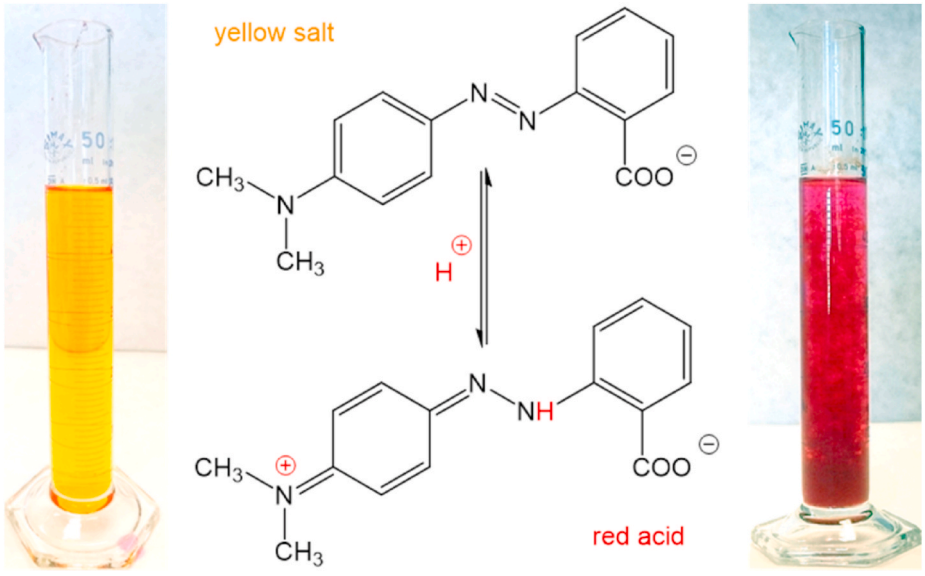

Fig. 3. Water-soluble yellow methyl red salt converts to insoluble methyl red acid upon protonation under acidic conditions. The transition takes place at pH 4.4–6.2. (For interpretation of the references to colour in this figure legend, the reader is referred to the Web version of this article.)

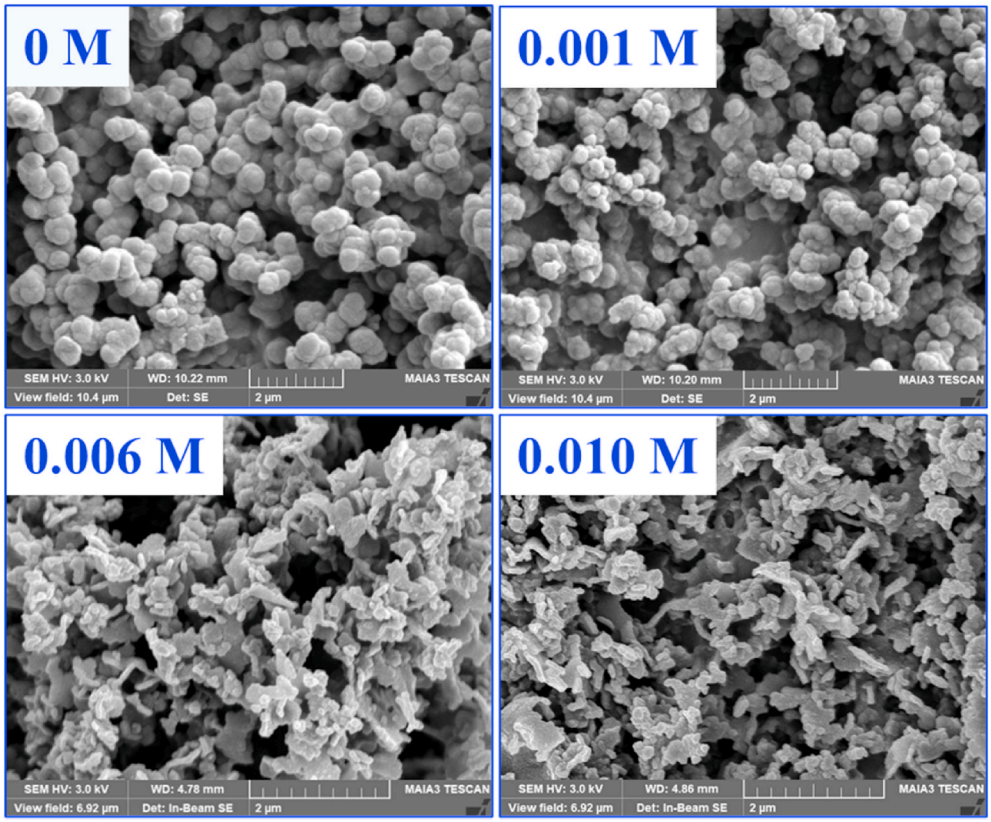

Fig. 4. Morphology of polypyrrole prepared at room temperature in the absence and in the presence of methyl red salt at 0.001, 0.006, 0.010 M concentration at 20 °C. (For interpretation of the references to colour in this figure legend, the reader is referred to the Web version of this article.)

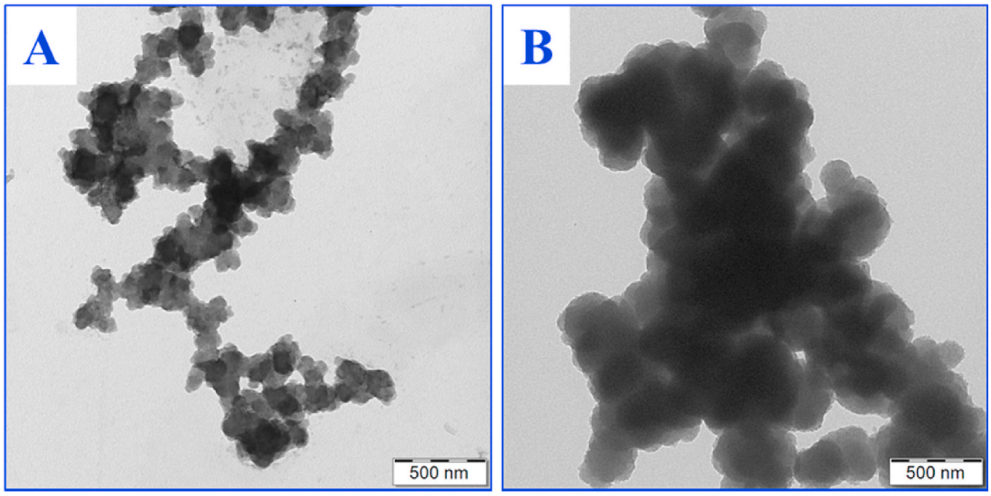

Fig. 5. Transmission electron micrographs of (A) polypyrrole prepared in the presence of methyl red salt (0.006 M) and (B) in the dye absence. (For interpretation of the references to colour in this figure legend, the reader is referred to the Web version of this article.)

Spectrometer equipped with DTGS detector. Raman spectra were recorded with a Renishaw InVia Raman microspectrometer. The excitation lines 514 nm and 785 nm were used.

3. Results and discussion

3.1. Preparation

Most of organic anionic dyes are commercially available as sodium salts due to their good solubility in water. Methyl red is an exception to this rule when both acid and sodium salt are supplied by Sigma-Aldrich. The preparation of polypyrrole in the first experiments involving acid form was rather disappointing. The presence of the dye had no effect at all on polypyrrole properties. The conductivity of polypyrrole was 2.9 S cm^{-1}, *i.e.* within the range of polypyrrole prepared repeatably in the dye absence, 1.5–4.4 S cm^{-1}. The globular morphology was also not affected. On the other hand, the analogous synthesis carried out in the presence of methyl red sodium salt yielded polypyrrole with strongly enhanced conductivity.

The clue to this observation is the solubility of the dye in the reaction

Table 1
Morphology and maximum conductivity of polypyrrole achieved when varying dye concentration in the reaction mixture at fixed monomer and oxidant molar concentrations, [Py] and [$FeCl_3$]. 20 °C.

Dye	[Py]/[$FeCl_3$]	Polypyrrole morphology	Maximum conductivity, S cm^{-1}	Reference
No dye	0.2/0.5	globules	1–5	[1,32–34]
Ethyl orange	0.05/0.05	globules	22	[1]
Safranin	0.2/0.5	nanorods	35	[5]
Methyl orange	0.05/0.05	nanotubes	40–50	[1,33]
Acid Blue 25	0.2/0.5	nanofibers	60	[3]
Methyl red	0.2/0.5	irregular	64, 84	this study

medium. Methyl red in acid form is insoluble in the reaction medium (Fig. 3) similarly like methyl orange [1]. When introduced in the reaction mixture, it does not affect the formation of polypyrrole in any way, and the morphology and conductivity corresponded to the preparation in the dye absence.

The use of the soluble methyl red salt follows another fate. Once the strongly acidic oxidant solution is added to the dye-containing solution of pyrrole, methyl red converts to its insoluble form and starts to precipitate. The forming precipitate acts as the adsorption site for pyrrole oligomers that it followed by the growth of polypyrrole chains [29]. The final morphology of polypyrrole is affected by the balance between both precipitation processes involving the dye and pyrrole oligomers. Such a template-supported growth of polypyrrole is believed to produce a better organization of polymer chains providing in addition to the morphology changes also an enhanced conductivity. The similar conductivity improvement based on the same principle has earlier been reported for methyl orange [1]. The synergistic effect, when the polypyrrole-coated substrate has a higher conductivity than separate components, has indeed been reported in the literature [30,31].

3.2. Morphology

Polypyrrole prepared in the absence of any dye has a typical globular morphology. Even a small concentration of a methyl red dye, 0.001 M, reduces the size of globules (Fig. 4). Above 0.002 M dye concentration, the polymer morphology changes to irregular flakes. Finally, at 0.010 M dye concentration, the features of morphology become preserved. We note that the presence of a similar dye, methyl orange, at the same concentration range led to the conversion of globules to nanotubes [1]. Another dye, ethyl orange, has not affected the type of morphology which remained globular.

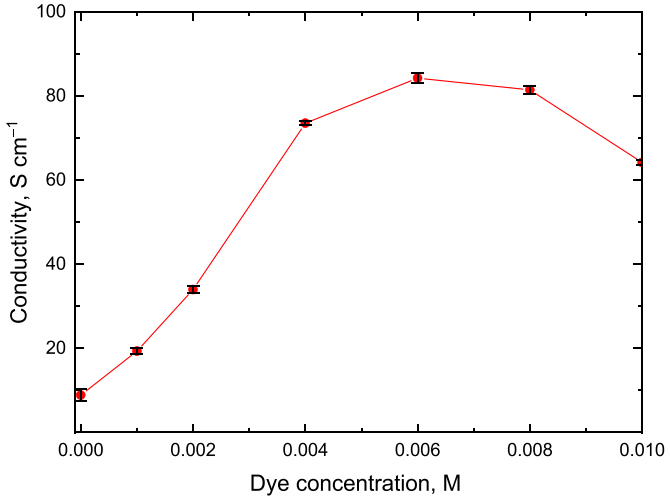

Fig. 6. The dependence of conductivity of polypyrrole on molar concentration of methyl red sodium salt in the reaction mixture. [Pyrrole] = 0.2 M, [$FeCl_3$] = 0.5 M; 20 °C. (For interpretation of the references to colour in this figure legend, the reader is referred to the Web version of this article.)

At closer inspection, the transmission electron microscopy reveals that the fragmentary morphology is represented by the irregular aggregates of small polypyrrole granules (Fig. 5A) that distinctly differ from the ordinary globular morphology originating in the dye absence (Fig. 5B). The trend of the reduction of the particle size with increasing dye concentration is clearly visible. The dye, represented by the hydrophilic carboxyl group and hydrophobic body, acts similarly like as a surfactant in this case.

3.3. Conductivity

It is tempting to correlate the polypyrrole conductivity with the morphology type. Polypyrrole prepared in the absence of dyes has a typical globular morphology and conductivity 1–5 S cm^{-1} [1,32–34]. In the presence of dyes at the order of 0.001 M concentration, the globular morphology either remained globular [1], or converted to one-dimensional nanotubes [1,33], nanofibers [3], nanorods [5] or to irregular globular aggregates in the present study (Table 1) depending on dye ability to form aggregates in acidic medium based on the dye pK_a, hydrophobicity and aggregation rate [1,3,35]. The conductivity substantially increased at the same time. This means that organic dyes may affect both the morphology and the conductivity of polypyrrole, but the effects on these entities are not in direct correlation.

The size of objects is another feature to consider. It has been reported that thinner nanotubes have higher conductivity than thick ones [29]. The unambiguous correlation between the conductivity and the specific surface area has been observed [1,36]. This was interpreted by better ordering of polymer chains in thinner or smaller objects compared with larger or thicker ones that contain less conducting disordered part. This trend is also supported by comparing the morphology (Fig. 4) and conductivity (Fig. 6) in present experiments. The largest polypyrrole globules prepared in the absence of a dye have the lowest conductivity.

3.4. Liquid and frozen reaction media

Reaction temperature is another parameter to be considered in the optimization of the morphology and conductivity. A series of polymerizations has been performed at various temperatures between 50 °C and −50 °C at fixed methyl red concentration (0.006 M) corresponding to the maximum conductivity of polypyrrole prepared at room temperature. The polypyrrole morphology became coarser as the reaction temperature was reduced and at −50 °C an unresolved morphology without any typical features was observed (Figs. 7 and 8).

The aqueous reaction mixtures freeze only below *ca* −20 °C due to the high concentration of iron(III) chloride salt present in the medium. It is well known that the polymerizations of both aniline and pyrrole [37–40] proceed easily in the frozen aqueous media, *i.e.* in ice. This was explained by the electron and proton transfer between the monomer and oxidant through the body of conducting polymer [41] without the need of the reactants to diffuse and meet each other in order to react. It is obvious that the size of ice crystals may become additional parameter to be able to affect the polypyrrole formation [37].

An inverse relationship between the polymerization temperature and the conductivity of the produced polypyrrole powders was found (Fig. 9). It was previously observed that by the decreasing of the

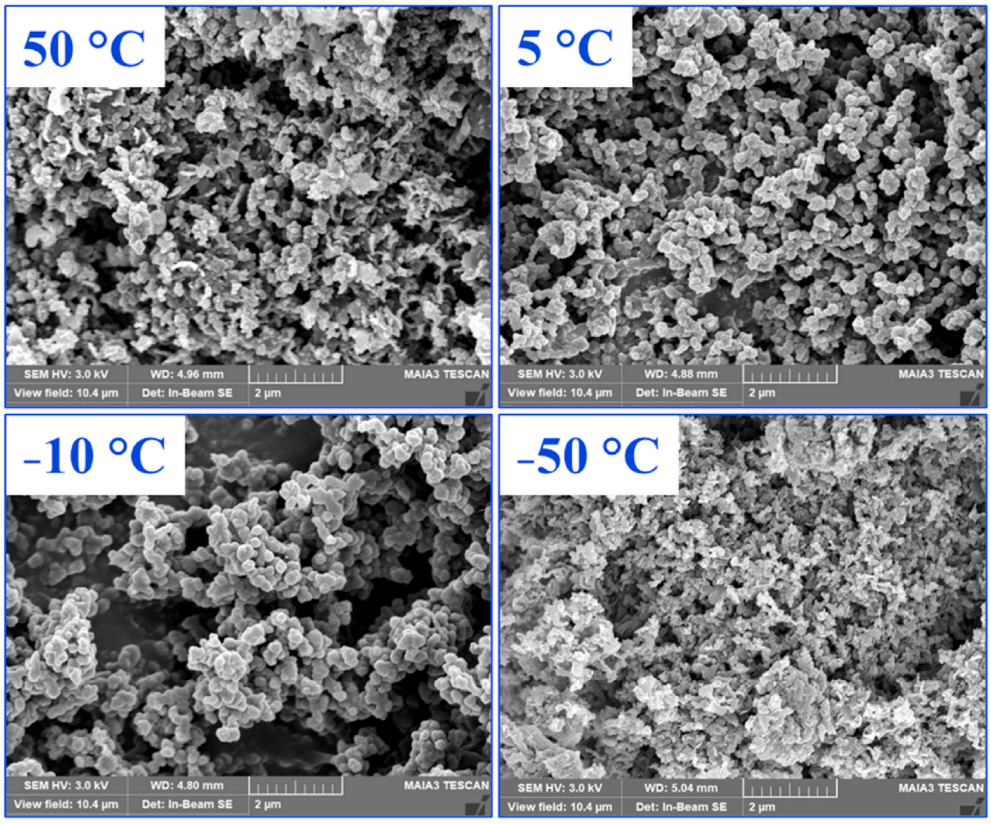

Fig. 7. Scanning electron microscopy of polypyrrole prepared at various temperatures in the presence of 0.006 M methyl red salt. (For interpretation of the references to colour in this figure legend, the reader is referred to the Web version of this article.)

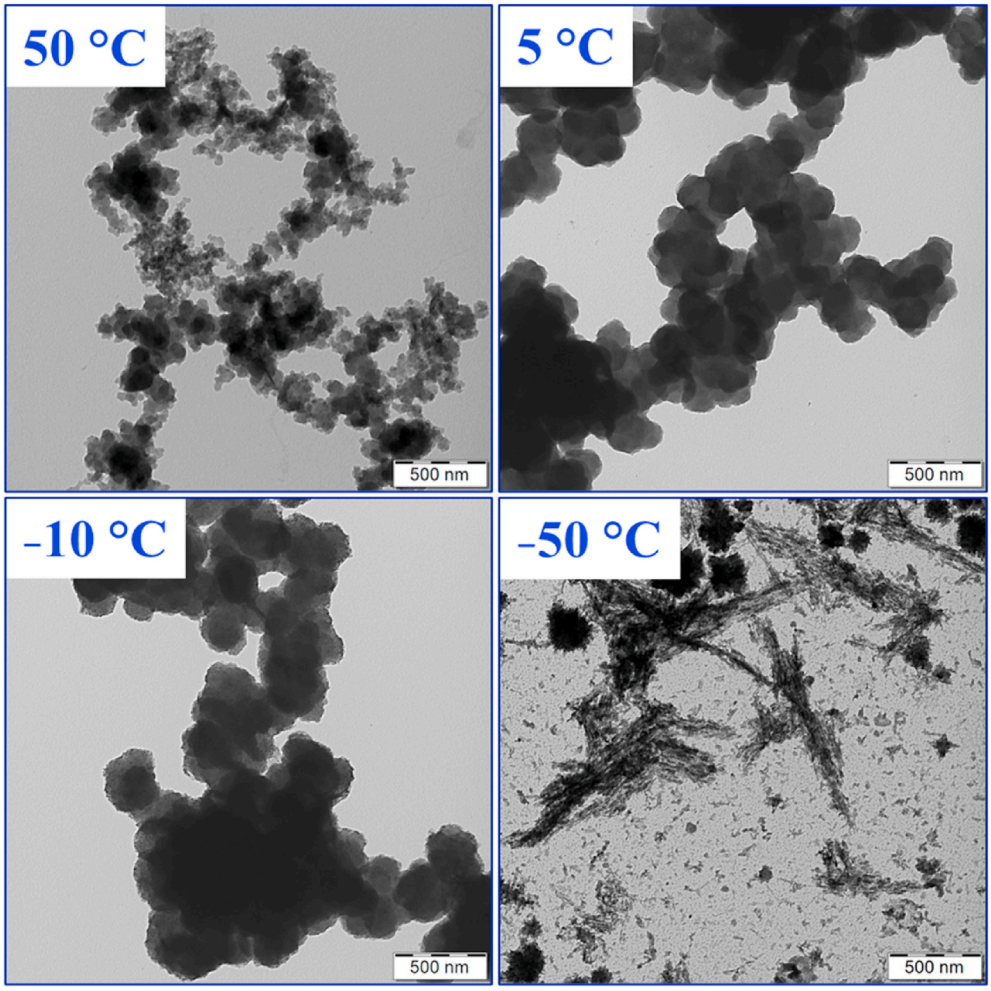

Fig. 8. Transmission electron microscopy of polypyrrole prepared at various temperatures in the presence of 0.006 M methyl red salt. (For interpretation of the references to colour in this figure legend, the reader is referred to the Web version of this article.)

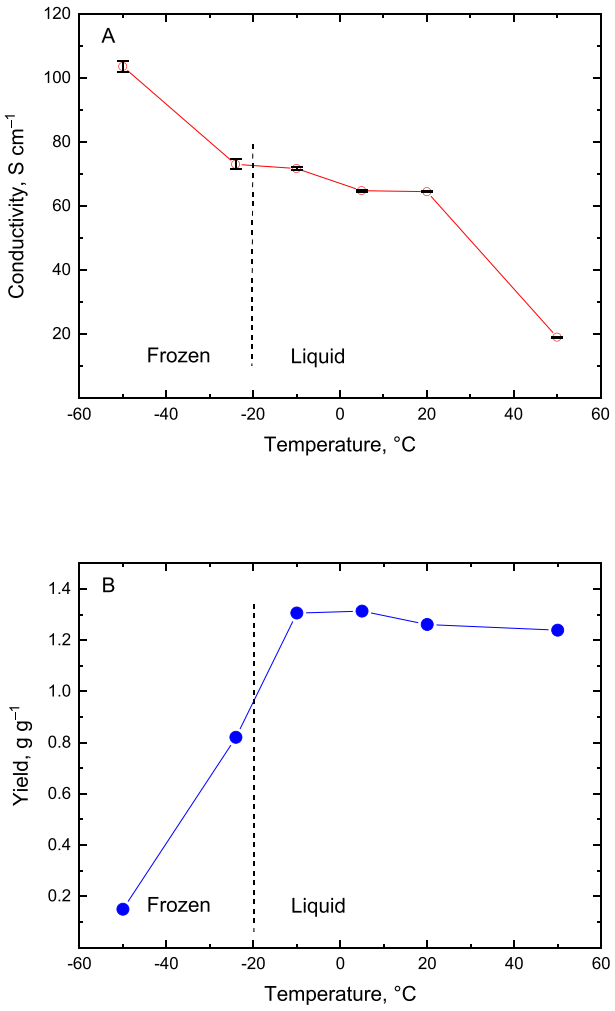

Fig. 9. The dependence of (A) conductivity and (B) the yield of polypyrrole on the temperature of synthesis. [Pyrrole] = 0.2 M, [$FeCl_3$] = 0.5 M, [methyl red] = 0.006 M. (For interpretation of the references to colour in this figure legend, the reader is referred to the Web version of this article.)

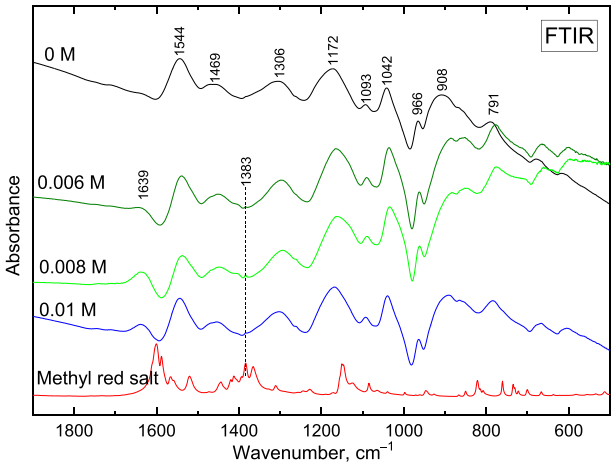

Fig. 10. FTIR spectra of methyl red and polypyrrole prepared with various concentration of methyl red. (For interpretation of the references to colour in this figure legend, the reader is referred to the Web version of this article.)

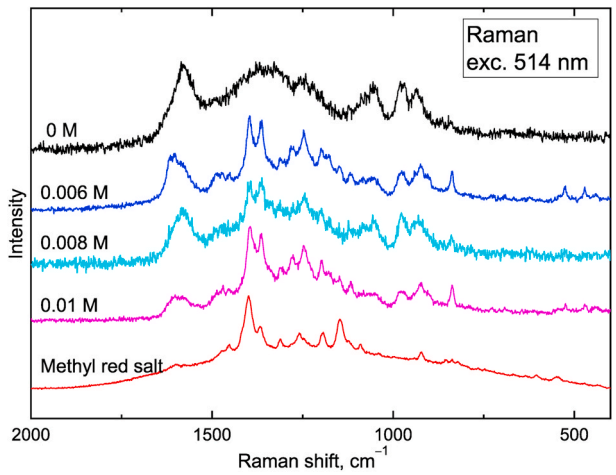

Fig. 11. Raman spectra (excitation line 514 nm) of polypyrrole with various concentration of methyl red. (For interpretation of the references to colour in this figure legend, the reader is referred to the Web version of this article.)

polymerization temperature, more organized polypyrrole chains with less defects and longer conjugation length are formed [4,42,43]. Polypyrrole prepared at 50 °C has the lowest conductivity, 19 S cm^{-1}, while that prepared at −50 °C the highest one, 104 S cm^{-1} (Fig. 9).

The polymerization of pyrrole is an exothermic reaction [44], and the optimum polymerization temperature was found to be at 5 °C where the highest yield was obtained. At lower polymerization temperatures (−50 and −24 °C), the polymerization takes place in frozen solid-state; this restricts pyrrole molecules to diffuse, which decreases the yield. Above room temperature (50 °C), the polymerization rate was higher with a slight decrease in the yield due to overoxidation and hydrolytic side reactions induced by elevated temperature [45,46].

3.5. FTIR and Raman spectroscopy

The formation of polypyrrole was confirmed by the FTIR spectra (Fig. 10). The typical bands of polypyrrole are observed at 1544 cm^{-1} (C–C stretching vibrations of the polypyrrole ring), 1469 cm^{-1} (C–N stretching band), 1306 cm^{-1} (deformation modes of C–N and C–H bond), 1172 cm^{-1} (breathing mode of the polypyrrole salt), 1042 cm^{-1} (in plane deformation of the C–N and N–H bond) and the band at 908 assigned to the out-of-plane deformation modes of the C–H group [47]. These main bands of polypyrrole remains virtually unchanged in the spectra of polypyrroles prepared with various concentration of methyl red salt. The positions and relative intensities of polypyrrole bands are in accordance with the presence of conducting form of polypyrrole. The polypyrrole prepared with higher concentration of methyl red salt were harder to disperse in the potassium bromide pellets, therefore the spectra contain the bands at 1639 cm^{-1} and 3430 cm^{-1} (not shown) connected with the stretching and deformation modes of OH group respectively, due to the water adsorbed in the pellet.

The spectra of polypyrrole prepared at higher concentration of methyl red salt confirm the presence of the dye as the band at 1383 cm^{-1} linked to the stretching vibration of the –N=N– bond together with the vibrations of the amino group [48]. The most intensive band from the spectrum of methyl red salt at 1600 cm^{-1} assigned to the breathing vibration of the benzene ring is not observed in the spectrum of the polypyrroles prepared in the presence of the dye.

The presence of methyl red is reflected in the Raman spectra excited by the laser at 514 nm as the excitation line is close to the electronic absorption of methyl red and the spectrum of the dye is enhanced (Fig. 11). The bands from the spectrum of the methyl red salt are shifted due to the acid–base transition to the methyl red acid. The enhanced bands of methyl red in the Raman spectra observed with 514 nm

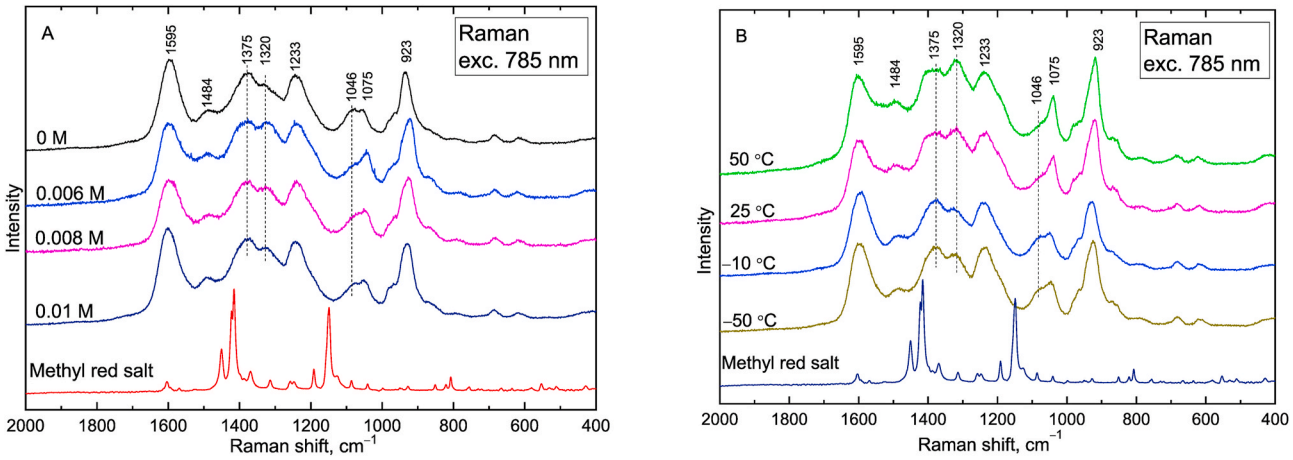

Fig. 12. Raman spectra of polypyrrole (A) prepared at various dye concentration and (B) at different temperatures at fixed 0.006 M methyl red concentration. Excitation wavelength 785 nm. (For interpretation of the references to colour in this figure legend, the reader is referred to the Web version of this article.)

excitation do not show any dependence on the dye concertation or on the preparation temperature.

The excitation line 785 nm was also used to study the molecular structure of polypyrrole (Fig. 12). The main bands, described in detail in Ref. [36], are found at 1595 cm^{-1} (stretching mode of C═C bond and inter-ring C–C bond), 1484 cm^{-1} (stretching skeletal, or C–C or C–N, vibrations), 1375 cm^{-1} (inter-ring stretching vibrations of C–N bond in the oxidized pyrrole units), 1320 cm^{-1} (inter-ring stretching vibrations of C–N bond in the neutral pyrrole units), 1233 cm^{-1} (in-plane deformation vibration of the C–H bond), 1046 cm^{-1} with the shoulder at 1075 cm^{-1} (C–H in plane deformation vibrations) and 923 cm^{-1} (in plane deformation vibration of the pyrrole ring). The ratio between neutral and oxidized (doped) units in the polypyrrole is reflected by the ratio of the bands at 1375 and 1320 cm^{-1} and by the intensity of the shoulder at 1075 cm^{-1} in comparison to the main maximum at 1046 cm^{-1} [36]. The presence of the methyl red increases the relative intensity of the bands linked to the neutral units of polypyrrole. The decrease in the temperature leads to the increase in the concentration of polarons/bipolarons states.

4. Conclusions

The presence of methyl red salt in the preparation of polypyrrole has led to the conductivity enhancement from 1–5 S cm^{-1} up to maximum 84 S cm^{-1} depending on the dye concentration. The morphology of polypyrrole, however, was neither globular nor nanotubular, as typical of polypyrrole prepared in the absence of dyes and in the presence of methyl orange, respectively, and irregular particulate fragments dominated. When the reaction temperature was reduced to −50 °C, the conductivity gradually increased to 104 S cm^{-1}. The morphology at the lowest preparation temperature was still rather unresolved with some atypical objects with starburst pattern being present. One-dimensional morphology of polypyrrole, nanofibers or nanotubes, is thus not an automatic prerequisite for the high conduction of polypyrrole, and the conductivity above 100 S cm^{-1} can be achieved even with other nanostructures. FTIR and Raman spectroscopies demonstrate that polypyrrole has been obtained at all polymerization temperatures (50 to –50 °C) and the concentration of polarons/bipolarons states increased with decreasing the polymerization temperature.

CRediT authorship contribution statement

Islam M. Minisy: Methodology, Investigation, Writing - original draft. **Patrycja Bober:** Conceptualization, Supervision. **Ivana Šeděnková:** Methodology, Writing - review & editing. **Jaroslav Stejskal:** Writing - review & editing, Funding acquisition.

Declaration of competing interest

The authors declare that they have no known competing financial interests or personal relationships that could have appeared to influence the work reported in this paper.

Acknowledgments

The authors wish to thank The Czech Science Foundation (19-04859S) for financial support. Ms. J. Hromádková and Dr. J. Prokeš are acknowledged for performing electron microscopy and conductivity measurements, respectively.

References

[1] Y. Li, P. Bober, M. Trchová, J. Stejskal, Polypyrrole prepared in the presence of methyl orange and ethyl orange: nanotubes versus globules in conductivity enhancement, J. Mater. Chem. C 5 (2017) 4236–4245, https://doi.org/10.1039/C7TC00206H.
[2] D. Kopecký, M. Varga, J. Prokeš, M. Vrňata, M. Trchová, J. Kopecká, M. Václavík, Optimization routes for high conductivity of polypyrrole nanotubes prepared in the presence of methyl orange, Synth. Met. 230 (2017) 89–96, https://doi.org/10.1016/j.synthmet.2017.06.004.
[3] P. Bober, Y. Li, U. Acharya, Y. Panthi, J. Pfleger, P. Humpolíček, M. Trchová, J. Stejskal, Acid Blue dyes in polypyrrole synthesis: the control of polymer morphology at nanoscale in the promotion of high conductivity and the reduction of cytotoxicity, Synth. Met. 217 (2018) 40–49, https://doi.org/10.1016/j.synthmet.2018.01.010.
[4] J. Stejskal, M. Trchová, Conducting polypyrrole nanotubes: a review, Chem. Pap. 72 (2018) 1563–1595, https://doi.org/10.1007/s11696-018-0394x.
[5] I.M. Minisy, P. Bober, U. Acharya, M. Trchová, J. Hromádková, J. Pfleger, J. Stejskal, Cationic dyes as morphology-guiding agents for one-dimensional polypyrrole with improved conductivity, Polymer 174 (2019) 11–17, https://doi.org/10.1016/j.polymer.2019.04.045.
[6] J.Y. Bo, X.F. Luo, H.B. Huang, L. Li, W. Lai, X.H. Yu, Morphology-controlled fabrication of polypyrrole hydrogel for solid-state supercapacitor, J. Power Sources 407 (2018) 105–111, https://doi.org/10.1016/j.jpowsour.2018.10.064.
[7] H.J. Liu, Q. Zhao, K.W. Wang, Z. Lu, F. Feng, Y. Guo, Facile synthesis of polypyrrole nanofiber (PPyNF)/NiO_x composites by a microwave method and application in supercapacitors, RSC Adv. 9 (2019) 6890–6897, https://doi.org/10.1039/c8ra09666j.
[8] X.M. Yang, Z.X. Zhu, T.Y. Dai, Y. Lu, Facile fabrication of functional polypyrrole nanotubes via a reactive self-degraded template, Macromol. Rapid Commun. 26 (2005) 1736–1740, https://doi.org/10.1002/marc.200500514.
[9] J. Kopecká, D. Kopecký, M. Vrňata, P. Fitl, J. Stejskal, M. Trchová, P. Bober, Z. Morávková, J. Prokeš, I. Sapurina, Polypyrrole nanotubes: mechanism of formation, RSC Adv. 4 (2014) 1551–1558, https://doi.org/10.1039/C3RA45841E.
[10] J. Stejskal, J. Prokeš, Conductivity and morphology of polyaniline and polypyrrole prepared in the presence of organic dyes, Synth. Met. 264 (2020), 116373, https://doi.org/10.1016/j.synthmet.2020.116373.
[11] J. Stejskal, Interaction of conducting polymers, polyaniline and polypyrrole with organic dyes: polymer morphology control, dye adsorption and photocatalytic

decomposition, Chem. Pap. 74 (2020) 1–54, https://doi.org/10.1007/s11696-019-00982-9.
[12] J.W. Lee, H.I. Lee, S.J. Park, Facile synthesis of petroleum-based activated carbons/tubular polypyrrole composites with enhanced electrochemical performance as supercapacitor electrode materials, Electrochim. Acta 263 (2018) 447–453, https://doi.org/10.1016/j.elecacta.2018.01.071.
[13] J. Lin, X.L. Xu, J. Wang, B.F. Zhang, D. Li, C. Wang, Y.L. Jin, J.B. Zhu, Nitrogen-doped hierarchically porous carbonaceous nanotubes for lithium ion batteries, Chem. Eng. J. 352 (2018) 964–971, https://doi.org/10.1016/j.cej.2018.06.057.
[14] B.M. Hryniewicz, R.V. Lima, L.F. Marchesi, M. Vidotti, Impedimetric studies about the degradation of polypyrrole nanotubes during galvanostatic change and discharge cycles, J. Electroanal. Chem. 855 (2019), 113636, https://doi.org/10.1016/j.jelechem.2019.113636.
[15] T.A. Le, N.Q. Tran, Y. Hong, H. Lee, Intertwined titanium carbide MXene within a 3 D Tangled polypyrrole nanowires matrix for enhanced supercapacitor performances, Chem. Eur J. 25 (2019) 1037–1043, https://doi.org/10.1002/chem.201804291.
[16] H. Mao, Z.Q. Cao, X. Guo, D.Y. Dyn, D.L. Liu, S.Y. Wu, Y. Zhang, X.M. Song, Ultrathin NiS/$NiOH_2$ nanosheets filled within ammonium polyacrylate-functionalized polypyrrole nanotubes as an unique nanoconfined system for nonenzymatic glucose sensors, ACS Appl. Mater. Interfaces 11 (2019) 10153–10162, https://doi.org/10.1021/acsami.8b20726.
[17] F.B. Pei, P. Wang, E.H. Ma, Q.S. Yang, H.X. Yu, J. Liu, H.H. Yin, Y.Y. Li, Q. Liu, Y. H. Dong, A sensitive label-free immunosensor for alpha fetoprotein detection using platinum nanodendrites loaded on functional MoS_2 hybridized polypyrrole nanotubes as signal amplifier, J. Electroanal. Chem. 835 (2019) 197–204, https://doi.org/10.1016/j.jelechem.2019.01.037.
[18] G. Ćirić-Marjanović, S. Mentus, I. Pašti, N. Gavrilov, J. Krstić, J. Travas-Sejdic, L. T. Strover, J. Kopecká, Z. Morávková, M. Trchová, J. Stejskal, Synthesis, characterization, and electrochemistry of nanotubular polypyrrole and polypyrrole-derived carbon nanotubes, J. Phys. Chem. C 118 (2014) 14770–14784, https://doi.org/10.1021/jp502862d.
[19] I. Sapurina, J. Stejskal, I. Šeděnková, M. Trchová, J. Kovářová, J. Hromádková, J. Kopecká, M. Cieslar, A. Abu El-Nasr, M.M. Ayad, Catalytic activity of polypyrrole nanotubes decorated with noble-metal nanoparticles and their conversion to carbonized analogues, Synth. Met. 214 (2016) 14–22, https://doi.org/10.1016/j.synthmet.2016.01.009.
[20] S.C. Xin, N. Yang, J. Zhao, L. Li, C. Teng, Three-dimensional polypyrrole-derived carbon nanotube framework for dye adsorption and and electrochemical supercapacitor, Appl. Surf. Sci. 414 (2017) 218–223, https://doi.org/10.1016/j.apsusc.2017.04.109.
[21] Z.P. Kang, Y.H.P.J. Zhang, Z.G. Zhu, A shriveled rectangular carbon tube with the concave surface for high-performance enzymatic glucose/O2 biofuel cells, Biosens. Bioelectron. 132 (2019) 76–83, https://doi.org/10.1016/j.bios.2019.02.044.
[22] I.M. Minisy, N. Gavrilov, U. Acharya, Z. Morávková, C. Unterweger, M. Mičušík, S. K. Filippov, J. Kredatusová, I.A. Pašti, S. Breitenbach, G. Ćirić-Marjanović, J. Stejskal, P. Bober, Tailoring of carbonized polypyrrole nanotubes core by different polypyrrole shells for oxygen reduction reaction selectivity modification, J. Colloid Interface Sci. 551 (2019) 184–194, https://doi.org/10.1016/j.jcis.2019.04.064.
[23] M.C. Wu, T.S. Zhao, R.H. Zhang, L. Wei, H.R. Jiang, Carbonized tubular polypyrrole with high activity for the Br_2/Br^- redox reaction in zinc-bromine flow batteries, Electrochim. Acta 284 (2018) 569–576, https://doi.org/10.1016/j.electacta.2018.07.192.
[24] D.J. Xiao, J. Ma, C.L. Chen, Q.M. Luo, J. Ma, L.R. Zheng, X. Zuo, Oxygen-doped carbonaceous polypyrrole nanotubes-supported Ag nanoparticle as electrocatalyst for oxygen reduction reaction in alkaline solution, Mater. Res. Bull. 105 (2018) 184–191, https://doi.org/10.1016/j.matresbull.2018.04.030.
[25] J.J. Dong, Y. Lin, H.W. Zong, H.B. Yang, Hierarchical LiFe5O8@PPy core-shell nanocomposites as electrode materials for supercapacitors, Appl. Surf. Sci. 470 (2019) 1043–1052, https://doi.org/10.1016/j.apsusc.2018.11.204.
[26] B.M. Hryniewicz, R.V. Lima, F. Wolfart, M. Vidotti, Influence of pH on the electrochemical synthesis of polypyrrole nanotubes and the supercapacitative performance evaluation, Electrochim. Acta 393 (2019) 447–457, https://doi.org/10.1016/j.electacta.2018.09.200.
[27] Y. Li, Y.P. Wang, C. Bian, J. Stejskal, Y.S. Zheng, X.L. Jing, Aggregates of azo dyes and their role on the morphology and conductivity of polypyrrole, Dyes Pigments 177 (2020), 108329, https://doi.org/10.1016/j.dyepig.2020.108329.
[28] G. Huseynova, S.H. Lee, C.W. Joo, Y.S. Lee, Y.J. Lim, J. Park, J. Yoo, et al., Dye-doped poly (3,4-ethylenedioxythiophene)-poly(styrenesulfonate) electrodes for the application in organic light-emitting diodes, Thin Solid Films 707 (2020) 138078, https://doi.org/10.1016/j.tsf.2020.138078.
[29] J. Stejskal, Strategies towards the control of one-dimensional polypyrrole nanomorphology and conductivity, Polym. Int. 67 (2018) 1461–1469, https://doi.org/10.1002/pi.5654.
[30] U. Acharya, P. Bober, M. Trchová, A. Zhigunov, J. Stejskal, J. Pfleger, Synergistic conductivity increase in polypyrrole/molybdenum disulfide composite, Polymer 50 (2018) 130–137, https://doi.org/10.1016/j.polymer.2018.07.004.
[31] J. Stejskal, U. Acharya, P. Bober, M. Hajná, M. Trchová, M. Mičušík, M. Omastová, I. Pašti, N. Gavrilov, Surface modification of tungsten disulfide with polypyrrole for enhancement of the conductivity and its impact on hydrogen evolution reaction, Appl. Surf. Sci. 492 (2019) 497–503, https://doi.org/10.1016/j.apsusc.2019.06.175.
[32] N.V. Blinova, J. Stejskal, M. Trchová, J. Prokeš, M. Omastová, Polyaniline and polypyrrole: a comparative study of the preparation, Eur. Polym. J. 43 (2007) 2331–2341, https://doi.org/10.1016/j.eurpolymj.2007.03.045.
[33] I. Sapurina, Y. Li, E. Alekseeva, P. Bober, M. Trchová, Z. Morávková, J. Stejskal, Polypyrrole nanotubes: the tuning of morphology and conductivity, Polymer 113 (2017) 47–258, https://doi.org/10.1016/j.polymer.2017.02.064.
[34] S. Valtera, J. Prokeš, J. Kopecká, M. Vrňata, M. Trchová, M. Varga, J. Stejskal, D. Kopecký, Dye-stimulated control of conducting polymer morphology, RSC Adv. 7 (2017) 51495–51505, https://doi.org/10.1039/c7ra10027b.
[35] M.F. Nazar, S.S. Shah, M.A. Khosa, Interaction of azo dye with cationic surfactant under different pH conditions, J. Surfactants Deterg. 13 (2010) 529–537, https://doi.org/10.1007/s11743-009-1177-8.
[36] M. Trchová, J. Stejskal, Resonance Raman spectroscopy of conducting polypyrrole nanotubes: disordered surface versus ordered body, J. Phys. Chem. 122 (2018) 9298–9306, https://doi.org/10.1021/acs.jpca.8b09794.
[37] J. Stejskal, P. Bober, M. Trchová, A. Kovalcik, J. Hodan, J. Hromádková, J. Prokeš, Polyaniline cryogels supported with poly(vinyl alcohol): soft and conducting, Macromolecules 50 (2017) 972–978, https://doi.org/10.1021/acs.macromol.6b02526.
[38] K.A. Milakin, U. Acharya, J. Hodan, M. Trchová, J. Stejskal, Effect of 1,3-phenylenediamine concentration on the properties of poly(aniline-*co*-1,3-phenylenediamine) cryogels, Mater. Lett. 229 (2018) 68–70, https://doi.org/10.1016/j.matlet.2018.06.080.
[39] Y. Yuan, W.L. Zhu, G. Du, D.Z. Wang, J.L. Zhu, G. Pezzotti, Two-step method for synthesizing polyaniline with bimodal nanostructures for high performance supercapacitors, Electrochim. Acta 282 (2018) 286–294, https://doi.org/10.1016/j.electacta.2018.06.006.
[40] L. Li, Y. Zhang, H.Y. Lu, Y.F. Wang, J.S. Xu, J.X. Zhu, C. Zhang, T.X. Liu, Cryopolymerization enables anisotropic polyaniline hybrid hydrogels with superelasticity and highly deformation-tolerant electrochemical energy storage, Nat. Commun. 11 (2020) 62, https://doi.org/10.1038/s41467-019-13959-9.
[41] E.N. Konyushenko, J. Stejskal, M. Trchová, N.V. Blinova, P. Holler, Polymerization of aniline in ice, Synth. Met. 158 (2008) 927–933, https://doi.org/10.1016/j.synthmet.2008.06.015.
[42] Z. Cai, C.R. Martin, Electronically conductive polymer fibers with mesoscopic diameters show enhanced electronic conductivities, J. Am. Chem. Soc. 111 (1989) 4138–4139, https://doi.org/10.1021/ja00193a077.
[43] G. Qi, L. Huang, H. Wang, Highly conductive free standing polypyrrole films prepared by freezing interfacial polymerization, Chem. Commun. 48 (2012) 8246–8248, https://doi.org/10.1039/C2CC33889K.
[44] S. Maiti, D. Das, K. Sen, An assessment of dynamics of electrochemical polymerization of pyrrole, J. Textile Inst. 109 (2018) 1232–1237, https://doi.org/10.1080/00405000.2017.1422963.
[45] C.H. Chen, Application of factorial experimental design to study the influence of polymerization conditions on the yield of polyaniline powder, J. Appl. Polym. Sci. 85 (2002) 1571–1580, https://doi.org/10.1002/app.10790.
[46] M.T. Cortes, E.V. Sierra, Effect of synthesis parameters in polyaniline: influence on yield and thermal behavior, Polym. Bull. 56 (2006) 37–45, https://doi.org/10.1007/s00289-005-0467-1.
[47] J. Stejskal, M. Trchová, P. Bober, Z. Morávková, D. Kopecký, M. Vrňata, J. Prokeš, M. Varga, E. Watzlová, Polypyrrole salts and bases: superior conductivity of nanotubes and their stability towards the loss of conductivity by deprotonation, RCS Adv 6 (2016) 88382–88391, https://doi.org/10.1039/c6ra19461c.
[48] N. Biswas, S. Umapathy, Structures, vibrational frequencies, and normal modes of substituted azo dyes: infrared, Raman, and density functional calculations, J. Phys. Chem. 104 (2000) 2734–2745, https://doi.org/10.1021/jp9929263.

Appendix 3

Highly conducting 1-D polypyrrole prepared in the presence of safranin

Journal of Materials Chemistry C

ROYAL SOCIETY OF CHEMISTRY

PAPER

View Article Online
View Journal

Cite this: DOI: 10.1039/d0tc02838j

Highly conducting 1-D polypyrrole prepared in the presence of safranin†

Islam M. Minisy, [ab] Udit Acharya,[ac] Libor Kobera, [a] Miroslava Trchová,[ad] Christoph Unterweger, [e] Stefan Breitenbach,[e] Jiří Brus, [a] Jiří Pfleger, [a] Jaroslav Stejskal [a] and Patrycja Bober *[a]

Received 15th June 2020,
Accepted 22nd July 2020

DOI: 10.1039/d0tc02838j

rsc.li/materials-c

A facile preparation of a conducting one-dimensional polypyrrole nanostructure (1-D PPy) was achieved in the presence of safranin dye. The polymerization temperature has a significant effect on the conductivity, specific surface area and morphology of PPy. A decrease in the polymerization temperature leads to a significant increase in the conductivity. The highest conductivity was obtained by frozen polymerization (−24 °C) with a value of 175 ± 4 and 23.7 ± 2.9 S cm^{-1} for 1-D PPy and globular PPy, respectively. The temperature dependence of the conductivity of 1-D PPy prepared at −24 °C revealed a semiconducting behaviour with a 3-D variable range hopping charge transfer mechanism. Raman spectroscopy results suggested that the high conductivity can be attributed to the high protonation level of 1-D PPy. Nuclear magnetic resonance spectroscopy has been used to study the chemical structure of 1-D PPy and the incorporation of safranin into the polymer matrix.

Introduction

Enhancing the electrical conductivity and mechanical properties of conducting polymers is an important prerequisite to improve the performance of soft electronics. Different approaches have been used to increase the conductivity of conducting polymers, such as the synthesis of composites with noble metals,[1,2] graphene,[3] dyes,[4] or doping with an anionic polyelectrolyte such as polystyrene sulfonate.[5] Among the various conducting polymers, polypyrrole (PPy) has attracted attention due to its unique physico-chemical properties and broad spectrum of applications, such as batteries,[6] supercapacitors,[7] chemical sensors,[8] biosensors,[9] conductive textiles,[10,11] antistatic coatings,[12] oxidation–reduction reactions,[13] dye removal,[14] drug delivery systems,[15] ion selective membranes[16,17] and tissue engineering.[18] Polypyrrole can be easily synthesized chemically or electrochemically by the oxidative polymerization of pyrrole.[19] Chemical synthesis allows for a low-cost mass production.

Polypyrrole can be obtained in different forms such as powders,[4] thin films,[20] colloids[21] and cryo- or aerogels,[22,23] and it can exhibit a conductivity of up to 100 S cm^{-1}.[24] Various types of nano-morphologies can be obtained by polymerization processes in which different templates are used as morphology-guiding agents. For example, organic dyes have been used as hard templates to produce PPy nanotubes[24] or nanofibers.[25] Recently, safranin, an organic cationic dye, has been used to obtain one dimensional (1-D) PPy with enhanced conductivity (35 S cm^{-1}) compared to conventional globular PPy (1–5 S cm^{-1}).[26]

The polymerization conditions applied during the preparation can strongly affect the morphology and conductivity of the resulting conducting polymers.[27] Although many reports studied the effect of the polymerization temperature of polyaniline (PANI) in a wide range of temperatures (−50 to +50 °C)[28–32] or that of PPy in the range of 0 to 60 °C,[33,34] to the best of our knowledge, no one has studied the chemical polymerization of pyrrole to PPy nanostructures in frozen medium. Polyaniline was prepared chemically at −24 °C,[31] which leads to an increase in the molecular weight followed by an increase in conductivity, and it even showed metallic character compared to the semiconductor behaviour obtained at room temperature. Reducing the temperature of PANI preparation to −40 °C led to the formation of a higher-molecular-weight product.[24] Stejskal *et al.*[29] reported the influence of the polymerization temperature of PANI in the range of −50 to +50 °C on its molecular weight, crystallinity, and electrical conductivity. They concluded that as the reaction temperature decreases, both the molecular weight of PANI and its crystallinity increase, but the conductivity improved only marginally. Similar to PANI, it was found that

[a] Institute of Macromolecular Chemistry, Academy of Sciences of the Czech Republic, 162 06 Prague 6, Czech Republic. E-mail: bober@imc.cas.cz
[b] Charles University, Faculty of Science, 128 43 Prague 2, Czech Republic
[c] Charles University, Faculty of Mathematics and Physics, 121 16 Prague 2, Czech Republic
[d] University of Chemistry and Technology Prague, 166 28 Prague 6, Czech Republic
[e] Wood K Plus – Kompetenzzentrum Holz GmbH, 4040 Linz, Austria

† Electronic supplementary information (ESI) available. See DOI: 10.1039/d0tc02838j

the conductivity of electrochemically prepared PPy increased with decreasing temperature of the preparation, the highest conductivity being 26.3 S cm^{-1} of PPy prepared at 1 °C compared to 0.04 S cm^{-1} obtained at 60 °C. The conductivity may be enhanced due to the higher doping level, longer conjugated chains and higher charge-carrier hopping frequency.[33]

In spite of the different approaches taken to improve the conductivity of PPy, the challenge remains to develop a low cost and scalable method to get highly conducting PPy. Recently, safranin has been used to enhance the conductivity of PPy prepared at room temperature.[26] In the present paper, we study the effect of polymerization temperature on the conductivity and the morphology of PPy in a wide range of temperatures from −80 to +50 °C. Safranin was used as a morphology-guiding agent to produce 1-D PPy. Various analytical techniques have been used to characterize the PPy prepared in the presence or absence of safranin. The morphology, conductivity and specific surface area of all the samples were examined. In addition, Raman and ssNMR spectroscopy were used to study the molecular structures of PPy in both its protonated and deprotonated forms, respectively.

Experimental

Chemicals and reagents

Pyrrole, iron(III) chloride hexahydrate, safranin (3,7-diamino-2,8-dimethyl-5-phenylphenazinium chloride; Safranin T, Basic Red 2) and ammonia solution (NH_4OH) 25% were obtained from Sigma-Aldrich. All chemicals were used as received.

Synthesis of polypyrrole

Polypyrrole was prepared by the polymerization of pyrrole (0.2 M, 1.34 g) with iron(III) chloride (0.5 M, 13.5 g) as the oxidant in the presence of an organic dye, safranin (4 mM, 0.14 g), or in its absence at various temperatures (from −80 to 50 °C). The total volume of the polymerization mixture was 100 mL. In a water/ethylene glycol bath adjusted to the desired temperature (−24 to 50 °C), 50 mL of a precooled aqueous solution of pyrrole with safranin was mixed with 50 mL of precooled oxidant solution. The mixtures were allowed to polymerize for 24 h at the particular temperatures. For the preparation of PPy at −50 °C, the polymerization mixture was frozen in a solid carbon dioxide/cyclohexanone bath for 30 min before leaving it to polymerize for one week in a freezer adjusted to −50 °C, while a carbon dioxide/ethanol bath was used for the preparation of PPy at −80 °C, and the reaction mixture was kept for 2 weeks in a freezer at −80 °C. Polypyrrole without safranin was prepared in the same manner. The obtained PPy powders were collected after thawing *via* vacuum filtration, rinsed with 0.2 M HCl solution, then with ethanol, and dried in air and in a desiccator over silica gel until constant weights were obtained.

A part of the samples was converted to the PPy base (deprotonated) form by suspension in 1 M or 16 M NH_4OH for 24 h, washed with acetone and left to dry in a desiccator over silica gel until constant weights were obtained.

Characterization

The morphology of PPy powders was characterized by using a MIRA3 TESCAN scanning electron microscope (SEM) and TECNAI G2 SPIRIT transmission electron microscope (TEM).

The DC conductivity was determined by employing the van der Pauw method on compressed pellets having a diameter of 13 mm and thickness of 1.0 ± 0.2 mm prepared under a pressure of 540 MPa using a hydraulic press (Trystom H-62, Trystom, Czech Republic). A Keithley 230 Programmable Voltage Source in serial connection with a Keithley 196 System DMM was used as a current source; the potential difference between the potential probes was measured using a Keithley 181 Nanovoltmeter (Keithley, USA) under constant ambient conditions (23 ± 1 °C and relative humidity 35 ± 5%). The conductivity of each sample was measured at least three times. For studying the temperature dependence of the DC electrical conductivity, the van der Pauw method was used using the same setup as described above, where the samples were mounted in the cryostat (Novocontrol, Germany) and the temperature (in the range of −160 to +160 °C) was controlled using a Novocontrol Quatro 4.0 temperature controller under a gas flow from the liquid nitrogen source. The measurements were taken after at least 30 min of temperature stabilization. Before taking the measurements, the samples were kept in the cryostat in a N_2 atmosphere at 60 °C for 3 h to remove residual humidity. The conductivity values were calculated as the average value of the measurements in two perpendicular directions.

The specific surface area of the samples was determined using physisorption measurements on an automatic volumetric sorption analyser (Autosorb-iQ, Anton Paar QuantaTec Inc.) with nitrogen at 77 K. 40–50 mg of the samples was outgassed for 2 h at 200 °C before the adsorbed gas volume was measured at a relative pressure of 0.1 to 0.4. Using the Brunauer–Emmett–Teller (BET) method, the specific surface areas of the samples were calculated.

Raman spectra were collected on a Renishaw inVia Reflex Raman spectrometer equipped with a near-infrared diode 785 nm laser (holographic grating 1200 lines mm^{-1}) and an argon-ion laser at 514 nm (2400 lines mm^{-1}). A research-grade Leica DM LM microscope with an objective of magnification 50× was used to focus the laser beam on the sample placed on an X–Y motorized sample stage. A Peltier-cooled CCD detector (576 × 384 pixels) registered the dispersed light.

Chemical structural studies on the deprotonated PPy samples were performed using ^{13}C and ^{15}N Magic Angle Spinning Nuclear Magnetic Resonance Spectroscopy (MAS NMR). Solid-state NMR (ssNMR) spectra were recorded under an 11.7 T magnetic field using an AVANCE III HD spectrometer, at Larmor frequencies $\nu(^{13}C)$ = 125.783 MHz and $\nu(^{15}N)$ = 202.478 MHz using 3.2 mm and 4 mm cross-polarization (CP) magic angle spinning (MAS) probes, respectively. The ^{13}C and ^{15}N CP/MAS NMR spectra were recorded at 20 kHz and 5 kHz MAS spinning speeds. The ^{13}C and ^{15}N NMR isotropic chemical shifts were calibrated using α-glycine (^{13}C: 176.03 ppm; carbonyl signal and ^{15}N: 11.59 ppm; amine signal) as the external

standard. The ^{15}N NMR chemical shift of the glycine amine signal is usually referenced to 34.35 ppm;[35] however, different ^{15}N shift values were used in agreement with literature data[32] for easier comparison of experimental results. The ^{13}C CP/MAS NMR spectra were measured with a recycle delay of 2 s. The number of scans was 5–25k at an 800 μs spin lock. The ^{15}N CP/MAS NMR experiment was recorded with a recycle delay of 5 s. The number of scans was 48k at a spin lock of 800 μs. The contact time for the cross-polarization experiment was used according to literature data.[36,37] The SPINAL64 decoupling sequence was applied for suppression of strong dipolar interactions in all cases. Frictional heating of the spinning samples was compensated by active cooling[38] and the dried samples were placed into ZrO_2 rotors. All NMR spectra were processed and fitted using the Top Spin 3.5 pl2 software package.

Results and discussion

Yield

The yield was found to increase linearly upon increasing the polymerization temperature from −80 °C to room temperature (Fig. 1), where the maximum yield was obtained. Upon further increasing the polymerization temperature up to 50 °C, a slight decrease of yield was observed due to the exothermic nature of the PPy polymerization reaction. Generally, the high yield of PPy (more than 100%) is attributed to the presence of chloride counter-ions in the polypyrrole chain (Scheme 1A), the hygroscopic nature of PPy, which contains water molecules, and oxygen uptake during the polymerization.[39,40] On the other hand, 1-D PPy prepared in the presence of safranin has a higher yield than globular PPy due to the incorporation of safranin molecules during the polymerization. The very low yield obtained at −80 °C in both cases, in the presence or absence of safranin, suggests the formation of pyrrole oligomers due to the restriction of long polymer chain formation under these conditions.

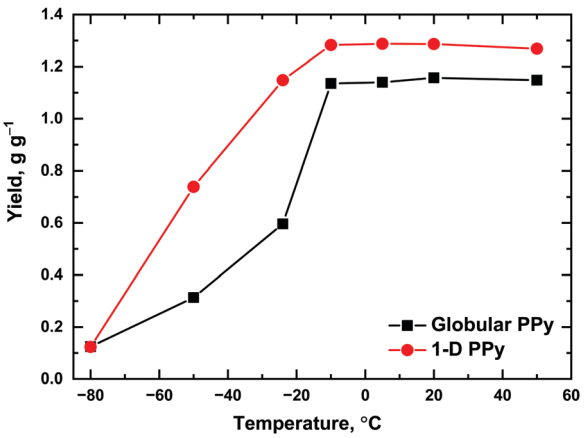

Fig. 1 The influence of the polymerization temperature on the yield of 1-D polypyrrole prepared in the presence of safranin and the globular (dye-free) polypyrrole. The yield was calculated in grams per gram of pyrrole.

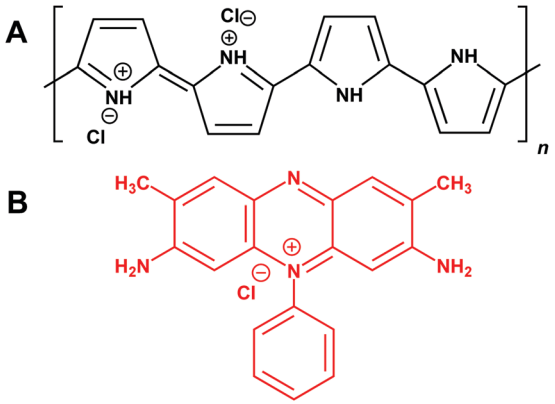

Scheme 1 Chemical formulae of polypyrrole (A) and safranin (B).

Morphology of the obtained polypyrrole

Dye-free PPy has a characteristic globular morphology; however, the addition of safranin into the polymerization medium leads to the formation of a 1-D morphology (Fig. 2). Safranin acts as a morphology-guiding agent. When mixed with iron(III) chloride, it precipitates as fibrillary aggregates (Fig. S1, ESI†), which act as a template for the deposition of PPy.[26] Such formation of fibrillar aggregates could be a consequence of complex formation between safranin and iron(III) chloride, or simply the oligomerization of safranin.[42] The polymerization temperature has a crucial impact on the morphology of PPy (Fig. 1 and Fig. S2, ESI†). The polymerization at 50 °C in the

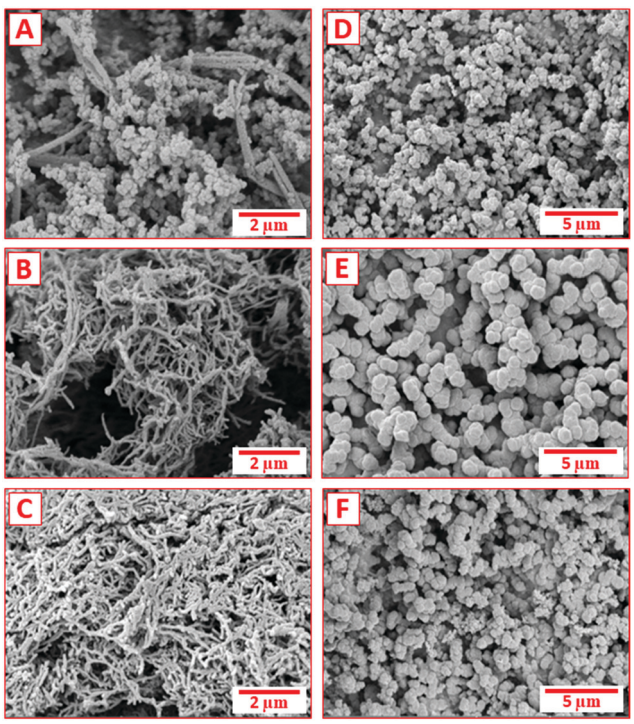

Fig. 2 SEM micrographs of 1-D polypyrrole obtained in the presence of safranin (A–C) and globular polypyrrole formed in its absence (D–F). Polymerization temperature: 50 °C (A and D), 5 °C (B and E) and −24 °C (C and F).

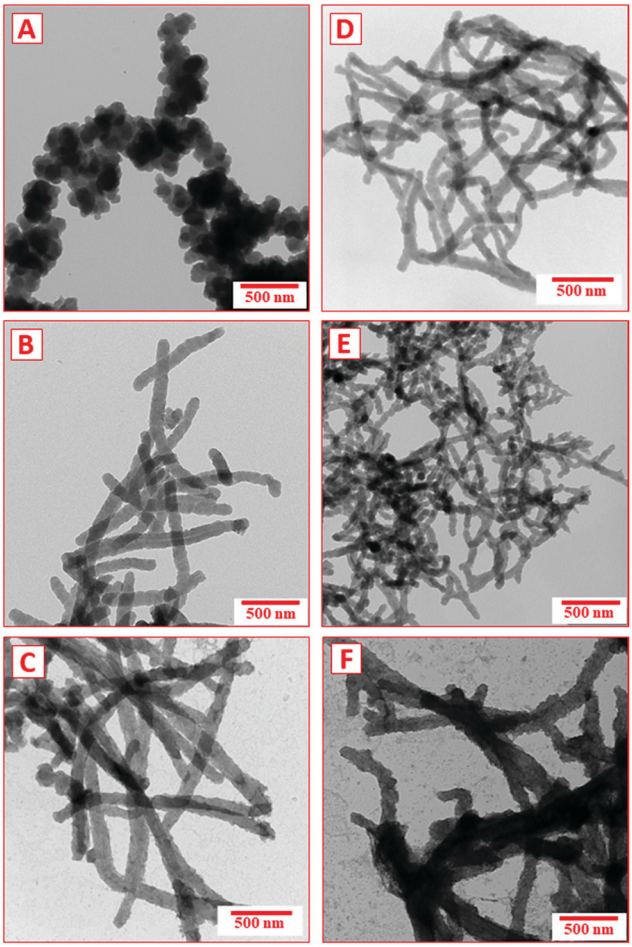

Fig. 3 TEM micrographs of 1-D polypyrrole prepared in the presence of safranin at 50 °C (A), 20 °C (B), 5 °C (C), −10 °C (D), −24 °C (E), and −50 °C (F).

presence of safranin led to the formation of a mixture of globular and fibrillary particles, probably due to the fast nature of the reaction and there being not enough time for the formation of the template facilitating the 1-D morphology. When the same polymerization was performed at room temperature, well-organized PPy nanofibers were formed (Fig. S2, ESI†). It should be noted that the polymerization temperature has a significant effect on the dimensions of the PPy fibres (Fig. 3). Under frozen polymerization conditions, at −24 °C, the produced PPy nanofibers are more interconnected and with smaller dimensions. Further decreasing the polymerization temperature to −50 °C led to the formation of thicker 1-D fibres, while polymerization at −80 °C led to the formation of a mixture of irregular flakes and nanotubes (Fig. S2 and S3, ESI†). On the other hand, all PPy samples prepared in the absence of safranin have a typical globular morphology, with the particle sizes strongly depending on the polymerization temperature. The smallest globular particles were formed at 50 °C and the largest particle size was obtained at −10 °C (Fig. 2).

Specific surface area

Polypyrrole with a 1-D morphology, prepared in the presence of safranin, had a higher specific surface area (S_{BET}) compared to the polymers with a globular morphology, similar to the trend reported in the literature.[4] The results of S_{BET} analysis (Table 1) correlated well with the morphology of the obtained PPy (see SEM and TEM images). A decrease in the polymerization temperature led to an increase in specific surface area of the 1-D PPy from 35.8 ± 6.4 $m^2 g^{-1}$ at 50 °C to 73.6 ± 7.5 $m^2 g^{-1}$ at −80 °C. In the case of the globular PPy, this trend was not observed. The specific surface area, S_{BET}, however, correlates with the particle size: the smaller the particle size, the higher the specific surface area. The highest S_{BET} for globular PPy was 66.8 $m^2 g^{-1}$. The largest surface area being achieved for 1-D PPy (73.6 ± 7.5 $m^2 g^{-1}$), obtained by polymerization at −80 °C, can be explained by the formation of oligomers and nanotubular structures.

Table 1 BET specific surface area, S_{BET}, of globular and 1-D polypyrrole prepared at various temperatures

Polymerization temperature, °C	Globular PPy S_{BET}, $m^2 g^{-1}$	1-D PPy S_{BET}, $m^2 g^{-1}$
50	37.6 ± 9.5	35.8 ± 6.4
20	13.5 ± 0.4	52.4 ± 2.5
5	18.2 ± 8.8	53.2 ± 8.8
−10	8.8 ± 3.5	65.7 ± 3.5
−24	24.4 ± 4.5	72.3 ± 2.5
−50	23.0 ± 4.7	49.6 ± 0.2
−80	66.8 ± 0.0	73.6 ± 7.5

Conductivity

The dependence of the electrical conductivity on the polymerization temperature was markedly different for PPy prepared with and without the safranin template. Whereas both forms of PPy polymerized at high temperature (50 °C) had nearly the same conductivity, with decreasing temperature of preparation, there was a much more pronounced increase of conductivity in 1-D PPy compared to the globular one, which showed only a small increase. When polymerized in a frozen state at −24 °C, both forms of PPy show a maximum but the conductivity value of 1-D PPy, polymerized in the presence of safranin, is almost one order of magnitude higher, reaching 175 S cm^{-1} compared to 23.7 S cm^{-1} found for globular PPy (Fig. 4A). With a further decrease in the polymerization temperature, the conductivity of globular PPy remained almost completely unchanged but the conductivity of 1-D PPy decreased, approaching the conductivity of the globular one when both were prepared at −80 °C. The much higher conductivity of 1-D PPy prepared at −24 °C can be attributed to a higher level of protonation, as evidenced by the Raman spectra (see below) and better rearrangement of the polymer chains resulting in thinner fibres with a higher specific surface area (Table 1). As has been published previously,[4] PPy polymerized in the presence of various dyes is composed of nanofibrils having a well-organized crystalline core surrounded by a disordered shell. The thickness of the core is limited, whereas the thickness of the disordered shell grows with increasing thickness of the fibrils. As can be seen from Fig. 2 and Fig. 3, 1-D PPy prepared at −24 °C, which exhibits the highest conductivity, also has the thinnest fibrils with a higher degree of protonation, as proved by Raman spectroscopy (see below).

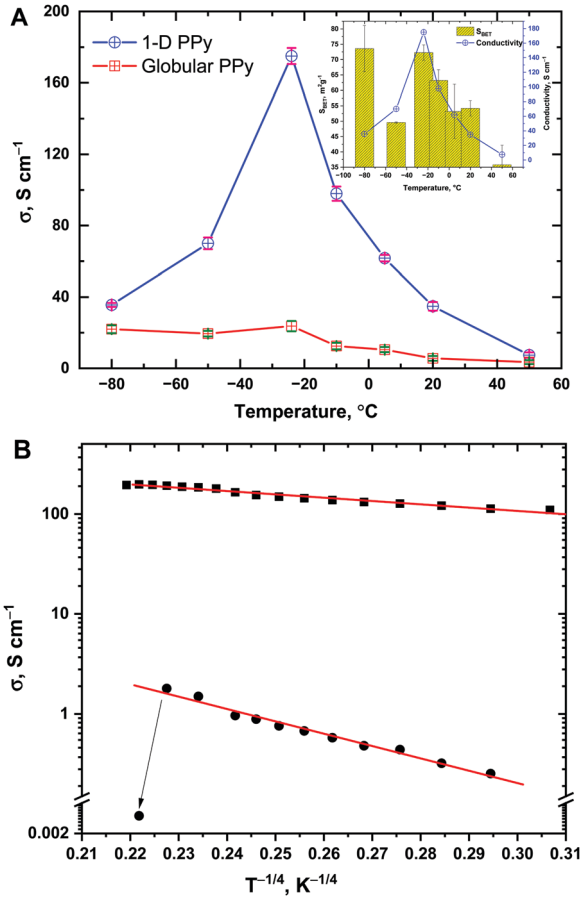

Fig. 4 The influence of the polymerization temperature on the conductivity of the 1-D polypyrrole prepared in the presence of safranin and the globular polypyrrole prepared without safranin; the inset shows the correlation between conductivity and specific surface area of 1-D polypyrrole (A). Temperature dependence of the conductivity of 1-D polypyrrole prepared at −24 °C (full squares) and globular polypyrrole (full circles, data obtained from ref. 41) as a function of $T^{-1/4}$ (B).

In order to get a better insight into the nature of the charge transport in the highly conductive 1-D PPy, the temperature dependence of conductivity was measured and compared to that of previously studied globular PPy[41] (Fig. 4B). The temperature dependence of conductivity of 1-D PPy shows a semiconducting behaviour with increasing conductivity when temperature increases in the range from −160 to 140 °C (113 to 413 K) but with a markedly smaller slope compared to that of the globular PPy. A slight decrease of conductivity was observed above 140 °C, which can be attributed to the deprotonation of the polypyrrole due to the release of HCl (dopant). This only small decrease is in contrast to the large drop in conductivity observed in the globular PPy and serves as another piece of evidence that the dopant is better anchored in the central part of the PPy fibrils. The conduction mechanism of PPy is mostly discussed within the framework of Mott's variable range hopping, using eqn (1).

$$\sigma_T = \sigma_0 \exp\left(-\frac{T_0}{T}\right)^{1/(n+1)} \quad (1)$$

where σ_0 is the preexponential factor resembling the high temperature limit of conductivity, σ_T is conductivity at temperature T, T_0 is the Mott characteristic temperature, indirectly proportional to the density of states at the Fermi level and to the localization length of the wave function of localized charge carriers, and n is the dimension in which the charge transport takes place. The conductivity *vs.* $(1/T)^{1/n}$ plot was fitted for different values of n using the least squares fit procedure. The data were well fitted with $n = 3$, pointing to 3-D variable range hopping. The smaller value of the T_0 obtained from the temperature dependence of the conductivity of 1-D PPy compared to the globular one agrees well with a longer delocalization of carriers and a higher level of doping in the molecularly well-ordered domains. Also, the frequency independent AC conductivity result (Fig. S4, ESI†) confirms that the charge transport proceeds through homogeneous and relatively compact grains.

The conductivity of all deprotonated 1-D PPy (under mild basic conditions, 1 M NH_3 solution) samples showed a decrease of their original conductivity by 5 orders of magnitude. For example, the conductivity of 1-D PPy prepared at −24 °C decreased from 175 to 1.3×10^{-3} S cm^{-1} while that of 1-D PPy prepared at 50 °C decreased from 7.5 to 5.7×10^{-5} S cm^{-1}. However, deprotonation under harsh conditions (16 M NH_3 solutions) led to fully deprotonated PPy samples with the same conductivity for all 1-D PPy samples with the value $\approx 2 \times 10^{-6}$ S cm^{-1}. Re-doping with 0.2 M HCl did not fully recover the original conductivity but it led to an increase by just 2 orders of magnitude for all the PPys prepared at different temperatures. During the deprotonation, the chain ordering is disturbed by the mass loss resulting in volume reduction and consequently shrinking of the chains. This factor limits the full recovery of PPy conductivity.[46]

Raman spectroscopy

Raman spectra provide information on the molecular structure of a polymer and on the charge distribution on the chains. They differ depending on the laser excitation line used.[43] The spectra recorded with a 785 nm excitation wavelength are in resonance with the electronic transitions in PPy. In the spectrum of standard globular PPy (Fig. 5A), which was earlier described in the literature,[43–48] the peak observed at 1595 cm^{-1} corresponds to the backbone stretching mode of C=C bonds and the inter-ring C–C mode in the backbone of the polaron structure. The band with a maximum at 1488 cm^{-1} is assigned to the skeletal, or C–C and C–N stretching vibrations. The shape of two peaks situated at 1380 cm^{-1} (antisymmetrical inter-ring stretching C–N vibration of oxidized, protonated PPy) and 1328 cm^{-1} (inter-ring stretching C–C vibration mode in neutral states of PPy) corresponds to the spectrum of protonated PPy. The band with a maximum at 1242 cm^{-1} is assigned to the antisymmetrical C–H in-plane bending vibrations. The shape of the double peaks observed at 1079 cm^{-1} (C–H in-plane deformation with oxidized, protonated species) and 1052 cm^{-1} (non-protonated PPy units) also corresponds to the spectrum of the protonated state of the prepared samples of PPy. The bands at 976 and 933 cm^{-1} can be assigned to the ring in-plane

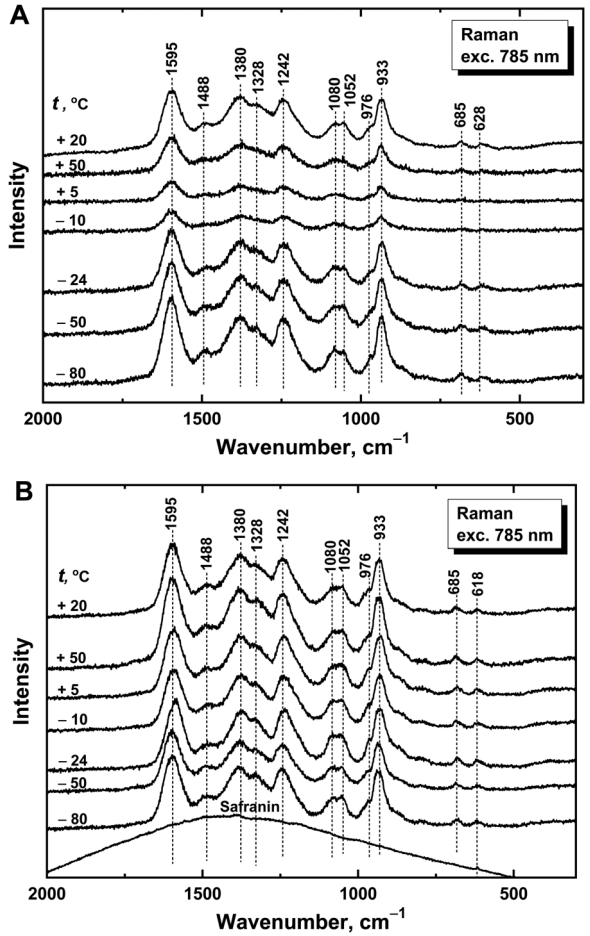

Fig. 5 Raman spectra of polypyrroles prepared without (A) and in the presence (B) of safranin at various temperatures. Laser excitation wavelength: 785 nm.

deformation associated with the polaron and bipolaron states of PPy, respectively.[45]

In the Raman spectra of PPy prepared in the presence of safranin (Fig. 5B), we do not observe any peaks of safranin when using the 785 nm laser excitation line. As this excitation line falls in the polaron absorption band of PPy, it is strongly absorbed and the penetration depth is only several nanometres, *i.e.* close to the surface.[49,50]

The energy of the 514 nm laser excitation line is close to the electronic absorption in safranin dye, which has maximum optical absorption at 538 nm.[42] In the Raman spectra of PPy prepared with safranin, we detect resonantly enhanced peaks of safranin, as marked with asterisks (see Fig. 6). Beside them, we detect peaks at 976 and 933 nm belonging to the polaron and bipolaron states of PPy, respectively. These peaks correspond to PPy in the interior of the nanostructures, which is in contact with the dye, because the energy of the laser excitation 514 nm is not in resonance with the electronic absorption band of PPy and the penetration depth is higher. From the ratio of the bands corresponding to polarons/bipolarons, we can conclude that PPy, which is inside the nanotubes or nanofibers and in contact with the safranin template, is in a more protonated

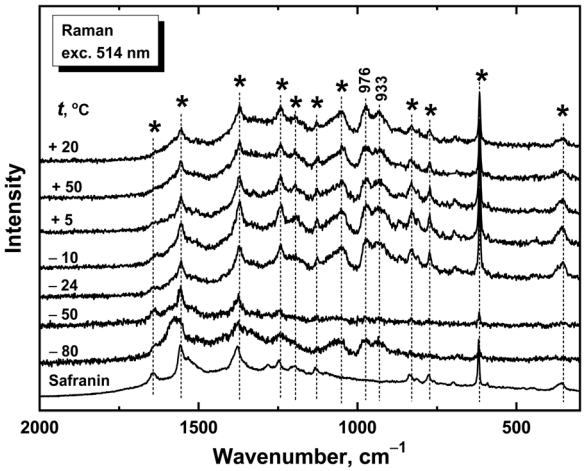

Fig. 6 Raman spectra of 1-D polypyrrole prepared in the presence of safranin at various temperatures. Laser excitation wavelength: 514 nm.

(polaronic) state. This correlates with the higher conductivity of these samples. This effect has been recently described in the literature.[43]

Solid-state NMR analysis

^{13}C and ^{15}N CP/MAS NMR spectroscopy was used for investigation of deprotonated 1-D PPy prepared at different polymerization temperatures. It is problematic to study conducting polymers, especially those possessing high conductivity, using the ssNMR technique, as with increasing conductivity, the signal broadens and loses intensity in addition to a very long time being needed to get an acceptable resolution.[51] The main goal of ssNMR analysis was to study the chemical structure of PPy prepared with safranin at different temperatures and to estimate the quantity of incorporated safranin.

The ^{13}C CP/MAS NMR spectra of deprotonated 1-D PPy (Fig. 7) clearly confirm the formation of the PPy structure with different residual amounts of safranin in all cases. The main signal consists of two peaks at 114 and 129 ppm, which were attributed to the =CH carbon and quaternary carbon of an aromatic form.[37,52] Moreover, the absence of the peak at 143 ppm in all spectra suggests that quinonoid structures are missing. Two relatively broad peaks at 165 ppm and 50 ppm were detected and attributed to the air-oxidized phase.[36] According to the literature, the existence of this phase can be identified using ^{15}N CP/MAS NMR spectroscopy by the presence of a ^{15}N NMR signal at 90 ppm. This signal, however, was not found in the present ^{15}N CP/MAS NMR spectrum, although only one sample (polypyrrole prepared at 5 °C, see Fig. S5, ESI†) was measured due to the long experimental time (72 h). Furthermore, the ^{15}N CP/MAS NMR spectrum was collected for the sample at natural isotopic abundance, in contrast to the spectrum referred to in the literature. Thus, an air-oxidized phase still has to be considered. However, a plausible alternative to the signal assignment reported by Korusu[53] for the resonances at 165 ppm and 50 ppm in the ^{13}C CP/MAS NMR spectra can also be made, namely that the signals belong

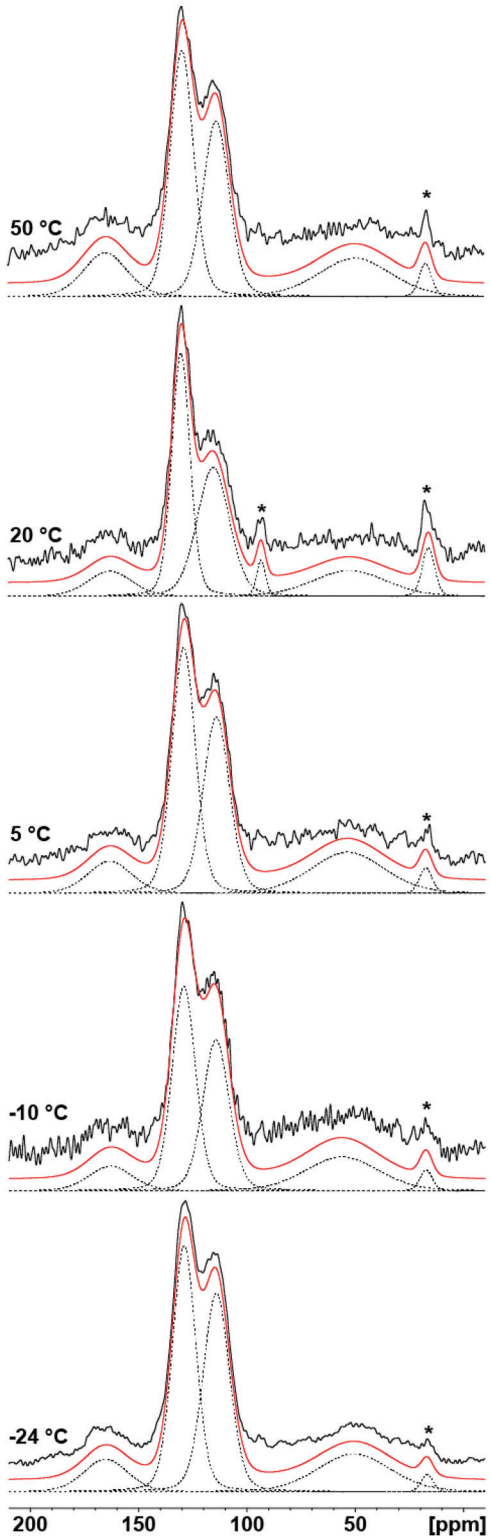

Fig. 7 Experimental ^{13}C CP/MAS NMR spectra (black solid line), simulations of the individual carbon atoms (dashed lines) and their sum (red solid line) of deprotonated 1-D polypyrrole prepared at various temperatures. The star symbol denotes resonance(s) corresponding to safranin.

to the disordered –N=**C**< and –NH-**CH**– groups[54] formed during pyrrole polymerization in the presence of safranin.

Table 2 The content of safranin (mol%) determined from the deconvolution of ^{13}C CP/MAS NMR spectra for the samples prepared at various temperatures. I_{CH}(polypyrrole) = 1

Polymerization temperature, °C	I_{CH_3}(safranin)	Safranin, mol% $(I_{CH3} \times 100)/(I_{CH3} + I_{CH})$
50	0.09	8.3
20	0.15	13.0
5	0.07	6.5
−10	0.07	6.5
−24	0.04	3.9

Furthermore, the right shoulder of the resonance at 165 ppm can be attributed to the NH_2–**C**< groups from safranin. The presence of safranin in the prepared systems is clearly confirmed by a sharp peak at 17 ppm (Fig. S6, ESI†). Additional information (mol% of safranin can be roughly estimated) was extracted from the deconvolution of the ^{13}C CP/MAS NMR spectra, from the ratio of integral areas of the methyl peak of safranin (17 ppm) to the CH carbon of PPy (114 ppm), since these peaks are basically unaffected. The resulting compositions in mol% are listed in Table 2, from which an increasing amount of safranin present in PPy with increasing temperature is evident. The results obtained from the NMR data indicate that with increasing polymerization temperature, the amount of safranin present in PPy increases. This finding also suggests that a higher amount of safranin can be associated with a reduced conductivity of PPy due to increasing the concentration of dyes and, consequently, the fraction of the non-conducting component in the 1-D PPy.[26]

Conclusions

Polypyrrole with a 1-D morphology was easily prepared by the addition of safranin into the polymerization medium. Polypyrrole prepared without the addition of safranin had, in contrast, a globular form. The dimensions of the PPy fibres in 1-D PPy or of the globules in PPy prepared without safranin, as well as conductivity and specific area of the as-prepared products were influenced by the polymerization temperature. Frozen polymerization (at −24 °C) resulted in polymers with the highest conductivity, reaching 175 S cm^{-1} and 23.7 S cm^{-1} for 1-D PPy and globular PPy, respectively. The high-conducting PPy samples possessed thinner fibres, a high specific surface area and a high level of protonation, as evidenced by TEM, BET measurements, and Raman spectroscopy. Raman spectroscopy and ssNMR analysis demonstrated the incorporation of safranin into the PPy fibres, which, in turn, facilitated a higher level of protonation. The mol% of safranin incorporated in deprotonated PPy was found to decrease upon decreasing the polymerization temperature.

Conflicts of interest

There are no conflicts to declare.

Acknowledgements

The authors wish to thank the Czech Science Foundation (18-04669S) for the financial support. Part of this work was carried out within the project BioCarb-K, co-financed by the European Regional Development Fund (EFRE) and the province of Upper Austria through the programme IWB 2014-2020.

Notes and references

1 L. V. Oliveira and F. F. Camilo, *Synth. Met.*, 2019, **247**, 219.
2 P. Bober, M. Trchová, J. Prokeš, M. Varga and J. Stejskal, *Electrochim. Acta*, 2011, **56**, 3580.
3 A. Liu, C. Li, H. Bai and G. Shi, *J. Phys. Chem. C*, 2010, **114**, 22783.
4 J. Stejskal and M. Trchová, *Chem. Pap.*, 2018, **72**, 1563.
5 T. M. Wu, H. L. Chang and Y. W. Lin, *Polym. Int.*, 2009, **58**, 1065.
6 J. Wang, J. Chen, K. Konstantinov, L. Zhao, S. H. Ng, G. X. Wang, Z. P. Guo and H. K. Liu, *Electrochim. Acta*, 2006, **51**, 4634.
7 L. Z. Fan and J. Maier, *Electrochem. Commun.*, 2006, **8**, 937.
8 G. Lisak, M. Wagner, C. Kvarnström, J. Bobacka, A. Ivaska and A. Lewenstam, *Electroanalysis*, 2010, **22**, 2794.
9 J. Wang and M. Musameh, *Anal. Chim. Acta*, 2005, **539**, 209.
10 M. Barakzehi, M. Montazer, F. Sharif, T. Norby and A. Chatzitakis, *Electrochim. Acta*, 2019, **305**, 187.
11 P. Bober, J. Stejskal, I. Šeděnková, M. Trchová, L. Martinková and J. Marek, *Appl. Surf. Sci.*, 2015, **356**, 737.
12 Ö. Yavuz, M. K. Ram, M. Aldissi, P. Poddar and H. Srikanth, *Synth. Met.*, 2005, **151**, 211.
13 I. M. Minisy, N. Gavrilov, U. Acharya, Z. Morávková, C. Unterweger, M. Mičušík, S. K. Filippov, J. Kredatusová, I. A. Pašti, S. Breitenbach and G. irić-Marjanović, *J. Colloid Interface Sci.*, 2019, **551**, 184.
14 M. M. Ayad, W. A. Amer, S. Zaghlol, I. M. Minisy, P. Bober and J. Stejskal, *Chem. Pap.*, 2018, **72**, 1605.
15 M. Sharma, G. I. Waterhouse, S. W. Loader, S. Garg and D. Svirskis, *Int. J. Pharm.*, 2013, **443**, 163.
16 M. Akieh-Pirkanniemi, G. Lisak, J. Arroyo, J. Bobacka and A. Ivaska, *J. Membr. Sci.*, 2016, **511**, 76.
17 J. Arroyo, M. Akieh-Pirkanniemi, G. Lisak, R. M. Latonen and J. Bobacka, *J. Membr. Sci.*, 2019, **581**, 50–57.
18 M. Talikowska, X. Fu and G. Lisak, *Biosens. Bioelectron.*, 2019, **135**, 50–63.
19 S. Demoustier-Champagne, J. Duchet and R. Legras, *Synth. Met.*, 1999, **101**, 20.
20 J. Kim, D. Sohn, Y. Sung and E. R. Kim, *Synth. Met.*, 2003, **132**, 309.
21 M. Omastová, P. Bober, Z. Morávková, N. Peřinka, M. Kaplanová, T. Syrový, J. Hromádková, M. Trchová and J. Stejskal, *Electrochim. Acta*, 2014, **122**, 296.
22 P. Bober, Z. Capáková, U. Acharya, B. A. Zasońska, P. Humpolíček, J. Hodan, J. Hromádková and J. Stejskal, *Synth. Met.*, 2019, **252**, 122.
23 H. An, Y. Wang, X. Wang, L. Zheng, X. Wang, L. Yi, L. Bai and X. Zhang, *J. Power Sources*, 2010, **195**, 6964.
24 Y. Li, P. Bober, M. Trchová and J. Stejskal, *J. Mater. Chem. C*, 2017, **5**, 4236.
25 P. Bober, Y. Li, U. Acharya, Y. Panthi, J. Pfleger, P. Humpolíček, M. Trchová and J. Stejskal, *Synth. Met.*, 2018, **237**, 40.
26 I. M. Minisy, P. Bober, U. Acharya, M. Trchová, J. Hromádková, J. Pfleger and J. Stejskal, *Polymer*, 2019, **174**, 11.
27 H. Kang and K. E. Geckeler, *Polymer*, 2000, **41**, 6931.
28 P. N. Adams and A. P. Monkman, *Synth. Met.*, 1997, **87**, 165.
29 J. Stejskal, A. Riede, D. Hlavatá, J. Prokeš, M. Helmstedt and P. Holler, *Synth. Met.*, 1998, **96**, 55.
30 M. Gholamian and A. Q. Contractor, *J. Electroanal. Chem. Interfacial Electrochem.*, 1988, **252**, 291.
31 P. Bober, J. Stejskal, M. Trchová and J. Prokeš, *J. Solid State Electrochem.*, 2011, **15**, 2361.
32 M. Blaha, M. Varga, J. Prokeš, A. Zhigunov and J. Vohlídal, *Eur. Polym. J.*, 2013, **49**, 3904.
33 A. Kassim, Z. B. Basar and H. E. Mahmud, *J. Chem. Sci.*, 2002, **114**, 155.
34 W. Liang, J. Lei and C. R. Martin, *Synth. Met.*, 1992, **52**, 227.
35 P. Bertani, J. Raya and B. Bechinger, *Solid State Nucl. Magn. Reson.*, 2014, **61**, 15.
36 H. Kurosu, M. Kikuchi and I. Ando, *J. Polym. Sci., Part B: Polym. Phys.*, 1995, **33**, 769.
37 M. Forsyth and V. T. Truong, *Polymer*, 1995, **36**, 725.
38 J. Brus, *Solid State Nucl. Magn. Reson.*, 2000, **16**, 151.
39 M. Salmon, K. K. Kanazawa, A. F. Diaz and M. Krounbi, *J. Polym. Sci., Polym. Lett. Ed.*, 1982, **20**, 187.
40 E. Jakab, E. Mészáros and M. Omastová, *J. Therm. Anal. Calorim.*, 2007, **88**, 515.
41 U. Acharya, B. Bober, M. Trchova, A. Zhigunov, J. Stejskal and J. Pfleger, *Polymer*, 2018, **150**, 130.
42 G. Ćirić-Marjanović, N. V. Blinova, M. Trchová and J. Stejskal, *J. Phys. Chem. B*, 2007, **111**, 2188.
43 M. Trchová and J. Stejskal, *J. Phys. Chem. A*, 2018, **122**, 9298.
44 Y. Furukawa, S. Tazawa, Y. Fuji and A. Harada, *Synth. Met.*, 1988, **24**, 329.
45 F. Chen, G. Q. Shi, M. X. Fu and L. G. Qu, *Synth. Met.*, 2003, **132**, 125.
46 S. Gupta, *J. Raman Spectrosc.*, 2008, **39**, 1343.
47 J. Stejskal, M. Trchová, Z. Morávková, P. Bober, D. Kopecký, J. Kopecká, E. Watzlová, M. Varga and J. Prokeš, *RSC Adv.*, 2016, **6**, 88382.
48 Ishpal and A. Kaur, *J. Nanopart. Res.*, 2013, **15**, 1637.
49 G. Gouadec and P. Colomban, *Cryst. Growth Charact. Mater.*, 2007, **39**, 1.
50 P. Colomban, S. Folch and A. Gruger, *Macromolecules*, 1999, **32**, 3080.
51 A. Mahun, S. Abbrent, P. Bober, J. Brus and L. Kobera, *Synth. Met.*, 2020, **259**, 116250.
52 M. Forsyth, V. T. Truong and M. E. Smith, *Polymer*, 1994, **35**, 1593.
53 H. Kurosu, M. Kikuchi and I. Ando, *J. Polym. Sci., Part B: Polym. Phys.*, 1995, **33**, 769.
54 E. Pretsch, P. Buehlmann, C. Affolter, E. Pretsch, P. Bhuhlmann and C. Affolter, *Structure determination of organic compounds*, Springer-Verlag, Berlin, 2000, p. 108.

Electronic Supplementary Material (ESI) for Journal of Materials Chemistry C.

Supporting information

Highly conducting 1-D polypyrrole prepared in the presence of safranin

Islam M. Minisy[a,b], Udit Acharya[a,c], Libor Kobera[a], Miroslava Trchová[a,d], Christoph Unterweger[e], Stefan Breitenbach[e], Jiří Brus[a], Jiří Pfleger[a], Jaroslav Stejskal[a], Patrycja Bober[a,*]

[a] *Institute of Macromolecular Chemistry, Academy of Sciences of the Czech Republic, 162 06 Prague 6, Czech Republic*

[b] *Charles University, Faculty of Science, 128 43 Prague 2, Czech Republic*

[c] *Charles University, Faculty of Mathematics and Physics, 121 16 Prague 2, Czech Republic*

[d] *University of Chemistry and Technology Prague, 166 28 Prague 6, Czech Republic*

[e] *Wood K Plus – Kompetenzzentrum Holz GmbH, 4040 Linz, Austria*

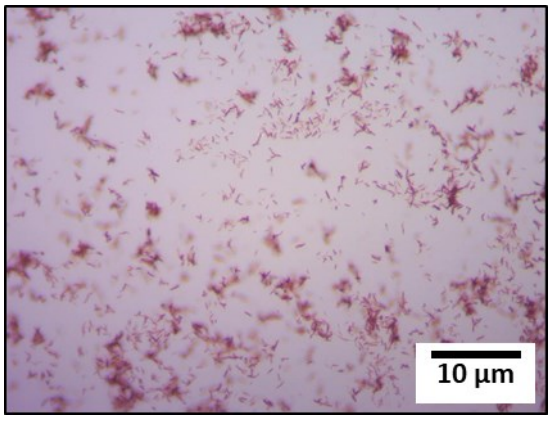

Fig. S1. Optical micrograph of fibrillary aggregates of safranin when mixed with iron(III) chloride solution.

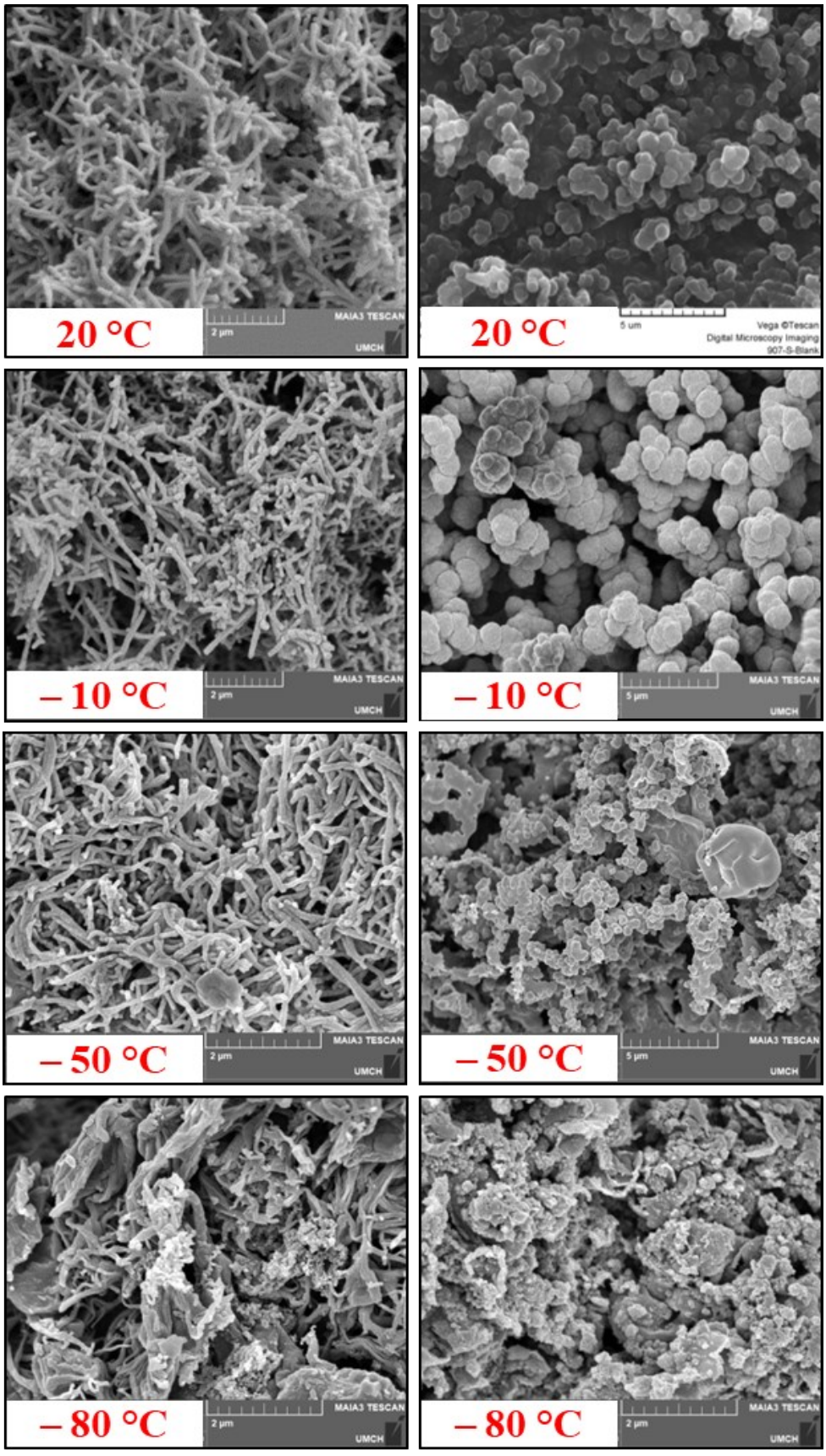

Fig. S2. SEM micrographs of polypyrrole prepared at different temperatures in the presence of safranin (left), and globular dye-free polypyrrole (right).

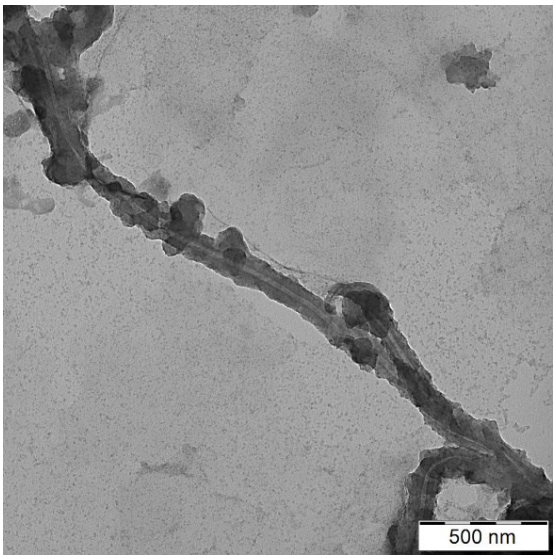

Fig. S3. TEM micrograph of polypyrrole prepared in the presence of safranin at −80 ºC.

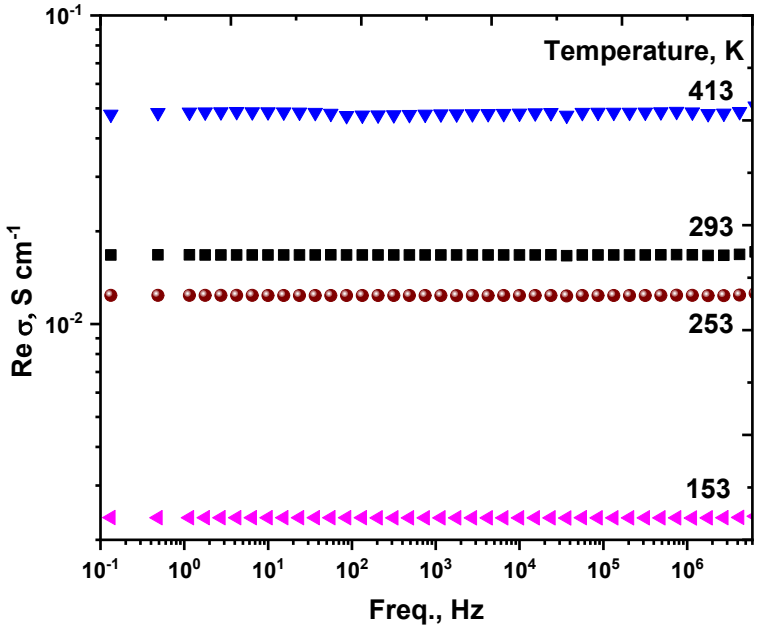

Fig. S4. Frequency dependence of conductivity at different temperatures of 1-D polypyrrole prepared in the presence of safranin at −24 °C.

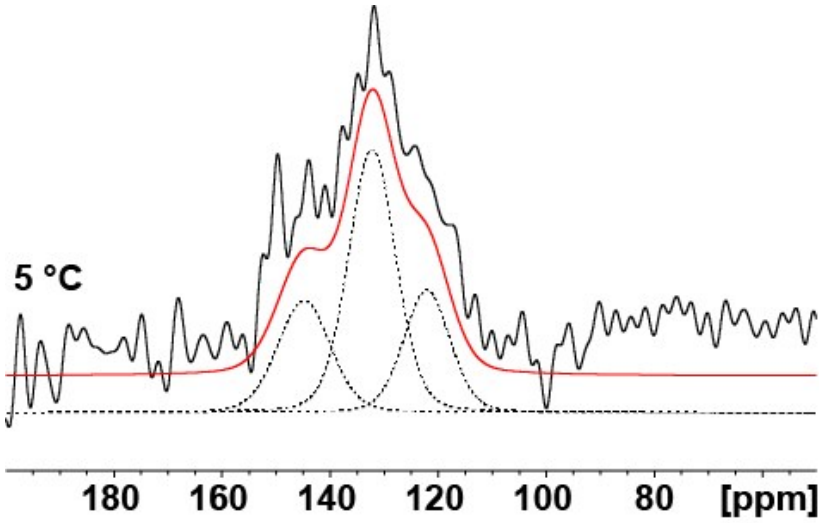

Fig. S5. Experimental ^{15}N CP/MAS NMR spectrum (black solid line), simulations of the individual nitrogen atoms (dashed lines) and their sum (red solid line) of prepared and deprotonated polypyrrole sample.

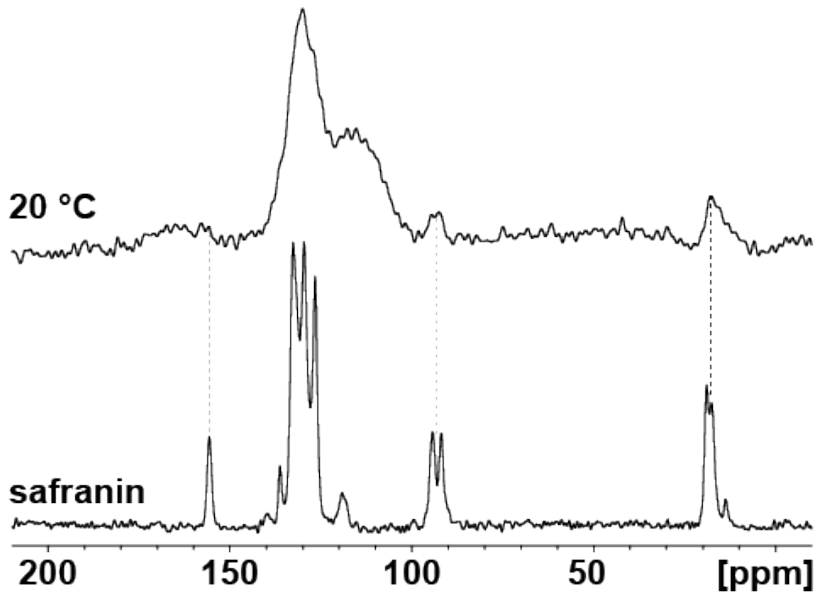

Fig. S6. The comparison of experimental ^{13}C CP/MAS NMR spectra of safranin with polypyrrole prepared in the presence of safranin at 20 °C.

Appendix 4

Highly conducting 1-D polypyrrole prepared in the presence of safranin

Macromolecular Rapid Communication
www.mrc-journal.de

Frozen-State Polymerization as a Tool in Conductivity Enhancement of Polypyrrole

*Islam M. Minisy and Patrycja Bober**

Polypyrrole (PPy) is oxidatively polymerized in the frozen state at −24 °C in the presence of various organic dyes as morphology guiding agents in order to form homogeneous 1D PPy nanoforms. The freezing polymerization of pyrrole has a significant influence on the electrical conductivity and thermal stability but negligible influence on the yield compared to widely used room temperature polymerization.

Polypyrrole (PPy) has gathered compelling attention among conducting polymers due to its facile preparation and unique physico-chemical properties.[1,2] As a result of its relatively high conductivity, environmental stability, and biocompatibility, PPy has been used in many applications, for example, bio and gas sensors,[3,4] micro-actuators,[5] battery electrodes,[6,7] supercapacitors[8,9] and adsorption.[10]

The insolubility and infusibility of PPy have restricted its practical applications; however, its processability and more importantly, conductivity can be improved by the formation of nanostructures. PPy has been synthesized as nanoparticles,[11] nanofibers,[12] nanorods,[13] and nanotubes.[14–16] Many additives, such as organic dyes, surfactants, or amino acids, are used as structure guiding agents to modify the PPy morphology.[17] The addition of organic dyes to PPy polymerization has noticeable influence on the conductivity. A typical example is methyl orange which is excessively used to prepare PPy nanotubes[14,16,18–20] with conductivity reaching 103 S cm^{-1}. Acid Blue 25 added to the polymerization medium leads to formation of nanofibers with conductivity of 60 S cm^{-1}.[12] Recently, PPy was prepared in the presence of safranin to obtain PPy nanorods, leading to the increase of conductivity from unit S cm^{-1} for globular PPy to 35 S cm^{-1} for nanorods.[13]

I. M. Minisy, Dr. P. Bober
Institute of Macromolecular Chemistry
Academy of Sciences of the Czech Republic
162 06, Prague 6, Czech Republic
E-mail: bober@imc.cas.cz
I. M. Minisy
Faculty of Science
Charles University
128 43, Prague 2, Czech Republic
The ORCID identification number(s) for the author(s) of this article can be found under https://doi.org/10.1002/marc.202000364.

DOI: 10.1002/marc.202000364

A plethora of work has been done to study the effect of additives or pyrrole-to-oxidant mole ratios, but the reports investigating the effect of polymerization temperature in the presence of additives on the resulting PPy are still neglected in the literature. Therefore, in this work, we investigate the effect of polymerization temperature on the formation of nanostructures and conductivity of PPy. For the first time we demonstrate the broad use of frozen-state polymerization resulting in significant increase of conductivity of PPy. The 1D PPy nanostructures were prepared by the aid of anionic or cationic organic dyes (methyl orange, Acid Blue 25, and safranin) in the frozen-state polymerization at −24 °C (**Figure 1**). Dyes when mixed with iron(III) chloride oxidant lead to the formation of solid templates that could guide the morphology of the PPy to nanostructures rather than the conventional globular beads.

PPy can be easily obtained by the oxidative polymerization of pyrrole with iron(III) chloride in aqueous medium. Three different PPy nanostructures were prepared at two different conditions, room temperature, and frozen state at −24 °C (Supporting Information). The concentration of pyrrole and oxidant was chosen based on previously published articles reporting the optimum conditions to obtain the highest conductivity of PPy nanostructure. PPy nanotubes were prepared by the polymerization of 0.15 M pyrrole with 0.3 M iron(III) chloride in the presence of 7.5 mM methyl orange.[14] PPy nanofibers were prepared by oxidation of 0.2 M pyrrole with 0.5 M iron(III) chloride in the presence of 10 mM Acid Blue 25.[12] Similarly, PPy nanorods were prepared when 0.2 M pyrrole was oxidized with 0.5 M iron(III) chloride in the presence of 4 mM safranin.[13] The same concentration of reactants was applied to frozen-state polymerization which proceeded in thermostatted water/ethylene glycol bath at −24 °C for 24 h (Figure 1E).

In a similar way to the polymerization at the room temperature, the frozen-state polymerization led to the PPy with good yield (**Figure 2**A). Theoretically, when 1 g of pyrrole is oxidized with iron(III) chloride, 1.1 g of PPy chloride is obtained, according to the reaction scheme when oxidant-to-pyrrole mole ratio is [Ox]/[Py] = 2.5.[12] It is well known that the polymerization of pyrrole can proceed easily at low temperatures.[21,22] Once the polymerization starts it can easily proceed by charges transfer (electrons and protons) between the reactants through the formed PPy clusters.[21,23] The yield of PPy nanostructures prepared in the presence of various dyes in the frozen condition was higher than the yield of the globular PPy (prepared without dye) (Figure 2A).

Macromolecular Rapid Communications
www.mrc-journal.de

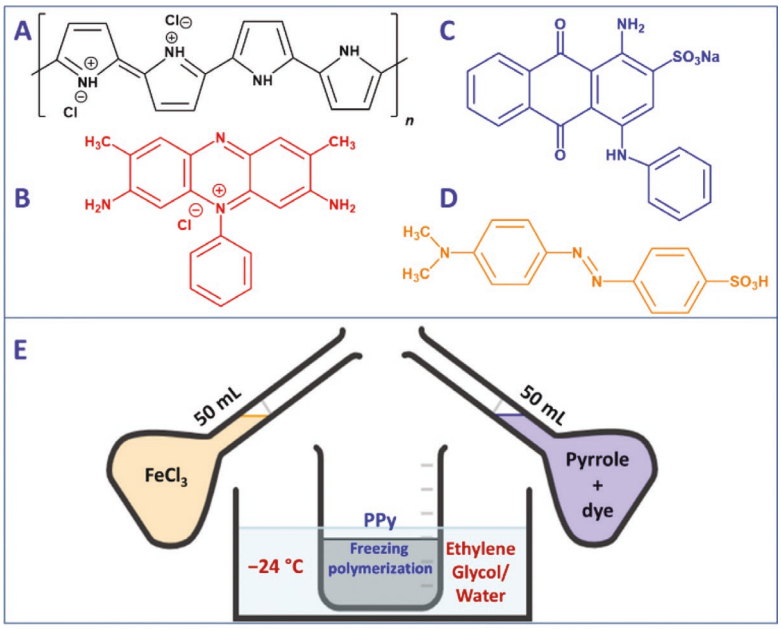

Figure 1. Chemical formulae of A) polypyrrole, B) safranin, C) Acid Blue 25, D) methyl orange, and E) the schematic representation of 1D polypyrrole freezing polymerization procedure.

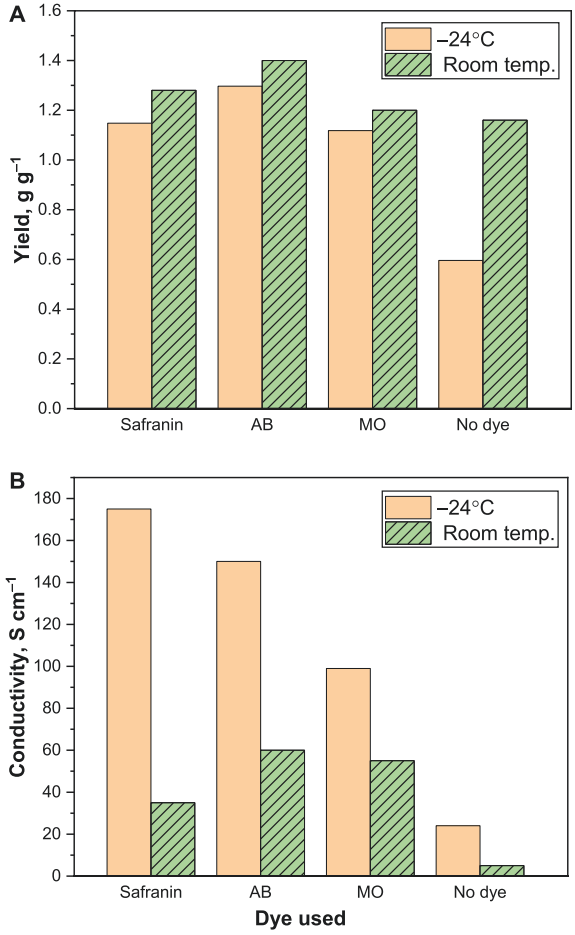

Figure 2. Comparison of polypyrrole A) yield and B) conductivity obtained by frozen-state polymerization and at room temperature.

This is connected to the dyes' incorporation into the final 1D PPy products, [13,18] either as PPy counter-ions or by physical entrapment inside the nanostructures. We can also speculate that addition of dyes may catalyze the polymerization of pyrrole at low temperatures.

SEM and TEM micrographs (**Figure 3**) clearly confirmed the formation of 1D PPy when polymerization was performed at frozen state. Interconnected nanorods were obtained by the use of safranin, entangled nanofibers in the case of Acid Blue 25 and PPy nanotubes when methyl orange was added. The solubility of reactants (pyrrole, dyes, and iron(III) chloride) is reduced under the frozen polymerization condition; however, the morphologies of 1D PPys remained unchanged compared to those obtained at room temperature, which is clearly visible on the TEM images (Figure 3B,D,F and Figure S1, Supporting Information). Freezing polymerization affected the dimensions, especially the thickness, of the formed 1D nanostructures. This might be because pyrrole molecules are forced to polymerize mainly between growing ice crystals.[24] The diameter of PPy nanorods reduced from 150 ± 10 nm (Figure S1A, Supporting Information) to ≈40 ± 5 nm (Figure 3B) when compared to those obtained at room temperature. Similarly, PPy nanofibers became thinner, 67 ± 19 nm in diameter (Figure S1B, Supporting Information) was decreased to ≈30 ± 3 nm (Figure 3D), when polymerization temperature was changed from room temperature to −24 °C. In the case of PPy nanotubes, there was only a slight change in the diameter from ≈80 ± 5 nm (Figure S1C, Supporting Information) obtained at room temperature to 71 ± 3 nm (Figure 3F) obtained at frozen state. Conventional PPy with the well-known globular morphology showed a reduction of the particle sizes when prepared in the freezing condition (Figure S2, Supporting Information).

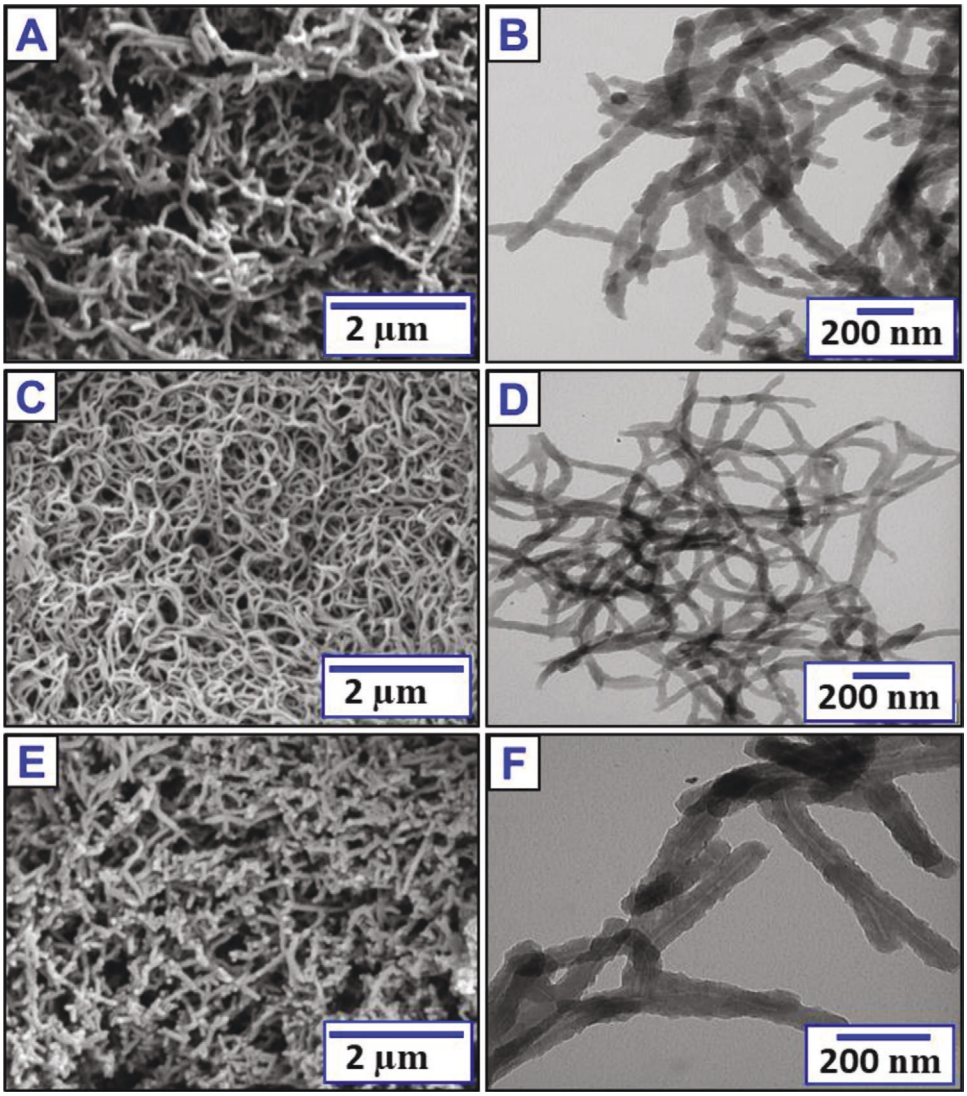

Figure 3. SEM and TEM micrographs of polypyrrole prepared by frozen-state polymerization, A,B) nanorods in the presence of safranin, C,D) nanofibers in the presence of Acid Blue 25, and E,F) nanotubes in the presence of methyl orange.

The conductivity results presented in Figure 2B and Table S2, Supporting Information, show significant dependence not only on the type of the dye but also on the polymerization temperature. Generally, the frozen-state polymerization undoubtedly enhanced the conductivity in all cases, even for globular PPy obtained in the absence of dye. The conductivity of the globular PPy prepared at room temperature (5 S cm^{-1}) increased almost five times (≈24 S cm^{-1}) when prepared at the frozen state. This fact is probably connected to the reduced size of PPy globules prepared at frozen state. Similar effect was reported earlier when size of PPy globules was reduced by the use of surfactant leading to the increase in conductivity.[25]

The conductivity of PPy nanorods, prepared in the presence of safranin, increased from 35 S cm^{-1} when polymerized at room temperature to 175 S cm^{-1} when prepared at –24 °C. For the PPy nanofibers which were prepared in the presence of Acid Blue 25, the conductivity of 150 S cm^{-1} was reached by frozen-state polymerization, compared to 32.5 S cm^{-1} obtained at room temperature. The same behavior was obtained for PPy nanotubes, prepared with methyl orange, and the conductivity was enhanced to 109 S cm^{-1}.

The conductivity mostly depends on the microscopic (intrinsic) as well as the macroscopic (extrinsic) properties of conducting polymers. Microscopic properties rely on the doping level, conjugation, intra-chain interaction, and the chain length, while the macroscopic ones depend mainly on the inter-chain interactions, morphology, and compactness of the chains.[26,27] Apparently, the freezing polymerization (at –24 °C) influences both micro- and macroscopic properties. Freezing polymerization most likely results in higher molecular weight and less defect in polymer chains leading to increase in conductivity. Bober et al. reported a similar effect for polyaniline (closely related polymer) polymerized in frozen state.[28] Preparation

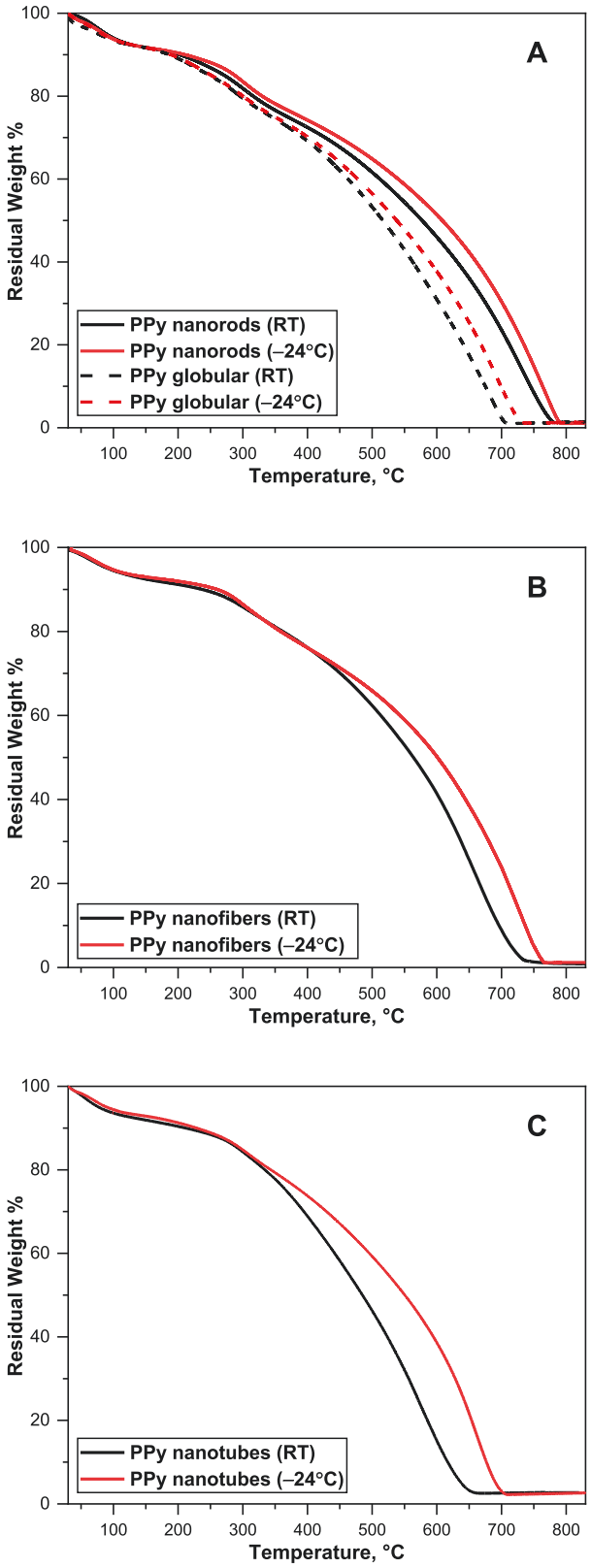

Figure 4. TGA in air of A) globular polypyrrole and polypyrrole nanorods (in the presence of safranin), B) polypyrrole nanofibers (in the presence of Acid blue 25), and C) polypyrrole nanotubes (in the presence of methyl orange), prepared at room temperature and frozen-state.

of 1D PPy nanostructures additionally results in better chain organization.[29]

TGA analysis in air (**Figure 4**) was used to evaluate the thermal stability of the PPy prepared at room temperature and at frozen state. The thermal stability of globular PPy and 1D PPy prepared at –24 °C is higher than corresponding PPy obtained at room temperature. In all cases PPy is stable up to ≈200 °C, however, small weight loss is observed, which can be connected with the release of residual moisture and/or protonating acid. PPy nanorods prepared at both room temperature and frozen state exhibited the highest thermal stability among all nanostructures and decomposed fully above 770 and 795 °C, respectively.

In conclusion, frozen-state polymerization of PPy (in the presence and absence of dyes) was successfully performed and led to the formation of nanostructures with enhanced conductivity and thermal stability. The highest conductivity, 175 S cm^{-1}, was obtained when PPy nanorods were prepared in the presence of safranin at –24 °C. It is the highest conductivity reported in the literature for PPy powder prepared by simple oxidative polymerization. Using the frozen-state polymerization for the preparation of highly conducting PPy seems to be the effective strategy to increase the potential applications of PPy in the field of electronics and energy.

Supporting Information

Supporting Information is available from the Wiley Online Library or from the author.

Acknowledgements

The authors wish to thank the Czech Science Foundation (18-04669S) for the financial support. Ms. J. Hromádková, Mr. U. Acharya, and Ms. M. Karbusická are acknowledged for performing electron microscopy, conductivity, and TGA measurements, respectively.

Conflict of Interest

The authors declare no conflict of interest.

Keywords

conducting polymers, frozen polymerization, organic dyes, polypyrrole

Received: July 8, 2020
Revised: July 24, 2020
Published online:

[1] J. Stejskal, M. Trchová, *Chem. Pap.* **2018**, *72*, 1563.
[2] I. Rawal, A. Kaur, *J. Nanopart. Res.* **2013**, *15*, 1637.
[3] S. Bibi, H. Ullah, S. M. Ahmad, A. U. H. A. Shah, S. Bilal, A. A. Tahir, K. Ayub, *J. Phys. Chem. C.* **2015**, *119*, 15994.
[4] R. Khoder, H. Korri-Youssoufi, *Mater. Sci. Eng., C.* **2020**, *108*, 110371.

[5] E. W. Jager, E. Smela, O. Inganäs, I. Lundström, *Synth. Met.* **1999**, *102*, 1309.
[6] C. Wang, W. Zheng, Z. Yue, C. O. Too, G. G. Wallace, *Adv. Mater.* **2011**, *23*, 3580.
[7] H. Kong, M. Yang, Y. Miao, X. Zhao, *Energy Technol.* **2019**, *7*, 1900835.
[8] Y. Huang, H. Li, Z. Wang, M. Zhu, Z. Pei, Q. Xue, C. Zhi, *Nano Energy.* **2016**, *22*, 422.
[9] S. Yang, L. Sun, X. An, X. Qian, *Carbohydr. Polym.* **2020**, *229*, 115455.
[10] M. M. Ayad, W. A. Amer, S. Zaghlol, I. M. Minisy, P. Bober, J. Stejskal, *Chem. Pap.* **2018**, *72*, 1605.
[11] W. J. Kwon, D. H. Suh, B. D. Chin, J. W. Yu, *J. Appl. Polym. Sci.* **2008**, *110*, 1324.
[12] P. Bober, Y. Li, U. Acharya, Y. Panthi, J. Pfleger, P. Humpolíček, M. Trchová, J. Stejskal, *Synth. Met.* **2018**, *237*, 40.
[13] I. M. Minisy, P. Bober, U. Acharya, M. Trchová, J. Hromádková, J. Pfleger, J. Stejskal, *Polymer* **2019**, *174*, 11.
[14] Y. Li, P. Bober, M. Trchová, J. Stejskal, *J. Mater. Chem. C.* **2017**, *5*, 4236.
[15] I. Sapurina, Y. Li, E. Alekseeva, P. Bober, M. Trchová, Z. Morávková, J. Stejskal, *Polymer.* **2017**, *113*, 247.
[16] I. M. Minisy, N. Gavrilov, U. Acharya, Z. Morávková, C. Unterweger, M. Mičušík, S. K. Filippov, J. Kredatusová, I. A. Pašti, S. Breitenbach, G. Ćirić-Marjanović, J. Stejskal, P. Bober, *J. Colloid Interface Sci.* **2019**, *551*, 184.
[17] J. Stejskal, M. Trchová, *Colloid Polym. Sci.* **2020**, *298*, 319.
[18] J. Kopecká, D. Kopecký, M. Vrňata, P. Fitl, J. Stejskal, M. Trchová, P. Bober, Z. Morávková, J. Prokeš, I. Sapurina, *RSC Adv.* **2014**, *4*, 1551.
[19] J. W. Lee, H. I. Lee, S. J. Park, *Electrochim. Acta* **2018**, *263*, 447.
[20] H. Mao, Z. Q. Cao, X. Guo, D. Y. Dyn, D. L. Liu, S. Y. Wu, Y. Zhang, X. M. Song, *ACS Appl. Mater. Interfaces* **2019**, *11*, 10153.
[21] G. Qi, L. Huang, H. Wang, *Chem. Comm.* **2012**, *48*, 8246.
[22] P. Bober, Z. Capáková, U. Acharya, B. A. Zasońska, P. Humpolíček, J. Hodan, J. Hromádková, J. Stejskal, *Synth. Met.* **2019**, *252*, 122.
[23] E. N. Konyushenko, J. Stejskal, M. Trchová, N. V. Blinova, P. Holler, *Synth. Met.* **2008**, *158*, 927.
[24] J. Stejskal, P. Bober, M. Trchová, A. Kovalcik, J. Hodan, J. Hromádková, J. Prokeš, *Macromolecules.* **2017**, *50*, 972.
[25] M. Omastova, M. Trchová, J. Kovářová, J. Stejskal, *Synth. Met.* **2003**, *138*, 447.
[26] M. Jaiswal, M. Reghu, *Polym. Int.* **2006**, *55*, 1371.
[27] U. Acharya, P. Bober, M. Trchová, A. Zhigunov, J. Stejskal, J. Pfleger, *Polymer* **2018**, *150*, 130.
[28] P. Bober, J. Stejskal, M. Trchová, J. Prokeš, *J. Solid State Electrochem.* **2011**, *15*, 2361.
[29] J. Stejskal, *Polym. Int.* **2018**, *67*, 1461.

Supporting Information

Frozen-state polymerization as a tool in conductivity enhancement of polypyrrole

*Islam M. Minisy[1,2] and Patrycja Bober[1]**

[1]Institute of Macromolecular Chemistry, Academy of Sciences of the Czech Republic, 162 06 Prague 6, Czech Republic

[2]Faculty of Science, Charles University, 128 43 Prague 2, Czech Republic.
E-mail: bober@imc.cas.cz

Chemicals and reagents

Pyrrole, iron(III) chloride hexahydrate, safranin, methyl orange and Acid Blue 25 were obtained from Sigma-Aldrich. All chemicals were used as received without any further purifications or recalculations of dye content.

Preparation of 1-D polypyrrole

Three various polypyrrole (PPy) nanostructures were prepared at two different conditions; at room temperature and at −24°C. PPy nanotubes were prepared by the oxidative polymerization of 0.15 M pyrrole (1.0 g) with 0.3 M iron(III) chloride (8.11 g) in the presence of 75 mM methyl orange (0.246 g).[1] PPy nanofibers was prepared by oxidation of 0.2 M pyrrole (1.34 g) with 0.5 M iron(III) chloride (13.5 g) in the presence of 10 mM Acid Blue 25 (0.416 g).[2] Similarly, PPy nanorods were prepared by polymerization of 0.2 M pyrrole (1.34 g) with 0.5 M iron(III) chloride (13.5 g) in the presence of 4 mM safranin (0.140 g).[3] Globular PPy (without dye) was prepared by mixing 0.2 M pyrrole (1.34 g) with 0.5 M Iron(III) chloride (13.5 g) solutions. The total volume of the polymerization mixture was 100 mL in each

polymerization experiment. The reactants for frozen-state polymerization were precooled slowly to −24°C while stirring, not to allow them to solidify, and the resulting semi-frozen slushy solutions was homogeneously mixed. The frozen-state polymerization precedes in water/ethylene glycol bath (−24°C) for 4 h. Then all polymerization mixtures were left in rest in a freezer at −24°C, after 24 h the black powders were collected by vacuum filtration, washed with 0.2 M HCl followed by ethanol, and left to fully dry at room temperature over silica gel beads.

Characterization and instrumentation

Conductivity of all prepared PPy products were measured in ambient conditions (23 ± 1°C and relative humidity 35 ± 5 %) by a four-point van der Pauw method on compressed pellets having 13 mm diameter and 1.0 ± 0.2 mm thickness prepared under pressure 530 MPa using a hydraulic press Trystom H-62. A Keithley 230 Programmable Voltage Source in serial connection with a Keithley 196 System DMM was used as a current source; the potential difference between the potential probes was measured with a Keithley 181 Nanovoltmeter (Keithley, USA). Each sample was measured at least three times.

Morphologies were examined using a MIRA3 TESCAN scanning electron microscope (SEM) and TECNAI G2 SPIRIT transmission electron microscope (TEM).

Thermogravimetric analysis (TGA) was carried out using Pyris 1 TGA Thermogravimetric Analyzer (Perkin Elmer, USA) in the condition of 10°C min^{-1} heating rate, 20 mL min^{-1} air flow in the heating range from 30 to 850°C.

Results

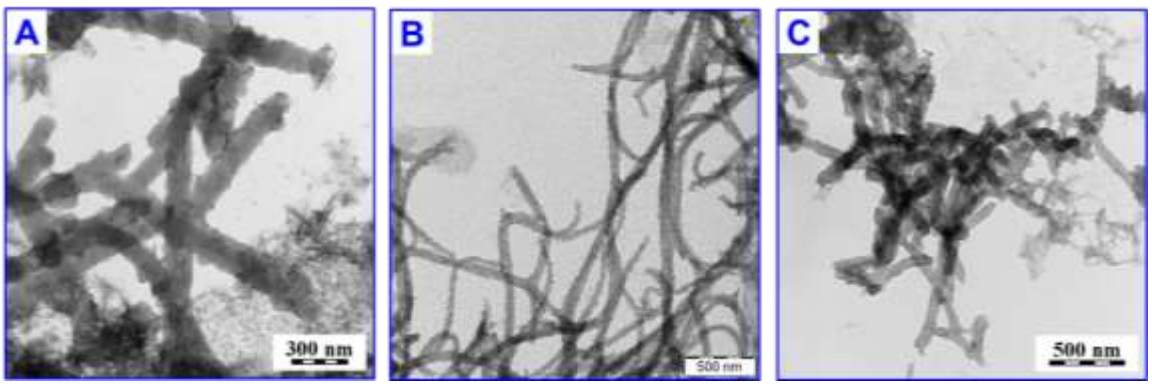

Figure S1. TEM of polypyrrole nanostructures prepared at room temperature in the presence of safranin (A), Acid Blue 25 (B), and methyl orange (C).

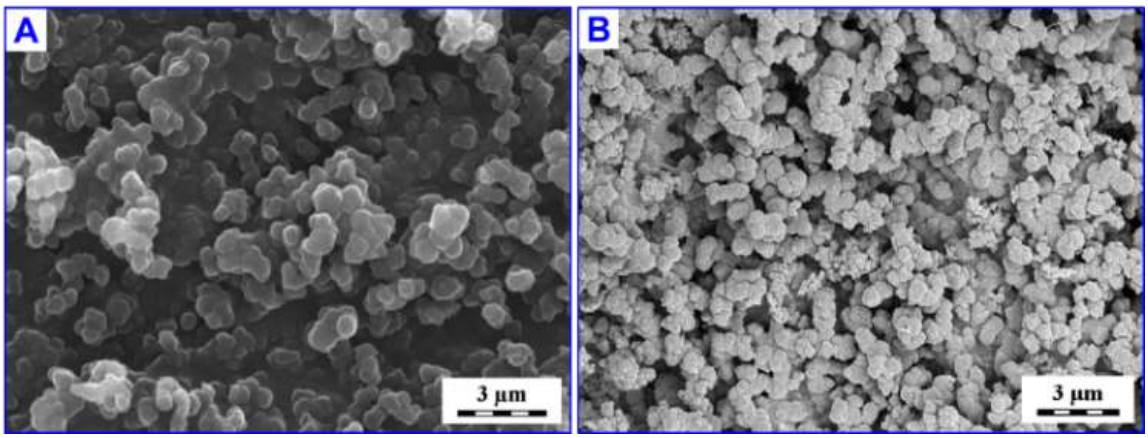

Figure S2. SEM micrograph of globular PPy (synthesized without dyes) prepared at room temperature (A) and at –24°C (B).

Table S1. The influence of polymerization temperature on the conductivity, and the yield of the produced polypyrrole.

Dye used	Preparation Temperature			
	Room temperature		Frozen condition (−24°C)	
	Yield, g/g[Py]	σ, S cm^{-1}	Yield, g/g[Py]	σ, S cm^{-1}
No dye	1.16	5	0.60	23.7
Safranin	1.28	35	1.15	175

Acid Blue 25	1.40	32.5	1.30	150
Methyl orange	1.19	55	1.12	99

REFERENCES

(1) Y. Li, P. Bober, M. Trchová and J. Stejskal, *J. Mater. Chem. C*, **2017**, 5, 4236.

(2) P. Bober, Y. Li, U. Acharya, Y. Panthi, J. Pfleger, P. Humpolíček, M. Trchová and J. Stejskal, *Synth. Met.* **2018**, 217, 40.

(3) I.M. Minisy, P. Bober, U. Acharya, M. Trchová, J. Hromádková, J. Pfleger and J. Stejskal, *Polymer*, **2019**, 174, 11.

Appendix 5

Sponge-like polypyrrole–nanofibrillated cellulose aerogels

Journal of Materials Chemistry C

ROYAL SOCIETY OF CHEMISTRY

PAPER

View Article Online
View Journal | View Issue

Cite this: J. Mater. Chem. C, 2021, 9, 12615

Sponge-like polypyrrole–nanofibrillated cellulose aerogels: synthesis and application

Islam M. Minisy, [ab] Udit Acharya,[a] Stefan Veigel,[c] Zuzana Morávková,[a] Oumayma Taboubi, [a] Jiří Hodan,[a] Stefan Breitenbach,[d] Christoph Unterweger, [d] Wolfgang Gindl-Altmutter[c] and Patrycja Bober *[a]

Received 28th June 2021,
Accepted 12th August 2021

DOI: 10.1039/d1tc03006j

rsc.li/materials-c

Nowadays, materials for soft electronics are in high demand; among the different forms of conducting materials, conducting gels have become promising candidates. They provide both the electrical conductivity and mechanical flexibility, which are prerequisites for such applications. Herein, one-step facile preparation of polypyrrole–nanofibrillated cellulose (PPy–NFC) cryogels and their conversion to aerogels are reported. PPy–NFC was prepared *via* an *in situ* oxidative polymerization of pyrrole with iron(III) chloride in the presence of NFC under frozen conditions. The mechanical properties of the cryogels were improved by increasing the NFC content from 0.1 to 2 wt%. The tensile modulii of 432 kPa and 1055 kPa were achieved for cryogels and aerogels with 2 wt% of NFC, respectively. SEM micrographs of the aerogels show the formation of entangled three-dimensional porous networks with various pore sizes depending on the NFC content. Lightweight, flexible and conducting aerogels with high specific surface area (34.5–67.3 $m^2 g^{-1}$) were obtained. The conductivity of 31 S cm^{-1} was attained when 0.7 wt% of NFC was used for cryogel preparation, which is significantly higher than conventional globular PPy. Additionally, aerogels showed improved ability to adsorb heavy metal ions (hexavalent chromium ions) from aqueous solutions owing to their high specific surface area and ion exchange properties.

Introduction

Polypyrrole, a conducting polymer, exhibits unique properties that synergize the features of conventional polymers and semiconductors.[1] It has high electrical conductivity compared to the other conducting polymers, in addition to its environmental stability, easy preparation methods and biocompatibility.[2] PPy has been synthesized in several forms, *e.g.* powders,[3] colloids,[4] films,[5] hydrogels[6] and cryogels.[7] It is found to be advantageous in a broad range of applications in various science and engineering fields, such as adsorption and catalytic degradation of water pollutants,[1,8–10] catalysis,[11] sensors,[10,12] actuators,[13] biomedicine,[14] electrodes in batteries,[5] supercapacitors,[15] electroactive membranes[16–18] and tissue engineering.[19,20]

However, insolubility, infusibility, low surface area and poor mechanical properties of PPy have restricted its potential applications. Hence, PPy gels are exploited to overcome the poor mechanical properties. Gels are an important class of soft materials possessing good mechanical properties,[21] which are mainly dependent on the three-dimensional (3-D) entangled networks, hydrogen bonding, π–π stacking, coordination bonding, hydrophobic effects and van der Waals interactions.[22] A new class of conducting gels, the cryogels, have been recently prepared in the frozen condition,[7] and can be designed in desired shapes by controlling the mold. Moreover, their physico-chemical properties can be tailored by controlling the preparation conditions. Bober *et al.*[7] have prepared macroporous, soft, biocompatible and mechanically stable PPy/poly(vinyl alcohol) (PVAL) cryogels, by single step polymerization, however, the specific surface area of such cryogels was low (0.45–14 $m^2 g^{-1}$). Milakin *et al.*[23] obtained biocompatible and antibacterial PPy-gelatin cryogels with good mechanical properties, but high contents of gelatin were used, resulting in low conductivity. Due to those drawbacks, further improvement in conducting cryogels' properties is still required to realize a wide variety of applications.

One of the worldwide environmental issue nowadays is the contamination of wastewater by heavy metal residues. For example, accumulation of toxic Cr(VI) ions in human body causes severe health problems, from skin irritation to lung cancer.[24] Various composites have been used for the

[a] Institute of Macromolecular Chemistry, Czech Academy of Sciences, 162 06 Prague 6, Czech Republic. E-mail: bober@imc.cas.cz
[b] Faculty of Science, Charles University, 128 43 Prague 2, Czech Republic
[c] Department of Material Sciences and Process Engineering, Institute of Wood Technology and Renewable Materials, BOKU–University of Natural Resources and Life Sciences Vienna, Tulln an der Donau A-3430, Austria
[d] Wood K plus–Kompetenzzentrum Holz GmbH, Linz 4040, Austria

remediation of Cr(VI) ions from wastewater.[25] Inorganic composites such as artificial zeolites loaded with bimetallic Fe–Al oxides have shown adsorption capability in a wide pH range.[26] Cellulose based composites such as a fibre ball loaded with $Fe(OH)_3$ and oxalic acid, or a Cu–Fe embedded cross-linked cellulose hydrogel have shown an efficiency towards Cr(VI) ions' reductive removal.[27,28] PPy and its composites have been widely used in water treatment to remove heavy metals and organic dyes.[1,29] Zhang *et al.* have used cellulose fiber balls loaded with PPy to improve the utilization of waste paper through "waste treatment by waste" strategy.[30] Hence, PPy aerogels are good candidates as adsorbents, in addition to the easy separation from the solution after the adsorption process, due to their high surface area, redox properties and straightforward preparation with low cost.

We report here the preparation of novel PPy–nanofibrillated cellulose (NFC) cryogels by facile cryopolymerization, and subsequent transformation of cryogels to conducting, porous, flexible and lightweight aerogels (Fig. 1). To the best of our knowledge such multifunctional materials have not been reported yet. In this paper we studied the influence of various contents of NFC on morphology, conductivity, mechanical properties and specific surface area of PPy–NFC aerogels. Additionally, to demonstrate the possible application of such materials, PPy–NFC aerogels were tested as promising adsorbents for the removal of Cr(VI) from aqueous solutions.

Experimental section

Materials

Pyrrole, iron(III) chloride hexahydrate and potassium dichromate ($K_2Cr_2O_7$) were purchased from Sigma-Aldrich (Germany). All chemicals were used as received without any further purification. NFC produced by mechanical fibrillation of bleached softwood Kraft pulp was purchased from University of Maine, Process Development Center (Orono, ME, USA) as a 3 wt% aqueous suspension. According to manufacturer specifications, the Kappa number of the material is 0.5 which corresponds to a lignin content of $<0.1\%$ while the hemicellulose content is in the range of 15–20%.

Preparation of polypyrrole–nanofibrillated cellulose cryogels and aerogels

Polypyrrole–nanofibrillated cellulose cryogels were synthesized *via in situ* oxidative polymerization of pyrrole (0.2 M, 0.67 g) with iron(III) chloride as an oxidant (0.5 M, 6.757 g) in the presence of various concentrations of NFC (0.1 to 2 wt%). The total volume of reaction mixtures was 50 mL. The precooled reaction solutions were mixed and instantly sucked into plastic syringes, as molding vessels, and promptly frozen in dry ice/ethanol bath (−78 °C) for 30 minutes before transferring to freezer (−24 °C), where they were left to polymerize for 7 days. After thawing at room temperature, cryogels were taken out from the syringes and washed thoroughly by immersion into excess of Milli-Q water (to reach pH 7) or 0.2 M HCl solution. The washing medium was exchanged with fresh one daily for two months to remove all the by-products and to stabilize the pH to obtain protonated (washed with acid) and deprotonated (washed in water) cryogels. Corresponding aerogels were obtained by freeze-drying of cryogels (GREGOR Instruments, L4-110 freeze-drier, Czech Republic) (Fig. 2).

Characterization

The morphology of the freeze-dried aerogels was examined with the scanning electron microscope (SEM, MAIA3 TESCAN, Czech Republic).

The FTIR spectra of the ground aerogels dispersed in potassium bromide pellets were registered using a Thermo Nicolet NEXUS 870 FTIR spectrometer with a DTGS TEC detector (Thermo-Nicolet, USA) in the 400–4000 cm^{-1} wavenumber region.

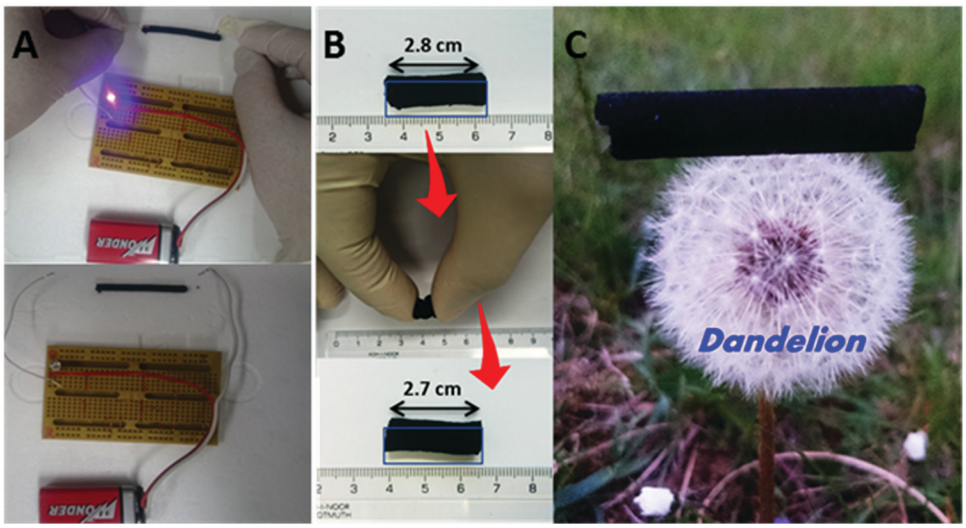

Fig. 1 Polypyrrole–nanofibrillated cellulose aerogel prepared with 0.7 wt% of nanofibrillated cellulose: (A) electrically conductive, (B) highly flexible and (C) lightweight.

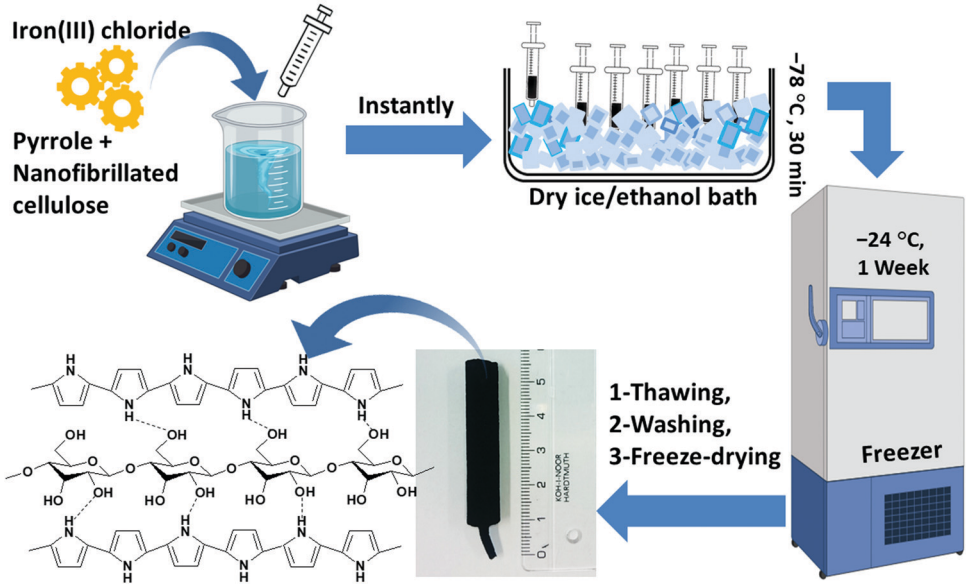

Fig. 2 Schematic representation of the cryogel preparation procedure.

Raman spectra excited with NIR diode laser emitting at 785 nm and HeNe laser at 633 nm were recorded with a Renishaw InVia Reflex Raman microspectrometer (Renishaw, UK). The scattered light was analyzed using a spectrograph with holographic gratings of 1200 lines mm^{-1} and 1800 lines mm^{-1}. A research-grade Leica DM LM microscope was used to focus the laser beam. A Peltier-cooled CCD detector (576 × 384 pixels) registered the dispersed light.

Thermogravimetric analysis was performed in air or under nitrogen flow at the heating rate of 10 °C min^{-1} up to 800 °C with Pyris 1 Thermogravimetric Analyzer (PerkinElmer, USA).

The specific surface area of PPy–NFC aerogels was estimated by the Brunauer–Emmett–Teller (BET) method using an automatic volumetric sorption analyser (Autosorb-iQ, Anton Paar QuantaTec Inc., USA) with nitrogen at 77 K. 40–50 mg of the PPy and PPy–NFC aerogels were outgassed for 1 h at 200 °C (NFC for 2 h at 110 °C) before the adsorbed gas volume was measured at a relative pressure of 0.1 to 0.3.

The DC conductivity measurements were performed by van der Pauw method under the ambient conditions (23 ± 1 °C and relative humidity 35 ± 5%). A programmable voltage source (Keithley 230) and a current source Keithley 196 system DMM digital multimeter were connected in series, and the potential drop measurements were carried out using a Keithley 181 nanovoltmeter (Keithley, USA). About 100 mg of aerogels were smashed and pressed into pellets (13 mm diameter, 1 ± 0.05 mm thickness) using a manual hydraulic press (Trystom H-62, Czech Republic). The conductivity was measured at least three times for each sample in two perpendicular directions and the average values were reported from the linear part of current–voltage curve.

The static mechanical properties of the cryogels and aerogels were investigated on electromechanical testing device Instron 6025/5800R (Instron Ltd, High Wycombe, UK), equipped with a 10 N load cell at room temperature and with a crosshead speed of 10 mm min^{-1}. Cylindrical specimens with 4.5 mm diameter and 60 mm length were employed in the environment of deionized water (cryogels) or in air (aerogels). An initial preload of 0.01 N was applied. At least 5 measurements had been performed and the results were averaged.

Removal of chromium ions

The adsorption property of PPy–NFC aerogels towards heavy metal ions *e.g.* Cr(VI) ions was tested in aqueous solutions. 10 mg of PPy–NFC aerogels were brought into contact with 50 mL of 100 mg L^{-1} $K_2Cr_2O_7$ (~35 mg L^{-1} of Cr(VI)) solutions adjusted at pH 2. The mixture was kept under mild stirring (200 rpm) for 24 hours at room temperature to attain the equilibrium. The UV–visible spectra of Cr(VI) ions were recorded using Lambda 950 spectrometer (PerkinElmer, UK).

Results and discussion

Morphology

The SEM micrographs (Fig. 3) of all the PPy–NFC aerogels prepared with different NFC contents show highly porous sponge-like 3-D network morphologies. The porous structure is formed due to the growth of ice crystals during the cryopolymerization. The SEM micrographs, also, prove the absence of PPy aggregates (globulus) and reveal the homogenous distribution of PPy onto the NFC fibrils. Pyrrole tends to polymerize on the NFC surface due to its hydrophobic nature and hence, higher affinity toward cellulose fibers than ice crystals. The entangled fibers of the NFC work as a template to form 3-D network structures, while PPy works as an adhesive coating to fix cellulose nanofibers together.[31,32] Moreover, hydrogen bonding between –N–H groups in polypyrrole and the hydroxyl

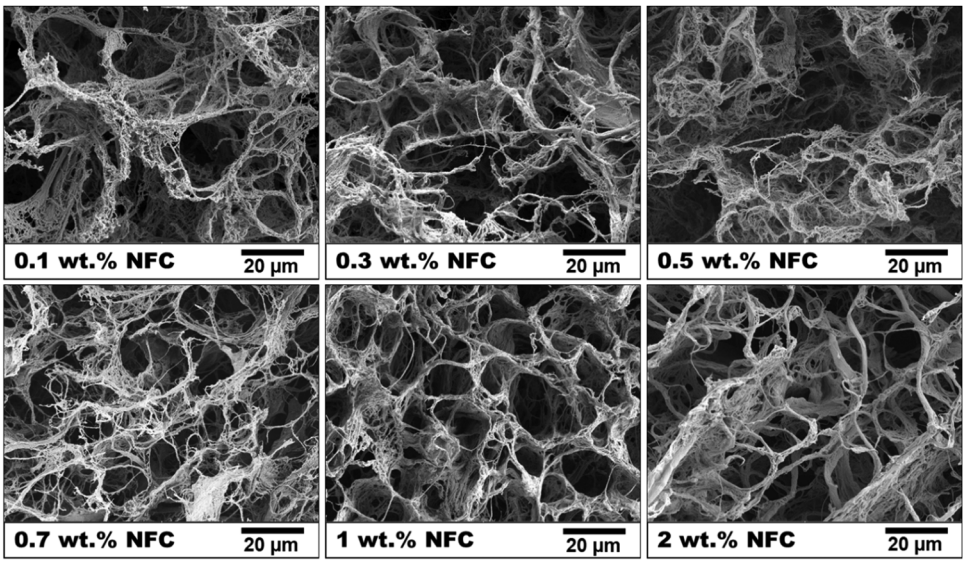

Fig. 3 SEM micrographs of polypyrrole–nanofibrillated cellulose aerogels prepared with various contents of nanofibrillated cellulose.

groups of the NFC ensures the uniform distribution of PPy onto the NFC fibers (see FTIR spectroscopy below).[31,32]

Cryopolymerization of PPy–NFC with low contents of NFC (0.1–0.5 wt%) preserves the separation of the fibrils and leads to thinner interconnected fibers, while for higher contents of NFC (0.7–2 wt%), the fibers tend to bundle creating thicker ones (with diameter increased with increasing the NFC contents).

FTIR and Raman spectroscopy

The FTIR spectra of PPy–NFC aerogels with various NFC contents are compared to the spectra of pristine PPy and NFC (Fig. 4). The spectrum of pristine PPy shows a series of stretching vibration bands; at 3416 cm^{-1} (N–H), 1632 (C═O), 1544 cm^{-1} (C═C), 1463 cm^{-1} (C–C) and 1310 cm^{-1} (C–N). The peak at 1041 cm^{-1} is assigned to C–H in-plane bending vibration.[33] The spectrum of pristine NFC shows a broad band at 3400 cm^{-1} which is assigned to the O–H stretching vibration of the cellulose. The asymmetric stretching vibration of C–H is located at 2922 cm^{-1}. The peaks in the range 1050–1170 cm^{-1} are related to C–O–C and C–O stretching vibrations in the pyranose ring of the cellulose.[33]

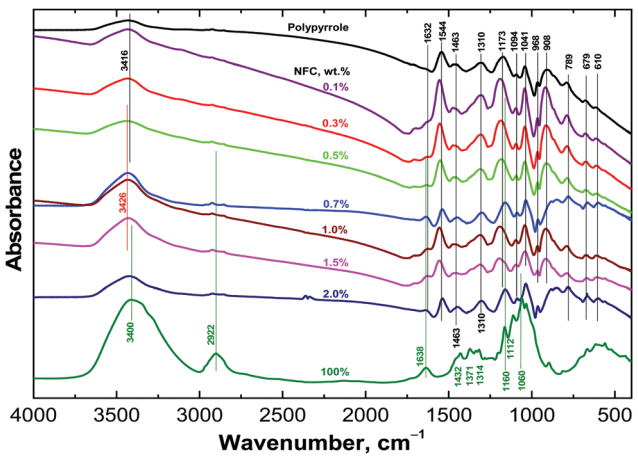

Fig. 4 FTIR spectra of polypyrrole, nanofibrillated cellulose and polypyrrole–nanofibrillated cellulose aerogels prepared with various contents of nanofibrillated cellulose.

The spectra of all PPy–NFC aerogels show the main characteristic peaks of PPy with slight changes. The bands related to C–O–C and C–O stretching vibrations, are overlapped with C–H characteristic bending modes of PPy. The band at 1632 cm^{-1} (PPy–NFC) is more pronounced at 0.7 wt% of cellulose contents in aerogel and can be related to the vibration of water molecules adsorbed onto cellulose or to the overoxidation of PPy. The band intensity at 3426 cm^{-1} for PPy–NFC has increased in comparison to pristine PPy (3416 cm^{-1}) and slightly shifted toward higher wavenumbers, due to hydrogen bonding interactions between hydroxyl groups in NFC and –N–H groups in PPy.[33,34]

The Raman spectra of pristine PPy, NFC and PPy–NFC with different NFC contents were collected using two different laser excitation lines; 633 nm and 785 nm (Fig. 5).

The spectrum of NFC displays only fluorescence and no Raman peaks were observed when laser excitation line 633 nm was used (Fig. 5A). However, some characteristic peaks of NFC can be detected by employing the near infrared laser 785 nm (Fig. 5B). The attribution of PPy and NFC peaks for both laser excitation lines is summarized in the Table 1.

The Raman spectra of PPy–NFC with different NFC contents exhibit the same features as pristine PPy and no cellulose peaks were detected at both excitation lines. The band intensity at 1078 cm^{-1} (attributed to the C–H deformation vibration in bipolaron structure in pristine PPy) is the highest when 0.7 wt% NFC was used. This means that at this condition (0.7 wt% NFC), the bipolaron to polaron ratio increases which indicates lower concentration of defects on PPy chains.[35] This result is in accordance with FTIR and the conductivity results (see Section

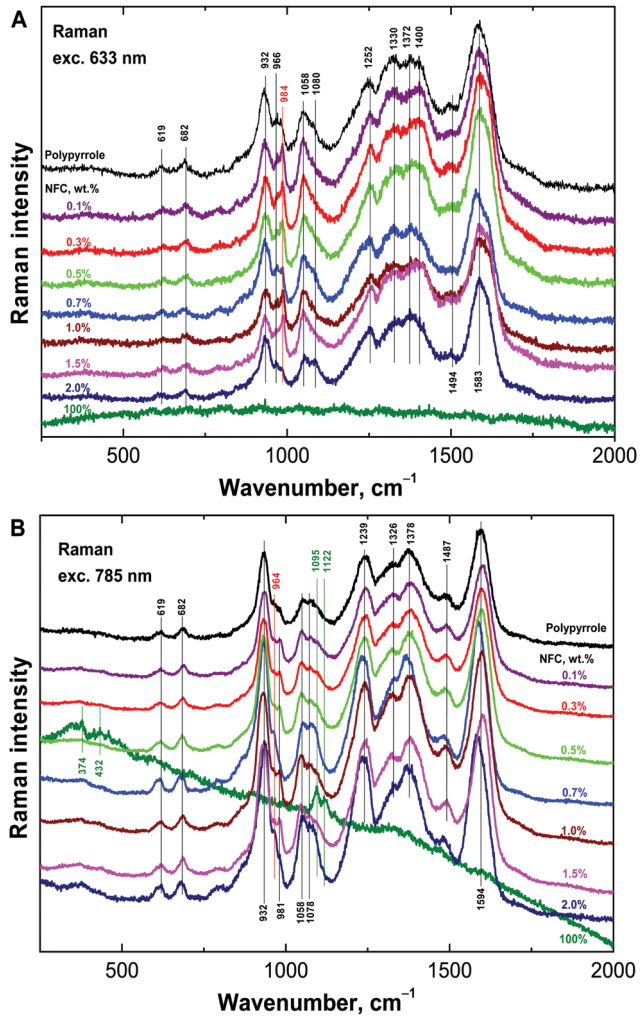

Fig. 5 Raman spectra of polypyrrole, nanofibrillated cellulose and polypyrrole–nanofibrillated cellulose aerogels prepared with various contents of nanofibrillated cellulose. Excitation wavelengths (A) 633 nm, and (B) 785 nm.

Conductivity). The Raman analysis was carried out at different points of the samples, and the results demonstrate homogenous coating of NFC with PPy. The absence of any characteristic features of NFC in PPy–NFC spectra indicates that the NFC fibers are successfully coated with PPy, and the FTIR results suggest that hydrogen bonding improves the adhesion of PPy onto NFC.

Conductivity

The DC conductivity of the compressed pellets of protonated PPy–NFC aerogels (cryogels were washed with 0.2 M HCl solution before freeze-drying) showed relatively high values (Fig. 6). Their conductivity is comparable to pristine PPy prepared in the same condition (freezing polymerization)[39] with the value of 24 S cm^{-1} and higher than previously reported for PPy/PVAL cryogels (18 S cm^{-1}).[7] All protonated PPy–NFC aerogels exceeded the conductivity of pristine PPy prepared at room temperature (units S cm^{-1}).[3] The PPy–NFC aerogel with the highest contents of NFC (2 wt%) showed the lowest conductivity (19 S cm^{-1}), while the highest conductivity with the value of 31 S cm^{-1} was found for the PPy–NFC aerogel with 0.7 wt% of NFC. As revealed by the Raman analysis, the PPy–NFC with 0.7 wt% of NFC has the highest bipolaron to polaron ratio, indicating lower concentration of defects on PPy chains which leads to the improved conductivity. Moreover, PPy–NFC aerogels partially preserved their conductivities still at neutral pH (cryogels were washed thoroughly with Milli-Q water before freeze-drying), the highest conductivity of 0.7 S cm^{-1} was obtained for PPy–NFC prepared with 0.7 wt% of NFC (Fig. 6). When the NFC content is less than 0.7 wt% the conductivity increases from 0.18 S cm^{-1} (0.1 wt% of NFC) to 0.68 S cm^{-1} (0.7 wt% of NFC), however is still of the same order of magnitude and it might be connected to the better chain ordering and less defect within the chain of PPy–NFC and higher amount of conducting phase in the aerogels. Further increased in NFC contents in aerogels led to the decrease of conductivity by one order of magnitude up to 0.025 S cm^{-1} (2 wt% of NFC).

Table 1 Assignments of the Raman peaks observed in Fig. 5

Peaks, cm^{-1}		
633 nm	785 nm	Assignments
1583	1594	C=C stretching vibrations in polaron structure of PPy[36]
1494	1487	C–C, C=N stretching vibrations[35,36]
1400	—	C–C stretching and C–N stretching vibrations of PPy[35]
1372	1378	C–C ring stretching vibrations in bipolaron structure of PPy[35]
1330	1326	Ring stretching vibrations in polaron structure of PPy[35]
1252	1239	Antisymmetric C–H in-plane bending vibrations of PPy[35]
—	1122	C–O–C symmetric stretching of NFC[37]
—	1095	C–O–C ring breathing of NFC[37]
1080	1078	C–H in-plane deformation in bipolaron structure of PPy[36]
1058	1058	C–H in-plane deformation in polaron structure of PPy[35,36]
966/984	964/981	C–C ring deformation vibration in polaron structure of PPy[35]
932	932	Ring deformation in bipolaron structure of PPy[35]
682	682	C–H out of plane deformation of PPy[35]
619	619	Ring deformation vibrations of PPy[35]
—	432	C–C–C, C–C–O ring deformation of NFC[38]
—	374	C–O, C–O–C ring deformation of NFC[38]

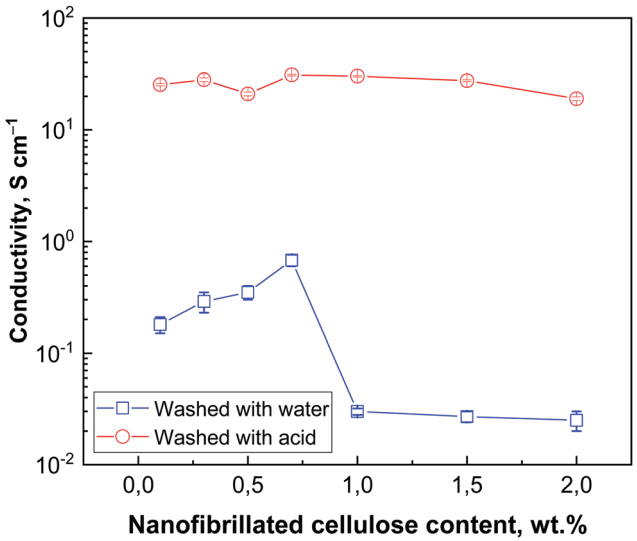

Fig. 6 Conductivity of polypyrrole–nanofibrillated cellulose aerogels with varying nanofibrillated cellulose content. Samples have been washed with 0.2 M HCl or Milli-Q water, respectively.

Mechanical properties

The mechanical properties of the cryogels are strongly dependent on the contents of the NFC as shown in Fig. 7 and Table 2. Mechanical properties proportionally increase with increasing the NFC contents in the cryogel. The highest tensile modulus, 432 ± 86 kPa, was achieved at the concentration of 2 wt% of NFC which has significantly improved compared to similar PPy/PVAL cryogel (22.8 ± 2.8 kPa when 7 wt% of PVAL was used).[7] The tensile strain at the break was in the range of 15.2% to 26.6%, which decreased by increasing the wt% of NFC. The mechanical properties of aerogels showed much higher tensile modulus than their corresponding cryogels. For instance, aerogels with 2 wt% of NFC content showed a tensile modulus of 1055 ± 200 kPa which is 2.5 times higher than their cryogel counterpart.

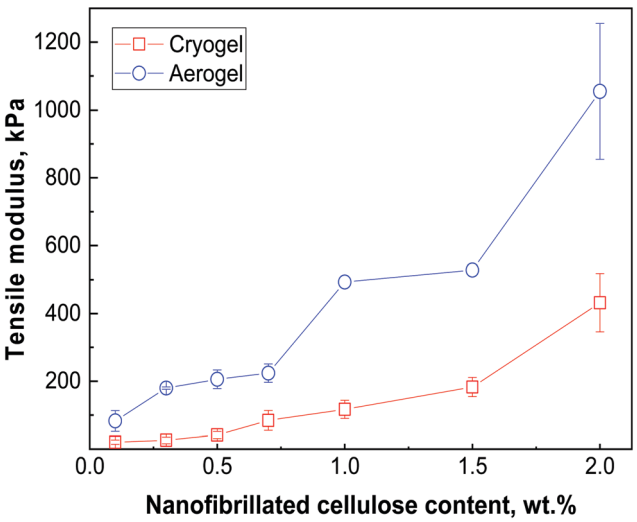

Fig. 7 Tensile modulus of polypyrrole–nanofibrillated cellulose cryo- and aerogels with varying nanofibrillated cellulose content.

Table 2 Mechanical properties of polypyrrole–nanofibrillated cellulose cryo- and aerogels and specific surface area (S_{BET}) of aerogels with varying NFC content

Contents of NFC, wt%	Tensile modulus, kPa	Tensile strength, kPa	Tensile strain at break, %	S_{BET}, m^2 g^{-1}
0	—	—	—	24.4[a]
0.1	20.6 ± 6.38 82.9 ± 30.7[b]	3.5 ± 0.65 2.8 ± 1.12[b]	26.6 ± 1.67 10.1 ± 1.96[b]	50.2
0.3	26.1 ± 9.8 180 ± 3.4[b]	3.8 ± 0.82 4.5 ± 0.37[b]	23.9 ± 1.34 8.3 ± 1.22[b]	50.1
0.5	41.8 ± 10.2 206 ± 27.7[b]	5.6 ± 1.64 6.2 ± 1.45[b]	20.5 ± 0.75 10.1 ± 4.6[b]	34.5
0.7	84.6 ± 29.2 224 ± 27.1[b]	10.7 ± 3.75 6.7 ± 2.13[b]	20.2 ± 0.92 12.0 ± 6.95[b]	63.7
1.0	117 ± 26.9 493[bc]	8.6 ± 2.83 12.1[bc]	15.2 ± 2.29 18.5[bc]	61.8
1.5	183 ± 28.1 528[bc]	13.9 ± 1.84 17.8[bc]	17.0 ± 3.11 27.6[bc]	67.3
2.0	432 ± 86 1055 ± 200[b]	18.7 ± 6.66 15.4 ± 5.41[b]	14.8 ± 2.12 17.6 ± 4.31[b]	46.3
100	—	—	—	39.2

[a] Value was taken from ref. 3 [b] Values of the aerogels. [c] Values are based on single analysis.

Specific surface area

Specific surface area (S_{BET}) of all PPy–NFC aerogels is listed in Table 2. The results show that all the aerogels have higher S_{BET} compared to the pristine individual components except the one prepared with 0.5 wt% of NFC. Pristine PPy has S_{BET} of 13.5 or 24.4 m^2 g^{-1} when prepared at room temperature or −24 °C, respectively.[3] The highest S_{BET} was obtained while 1.5 wt% of NFC was used for cryogel preparation. Cryopolymerization and freeze-drying conditions support the formation of highly porous PPy–NFC aerogels (as previously discussed in Section Morphology). The S_{BET} values obtained for PPy–NFC are much higher than the values of porous PPy/PVAL cryogel (0.45–14 m^2 g^{-1}) prepared by Bober *et al.*,[7] and NFC aerogels (11–15 m^2 g^{-1}) reported by Aulin *et al.*[40] The specific surface area of PPy–NFC aerogels is similar to this of cellulose nanofibers aerogels prepared with 2 wt% of NFC (20 or 66 m^2 g^{-1}, respectively, based on the variation of freeze-drying method).[41]

Thermal stability

The thermal stability of the various PPy–NFC aerogels was found to decrease by increasing the NFC contents (Fig. 8). The similar behavior of the thermal degradation of PPy–NFC aerogels was observed while heating in air or under nitrogen. In both cases the first weight loss, up to 120 °C, occurs due to the loss of the moisture. The second weight loss at ≈ 270 °C is assigned to the degradation of cellulose macromolecules[42] and the loss of PPy dopant. The complete decomposition of all aerogels in air took place above 700 °C while pristine NFC and PPy decomposed completely at 475 °C and 680 °C, respectively.

PPy under inert atmosphere converts into nitrogen-enriched carbon with a residual mass about 51% at 650 °C and 41% at 800 °C, which is in good agreement to the results previously

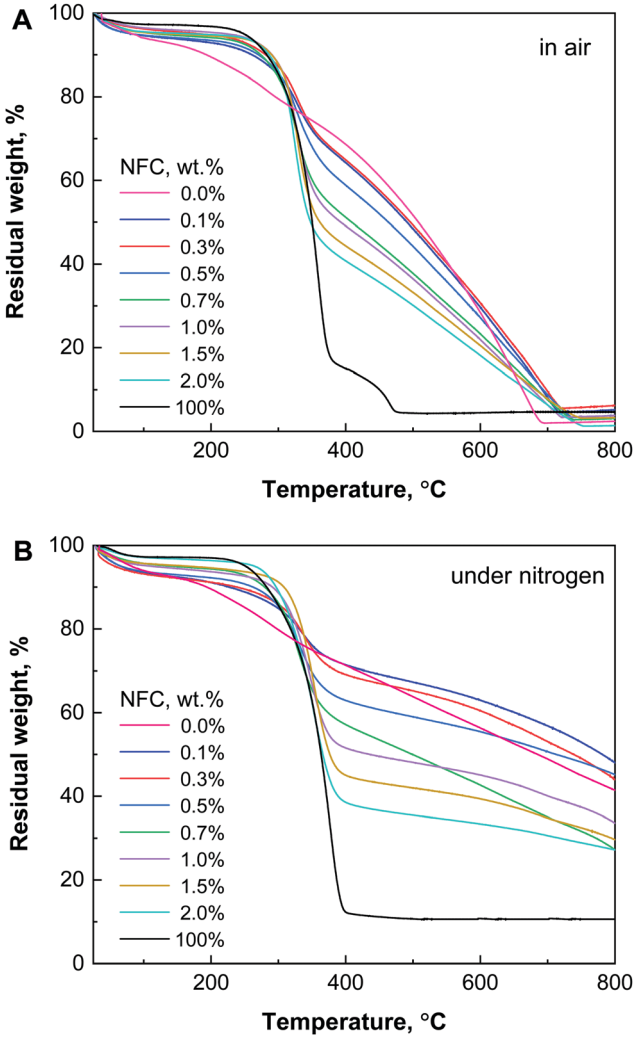

Fig. 8 Thermogravimetric analysis of polypyrrole, nanofibrillated cellulose and polypyrrole–nanofibrillated cellulose aerogels, performed (A) in air, and (B) under nitrogen atmosphere.

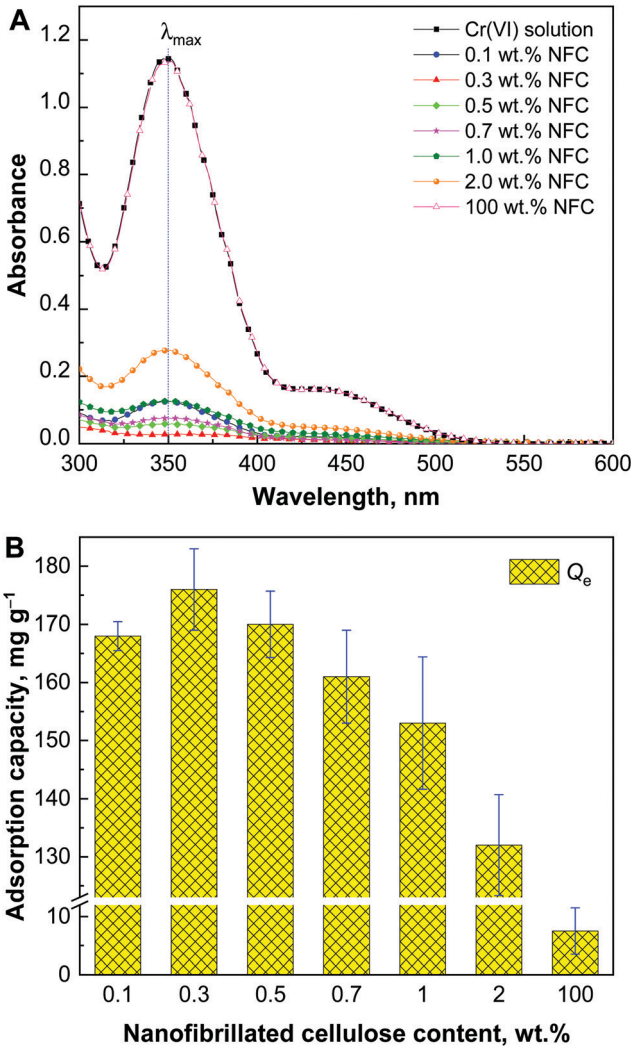

Fig. 9 (A) UV-Visible spectra of Cr(VI) ions (35 mgL^{-1}) and its solutions (50 mL) after adsorption onto pristine nanofibrillated cellulose and polypyrrole–nanofibrillated cellulose aerogels with various nanofibrillated cellulose contents (10 mg), and (B) their corresponding adsorption capacities (Q_e).

reported in the literature.[43] PPy–NFC aerogel prepared with 0.1 wt% of NFC retained ≈ 60% residual weight at 650 °C and ≈ 48% at 800 °C. Thermal stability enhancement can be explained based on the formation of PPy coatings onto NFC fibers, confirmed by Raman spectroscopy (see Section FTIR and Raman spectroscopy), which acts as a flame retardant and protects the NFC fibers against thermal degradation.[44] However, increasing the NFC contents in the sample leads to the decrease of residual weight (less thermal stability), and in the case of PPy–NFC prepared with 2 wt% of NFC only 27% of residual weight remained at 800 °C.

Hexavalent chromium ions removal from aqueous solutions

Polypyrrole–nanofibrillated cellulose aerogels could be effectively used for the adsorption of heavy metal ions from wastewater. The intensive yellow color of the Cr(VI) ions solution was strongly reduced when it came into contact with the aerogels. Spectroscopic results revealed a dependence of the removal capacity on the NFC contents in the PPy–NFC aerogels (Fig. 9). Adsorption capacity of the different aerogels Q_e (mg g^{-1}) and the removal efficiency, R (%), were calculated using the following equations:[45]

$$Q_e = (C_i - C_e) \times V/m \quad (1)$$

$$R = (C_i - C_e) \times 100/C_i \quad (2)$$

where, C_i is the initial Cr(VI) ions concentration (mg L^{-1}), C_e is the concentration at equilibrium (mg L^{-1}), V is the volume of Cr(VI) solution (L) and m is the mass of the various PPy–NFC aerogels (g).

It was proven that the adsorption of Cr(VI) is more efficient at low pH.[26,30] Cr(VI) ions mainly exist in the form of $HCrO_4^-$ ions in acidic conditions, which facilitate the electrostatic interactions with the protonated PPy chains. Owing to the high specific surface area and ion exchange capacity, PPy–NFC

Table 3 Adsorption capacities (mg g^{-1}) of different polypyrrole based materials towards Cr(VI) ions

Adsorbent	Adsorption capacity, mg L^{-1}	Method	Conditions	Ref.
PPy/wood sawdust	3.4	Langmuir	pH 1, RT	49
PPy functionalized chitin	28.9–35.2	Langmuir	30–50 °C	46
Polyaniline/PVAL aerogels	41.2	Langmuir	pH 2, 25 °C	48
PPy/Fe_3O_4/attapulgite	53.37	Experimentally	pH 2, 20 °C	50
Chitosan/PPy	78.6	Langmuir	pH 4, 30 °C	47
Polyaniline/cellulose	86.74	Experimentally	pH 2, RT	51
PPy/Fe_3O_4	169.5	Langmuir	pH 2, 25 °C	52
PPy–NFC (0.3 wt%)	183.6	Experimentally	pH 2, 20 °C	Current work
PPy coated on cellulose sulphate fibers	198	Langmuir	pH 2	53

aerogels prepared with various NFC contents possessed high adsorption capacity towards Cr(VI) ions (Fig. 9). The adsorption capacity was found to increase by decreasing the NFC contents. Pristine NFC revealed no affinity towards Cr(VI) with removal efficiency less than 2%. Among the various PPy–NFC aerogels, PPy–NFC with 2 wt% of NFC has the lowest adsorption capacity, 142.4 mg g^{-1}, and the lowest removal efficiency, 75%. PPy–NFC with 0.3 wt% of NFC has the maximum adsorption capacity of 183.6 mg g^{-1} and 98% removal efficiency. The adsorption capacity of PPy–NFC prepared with 0.3 wt% of NFC aerogels was compared to PPy based composites reported in the literature (Table 3). It can be seen that PPy–NFC aerogel (0.3 wt%) is more effective for the removal of Cr(VI) ions than the most of the reported substrates. For instance, PPy functionalized chitin has only 28.9 mg g^{-1} adsorption capacity at 30 °C.[46] While, chitosan/PPy has 78.6 mg g^{-1} removal capacity, towards Cr(VI).[47] Recently, polyaniline/PVAL aerogels,[48] similarly prepared by cryopolymerization, were used to remove Cr(VI) from solutions and showed a maximum adsorption capacity of 41.2 mg g^{-1}.

Conclusions

Pyrrole was polymerized under frozen condition in the presence of NFC to form 3-D PPy–NFC cryogels. Unlike other stabilizing agents used for the preparation of conducting aerogels, low content of NFC led to sponge-like and lightweight PPy–NFC aerogels with excellent mechanical properties and high conductivity. The aerogels were obtained by facile freeze-drying of their corresponding cryogels. The conductivity values of all PPy–NFC aerogels were higher than for conventional globular PPy powders. The highest conductivity, 31 S cm^{-1}, was achieved for aerogels containing 0.7 wt% NFC. The highest specific surface area, 67.3 m^2 g^{-1}, was obtained for PPy–NFC with 1.5 wt% of NFC. PPy–NFC aerogels have shown high adsorption capacities towards Cr(VI) metal ions, and the highest value of 183.6 mg g^{-1} and 98% removal efficiency was attained for aerogel with 0.3 wt% of NFC. Such novel PPy–NFC cryogels/aerogels are also expected to find the application in the fields of semi-conductors or energy storage and conversion.

Conflicts of interest

The authors declare no conflict of interest.

Acknowledgements

The authors wish to thank the Czech Science Foundation (21-01401S) for the financial support. Part of this work was carried out within the project BioCarb-K, co-financed by the European Regional Development Fund (EFRE) and the province of Upper Austria through the programme IWB 2014–2020. Ms J. Hromádková and Ms M. Karbusická are acknowledged for performing SEM and TGA measurements, respectively.

Notes and references

1 S. Majumdar, R. Moral and D. Mahanta, *Colloids Surf., A*, 2020, **595**, 124643.
2 V. V. Tat'yana and O. N. Efimov, *Russ. Chem. Rev.*, 1997, **66**(5), 443–457.
3 I. M. Minisy, U. Acharya, L. Kobera, M. Trchová, C. Unterweger, S. Breitenbach, J. Brus, J. Pfleger, J. Stejskal and P. Bober, *J. Mater. Chem. C*, 2020, **8**(35), 12140–12147.
4 Y. Li, P. Bober, D. H. Apaydin, T. Syrový, N. S. Sariciftci, J. Hromádková, I. Sapurina, M. Trchová and J. Stejskal, *Synth. Met.*, 2016, **221**, 67–74.
5 T. F. Otero, J. G. Martinez, M. Fuchiwaki and L. Valero, *Adv. Funct. Mater.*, 2014, **24**(9), 1265–1274.
6 Y. Shi, L. Pan, B. Liu, Y. Wang, Y. Cui, Z. Bao and G. Yu, *J. Mater. Chem. A*, 2014, **2**(17), 6086–6091.
7 P. Bober, Z. Capáková, U. Acharya, B. A. Zasońska, P. Humpolíček, J. Hodan, J. Hromádková and J. Stejskal, *Synth. Met.*, 2019, **252**, 122–126.
8 M. Abinaya, R. Rajakumaran, S. M. Chen, R. Karthik and V. Muthuraj, *ACS Appl. Mater. Interfaces*, 2019, **11**(41), 38321–38335.
9 L. Xie, Z. Yu, S. M. Islam, K. Shi, Y. Cheng, M. Yuan, J. Zhao, G. Sun, H. Li, S. Ma and M. G. Kanatzidis, *Adv. Funct. Mater.*, 2018, **28**(20), 1800502.
10 P. Hu, L. Han and S. Dong, *ACS Appl. Mater. Interfaces*, 2014, **6**(1), 500–506.
11 X. Yuan, X. L. Ding, C. Y. Wang and Z. F. Ma, *Energy Environ. Sci.*, 2013, **6**(4), 1105–1124.
12 J. Qin, J. Gao, X. Shi, J. Chang, Y. Dong, S. Zheng, X. Wang, L. Feng and Z.-S. Wu, *Adv. Funct. Mater.*, 2020, **30**(16), 1909756.
13 B. Roschning and J. Weissmüller, *Electrochim. Acta*, 2019, **318**, 504–512.

14 S. S. Nair, S. K. Mishra and D. Kumar, *Polym. Adv. Technol.*, 2019, **30**, 2932–2953.
15 X. Liu, L. Xue, Y. Lu, Y. Xia and Q. Li, *J. Electroanal. Chem.*, 2020, **862**, 114006.
16 M. Akieh-Pirkanniemi, G. Lisak, J. Arroyo, J. Bobacka and A. Ivaska, *J. Membr. Sci.*, 2016, **511**, 76–83.
17 J. Arroyo, M. Akieh-Pirkanniemi, G. Lisak, R. M. Latonen and J. Bobacka, *J. Membr. Sci.*, 2019, **581**, 50–57.
18 X. Fu, J. K. Wang, A. C. Ramírez-Pérez, C. Choong and G. Lisak, *Mater. Sci. Eng., C*, 2020, **108**, 110392.
19 M. Talikowska, X. Fu and G. Lisak, *Biosens. Bioelectron.*, 2019, **135**, 50–63.
20 X. Fu, W. Zeng, A. C. Ramírez-Pérez and G. Lisak, *Chem. Commun.*, 2018, **54**(8), 980–983.
21 P. Chakraborty, S. Das and A. K. Nandi, *Prog. Polym. Sci.*, 2019, **88**, 189–219.
22 G. O. Lloyd and J. W. Steed, *Nat. Chem.*, 2009, **1**(6), 437.
23 K. A. Milakin, Z. Capáková, U. Acharya, J. Vajďák, Z. Morávková, J. Hodan, P. Humpolíček and P. Bober, *Polymer*, 2020, **197**, 122491.
24 M. Bhaumik, A. Maity, V. V. Srinivasu and M. S. Onyango, *Chem. Eng. J.*, 2012, **181**, 323–333.
25 Q. Wang, J. S. Li and C. S. Poon, *Chemosphere*, 2021, **285**, 131434.
26 F. Kong, Y. Zhang, H. Wang, J. Tang, Y. Li and S. Wang, *Chemosphere*, 2020, **257**, 127224.
27 W. Niu, J. Sun, L. Zhang and F. Cao, *Chemosphere*, 2021, **262**, 127806.
28 Y. Wang, N. Lin, Y. Gong, R. Wang and X. Zhang, *Chemosphere*, 2021, **280**, 130663.
29 J. Li, J. Feng and W. Yan, *Appl. Surf. Sci.*, 2013, **279**, 400–408.
30 L. Zhang, W. Niu, J. Sun and Q. Zhou, *Chemosphere*, 2020, **248**, 126102.
31 L. Yue, Y. Xie, Y. Zheng, W. He, S. Guo, Y. Sun, T. Zhang and S. Liu, *Compos. Sci. Technol.*, 2017, **145**, 122–131.
32 Q. Ding, X. Xu, Y. Yue, C. Mei, C. Huang, S. Jiang, Q. Wu and J. Han, *ACS Appl. Mater. Interfaces*, 2018, **10**(33), 27987–28002.
33 A. Hebeish, S. Farag, S. Sharaf and Th. I. Shaheen, *Carbohydr. Polym.*, 2016, **151**, 96–102.
34 P. Bober, J. Liu, K. S. Mikkonen, P. Ihalainen, M. Pesonen, C. Plumed-Ferrer, A. von Wright, T. Lindfors, C. Xu and R.-M. Latonen, *Biomacromolecules*, 2014, **15**, 3655–3663.
35 Z. Morávková, O. Taboubi, I. M. Minisy and P. Bober, *Synth. Met.*, 2021, **271**, 116608.
36 M. Šetka, R. Calavia, L. Vojkůvka, E. Llobet, J. Drbohlavová and S. Vallejos, *Sci. Rep.*, 2019, **9**, 8465.
37 Y. Liu, *Analyst*, 1998, **123**(4), 633–636.
38 K. Schenzel and S. Fischer, *Cellulose*, 2001, **8**, 49–57.
39 I. M. Minisy and P. Bober, *Macromol. Rapid Commun.*, 2020, **41**(17), 2000364.
40 C. Aulin, J. Netrval, L. Wågberg and T. Lindström, *Soft Matter*, 2010, **6**(14), 3298–3305.
41 M. Pääkkö, J. Vapaavuori, R. Silvennoinen, H. Kosonen, M. Ankerfors, T. Lindström, L. A. Berglund and O. Ikkala, *Soft Matter*, 2008, **4**(12), 2492–2499.
42 V. H. Sangeetha, T. O. Varghese and S. K. Nayak, *Iran. Polym. J.*, 2019, **28**(8), 673–683.
43 J. Kopecká, M. Mrlík, R. Olejník, D. Kopecký, M. Vrňata, J. Prokeš, P. Bober, Z. Morávková, M. Trchová and J. Stejskal, *Sensors*, 2016, **16**, 1917.
44 H. Wang, L. Bian, P. Zhou, J. Tang and W. Tang, *J. Mater. Chem. A*, 2013, **1**(3), 578–584.
45 I. M. Minisy, N. A. Salahuddin and M. M. Ayad, *Appl. Clay Sci.*, 2021, **203**, 105993.
46 R. Karthik and S. Meenakshi, *Synth. Met.*, 2014, **198**, 181–187.
47 R. Karthik and S. Meenakshi, *Desalin. Water Treat.*, 2015, **56**(6), 1587–1600.
48 S. Zaghlol, W. A. Amer, M. H. Shaaban, M. M. Ayad, P. Bober and J. Stejskal, *Chem. Pap.*, 2020, **74**, 3183–3193.
49 R. Ansari and N. K. Fahim, *React. Funct. Polym.*, 2007, **67**(4), 367–374.
50 W. Sun, W. Zhang, H. Li, Q. Su, P. Zhang and L. Chen, *RSC Adv.*, 2020, **10**(15), 8790–8799.
51 L. Zhang, W. Niu, J. Sun and Q. Zhou, *Chemosphere*, 2020, **248**, 126102.
52 M. Bhaumik, A. Maity, V. V. Srinivasu and M. S. J. Onyango, *J. Hazard. Mater.*, 2011, **190**, 381–390.
53 A. Hosseinkhani, B. F. Rad and M. Baghdadi, *J. Environ. Manage.*, 2020, **274**, 111153.

Appendix 6

Tailoring of carbonized polypyrrole nanotubes core by different polypyrrole shells for oxygen reduction reaction selectivity modification

Journal of Colloid and Interface Science 551 (2019) 184–194

Contents lists available at ScienceDirect

Journal of Colloid and Interface Science

journal homepage: www.elsevier.com/locate/jcis

Regular Article

Tailoring of carbonized polypyrrole nanotubes core by different polypyrrole shells for oxygen reduction reaction selectivity modification

Islam M. Minisy [a,b], Nemanja Gavrilov [c], Udit Acharya [a,d], Zuzana Morávková [a], Christoph Unterweger [e], Matej Mičušík [f], Sergey K. Filippov [a,g], Jana Kredatusová [a], Igor A. Pašti [c], Stefan Breitenbach [e], Gordana Ćirić-Marjanović [c], Jaroslav Stejskal [a], Patrycja Bober [a,*]

[a] Institute of Macromolecular Chemistry, Academy of Sciences of the Czech Republic, 162 06 Prague 6, Czech Republic
[b] Faculty of Science, Charles University, 128 43 Prague 2, Czech Republic
[c] University of Belgrade, Faculty of Physical Chemistry, Belgrade 11158, Serbia
[d] Faculty of Mathematics and Physics, Charles University, 182 00 Prague 8, Czech Republic
[e] Wood K plus - Kompetenzzentrum Holz GmbH, 4040 Linz, Austria
[f] Polymer Institute, Slovak Academy of Sciences, 845 41 Bratislava, Slovak Republic
[g] Harvard John A. Paulson School of Engineering and Applied Sciences, Harvard University, Cambridge, MA 02138, USA

GRAPHICAL ABSTRACT

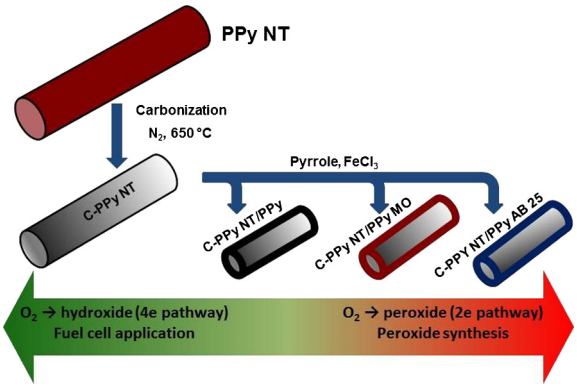

ARTICLE INFO

Article history:
Received 22 February 2019
Revised 16 April 2019
Accepted 19 April 2019
Available online 27 April 2019

Keywords:
Polypyrrole
Nanotubes
Coating
Carbonization
Conductivity
Oxygen reduction reaction

ABSTRACT

By using methyl orange template, polypyrrole nanotubes were obtained by the oxidative polymerization of pyrrole. The nanotubes were carbonized in inert atmosphere to nitrogen-enriched carbon nanotubes. These were subsequently coated with 20 wt% of polypyrrole prepared in the absence or the presence of anionic dyes (methyl orange or Acid Blue 25). The morphology of all the samples was examined by the electron microscopies, FTIR and Raman spectroscopies. Moreover, X-ray photoelectron spectroscopy and elemental analysis were used to prove the chemical structure and the successful coating process. Electron paramagnetic resonance analysis was used to calculate the spin concentrations. Significant impact of coating method is evidenced with neat polypyrrole coating providing a two-fold capacitance increase compared to uncoated nanotubes, while coating in the presence of Acid Blue 25 decreasing it slightly. With respect to oxygen reduction reaction, coatings irreversibly transformed in the first few cycles in the presence of the products of O_2 reduction, presumably hydrogen peroxide, altering the oxygen reduction mechanism. This transformation allows the tailoring of the polymeric shell, over ORR

* Corresponding author.
E-mail address: bober@imc.cas.cz (P. Bober).

https://doi.org/10.1016/j.jcis.2019.04.064

active carbonaceous core, and tuning of the catalyst selectivity and optimization of materials performance for a given application – from alkaline fuel cells to hydrogen peroxide generation.

1. Introduction

Development and characterization of electroactive materials, such as conducting polymer composites with specific redox behaviour, have recently become a main focus. These novel materials are used in supercapacitors [1–5], batteries [2,6–8], energy-storage systems [9] and sensors [2,10]. The next generation of energy-conversion and energy-storage systems, however, still demands higher energy and power densities, longer life cycle and especially the lower cost of production. For example, the modification of carbon fabric with polyaniline can enhance the specific capacitance from 30 F g^{-1} to 150 F g^{-1} [11]. The most common way how to significantly improve the capacitance and prolong the cycle life in supercapacitors is the preparation of conducting polymer composites with graphene [4], carbon nanotubes [12] or transition-metal dichalcogenides [1,2,13]. Nevertheless, the price of such supercapacitors becomes the limiting factor in practical applications.

Conducting polymers, such as polyaniline (PANI) or polypyrrole (PPy), are easily carbonized in inert atmosphere to carbon analogues enriched by nitrogen atoms [10,14–16]. At the same time, the initial morphology remains preserved and the specific surface area substantially increases. The conversion of PPy nanotubes to carbonized analogues [10,17,18] or cellulose-coated with PANI to twin carbons [19] are examples. Further, by the control of the polymerization conditions, by the preparation of composites based on conducting polymers or by the modification of conducting polymers, it is possible to design the desired morphology and also to introduce various additional atoms to the structure of novel carbon materials [3,6,16,20].

Polypyrrole has recently become the most studied conducting polymer, due to its high electrical conductivity, good environmental stability, biocompatibility, electroactivity and redox properties [13,21,22]. One of the most promising ways how to tune the morphology and improve the properties of PPy is the use of organic dyes as morphology-guiding agents during the oxidation of pyrrole [23–27]. One-dimensional PPy morphologies, such as nanotubes (PPy NT) or nanofibres, generally perform better in many respects than the classical globular one. Methyl orange (MO) is one the most frequently used dyes, which leads to the formation of PPy NT with conductivity up to 100 S cm^{-1} [25]. In addition to MO, Acid Blue 25 (AB 25) promotes the formation of highly conducting PPy nanofibers [23,26].

Various strategies have been used for the preparation of advanced one-dimensional conducting composite morphologies. For instance, multiwall carbon nanotubes have been coated with PANI [28–31] by *in-situ* surface polymerization of aniline [32]. The coating was subsequently used for the reduction of noble-metal ions to corresponding metal nanoparticles [18,33], and such materials were proposed as electrocatalysts in fuel-cell electrodes. Alternatively, the PPy NT were coated with PANI or poly(*p*-phenylenediamine) and eventually carbonized [34].

Herein, highly conducting PPy NT have been prepared according to the procedure published earlier by Li et al. [25], carbonized in an inert atmosphere to nitrogen-enriched carbon materials, and subsequently coated with PPy prepared in the absence or presence of MO or AB 25 (Fig. 1). The decisive parameters for the application of such novel materials, the conductivity and specific surface area, have been investigated. In addition to detailed analysis of the obtained products, we describe potential applications of these materials for electrochemical charge storage and electrocatalysis. Carbonized conductive polymers have a great potential for the applications in these fields [35], but the question associated with the link between physico-chemical properties and their electrochemical performance remains unsolved to these days. However, it is unambiguous that electrochemical performance is clearly associated with surface properties which define interfacial behaviour of carbon materials in electrochemical systems. Hence, our main premise is that coating of carbonized PPy nanotubes and conversion of such modified precursor could lead to novel carbon materials with specific properties tailored for different electrochemical applications.

2. Experimental

2.1. Chemicals

Pyrrole (≥98%), iron(III) chloride hexahydrate, methyl orange (Fig. 2A; sodium 4-[(4-dimethylamino)phenylazo] benzenesulfonate) and Acid Blue 25 (Fig. 2B; sodium 1-amino-4-anilinoanthra quinone-2-sulfonate, dye content 45%) were purchased from Sigma-Aldrich (Germany). All chemicals were used as received without any further purifications or any correction for true dye content.

2.2. Preparation of polypyrrole nanotubes

Firstly, MO (0.015 mol, 2.455 g) was dissolved in 450 mL of distilled water in the volumetric flask, then pyrrole (0.3 mol, 10.06 g) was added and total volume was adjusted to 500 mL with distilled water. Iron(III) chloride hexahydrate (0.6 mol, 81.09 g) was dissolved in another 500 mL flask in distilled water. Finally, both solutions were mixed and left to react for 24 h at room temperature. The concentrations of reactants thus were 0.15 M pyrrole, 0.3 M iron(III) chloride, and 0.0075 M MO. The solid product composed mainly of PPy hydrochloride (Fig. 2C) was collected by filtration, washed with 0.2 M hydrochloric acid (500 mL), then with ethanol (500 mL), left to dry in air and then over silica gel till constant weight was achieved.

2.3. Carbonization of polypyrrole nanotubes

PPy NT produced from the previous step (≈11 g) using MO template were carbonized in the electric furnace under inert nitrogen atmosphere. The sample was heated up to 650 °C with the heating rate of 10 °C min^{-1}, then the furnace was switched off and the sample was left to cool under nitrogen flow.

2.4. Coating of carbonized polypyrrole nanotubes

Carbonized PPy NT (C-PPY NT) was coated with 20% (w/w) of PPy prepared in three different ways; in the presence of MO or AB 25 or without any dye (Fig. 1). 2 g of carbonized PPy NT were dispersed in 30 mL aqueous solution of pyrrole (0.3 mol, 0.31 g), the solution was left under stirring for 1 h. Then 30 mL solution of iron(III) chloride hexahydrate (0.6 mol, 2.514 g) was added and kept under the stirring for 1 h, then the polymerization mixture

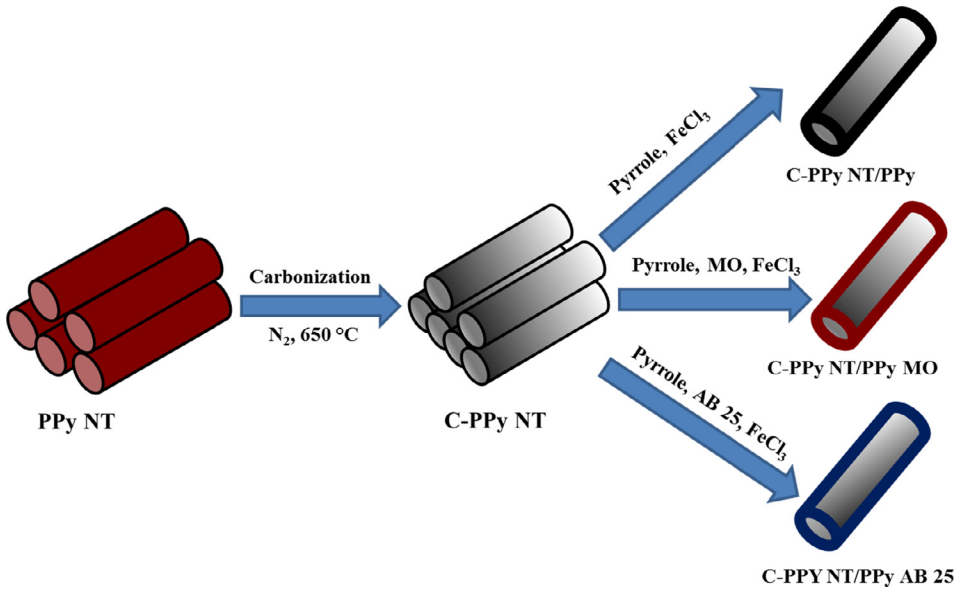

Fig. 1. Pyrrole was oxidized in the presence of methyl orange to polypyrrole nanotubes. These were carbonized to carbon nanotubes, and subsequently coated with polypyrrole in the absence or presence of MO, AB 25.

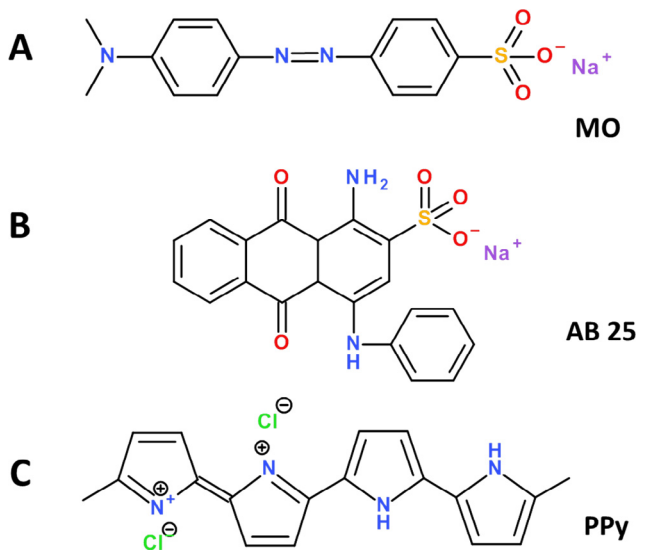

Fig. 2. Chemical formule of methyl orange (A), Acid Blue 25 (B) and polypyrrole hydrochloride (C).

was left for 24 h. The reaction mixture was thus composed of 0.15 M pyrrole and 0.3 M iron(III) chloride. Next, carbonized PPy NT coated with neat PPy were isolated, rinsed with 0.2 M hydrochloric acid (500 mL), followed by 500 mL of ethanol and dried as above. For coating in the presence of dyes the same procedure was followed, however, in the presence of 0.0075 M, MO (0.0761 g/60 mL) or AB 25 (0.0968 g/60 mL).

2.5. Characterization

The morphology of the PPy powders was investigated with the scanning (SEM) and transmission (TEM) electron microscopies using a JEOL 6400 and JEM 2000 FX microscopes, respectively. Thermogravimetric analysis was performed in 50 cm^3 min^{-1} air or nitrogen flow at the heating rate of 10 °C min^{-1} to 800 °C with a Pyris 1 Thermogravimetric Analyzer (Perkin Elmer, USA). Elemental Analysis was determined on a Perkin-Elmer 2400 CHN elemental analyzer (Waltham, MA, USA).

Infrared spectra were recorded using a Thermo Nicolet NEXUS 870 FTIR Spectrometer (DTGS TEC detector; 64 scans; resolution 2 cm^{-1}) in transmission mode in potassium bromide pellets. The spectra were corrected for the carbon dioxide and humidity in the optical path. Raman spectra were collected on a Renishaw inVia Reflex Raman spectrometer (Leica DM LM microscope; objective magnification × 50) with a HeNe 633 nm laser (holographic grating 1800 lines mm^{-1}) and Ar-ion 514 nm laser (holographic grating 2400 lines mm^{-1}).

X-ray photoelectron spectroscopy (XPS) signals were recorded using a Thermo Scientific K-Alpha XPS system (Thermo Fisher Scientific, UK) equipped with a micro-focused, monochromatic Al Kα X-ray source (1486.68 eV). An X-ray beam of 400 μm size was used at 6 mA × 12 kV. The spectra were acquired in the constant analyser energy mode with pass energy of 200 eV for the survey. Narrow regions were collected with pass energy of 50 eV. Charge compensation was achieved with the system Ar Flood gun. The Thermo Scientific Avantage software, version 5.9902 (Thermo Fisher Scientific), was used for digital acquisition and data processing. Spectral calibration was determined by using the automated calibration routine and the internal Au, Ag and Cu standards supplied with the K-Alpha system.

The specific surface area of the samples was determined using physical adsorption of nitrogen at −196 °C on an automatic volumetric sorption analyzer AutosorbiQ MP-XR (Quantachrome Instruments, USA) using the Brunauer-Emmet-Teller (BET) method. The adsorbed gas volume was measured at a relative pressure range of 0.1–0.3 using 40–50 mg of the sample. Prior to the gas sorption measurements, the samples were outgassed at 100 °C for 1 h under vacuum.

For the conductivity measurement, a Novocontrol Alpha Analyzer BDS was used. The 80 mg of sample powder was placed in a cylindrical Teflon sample holder (volume 5000 mm^3) and was closed from both sides with gold-plated brass disk electrodes having 20 mm diameter and firmly pressed manually. AC RMS voltage 1 V was applied at frequency 0.1 Hz.

Electron paramagnetic resonance (EPR) measurements were performed using a quartz capillary on a Bruker ELEXSYS E-540 X-band spectrometer equipped with a Bruker ER 049X microwave bridge. Spectra were recorded at room temperature with a sweep width of 1000 G, and microwave power output of 6 mW, a

modulation frequency of 100 kHz. The modulation amplitude was optimized to the line width of the spectrum (of the order of 0.5–2.0 G). No artificial broadening of EPR spectra was detected at such modulation amplitudes. Absolute spin concentration was determined using HSL calibration. Experimental error of spin concentration was calculated on the basis of three independent experiments for each sample.

2.6. Electrochemistry

In order to prepare the electrodes for the electrochemical measurements, 5 mg of each sample was suspended in a mixture of 400 μL of absolute ethanol and 590 μL of deionized water, followed by homogenization in an ultrasonic bath for 30 min. Then, 10 μL of 0.5 wt% Nafion solution in ethanol was added to the suspension, in order to improve the adhesion of thin films on the glassy carbon (GC) surface and ensure their integrity during the electrochemical measurements [17]. Total volume of 10 μL of the suspension was transferred onto the GC disk electrode (geometrical surface area 0.196 cm^2) and dried under a gentle nitrogen stream. The obtained material loading of each sample was 250 μg cm^{-2}. Electrochemical measurements were performed in a conventional one-compartment three-electrode electrochemical cell with graphite rod as a counter electrode and a saturated calomel electrode (SCE) as a reference electrode. Capacitances of investigated materials were evaluated using cyclic voltammetry (CV) in 0.5 M H_2SO_4. Gravimetric capacitances (C, in F g^{-1}) were evaluated as:

$$C = \frac{Q}{2 \cdot \Delta V \cdot m} = \frac{\int i dt}{2 \cdot \Delta V \cdot m} \quad (2)$$

where Q stands for the voltammetric charge obtained by integration of positive and negative sweep in cyclic voltammograms, ΔV is the width of the potential window and m is the mass of the active material loaded on the GC electrode surface. Catalytic activity towards oxygen reduction reaction (ORR) was investigated in 0.1 M KOH. Measurements were done using Ivium VO1107 potentiostat/galvanostat, combined with electrode rotator (PINE) for the ORR measurements using rotating disk electrode (RDE) technique. Before and during the measurements, a gentle gas flow of nitrogen or oxygen (both 99.999%) was introduced just beneath the electrolyte surface. All measurements were carried out at room temperature, 25.0 ± 0.5 °C.

3. Results and discussion

3.1. Morphology

Oxidation of pyrrole with iron(III) chloride has led to the formation of PPy with globular morphology and conductivity of ≈1 S cm^{-1} [13]. It was reported in the literature that when the MO was added to the polymerization mixture, highly conducting PPy NT were produced [25]. Such one-dimensional PPy nanostructures (Fig. 3a and b) can be easily converted to one-dimensional carbons enriched with nitrogen atoms (Fig. 3c and d) by simple pyrolysis at 650 °C in inert atmosphere. During carbonization, the morphology of original material was preserved; however, the nanotubes became shorter due to shrinkage and mass loss by heating (Fig. 3d).

The carbonized nanotubes may serve as a template for the deposition of PPy. Any surface immersed in the reaction mixture during the oxidation of pyrrole becomes coated with PPy. The coating of carbonized PPy NT does not lead to the change in its morphology, and from TEM it is clearly visible that all newly produced PPy is deposited on the surface of the carbonized PPy NT (Fig. 4). No additional globules, nanofibers or long nanotubes were produced outside the carbonized nanotubes. Carbonized PPy NT have about 27 nm average thickness of the walls and successful coating manifests itself as increasing thickness of the walls of nanotubes. For the PPy coating in the absence of the dyes the

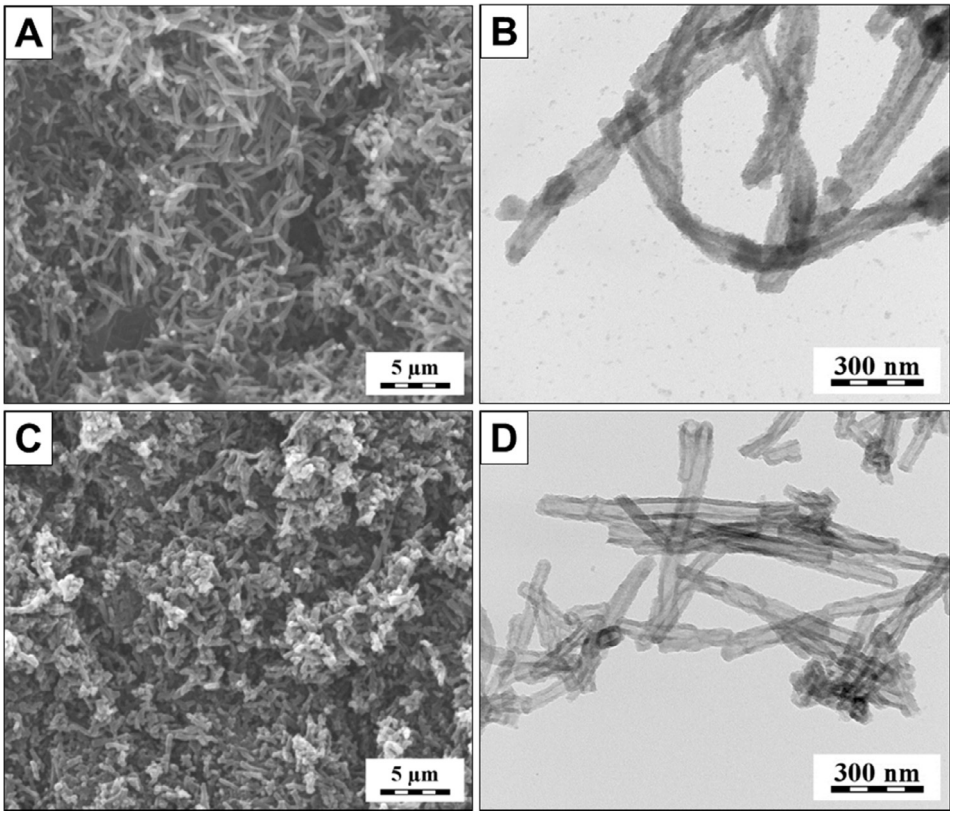

Fig. 3. SEM and TEM images of PPy nanotubes before (A, B) and after carbonization (C, D).

wall thickness increased to 42 nm, while in the presence of MO or AB 25 up to 40 or 36 nm, respectively. Based on the wall thickness we can estimate that the coated film thickness are about 15, 13 and 9 nm for neat PPy, PPy MO and PPy AB 25, respectively.

3.2. Thermogravimetric analysis

The process of carbonization can be easily traced by TGA in an inert atmosphere (Fig. 5). In air, PPy NT are decomposed completely above 650 °C, while in inert nitrogen they carbonized to nitrogen enriched carbon leaving the residue over 50 wt% (Fig. 5a). It is clearly visible that those carbonized PPy NT before and after coating with three types of PPy are more stable than as-prepared PPy NT (Fig. 5b). PPy NT start to decrease their mass above 300 °C, while rest of the samples (C-PPy NT, C-PPy NT/PPy-MO, C-PPy NT/PPy and C-PPy NT/PPy AB 25) start to decompose above 500 °C (Fig. 5b).

3.3. FTIR and Raman spectroscopy

To confirm the expected molecular structure of PPy, the samples were analyzed by vibrational spectroscopies (Fig. 6). Since FTIR spectroscopy is more sensitive to polar bonds, it is an ideal technique for proving of the polymer presence in the sample. Indeed, for all three coated samples, typical spectra of PPy [36] were observed.

Carbon materials, on the other hand, are strong Raman scatterers. The G- and D-band of disordered carbon [37] dominate the spectra of all carbonized substrate coated samples. In addition, several bands connected with PPy can be observed in the spectra of carbonized PPy NT coated with PPy: 920 cm^{-1} (out-of-plane C—H deformation vibrations in bipolaron structure), 1040 cm^{-1} (in-plane C—H deformation vibrations in neutral rings), 1095 cm^{-1} (in-plane C—H deformation vibrations in charged rings), and 1230 cm^{-1} (skeletal vibration of bipolaron structure) [38,39]. These PPy-bands are a bit weaker in the spectrum of C-PPy NT/PPy MO). In the spectrum of C-PPy NT/PPy AB 25, Raman bands of AB 25 dye can be detected due to resonance enhancement: 1402 (C—C stretching in the anthracene structure), 1325 (N—H stretching), and 1270 (C—H in-plane deformation of the phenyl group) cm^{-1}. We can thus conclude that AB 25 is incorporated in the sample coating. No bands of MO can be detected in the spectrum of C-PPy/PPy MO, not even in the spectrum excited with a 514 nm laser line where they should be resonantly enhanced [40]. We suspect that MO is incorporated in PPy coating in only a small amount or not at all.

The Raman spectra were obtained at several points of the samples (not shown) and no significant heterogeneity was detected. We thus conclude that the PPy forms a continuous coating on the carbonized nanotubes rather than creating separated islands of polymer.

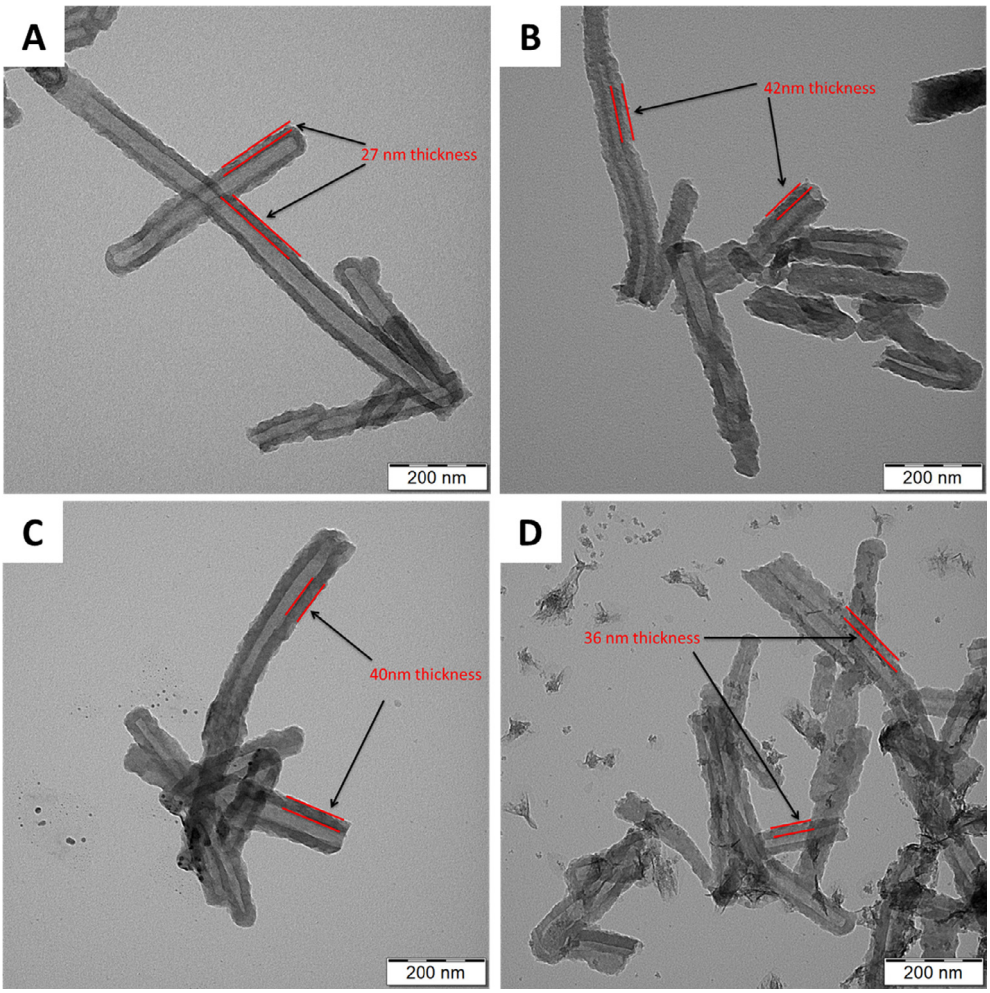

Fig. 4. TEM images of carbonized PPy nanotubes (A), coated in different ways, neat PPy (B), PPy in the presence of MO (C), and PPy in the presence of AB 25 (D).

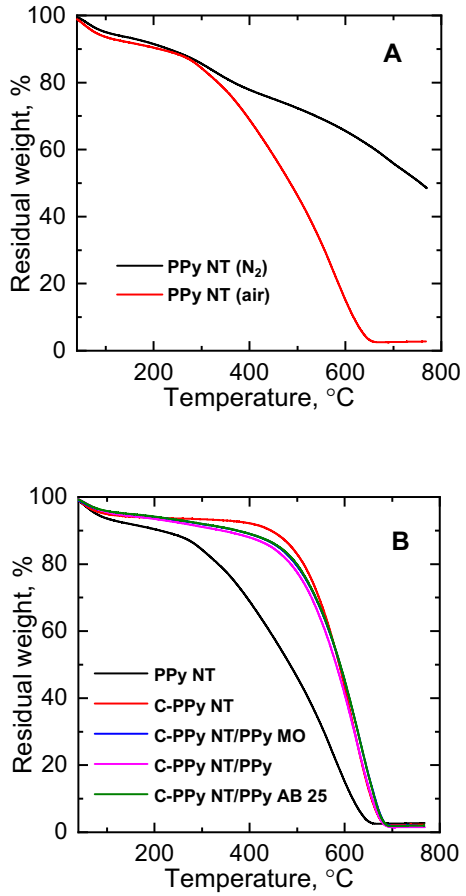

Fig. 5. Thermogravimetric analysis of polypyrrole nanotubes in air and in nitrogen (A), and all the samples in air (B).

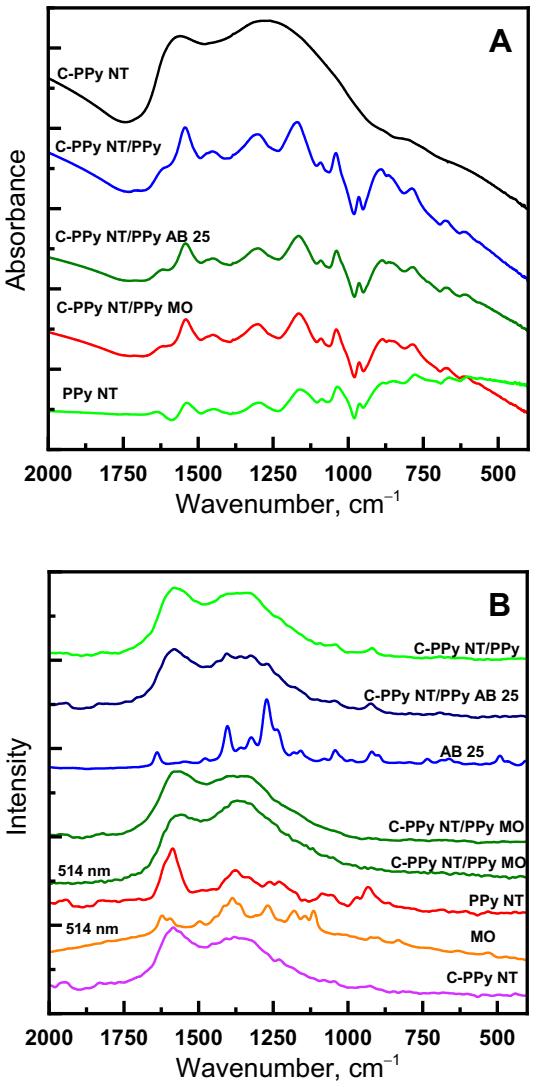

Fig. 6. FTIR (A) and Raman spectra (B) of the PPy nanotubes, carbonized PPy nanotubes and coated samples. Raman spectra of MO and AB 25 are shown for comparison. The spectra are obtained with 633 nm laser line, additionally the spectra of MO and C-PPy NT/PPy MO are recorded with a 514 nm laser line.

3.4. Elemental analysis

Elemental analysis showed about 15 wt% of nitrogen in original PPy NT and C-PPy NT before and after coating with three types of PPy (Table 1). As a result of carbonization of PPy NT, the content of carbon increased from 55.6 wt% to 69.7 wt% and the amount of hydrogen atoms decreased from 4.6 wt% to 2.2 wt%. The content of carbon slightly decreased after PPy coating to 67.4–66.7 wt%, due to the presence of chlorine counter-ions (Fig. 2C).

3.5. X-ray photoelectron spectroscopy

Surface composition was evaluated by XPS (Table 2). XPS results of PPy NT are very similar to the bulk elemental analysis (Table 1) indicating homogeneous material with no difference between the surface and the bulk. The carbonized substrate and different PPy coatings, however, had higher chlorine content on the surface than in the bulk. This indicates that on the surface of C-PPy NT/PPy there is very thin layer of PPy giving high chlorine content. Nitrogen content did not change after carbonization (N1s *ca* 15–16 at%, Table 2), and is very similar to the bulk elemental analysis. This indicates that nitrogen after carbonization is incorporated in the carbon-nitrogen heterostructures. In Fig. 7 of C1s region it is visible that after carbonization the typical PPy signals (C_β at ~284 eV, C_α at ~285 eV, C—N at ~286 eV) were suppressed. In the C-PPy NT/PPy composites the C1s signal resembles to that of neat PPy (the increase of C—N signal typical for PPy shown in Fig. 7c), which demonstrates thin PPy layer on the surface as discussed above. PPy has usually four signals of nitrogen (see Fig. 8a), that at ~400 eV is assigned to the NH group of the pyrrole unit, at ~398 eV the C=N defects of PPy was detected, at ~401 eV the polaron (C—N^+) and at ~402 eV the bipolaron (C=N^+) structures are present [41]. After carbonization, the signal at ~398 eV corresponding to some pyridinic structures substantially increased (Fig. 8b, Table 2). There is also some increase at 401–402 eV, which could be attributed to the graphitic nitrogen confirming the presence of nitrogen-enriched graphitic carbon [42]. In the neat PPy NT and in the coating of C-PPy NT/PPy MO and C-PPy NT/PPy AB 25 some signals of sulfur (signal of S2p at ~168 eV corresponding to —SO_3) were detected. This indicates the incorporation of the dyes, AB 25 and MO, into the coating, in accordance with Raman spectroscopic study.

3.6. Specific surface area

Specific surface area of PPy NT was found to be 86 m^2 g^{-1} (Table 1), which is higher than for globular PPy (26 m^2 g^{-1}) [10], and even for the PPy NT reported earlier [17]. After carbonization, the specific surface area increased to 105 m^2 g^{-1}, however, after coating it even decreased below the specific surface area of original

Table 1
Elemental analysis, conductivity and specific surface area of polypyrrole nanotubes, carbonized nanotubes and polypyrrole-coated carbonized nanotubes.

Sample	Elemental analysis, wt%					Conductivity S cm^{-1}	Surface area, m^2 g^{-1}
	C	H	N	Cl	Others		
PPy NT	55.6	4.6	15.5	10.1	14.2	0.10	86
C-PPy NT	69.7	2.2	15.9	2.2	10	3×10^{-4}	105
C-PPy NT/PPy MO	67.4	2.4	15.6	3.1	11.5	0.15	69
C-PPy NT/PPy AB 25	66.7	2.2	15.5	3.8	11.8	0.08	57
C-PPy NT/PPy	66.9	2.3	15.5	4.2	11.1	0.03	83

Table 2
Apparent surface chemical composition of all samples as determined by XPS.

	Surface chemical composition, at% (wt%)				
	C1s $C_\beta/C_\alpha/C{-}N/C{=}N^+/COOH/\pi\text{-}\pi^*$	O1s	N1s $C{=}N/NH/CN^+/C{=}N^+$	Cl2p	S2p
PPy NT	74.2 (65.2) 21.6/37.7/21.6/10.0/4.3/4.7	4.3(5.0)	16.5 (16.9) 5.1/60.9/22.9/11.1	4.4(11.4)	0.6(1.5)
C-PPy NT	79.0(75.5) 29.4/33.8/15.0/11.3/5.4/5.2	5.4(6.9)	15.5(17.3) 34.7/27.5/25.0/8.5	0.1(0.3)	–
C-PPy NT/PPy MO	75.3(68.0) 18.0/27.4/31.5/12.6/5.3/5.2	4.9(5.9)	16.4(17.3) 14.5/48.1/28.4/9.0	2.8(7.6)	0.5(1.2)
C-PPy NT/PPy AB 25	76.3(69.3) 13.2/29.7/34.1/12.9/4.8/5.2	5.3(6.4)	15.4(16.4) 14.6/52.0/24.3/9.1	2.5(6.8)	0.5(1.3)
C-PPy NT/PPy	76.6(69.1) 19.5/30.4/27.1/12.8/5.5/4.7	4.2(5.0)	15.6(16.4) 14.5/51.2/24.9/9.4	3.5(9.4)	–

PPy NT (Table 1). This can be explained by the fact that coating of C-PPy NT led to the blocking of pores by newly formed PPy.

3.7. Conductivity

The conductivity of PPy NT compressed into pellet and measured by van der Pauw method was 55 S cm^{-1}. In order to compare this value with carbonized materials, which were not possible to compress into pellets, it was necessary to investigate the conductivities of powders measured by using a Novocontrol device. Conductivity of starting PPy NT in powder form was 0.1 S cm^{-1} (Table 1). After carbonization this value decreased to 3×10^{-4} S cm^{-1} due to conversion of PPy NT to nitrogen-containing carbon, as proved by TGA and Raman spectroscopy. Subsequent coating with three types of PPy has led to the increase in the conductivity to 0.03–0.15 S cm^{-1} (Table 1). The conductivity of C-PPy NT/PPy MO was slightly higher than conductivity of original PPy NT.

3.8. EPR analysis

To have deeper insight on the origin of conductivity change as a result of modification, EPR experiments were performed (Fig. 9). Carbonized PPy NT and coated samples display the presence of paramagnetic centers that manifest themselves in a single line in EPR spectrum that was further used for calculation of spin concentration. The calculated spin concentration was nearly the constant inside experimental error for three types of coating and non-coated sample, which implying that paramagnetic centers stay intact during modification.

3.9. Electrochemistry

The samples were investigated as potential materials for electrochemical capacitors and/or electrocatalysts for ORR or both. Fig. 10A shows cyclic voltammograms in acidic solution at a common potential sweep rate of 100 mV s^{-1}. It can be seen that PPy NT had the highest capacitive response with contribution of pseudo-faradaic processes, ascribed to electrochemical transformations of PPy. However, the other four materials displayed quite similar, rather featureless, response. Evaluated capacitances, Fig. 10B, span in a quite wide region. When measured at 5 mV s^{-1} the values between 90 and 245 F g^{-1} were found, depending on the preparation route. The capacitive response described here of PPy NT is similar to that of previously reported PPy NT base but almost two times higher [17]. A very high sensitivity to the potential sweep rate is another striking property. The capacitances fade very quickly with increasing the potential sweep rate. Although there is a strong dependence of the measured capacitances on the synthetic route and the type of PPy deposited over C-PPy NT, no distinct correlation with the conductivity of the investigated samples can be outlined. Nevertheless, considering the samples obtained by coating C-PPy NT with different forms of conducting PPy, it seems that capacitive response correlates with the specific surface area and the coated PPy film thickness, this being the highest for C-PPy NT/PPy followed by C-PPy NT/PPy MO and C-PPy NT/PPy AB 25 (Table 3 and Fig. 10). It is interesting to observe that, compared to previously reported PPy NT and C-PPy NT [17], the differences in specific surfaces can explain different gravimetric capacitances. In earlier report PPy NT had specific surface area of 52.8 m^2 g^{-1} while carbonized form had specific surface of ≈250 m^2 g^{-1}. Last material displayed capacitance of 220 F g^{-1} (5 mV s^{-1}) which is in good agreement with C-PPy NT reported here with specific surface area of 105 m^2 g^{-1} and capacitance of 95 F g^{-1} (5 mV s^{-1}).

As polymer-derived carbons are, as a rule, active for ORR in alkaline media [43], we investigated catalytic properties in KOH solution. An interesting effect, "deactivation" of materials obtained by coating of C-PPy NT is noticed upon cycling in O_2-saturated alkaline solutions (Fig. 11). This process is witnessed by both the reduction of faradaic response in O_2-saturated solution and by the decrease of capacitive response during the cycling in the presence of O_2. We suspect that this process can be ascribed to deprotonation of PPy shell over C-PPy NT core and its irreversible transformation in the presence of the products of O_2 reduction,

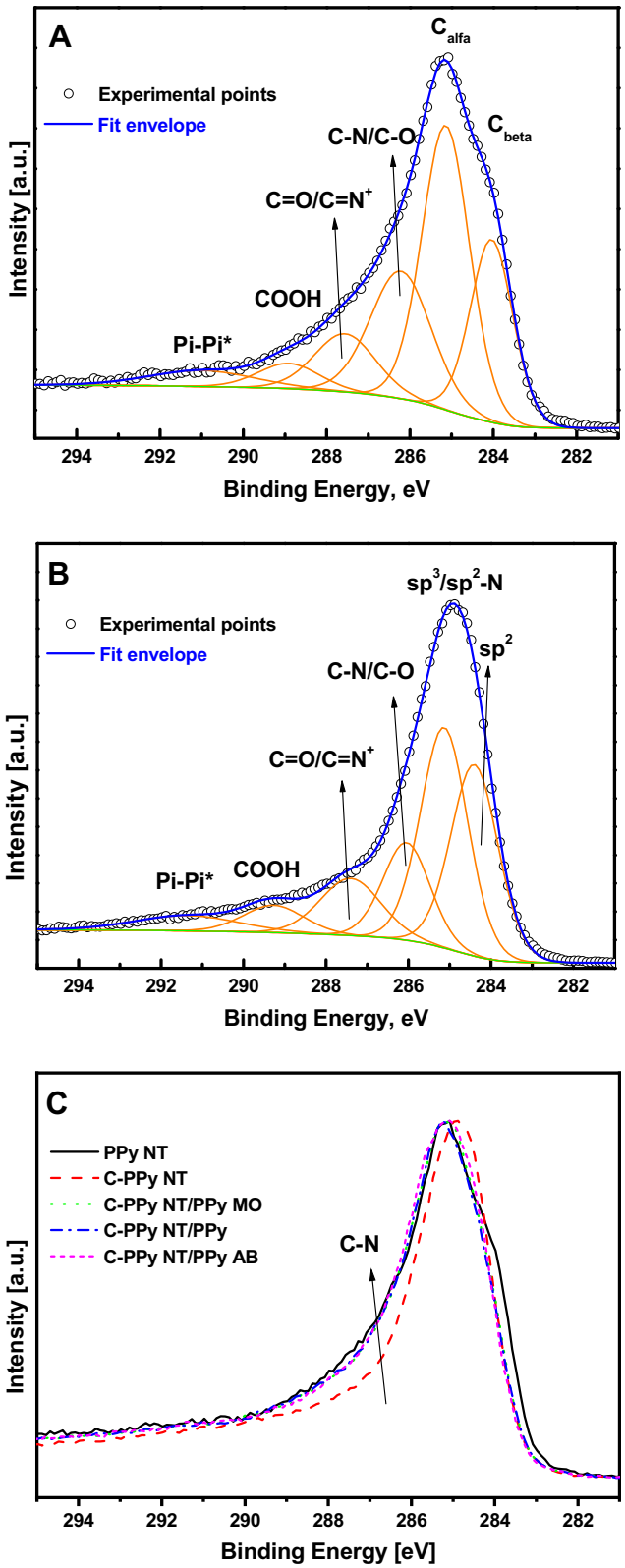

Fig. 7. XPS C1s region of PPy nanotubes (A), carbonized PPy nanotubes (B), and C1s comparison of all samples (C).

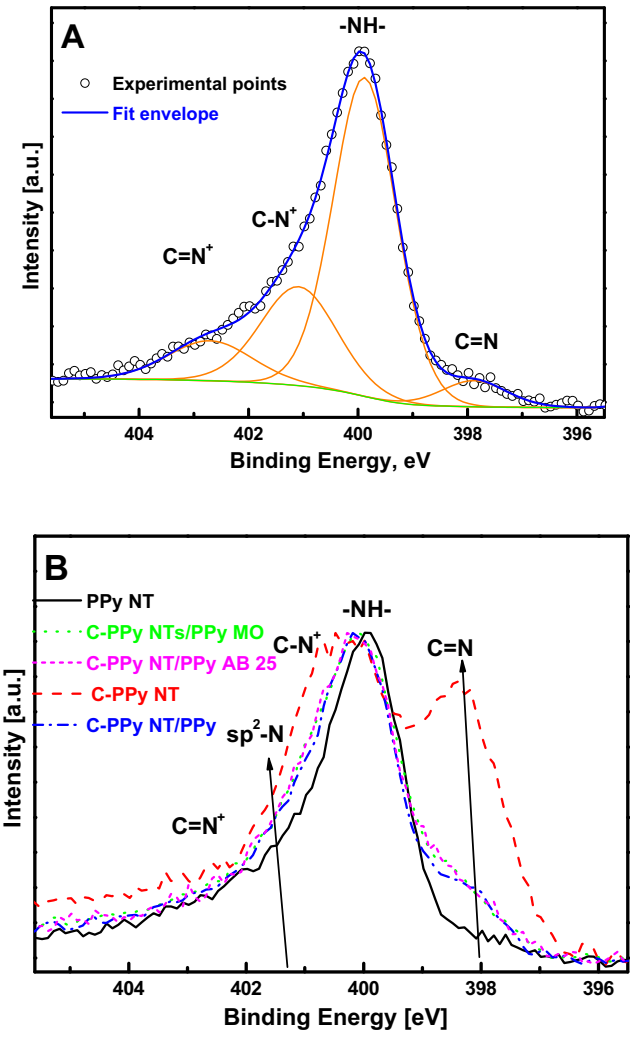

Fig. 8. XPS N1s region of PPy nanotubes (A) and N1s comparison of all samples (B).

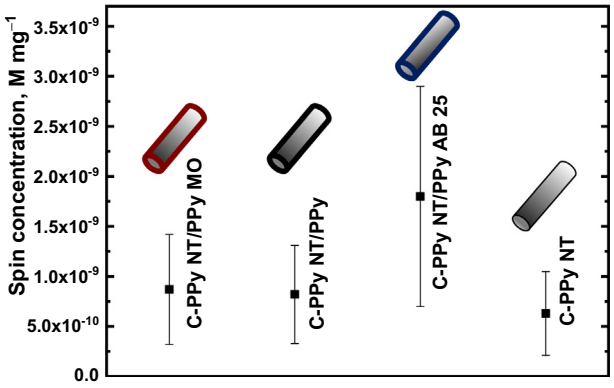

Fig. 9. Spin concentration of carbonized PPy nanotubes and coated samples.

mainly hydrogen peroxide. Before proceeding further, we note that non-carbonized PPy NT alone is not active for ORR under investigated conditions, in agreement with previous reports [17].

Among four materials containing C-PPy NT, the best activity was displayed by neat C-PPy NT (Fig. 12). Yet again, comparison can be made with previously reported C-PPy NT [17] and better ORR performance can be observed, which we ascribe to higher nitrogen content in the surface layer, observed by XPS (compared to C-PPy NT reported in [17], N content in C-PPy NT described here is by 34% higher). However, it can also be observed that, in the series of materials reported here, ORR response increases as the specific surface area increases (Fig. 12). For C-PPy NT ORR

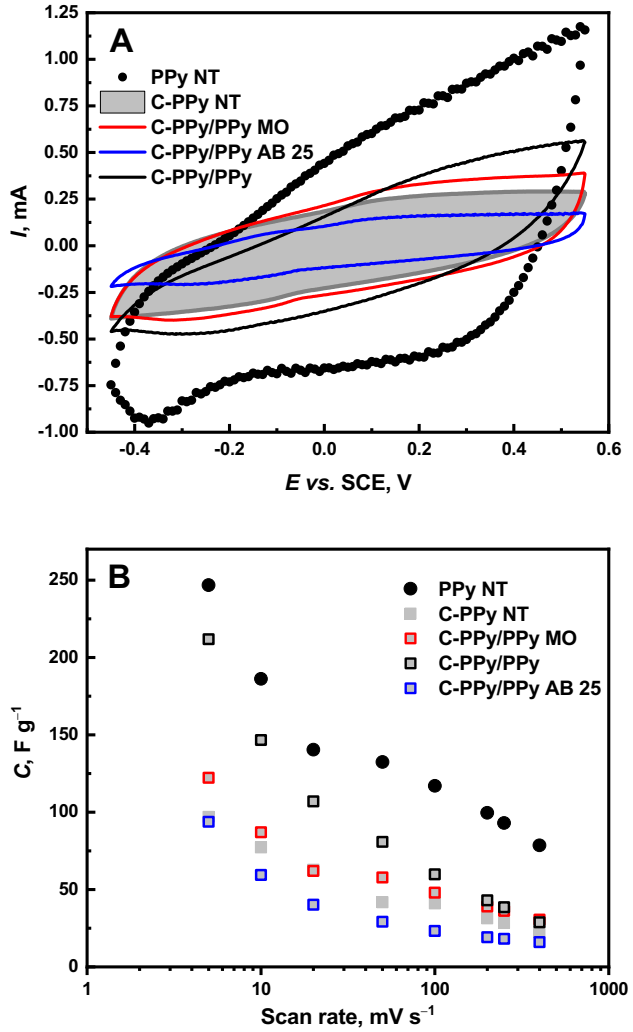

Fig. 10. Cyclic voltammograms of the investigated materials recorded in quiescent N_2-purged 0.5 mol L^{-1}M H_2SO^4 solution at the scan rate of 100 mV s^{-1} (A) and evaluated gravimetric capacitance measured evaluated at different scan rates (B).

commences above −0.2 V *vs*. SCE, while for PPy-covered C-PPy NT ORR starts between −0.3 and −0.2 V *vs*. SCE, suggesting hindered ORR kinetics on PPy-coated C-PPy NT.

Next, the polarization ORR curves were subjected to the Koutecky-Levich (K-L) analysis [44]. This procedure allows for the determination of the apparent number of electrons consumed *per* O_2 molecule (n), or, in other words, catalyst selectivity. The apparent number of electrons is determined from the slope of the K-L line defined by:

$$\frac{1}{j(E)} = \frac{1}{j_k(E)} + \frac{1}{j_d} = \frac{1}{j_k} - \frac{1}{0.62 \cdot n \cdot F \cdot D(O_2)^{2/3} \cdot \nu^{-1/6} \cdot \omega^{1/2} \cdot c(O_2)} \quad (3)$$

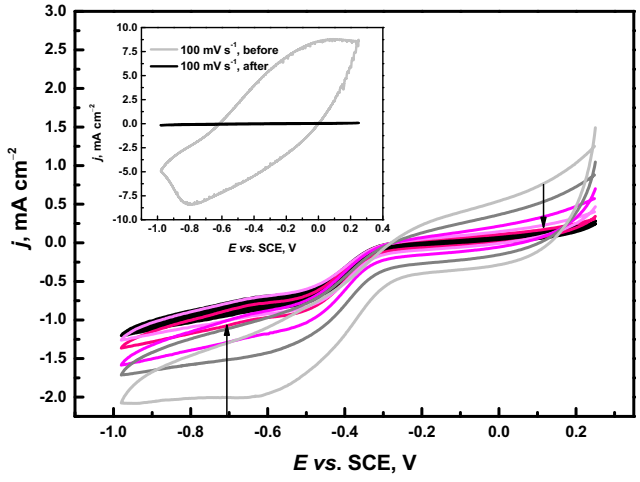

Fig. 11. Consecutive cyclic voltammograms of C-PPy NT/PPy sample in O_2-saturated 0.1 M KOH (potential sweep rate 20 mV s^{-1}, electrode rotation rate 600 rpm). Inset depicts base lines recorded in N_2-purged 0.1 M KOH at 100 mV s^{-1} before and after potentiodynamic cycling in O_2-saturated solution.

$j(E)$ and $j_k(E)$ are the measured current density and the kinetic current density at a given electrode potential (E), respectively. Next, j_d is the limiting diffusion current density, ν represents the kinematic viscosity of the solution (0.01 cm^2s^{-1}), $D(O_2)$ is the diffusion coefficient of O_2 (1.9×10^{-5} cm^2 s^{-1}) and $c(O_2)$ is the concentration of dissolved O_2 (1.2×10^{-6} mol cm^{-3}) [45]. The obtained results (Table 3) clearly demonstrate that neat C-PPy NT are very selective and allow for almost complete reduction of O_2 to OH^- with nearly 4 electrons consumed per O_2 molecule. However, the results also suggest that it is possible to finely modulate ORR selectivity of C-PPy NT core by tailoring the structure of PPy shell. All three PPy-coated C-PPy NT materials display different selectivity towards O_2 reduction. C-PPy NT/PPy MO and C-PPy NT/PPy AB 25 seems to allow for $2e^-$ reduction, i.e. conversion of O_2 to hydrogen peroxide (that is HO_2^- in alkaline media). We ascribe this effect to a reduced specific surface area, resulting with lower number of active sites for O_2 reduction, when compared to bare C-PPy NT, and the formation of molecular shell over carbonaceous core, which hinders effective conversion of O_2 to OH^-. As in the series of investigated materials n varies between 2 and 4, and also with the electrode potential (Table 3), we believe that ORR actually proceed *via* $2e^-$ reduction to peroxide (HO_2^-) which further goes into chemical disproportiation to OH^- and O_2 [46]. O_2 molecule formed in this chemical step enters next electrochemical reduction effectively increasing n above 2. Hence, when surface area is reduced chemically, formed O_2 leaves the interfacial region and the overall reduction product is dominantly peroxide.

We consider this observation as particularly important as it shows that tailoring of the polymeric shell over ORR active carbonaceous core allows for the tuning of the catalyst selectivity and optimization of materials performance for given application, from cathode catalysts for alkaline hydrogen fuel cells to electrochemical synthesis of hydrogen peroxide.

Table 3
Calculated number of electrons *per* O_2 molecule using K-L analysis.

	Number of electrons *per* O_2 molecule			
E vs SCE/V	C-PPy NT	C-PPy NT/PPy	C-PPy NT/PPy MO	C-PPy NT/PPy AB 25
−0.50	4.2 ± 0.1	2.5 ± 0.1	1.9 ± 0.2	2.20 ± 0.10
−0.60	4.03 ± 0.05	2.5 ± 0.1	1.7 ± 0.2	2.10 ± 0.10
−0.70	3.85 ± 0.02	2.4 ± 0.1	1.7 ± 0.2	2.03 ± 0.08
−0.80	3.55 ± 0.06	2.3 ± 0.1	1.7 ± 0.2	1.92 ± 0.08

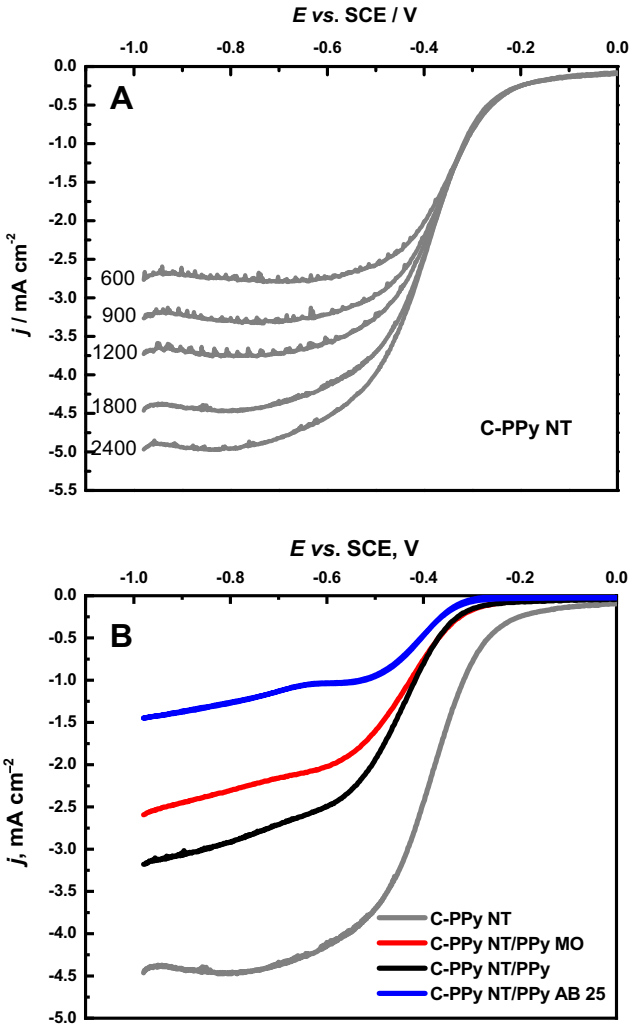

Fig. 12. ORR polarization curves recorded under RDE conditions for C-PPy NT in O_2-saturated 0.1 M KOH with different electrode rotation rates (A), and comparison of ORR polarization curves for four different samples recorded at the electrode rotation rate of 1800 rpm (B).

4. Conclusions

Carbonized PPy NT coated with various types of PPy were successfully prepared with high specific surface area and conductivity. Raman and X-ray photoelectron spectroscopies indicated the homogeneous coating and the incorporation of dyes traces into the formed PPys. Thickness of the coating PPy films proved to have a marked effect on the capacitive and performance. The neat PPy coating was shown to be the most beneficial for capacitance doubling its value compared to the carbon core. PPy coating in the presence of MO provided a negligible increase while in the presence of AB 25 even decreased the capacitance. All three coating forms were transformed in the presence of products of oxygen reduction, most probably hydrogen peroxide, in the first ten cycles. Change of the materials activity towards different reactions makes them a multipurpose materials enabling fine tuning of their activity for a specific application, be it an alkaline fuel cell or a supercapacitor.

Acknowledgements

The authors wish to thank the Czech Science Foundation (18-04669S) for the financial support. The coordination within the Programme for Funding Multilateral Scientific and Technological Cooperation Projects in the Danube Region 2017–2018 (DS-2016-0027) was financially supported for the individual participants by the Austrian Federal Ministry of Science, Research and Economy (BMWFW, under project No: MULT_DR 06/2017), by the Ministry of Education, Youth and Sports of the Czech Republic (8X17027), by the Serbian Ministry of Education, Science and Technological Development (DS-027) and by the Ministry of Education, Science, Research and Sport of the Slovak Republic (APVV DS-2016-0027). Part of this work was also carried out within the project BioCarb-K, co-financed by the European Regional Development Fund (EFRE) and the province of Upper Austria through the programme IWB 2014-2020.

References

[1] H.J. Tang, J.Y. Wang, H.J. Yin, H.J. Zhao, D. Wang, Z.Y. Tang, Growth of polypyrrole ultrathin films on MoS_2 monolayers as high-performance supercapacitor electrodes, Adv. Mater. 27 (2015) 1117–1123.
[2] A. Sajedi-Moghaddam, E. Saievar-Iranizad, M. Pumera, Two-dimensional transition metal dichalcogenide/conducting polymer composites: synthesis and applications, Nanoscale 9 (2017) 8052–8065.
[3] Q. Zhang, N. Wang, P. Zhao, M.Q. Yao, W.C. Hu, N-doped mesoporous carbon integrated on carbon cloth for flexible supercapacitors with remarkable performance, J. Mater. Sci. 53 (2018) 14573–14585.
[4] K.W. Shu, Y.F. Chao, S.L. Chou, C.Y. Wang, T. Zheng, S. Gambhir, et al., A "Tandem" strategy to fabricate flexible graphene/polypyrrole nanofiber film using the surfactant-exfoliated graphene for supercapacitors, ACS Appl. Mater. Interfaces 10 (2018) 22031–22041.
[5] J.W. Lee, H.I. Lee, S.J. Park, Facile synthesis of petroleum-based activated carbons/tubular polypyrrole composites with enhanced electrochemical performance as supercapacitor electrode materials, Electrochim. Acta 263 (2018) 447–453.
[6] Y.L. Xing, S.B. Wang, B.Z. Fang, G. Song, D.P. Wilkinson, S.C. Zhang, N-doped hollow urchin-like anatase TiO_2@C composite as a novel anode for Li-ion batteries, J. Power Sources 385 (2018) 10–17.
[7] Y. Liu, W.J. Yan, X.W. An, X. Du, Z.D. Wang, H.L. Fan, et al., A polypyrrole hollow nanosphere with ultra-thin wrinkled shell: synergistic trapping of sulfur in lithium-sulfur batteries with excellent elasticity and buffer capability, Electrochim. Acta 271 (2018) 67–76.
[8] Z.G. Zhao, T.T. Yu, Y.C. Miao, X.C. Zhao, Chloride ion-doped polyaniline/carbon nanotube nanocomposite materials as new cathodes for chloride ion battery, Electrochim. Acta 270 (2018) 30–36.
[9] X.L. Li, R. Liu, C.Y. Xu, Y. Bai, X.M. Zhou, Y.J. Wang, et al., High-performance polypyrrole/graphene/$SnCl_2$ modified polyester textile electrodes and yarn electrodes for wearable energy storage, Adv. Funct. Mater. 28 (2018) 1800064.
[10] J. Kopecká, M. Mrlík, R. Olejník, D. Kopecký, M. Vrňata, J. Prokeš, et al., Polypyrrole nanotubes and their carbonized analogs: Synthesis, characterization, gas sensing properties, Sensors 16 (2016) 1917.
[11] K. Jurewicz, E. Frackowiak, Modified carbon materials for electrochemical capacitors, Mol. Phys. Rep. 27 (2000) 38–45.
[12] Y. Bo, Y.P. Zhao, Z.S. Cai, A. Bahi, C.H. Liu, F. Ko, Facile synthesis of flexible electrode based on cotton/polypyrrole/multi-walled carbon nanotube composite for supercapacitors, Cellulose 25 (2018) 4079–4091.
[13] U. Acharya, P. Bober, M. Trchová, A. Zhigunov, J. Stejskal, J. Pfleger, Synergistic conductivity increase in polypyrrole/molybdenum disulfide composite, Polymer 150 (2018) 130–137.
[14] M. Trchová, E.N. Konyushenko, J. Stejskal, J. Kovářová, G. Ćirić-Marjanović, The conversion of polyaniline nanotubes to nitrogen-containing carbon nanotubes and their comparison with multi-walled carbon nanotubes, Polym. Degrad. Stab. 94 (2009) 929–938.
[15] J.W.F. To, J.J. He, J.G. Mei, R. Haghpanah, Z. Chen, T. Kurosawa, et al., Hierarchical N-doped carbon as CO_2 adsorbent with high CO_2 selectivity from rationally designed polypyrrole precursor, J. Am. Chem. Soc. 138 (2016) 1001–1009.
[16] P. Bober, M. Trchová, Z. Morávková, J. Kovářová, I. Vulić, N. Gavrilov, et al., Phosphorus and nitrogen-containing carbons obtained by the carbonization of conducting polyaniline complex with phosphites, Electrochim. Acta 246 (2017) 443–450.
[17] G. Ćirić-Marjanović, S. Mentus, I. Pašti, N. Gavrilov, J. Krstić, J. Travas-Sejdic, et al., Synthesis, characterization, and electrochemistry of nanotubular polypyrrole and polypyrrole-derived carbon nanotubes, J. Phys. Chem. C 118 (2014) 14770–14778.
[18] I. Sapurina, J. Stejskal, I. Šeděnková, M. Trchová, J. Kovářová, J. Hromadková, et al., Catalytic activity of polypyrrole nanotubes decorated with noble-metal nanoparticles and their conversion to carbonized analogues, Synth. Met. 214 (2016) 14–22.
[19] P. Bober, J. Kovářová, J. Pfleger, J. Stejskal, M. Trchová, I. Novák, et al., Twin carbons: the carbonization of cellulose or carbonized cellulose coated with a conducting polymer, polyaniline, Carbon 109 (2016) 836–842.

[20] P. Bober, N. Gavrilov, A. Kovalcik, M. Mičušík, C. Unterweger, I.A. Pašti, et al., Electrochemical properties of lignin/polypyrrole composites and their carbonized analogues, Mater. Chem. Phys. 213 (2018) 352–361.
[21] B.X. Yan, Y. Wu, L. Guo, Recent advances on polypyrrole electroactuators, Polymers 9 (2017) 446.
[22] P. Humpolíček, V. Kašpárková, J. Pacherník, J. Stejskal, P. Bober, Z. Capáková, et al., The biocompatibility of polyaniline and polypyrrole: a comparative study of their cytotoxicity, embryotoxicity and impurity profile, Mater. Sci. Eng., C 91 (2018) 303–310.
[23] Y.J. Wang, C. Yang, P. Liu, Acid blue AS doped polypyrrole (PPy/AS) nanomaterials with different morphologies as electrode materials for supercapacitors, Chem. Eng. J. 172 (2011) 1137–1144.
[24] L. Zang, J. Qiu, C. Yang, E. Sakai, Enhanced conductivity and electrochemical performance of electrode material based on multifunctional dye doped polypyrrole, J. Nanosci. Nanotechnol. 16 (2016) 2564–2570.
[25] Y. Li, P. Bober, M. Trchová, J. Stejskal, Polypyrrole prepared in the presence of methyl orange and ethyl orange: nanotubes versus globules in conductivity enhancement, J. Mater. Chem. C 5 (2017) 4236–4245.
[26] P. Bober, Y. Li, U. Acharya, Y. Panthi, J. Pfleger, P. Humpolíček, et al., Acid Blue dyes in polypyrrole synthesis: the control of polymer morphology at nanoscale in the promotion of high conductivity and the reduction of cytotoxicity, Synth. Met. 237 (2018) 40–49.
[27] J. Stejskal, M. Trchová, Conducting polymer nanotubes: a review, Chem. Pap. 72 (2018) 1563–1595.
[28] E.N. Konyushenko, J. Stejskal, M. Trchová, J. Hradil, J. Kovářová, J. Prokeš, et al., Multi-wall carbon nanotubes coated with polyaniline, Polymer 47 (2006) 5715–5723.
[29] T. Mao, Y.J. Tang, Y. Zhang, J.H. Zhang, D.L. Guo, Carbon nanotubes/polyaniline nanocomposite coatings: preparation, rheological behavior, and their application in paper surface treatment, J. Appl. Polym. Sci. 135 (2018) 46329.
[30] X.H. Ou, X.C. Xu, Highly improved conductivity of polyaniline-carbon nanotubes composites doped by liquid bromine with a synergistic effect, Polym. Compos. 39 (2018) E1034–E1040.
[31] T. Hussain, S. Jabeen, K. Shehzad, A. Mujahid, M.N. Ahmad, Z.H. Farooqi, et al., Polyaniline/silver decorated-MWCNT composites with enhanced electrical and thermal properties, Polym. Compos. 39 (2018) E1346–E1353.
[32] J. Stejskal, M. Trchová, S. Fedorova, I. Sapurina, J. Zemek, Surface polymerization of aniline on silica gel, Langmuir 19 (2003) 3013–3018.
[33] I. Sapurina, J. Stejskal, Ternary composites of multi-wall carbon nanotubes, polyaniline, and noble-metal nanoparticles for potential applications in electrocatalysis, Chem. Pap. 63 (2009) 579–585.
[34] J. Stejskal, I. Sapurina, M. Trchová, I. Šeděnková, J. Kovářová, J. Kopecká, et al., Coaxial conducting polymer nanotubes: polypyrrole nanotubes coated with polyaniline or poly(*p*-phenylenediamine) and products of their carbonisation, Chem. Pap. 69 (2015) 1341–1349.
[35] I.A. Pašti, A.J. Ležaić, N.M. Gavrilov, G. Ćirić-Marjanović, S.V. Mentus, Nanocarbons derived from polymers for electrochemical energy conversion and storage – a review, Synth. Met. 246 (2018) 267–281.
[36] R. Kostić, D. Raković, S.A. Stepanyan, I.E. Davidova, L.A. Gribov, Vibrational spectroscopy of polypyrrole, theoretical-study, J. Chem. Phys. 102 (1995) 3104–3109.
[37] J. Robertson, Diamond-like amorphous carbon, Mater. Sci. Eng., R 37 (2002) 129–281.
[38] Y. Furukawa, S. Tazawa, Y. Fuji, I. Harada, Raman spectra of polypyrrole and its 2,5–^{13}C-substituted and C-deuterated analogues in doped and undoped states, Synth. Met. 24 (1988) 329–341.
[39] F. Chen, G.Q. Shi, M.X. Fu, L.T. Qu, X.Y. Hong, Raman spectroscopic evidence of thickness dependence of the doping level of electrochemically deposited polypyrrole film, Synth. Met. 132 (2003) 125–132.
[40] J. Kopecká, D. Kopecký, M. Vrňata, P. Fitl, J. Stejskal, M. Trchová, et al., Polypyrrole nanotubes: mechanism of formation, RSC Adv. 4 (2014) 1551–1558.
[41] J. Tabačiarová, M. Mičušík, P. Fedorko, M. Omastová, Study of polypyrrole aging by XPS, FTIR and conductivity measurements, Polym. Degrad. Stab. 120 (2015) 392–401.
[42] Y.H. Su, H.L. Jiang, Y.H. Zhu, X.L. Yang, J.H. Shen, W.J. Zou, et al., Enriched graphitic N-doped carbon-supported Fe_3O_4 nanoparticles as efficient electrocatalysts for oxygen reduction reaction, J. Mater. Chem. A 2 (2014) 7281–7287.
[43] I.A. Pašti, A.J. Ležaić, N.M. Gavrilov, G. Ćirić-Marjanović, S.V. Mentus, Nanocarbons derived from polymers for electrochemical energy conversion and storage – a review, Synth. Met. 246 (2018) 267–281.
[44] A.J. Bard, L.R. Faulkner, Electrochemical Methods Fundamentals and Applications, second ed., Wiley, 2001.
[45] R.E. Davis, G.L. Horvath, C.W. Tobias, The solubility and diffusion coefficient of oxygen in potassium hydroxide solutions, Electrochim. Acta 12 (1967) 287–297.
[46] G. Ćirić-Marjanović, I. Pašti, S. Mentus, One-dimensional nitrogen-containing carbon nanostructures, Prog. Mater. Sci. 69 (2015) 61–182.

Appendix 7

Poly(*p*-phenylenediamine)/maghemite composite as highly effective adsorbent for anionic dye removal

Reactive and Functional Polymers 146 (2020) 104436

Contents lists available at ScienceDirect

Reactive and Functional Polymers

journal homepage: www.elsevier.com/locate/react

Poly(*p*-phenylenediamine)/maghemite composite as highly effective adsorbent for anionic dye removal

Islam M. Minisy[a,1], Beata A. Zasońska[a], Eduard Petrovský[b], Pavel Veverka[c], Ivana Šeděnková[a], Jiřina Hromádková[a], Patrycja Bober[a,*]

[a] Institute of Macromolecular Chemistry, Academy of Sciences of the Czech Republic, Prague 162 06, Czech Republic
[b] Institute of Geophysics, Academy of Sciences of the Czech Republic, 141 00 Prague, Czech Republic
[c] Institute of Physics, Academy of Sciences of the Czech Republic, Prague 162 00, Czech Republic

ARTICLE INFO

Keywords:
Poly(*p*-phenylenediamine)
Maghemite
Dye removal
Adsorption
Reactive Black 5

ABSTRACT

Poly(*p*-phenylenediamine)/maghemite (PPDA/γ-Fe_2O_3) composites were prepared by the oxidative polymerization of *p*-phenylenediamine with ammonium peroxodisulfate as an oxidizing agent in the presence of γ-Fe_2O_3 nanoparticles. Morphology of the prepared composites was examined by the scanning and transmission electron microscopies. X-ray diffraction and EDX were used to study crystallinity and chemical composition, respectively. TGA demonstrated that only 7 and 45 wt% of γ-Fe_2O_3 were incorporated into PPDA prepared with 25 and 50 wt% of γ-Fe_2O_3, respectively. Adsorption property of the composites was examined towards the anionic dye, Reactive Black 5. The adsorption results were fitted to different kinetics and isotherm models. The highest adsorption capacity (Q_{max}) was estimated to be 223 mg g^{-1} in case of PPDA with the highest specific surface area (70.6 m^2 g^{-1}) prepared with 25 wt% of γ-Fe_2O_3. Q_{max} of neat PPDA was estimated to be 185.2 mg g^{-1} and 123.2 mg g^{-1} for PPDA prepared with 50 wt% of γ-Fe_2O_3. In addition to the enhancing of the adsorption capacity, the incorporation of γ-Fe_2O_3 particles provided an easy separation of the composites from the adsorption medium.

1. Introduction

The dramatic increase of the environmental pollution has led to dangerous side effects on all the components of our planet (water, soil, and atmosphere) and has vigorously threatened human health and life quality. Regarding water; dyes, heavy metals, pesticides and even drugs are typical wastewater pollutants that may display eco-toxic hazards and potential bioaccumulation dangers [1]. With growing human population, large amounts of synthetic organic dyes are annually produced and employed in many industrial fields, such as textile, pharmaceutical, paper mill, leather, and food. Different approaches are used to remove organic and inorganic pollutants from wastewater, such as coagulation, flocculation, biodegradation, adsorption, ion-exchange, oxidation [2] and photocatalytic degradation [3–6]. Among these methods, adsorption is the most promising technique, due to high efficiency, low cost and reusability [7,8]; however, preparation of a new adsorbent fulfilling the criteria of selectivity, stability and cost-effective production is still a challenge.

Recently, conducting polymer composites have been used as adsorbents to remove pollutants from wastewater [9–14]. Among them poly(*p*-phenylenediamine) (PPDA) (Fig. 1A, B) and its composites have been intensively investigated as adsorbents for heavy metals, such as Cr (VI) [15,16], Pb(II) [17], As(V) [18], and pesticides [19,20]. This conjugated polymer, rated mostly as non-conducting, shows good redox properties, salt-base transition and chelation ability [21]. PPDA is easily prepared by a low cost method, has excellent environmental and thermal stability [17], and it is mostly used in biomedical applications where the potential toxicity of aniline and its oligomers is unacceptable [22]. PPDA composites are widely used as supercapacitors [23], in photothermal therapy [24] or in biosensors [25]. The incorporation of iron oxide nanoparticles to the conducting polymers allows for the preparation of hybrid composites which possess magnetoconductive properties and can be easily targeted and manipulated by a magnet [26–28].

We report here a simple, two step preparation of hybrid poly(*p*-phenylenediamine)/maghemite (PPDA/γ-Fe_2O_3) composites and their application as adsorbent for the removal of organic dye, Reactive Black 5 (RB, Fig. 1C), from aqueous solutions. RB dye is a highly water-

* Corresponding author.
E-mail address: bober@imc.cas.cz (P. Bober).
[1] I. M. Minisy is a PhD student at the Faculty of Science, Charles University, Prague, Czech Republic.

https://doi.org/10.1016/j.reactfunctpolym.2019.104436
Received 4 September 2019; Received in revised form 22 November 2019; Accepted 23 November 2019
Available online 26 November 2019
1381-5148/

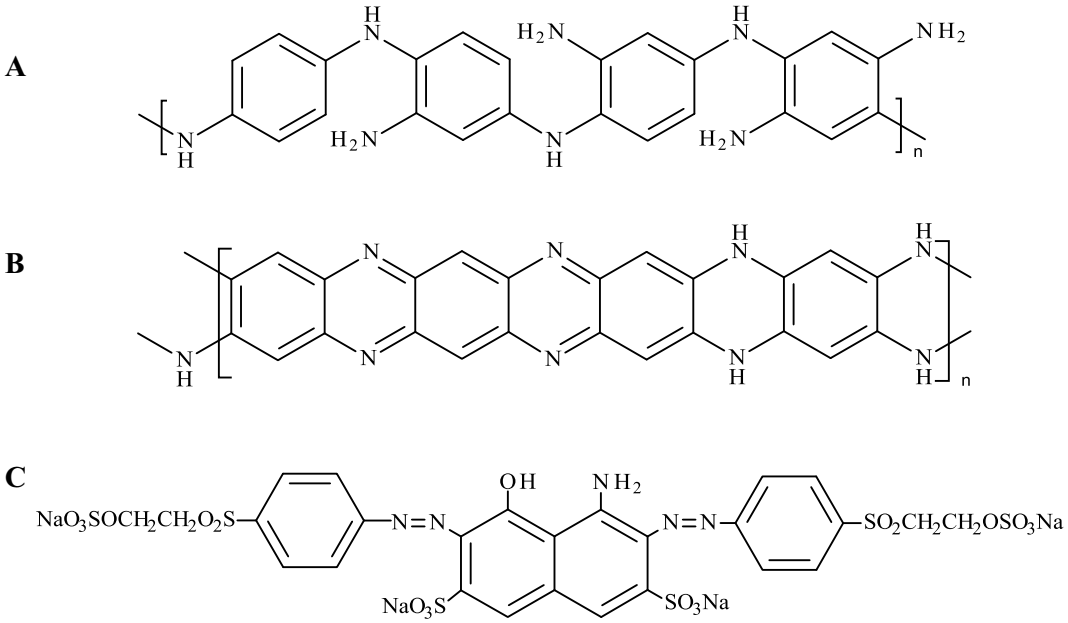

Fig. 1. The idealized chemical formulae of poly(*p*-phenylenediamine) (A and B) [29] and chemical structure of Reactive Black 5 (C).

soluble diazo dye with polyaromatic non-degradable structure used in textile industry. To the best of our knowledge, the removal of RB from water by PPDA has not been reported before. Moreover, the incorporation of magnetic nanoparticles provided an increase in specific surface area of the composites and allowed for easy separation of the adsorbent from the solutions.

2. Experimental

2.1. Chemicals

p-Phenylenediamaine dihydrochloride (≥98%), ammonium peroxidisulfate, $FeCl_2.4H_2O$ and $FeCl_3.6H_2O$, and Reactive Black 5 were purchased from Sigma-Aldrich (Germany). Aqueous ammonia was obtained from Lach-Ner (Czech Republic) and sodium hypochlorite (NaOCl) solution (5 wt%) was obtained from Bochemie (Czech Republic). All chemicals were used as received without any further purification. Ultrapure Q-water ultra-filtered in a Milli-Q Gradient A10 system (Millipore, Molsheim, France) was used for the preparation of solutions.

2.2. Synthesis of maghemite nanoparticles

In a typical procedure [28], aqueous iron (III) chloride (0.2 M, 100 mL) and iron (II) chloride (0.2 M, 50 mL) solutions were mixed with NH_4OH solution (0.5 M, 100 mL) under sonication (Hielscher, Ultrasonic Processor UP400St, Teltow, Germany) for 5 min. In the next step, the solution was added to NH_4OH solution (0.5 M, 400 mL) and stirred for 1 h (200 rpm). Then the resulting precipitate was magnetically separated, washed with ultrapure water until peptization and sonicated with NaOCl solution (5 wt%, 16 mL) for 5 min. The resulting γ-Fe_2O_3 particles were five times magnetically separated and washed with ultrapure water and dried.

2.3. Synthesis of poly(p-phenylenediamine)/maghemite composite

Poly(*p*-phenylenediamine)/maghemite composites were prepared by oxidation of *p*-phenylenedianine dihydrochloride (0.2 M) with ammonium peroxidisulfate (0.25 M) in the aqueous suspension of various amount of γ-Fe_2O_3 (12.5, 25 and 50 wt% of *p*-phenylenedianine dihydrochloride weight) at room temperature, and the resulting composites are denoted as PPDA/γ-Fe_2O_3/12.5, PPDA/γ-Fe_2O_3/25 and PPDA/γ-Fe_2O_3/50. The total volume of the reaction mixture was 50 mL. The reaction mixture was stirred for 1 h and then left for 24 h at rest. The synthesised composite was collected by filtration, washed throughly with 0.2 M hydrochloric acid and ethanol to entirely remove all the soluble residuals and oligomers. After that samples were left to dry in a desiccator over silica gel till constant weight. The neat PPDA was prepared by the same procedure excluding the γ-Fe_2O_3 from the reaction medium.

2.4. Characterization

The morphology and elemental composition of all the samples were examined by scanning electron microscope (SEM, VEGA Tescan) equipped with energy-dispersive X-ray spectroscope (EDX) and transmission electron microscope (TEM, TECNAI G2 SPIRIT).

The X-ray diffraction patterns (XRD) of powder samples were determined using powder X-ray Bruker D8 Advance diffractometer with a scintillation detector under CuKα irradiation in the angular range 10–100° 2theta and step 0.04°. Diffraction patterns were analyzed by the Rietveld method in the FULLPROF program.

The solubility of PPDA and its composites were measured according to Li et al. [30]. 5 mg of powder was added into 1 mL of various solvents (H_2O, 0.2 M HCl, 0.1 M H_2SO_4, 0.2 M NaOH, DMSO and NMP), then the mixtures were shaken continously for 24h at room temperature and the solubility was characterized semiquantitatively.

The magnetization was measured using EV9 vibrating sample magnetometer (VSM; DSM Magnetics, ADE Corporation; Lowell, MA, USA) at a room temperature.

Thermogravimetric analysis was performed in 50 cm^3 min^{-1} airflow, with a heating rate of 10 °C min^{-1} to 800 °C. Pyris 1 TGA Thermogravimetric Analyzer (Perkin Elmer, USA) was used. Elemental Analysis was performed on a Perkin-Elmer 2400 CHN elemental analyzer (Waltham, MA, USA).

The BET (Brunauer, Emmett and Teller) specific surface area (S_{BET}) of the samples was determined using Gemini VII 2390 (Micromeritics, Instruments Corp, Norcross, USA) with nitrogen as the sorbate. The samples were vacuum-dried at 90 °C for 50 h.

The electrical conductivity of all the samples was measured by the van der Pauw method. For this the powdered samples were pressed into

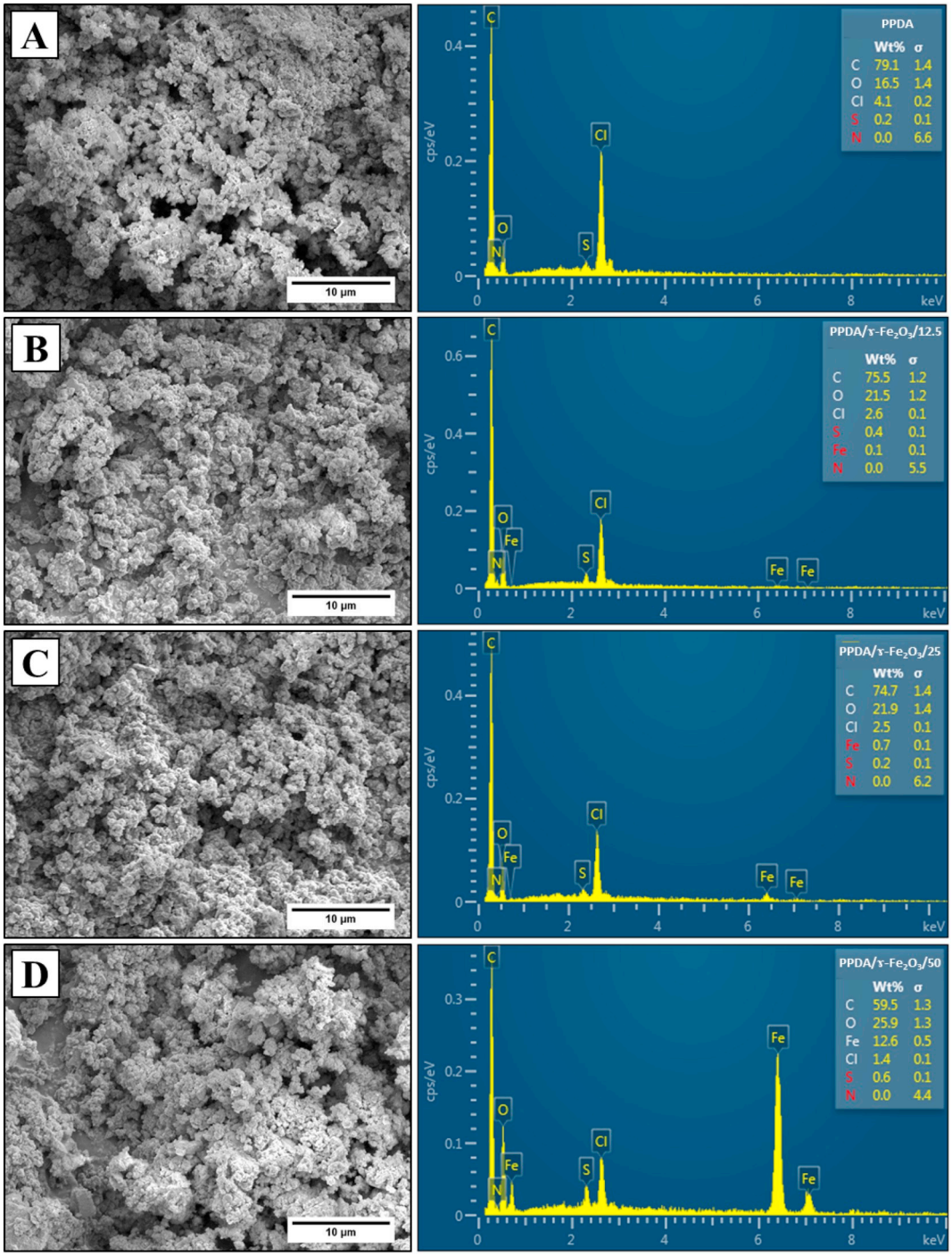

Fig. 2. SEM micrographs and the corresponding EDX analysis of poly(*p*-phenylenediamine) (A) and its composites with 12.5 (B), 25 (C) and 50 wt% (D) of maghemite.

pellets (13 mm diameter, 1 mm thickness) at pressure of 70 kN.

A UV-Vis spectrometer (LAMBDA 950 UV/Vis Spectrophotometer, PerkinElmer, UK) was used to estimate the RB solution concentrations by using the Beer-Lambert's law at λ_{max} = 598 nm.

The Thermo Nicolet NEXUS 870 FTIR Spectrometer was used to record infrared spectra of powdered samples dispersed in potassium bromide (DTGS detector, 64scans, resolution 2 cm^{-1}). The spectra were corrected for the humidity and the carbon dioxide in the optical path.

Raman spectra were recorded with a Renishaw inVia Reflex Raman microspectrometer (Leica SM LM microscope, objective 50×) using argon ion laser with wavelength 514 nm (holographic grating 2400 lines mm^{-1}).

2.5. Dye adsorption

Stock solution (500 mg L^{-1}) of RB was prepared in freshly distilled water. The particular desired concentrations were prepared by successive dilutions. All adsorption experiments were conducted in the dark at the room temperature (25 ± 2 °C). Samples containing γ-Fe_2O_3 were separated from the dye solution by using a magnet while the samples without γ-Fe_2O_3 (pure PPDA) were separated by a centrifuge. For a typical adsorption experiment, 20 mg of substrates were dispersed in RB solutions (50 mL) with different dye concentrations. At definite time intervals, the dye concentration was estimated using UV-Vis spectrometer.

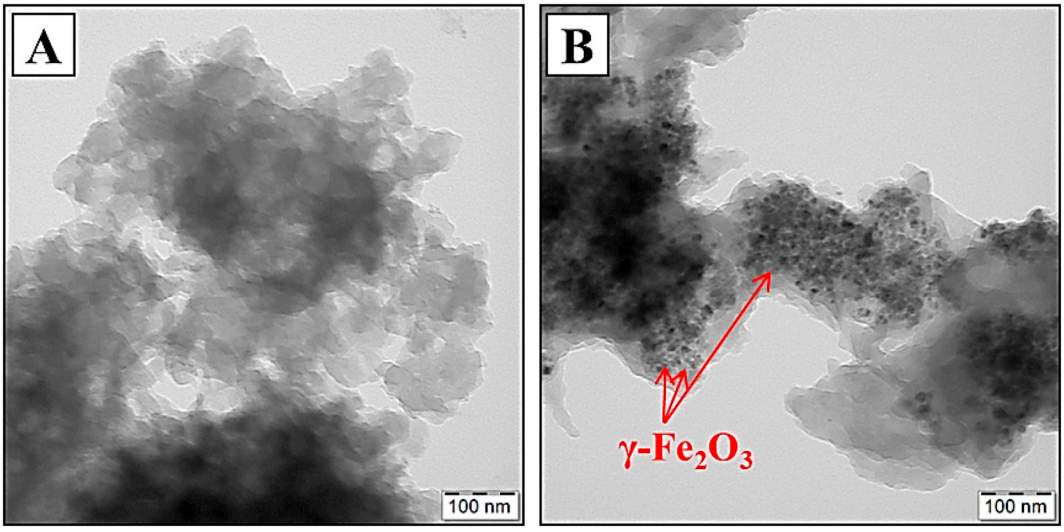

Fig. 3. TEM micrographs of pure poly(*p*-phenylenediamine) (A) and poly(*p*-phenylenediamine) prepared with 50 wt% of maghemite (B).

Table 1
The specific surface area and conductivity of the produced composites.

Sample code	S_{BET}, $m^2\ g^{-1}$	Micropore volume, $cm^3\ g^{-1}$	Conductivity, S cm^{-1}	Solubility[a]				
				water	HCl	H_2SO_4	NMP	DMSO
PPDA	57.2 ± 1.1	0.012	1.0×10^{-12}	IS	IS	IS	PS	S
PPDA/γ-Fe_2O_3/12.5	56.1 ± 1.7	0.015	1.0×10^{-11}	IS	IS	IS	PS	S
PPDA/γ-Fe_2O_3/25	70.6 ± 0.7	0.022	1.1×10^{-10}	IS	IS	IS	PS	S
PPDA/γ-Fe_2O_3/50	56.9 ± 0.6	0.005	2.0×10^{-10}	IS	IS	IS	PS	S

[a] IS = insoluble; PS = partially soluble; S = soluble.

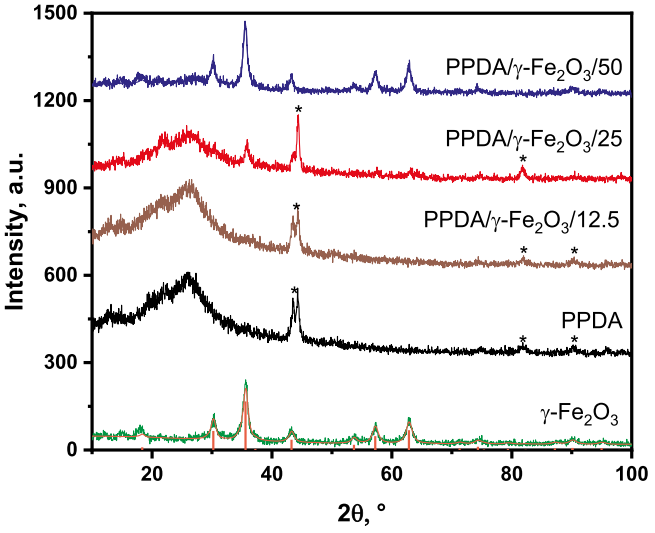

Fig. 4. The XRD patterns of powder samples. Observed data are depicted by dotted line. Calculated data are depicted by solid line. Diffraction lines corresponding to the phase γ-Fe_2O_3 are depicted in the pattern of pure γ-Fe_2O_3 sample. PPDA crystalline phase is marked with symbol *.

Adsorption capacity Q_e (mg g^{-1}) and dye removal efficiency (R%) were calculated by the following equations:

$$Q_e = \frac{(C_i - C_e)}{m} \times V \quad (1)$$

$$R\% = \frac{(C_i - C_e)}{C_i} \times 100 \quad (2)$$

Table 2
Magnetic properties (M_s - saturation magnetization; M_{rs} - the saturation remanent magnetization; H_c - coercive force; H_{cr} - the coercivity of remanence) of the produced composites.

Sample code	M_s, $Am^2\ kg^{-1}$	M_{rs}, $Am^2\ kg^{-1}$	H_c, $A\ m^{-1}$	H_{cr}, $A\ m^{-1}$
PPDA	1.9×10^{-2}	6.6×10^{-4}	1532	21308.1
PPDA/γ-Fe_2O_3/12.5	4.3×10^{-2}	6.6×10^{-3}	3021.6	9749.4
PPDA/γ-Fe_2O_3/25	2.3	1.4×10^{-1}	1261.8	9011.3
PPDA/γ-Fe_2O_3/50	24.2	3.5×10^{-1}	406.6	8303.9
γ-Fe_2O_3	42.6	6.1×10^{-1}	397.9	7572.4

where, C_i is the initial dye concentration (mg L^{-1}), C_e is the dye concentration at equilibrium (mg L^{-1}), V is the volume of dye solution (L) and m is the mass of the adsorbent (g).

Kinetics of adsorption describes the rate of adsorbate molecules uptake onto the adsorbents. The kinetics of RB adsorption has been studied using the pseudo-first-order, pseudo-second-order, and intraparticle diffusion models. Those models can be described as follows [14]:

$$\text{Pseudo-first-order equation: } \log(Q_e - Q_t) = \log Q_e - \frac{k_1}{2.303} t \quad (3)$$

$$\text{Pseudo-second-order equation: } \frac{t}{Q_t} = \frac{1}{k_2 Q_e^2} + \frac{t}{Q_e} \quad (4)$$

$$\text{Intraparticle diffusion equation: } Q_t = k_i t^{1/2} + c \quad (5)$$

where, Q_e and Q_t (mg g^{-1}) refer to the amount of dye adsorbed at equilibrium and time t (min), respectively, k_1 is the pseudo-first-order rate constant (min^{-1}), k_2 is the rate constant of pseudo-second-order (g mg^{-1} min^{-1}), k_i is the intraparticle diffusion rate constant (mg g^{-1}

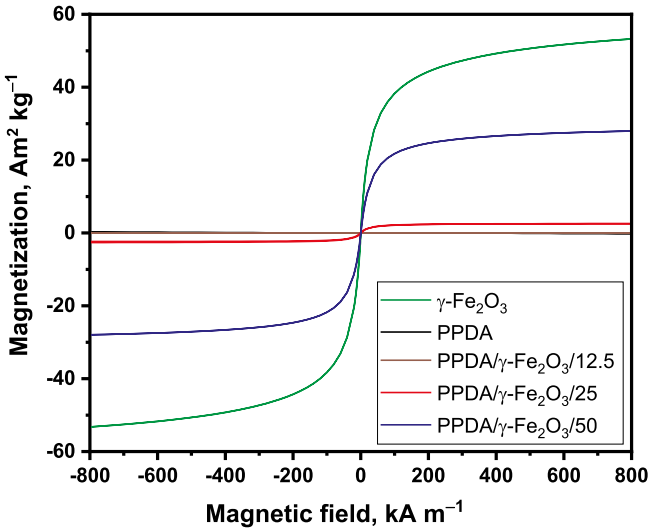

Fig. 5. Hysteresis curves of neat poly(*p*-phenylenediamine), maghemite and their composites.

$min^{-1/2}$) and c is the intraparticle diffusion constant.

The most common and well-known adsorption isotherm models: Langmuir, Freundlich and Temkin were used to estimate the adsorbate-adsorbent interactions by fitting the experimental data, the linearized equation of these models are expressed as [32]:

$$\text{Langmuir} \quad \frac{C_e}{Q_e} = \frac{1}{Q_{max} K_L} + \frac{C_e}{Q_{max}} \tag{6}$$

$$\text{Freundlich} \quad \ln Q_e = \ln K_F + \frac{1}{n} \ln C_e \tag{7}$$

$$\text{Temkin} \quad Q_e = b \ln K_T + b \ln C_e \tag{8}$$

where, K_L (L mg^{-1}) is the Langmuir constant, Q_{max} is the maximum adsorption capacity at saturation (mg g^{-1}), n is the Freundlich constant which refers to the degree of nonlinearity between the dye concentration and adsorption process: if $n = 1$, then adsorption is linear; if $n < 1$, then adsorption is a chemical process; if $n > 1$, then adsorption is a physical process [32]. K_F is the Freundlich constant which is correlated to the maximum adsorption capacity. K_T is the Temkin isotherm constant which corresponds to the maximum binding energy and b is a constant related to the heat of sorption.

Validity of the models was verified by the good correlation with the empirical data. The best fit among the kinetic and isotherm models is assessed by the linear regression coefficient (R^2) value.

3. Results and discussion

3.1. Composites characterization

Surface morphology of PPDA and its composite with γ-Fe_2O_3 was investigated by SEM (Fig. 2) and the micrographs show a homogenous morphology in all cases with small granular nanoparticles agglomerated together to larger shapeless particles. The relatively uniform distribution of γ-Fe_2O_3 within PPDA matrix can be demonstrated by TEM (Fig. 3). It is clearly visible from Fig. 3B that γ-Fe_2O_3 particles are fully covered by PPDA and concentrated inside the PPDA globules.

EDX analysis was used to estimate the elemental composition of the neat PPDA and composites with different content of γ-Fe_2O_3 (Fig. 2). The composite particles contained 0.1 to 12.6 wt% of iron particles. It should be noted that EDX characterized the surface of the materials, thus TGA was performed to obtain the content of γ-Fe_2O_3 in the bulk. The content of γ-Fe_2O_3 from TGA is 2, 7, and 45 wt% for PPDA/γ-Fe_2O_3/12.5, PPDA/γ-Fe_2O_3/25 and PPDA/γ-Fe_2O_3/50, respectively. This result suggests that γ-Fe_2O_3 particles are fully covered by PPDA.

The neat PPDA has the low conductivity, 1.0×10^{-12} S cm^{-1}, which increased two orders of magnitude by increasing the content of the γ-Fe_2O_3 in the sample (Table 1). This could be due to the presence of iron oxide nanoparticles which can act as a dopant to enhance the electrical conductivity of PPDA [33].

The solubility results revealed that PPDA is insoluble in water and in the acidic solutions. This behaviour suggests that PPDA can be used as adsorbent [34]. It is connected with possible ladder structure of prepared PPDA (Fig. 1B) with higher aromaticity. The second possible structure is represented by partial ladder structure (Fig. 1A) and its possess higher solubility in common organic solvents compared to the ladder one [35,36].

The specific surface area and the total micropore volume of the samples may have a great effect on their adsorption behaviour. The specific surface area (S_{BET}) values are presented in Table 1. S_{BET} varied from 56.1–70.6 m^2 g^{-1}, the highest value was obtained for composite PPDA/γ-Fe_2O_3/25, at the same time it possesses the highest micropore volume. S_{BET} suggests that PPDA/γ-Fe_2O_3/25 composite should have high dye adsorption compared to the others composites.

XRD patterns of the samples are depicted in Fig. 4. In the neat γ-Fe_2O_3, the presence of the γ-Fe_2O_3 phase was confirmed. This phase was also found in the composites PPDA/γ-Fe_2O_3/25 and PPDA/γ-Fe_2O_3/50. In the composite with lower amount of γ-Fe_2O_3, PPDA/γ-Fe_2O_3/12.5, the γ-Fe_2O_3 phase was not observed. Instead of it, the PPDA crystalline phase was found at $2\theta = 43^\circ$. Mean sizes of the crystallites of the γ-Fe_2O_3 phase were calculated for the samples γ-Fe_2O_3 and PPDA/γ-Fe_2O_3/50 and the values are 6 and 10 nm, respectively.

The saturation magnetizations of all measured materials (Table 2,

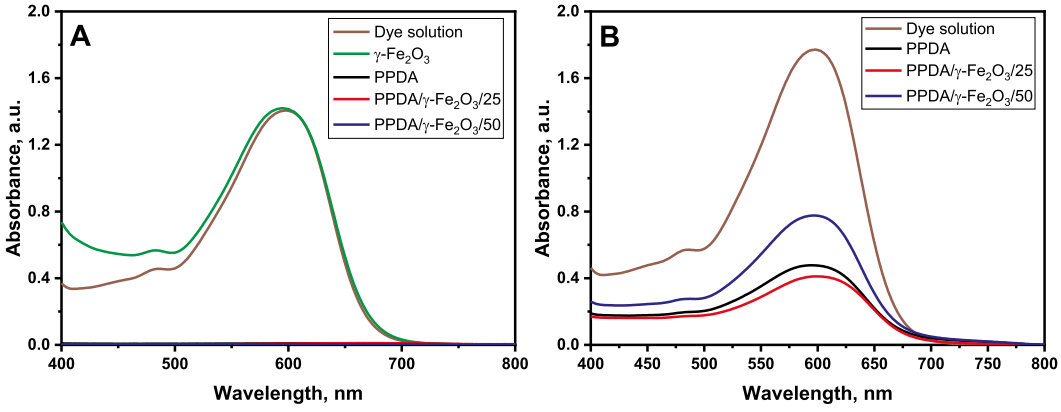

Fig. 6. UV-Vis spectra of 30 mg L^{-1} (A) and 50 mg L^{-1} (B) of Reactive Black 5 solution before and after contact with 20 mg of poly(*p*-phenylenediamine), its composite with maghemite and neat maghemite.

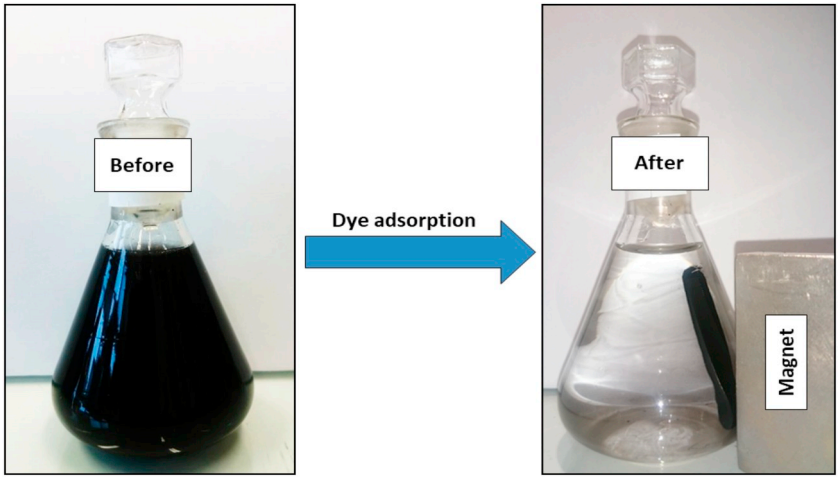

Fig. 7. Aqueous solution of Reactive Black 5 before and after adsorption by poly(*p*-phenylenediamine)maghemite/50 composite and separation by an external magnet.

Fig. 5) are in a good agreement with the TGA and EDX analyses. PPDA/γ-Fe_2O_3/12.5 showed the lowest, almost negligible value of 4.3×10^{-2} $Am^2\,kg^{-1}$ (higher than diamagnetic PPDA without any presence of Fe). In all the samples a slight remanent magnetization and coercivity can be observed. The correction for linear paramagnetic (PPDA sample) part was done in the field range above 5000 Oe (397.9 kA m^{-1}). The hysteresis loops of PPDA/γ-Fe_2O_3/25 and neat PPDA samples are not closed at −795.7 kA m^{-1}. This can be due to the motion of the powder particles in the holder. However, the error is negligible; the resulting parameters are averaged from the ascending and descending branch. The remagnetization curves were also measured and they showed remanent magnetization removed after application of increasing field in the direction opposite to the saturation remanence. In case of non-interacting superparamagnetic particles remanent magnetization should be zero. In our samples, saturation remanence was well determined and removed by the back-field.

3.2. Adsorption affinity of Reactive Black 5 to poly(p-henylenediamine)/maghemite composites

Adsorption efficiency of PPDA and its composites for the removal of RB from aqueous solution was studied. The composite PPDA/γ-Fe_2O_3/12.5 was not considered for the adsorption experiments, since it has very poor magnetic properties, and the same S_{BET} value as PPDA. Fig. 6A shows that γ-Fe_2O_3 itself has no affinity towards adsorption of RB, and all other composites (PPDA/γ-Fe_2O_3/25 and PPDA/γ-Fe_2O_3/50) adsorb RB with 100% dye uptake at the conditions of 30 mg L^{-1} dye concentration at pH 7. To differentiate between adsorption capacities of the composites with different contents of γ-Fe_2O_3, higher dye concentration was used (50 mg L^{-1}). Fig. 6B shows that PPDA/γ-Fe_2O_3/25 has the highest adsorption capacity towards the RB dye, followed by pure PPDA and the lowest was of PPDA/γ-Fe_2O_3/50. The results are in good agreement with specific surface area and wt% of active PPDA phase in the composites, where 93 and 55% of the weight is effective for the adsorption for PPDA/γ-Fe_2O_3/25 and PPDA/γ-Fe_2O_3/50, respectively. Doped (positively charged) PPDA can easily adsorb the anionic RB dye by electrostatic attraction in addition to the π-π stacking of aromatic rings. Fig. 7 shows a complete removal of RB (30 mg L^{-1}) by PPDA/γ-Fe_2O_3/50 composite that was perfectly separated by an external magnet.

An effect of contact time on the adsorption of RB was also studied; 20 mg of PPDA and its composites (PPDA, PPDA/γ-Fe_2O_3/25 and PPDA/γ-Fe_2O_3/50) were brought into a contact with a RB solution (50 ml, 40 mg L^{-1}). All samples showed rapid dye adsorption during the initial stage of the adsorption process, with time (contact time) the adsorption process proceeded at a relatively slow speed till reaching an equilibrium (Fig. 8B). PPDA/γ-Fe_2O_3/25 sample achieved the equilibrium faster than PPDA and the lowest rate was in case of PPDA/γ-Fe_2O_3/50. PPDA/γ-Fe_2O_3/25 with the highest S_{BET} and the largest micropore volume (Table 1) allows the dye molecules to diffuse faster. At these particular conditions, PPDA and PPDA/γ-Fe_2O_3/25 attained 100% RB dye removal in 2 hours compared to 93% in case of PPDA/γ-Fe_2O_3/50 achieved after 6 hours.

Pseudo-first-order (Fig. 8D), pseudo-second-order (Fig. 8E) and intraparticle diffusion (Fig. 8F) models were plotted to study the fitting and to estimate the rate of RB removal from the solution, the results are summarized in Table 3. According to correlation coefficient (R^2), the adsorption of RB by neat PPDA and PPDA/γ-Fe_2O_3/25 follows the pseudo-second-order kinetics which implies that two reactions, either in series or in parallel, are occurring; the first one is fast and quickly reaches an equilibrium, while the second is a slower reaction that continues for a long period of time [37]. However, PPDA/γ-Fe_2O_3/50 follows the pseudo-first-order kinetics which indicates that the reaction is more inclined towards physisorption. Moreover, the plots of Q_t versus $t^{1/2}$ (the intraparticle diffusion model) suggest that the adsorption is highly controlled by the intraparticle diffusion with a rate constant k_i calculated from the slope. A very low value of the intercept (c) suggests that surface diffusion has very low activation energy.

In order to study the adsorption isotherms, a series of adsorption experiments was performed with different initial concentrations of RB solutions, in which the same weight of the adsorbents (20 mg) was kept for 24 h to attain an equilibrium. Table 4 summarizes the results obtained from the fitting plots (Fig. 9). The correlation coefficient (R^2) value is used to judge the fitting which suggests that Langmuir model is the best to represent the adsorption. Langmuir model assumes a homogenous surface of an adsorbent with equivalent energy of adsorption sites. Moreover, enthalpy of adsorption is assumed to be independent of the amount of the molecules adsorbed. This leads to formation of a monolayer of the dye molecules on the surface of the adsorbent; one binding site can adsorb only one dye molecule with a maximum adsorption capacity (Q_{max}). The estimated Q_{max} value of neat PPDA is 185.2 mg g^{-1} which was enhanced for PPDA/γ-Fe_2O_3/25 with the value 232 mg g^{-1}, however, PPDA/γ-Fe_2O_3/50 had only 123.2 mg g^{-1}. The fitting to Freundlich model suggested a favourable adsorption process [32], the values of n are in the range of 8.51 to 9.74 (Table 4). Temkin isotherm assumes that the enthalpy of all adsorbate (RB) molecules decreases linearly with the interaction. The value of b (constant related to the heat of adsorption) in the range of 11.2 to 21.6 J mol^{-1} suggests the physical adsorption process.

Langmuir model represents the equilibrium distribution of dye

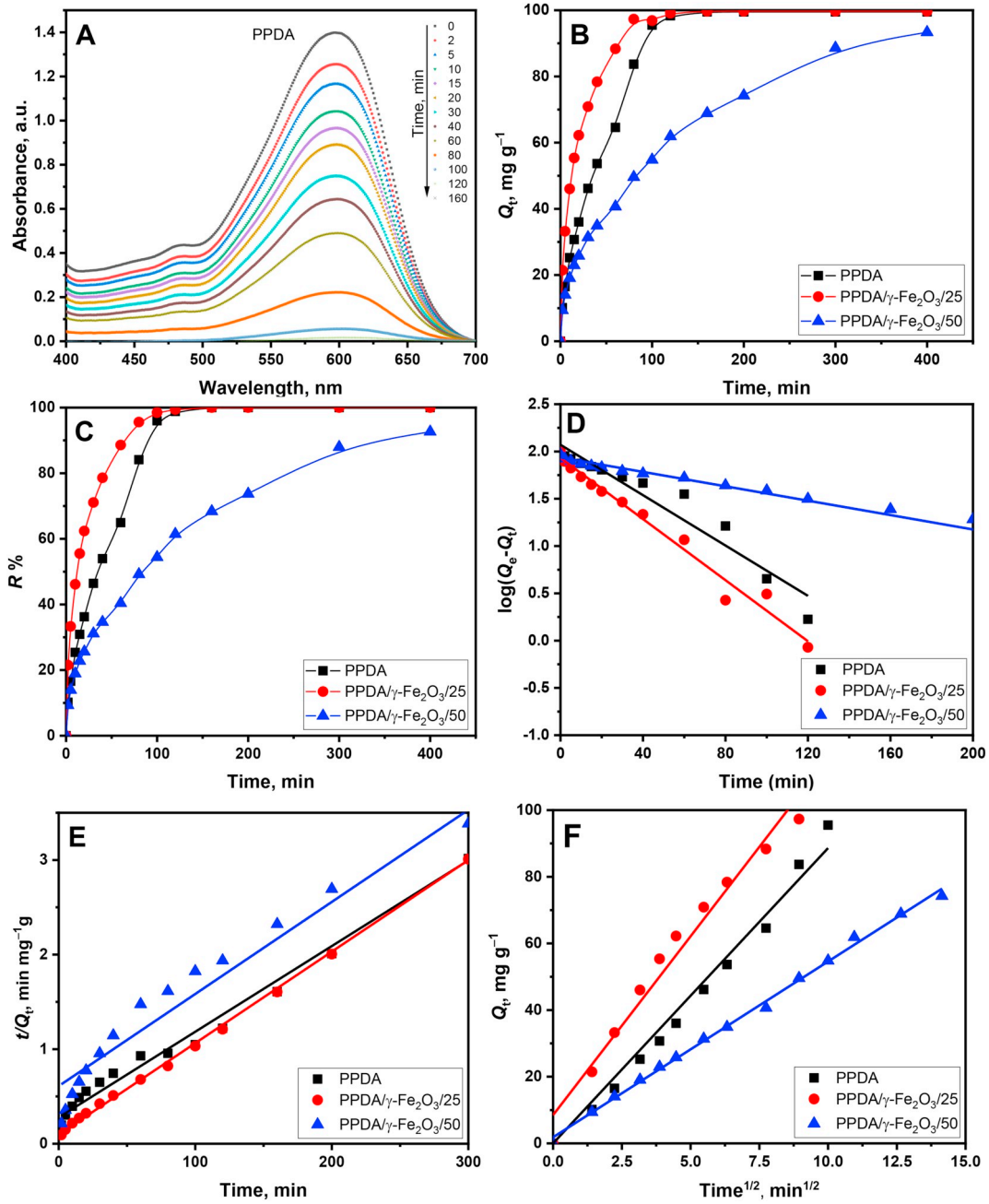

Fig. 8. UV-Vis spectra of the absorption of Reactive Black 5 (20 mg, pH 7) onto poly(*p*-phenylenediamine) with time (A), effect of contact time on the removal of Reactive Black 5 (40 mg L^{-1}, 50 mL) by poly(*p*-phenylenediamine) and its composites (B), removal efficiency of the dye (C), pseudo-first-order kinetics (D), pseudo-second-order kinetics (E), intraparticle diffusion (F) modeling.

Table 3
Adsorption kinetic parameters.

Sample code	Pseudo-first-order			Pseudo-second-order			Intraparticle diffusion		
	k_1, min^{-1}	Q_e, mg g^{-1}	R^2	k_2, g mg^{-1} min^{-1}	Q_e, mg g^{-1}	R^2	k_i, mg g^{-1} min$^{-1/2}$	c, mg g^{-1}	R^2
PPDA	0.0306	117.68	0.933	0.0003	110.38	0.991	9.5	0.0	0.990
PPDA/γ-Fe_2O_3/25	0.0306	85.51	0.979	0.001	103.31	0.999	10.73	8.48	0.973
PPDA/γ-Fe_2O_3/50	0.0088	86.30	0.986	0.0002	102.67	0.966	5.28	1.83	0.997

molecules between the solid and liquid phases. The essential characteristic of the Langmuir isotherm can be expressed in terms of a dimensionless constant (separation factor or equilibrium parameter, R_L) which is expressed as:

$$R_L = 1/(1 + K_L C_0) \quad (9)$$

where C_o (mg L^{-1}) is the initial adsorbate concentration, K_L (L mg^{-1}) is the Langmuir constant related to the energy of adsorption. The value of R_L indicates the shape of the isotherm to be either

Table 4
Equilibrium isotherms parameters.

Sample code	$Q_{m,\ exp}$, mg g^{-1}	Langmuir model			Freundlich model			Temkin model		
		Q_{max}, mg g^{-1}	K_L, L mg^{-1}	R^2	K_F, mg g^{-1}	n	R^2	K_T, L g^{-1}	b, J mol^{-1}	R^2
PPDA	184.4	185.2	0.454	0.989	119.64	9.74	0.424	194.2	15.55	0.385
PPDA/γ-Fe_2O_3/25	193.8	232.0	0.365	0.995	135.84	8.51	0.953	522.8	21.06	0.924
PPDA/γ-Fe_2O_3/50	141.8	123.2	0.233	0.961	71.88	8.56	0.179	542.3	11.20	0.134

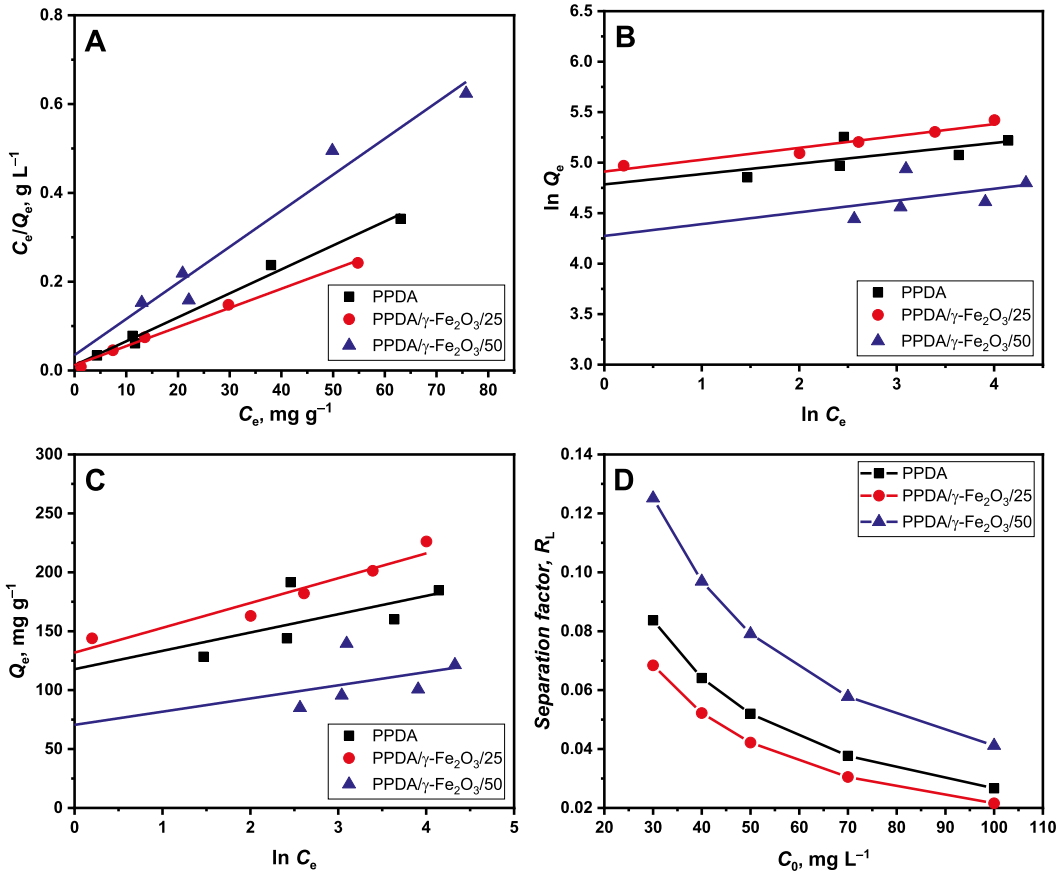

Fig. 9. Adsorption isotherms of Reactive Black 5 by poly(*p*-phenylenediamine) and its composites, Langmuir (A), Freundlich (B), Temkin (C) and Langmuir separation factor (D).

unfavourable ($R_L > 1$), linear ($R_L = 1$), favourable ($0 < R_L < 1$), or irreversible ($R_L = 0$). Lower R_L value reflects that adsorption is more favourable.

For all the materials the results showed that R_L values were in the range of 0.02 to 0.125, which indicate that the adsorption of RB onto PPDA is a very favourable process [31]. Fig. 9 D shows that R_L value is decreased by increasing the initial concentrations of RB. Moreover, the lowest R_L value was found for PPDA/γ-Fe_2O_3/25 composites reflecting the most favourable adsorption process.

3.2.1. Comparison to other adsorbents' capacities

Polypyrrole and its composites [38,39], and polyaniline and its derivatives (phenylenediamines) [40] have been widely used for removal of heavy metal ions and dyes. Polyaniline and its composites have been used for the removal of different anionic dyes from aqueous solutions by adsorption [41–43]. For example, polyaniline nanofibers showed a high adsorption capacity of RB 5 [43]. Poly(o-phenylenediamine) and poly(m-phenylenediamine) have been extensively used in water purification. They are strong heavy-metal-ions sorbents [44,45]. Moreover, poly(m-phenylenediamine) magnetic composites with graphene oxide and nickel ferrite exhibit excellent removal ability of dyes as Congo Red, methyl orange and methyl blue [46]. Table 5 summarizes the adsorption capacity of various natural, inorganic and synthetic adsorbents from previous studies. Comparison of PPDA and its composites with γ-Fe_2O_3 to those in the literature reveals that PPDA/γ-Fe_2O_3/25 possesses relatively high adsorption capacity of 223 mg g^{-1} for RB with magnetically separable behaviour. For instance, composite of core-shell Fe_3O_4@PANI showed only 63.7 mg g^{-1} [42] adsorption capacity for RB at similar adsorption conditions.

3.2.2. FTIR and Raman spectroscopy

The FTIR spectrum of PPDA (Fig. 10) shows characteristic bands at 1573 cm^{-1} and 1505 cm^{-1} which can be assigned to the stretching vibrations of quinoid and benzenoid units respectively. The band at 1415 cm^{-1} is linked to phenazine-like segments. The stretching vibrations of the C-N group in benzenoid rings are linked to the band at 1297 cm^{-1}. The deformation vibration of the C-H group in the rings is then reflected as the band at 1171cm^{-1}. The out-of-plane deformation vibration of the C-H groups are then assigned to the band at 830 cm^{-1} [56,57]. These spectral bands of PPDA are virtually unchanged in the samples of PPDA prepared in the presence of γ-Fe_2O_3, as the chemical structure of PPDA is not influenced by γ-Fe_2O_3. The two bands at 628

Table 5
Comparison of adsorption capacity (Q_{max}) of various natural, inorganic and synthetic adsorbents for Reactive Black 5.

Adsorbent	Adsorption capacity, mg g^{-1}	References
Core-shell magnetic adsorbent (Fe_3O_4@PANI)	63.7	[42]
Polyaniline nanofibers	312.5	[43]
Activated carbon powder	58.8	[47]
Fly ash	7.9	
Activated carbons F400	198.0	[48]
Bone char	160.0	
BACX2	286.0	
BACX6	473.0	
Al_2O_3@TiO_2 nanocomposite	322.6	[49]
Walnut activated carbon	19.3	[50]
Activated red mud	35.6	[51]
Chitosan/polyamide nanofibers	198.6	[52]
Polyhydroxyl dendrimer magnetic nanoparticles	62.1	[53]
Multi-walled carbon nanotube, at natural pH	36.2	[54]
ZnO nanoparticles	27.6	[55]

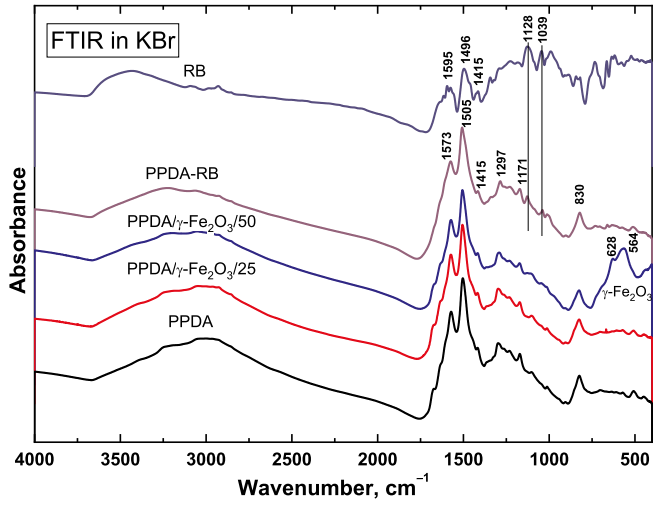

Fig. 10. FTIR spectra measured in KBr pellets of Reactive Black 5, poly(*p*-phenylenediamine), poly(*p*-phenylenediamine) with different concentrations of maghemite and poly(*p*-phenylenediamine)/Reactive Black 5.

and 564 cm^{-1} from the spectrum of γ-Fe_2O_3 are present in the spectrum of the sample PPDA/γ-Fe_2O_3/50. However, the presence of γ-Fe_2O_3 is not reflected in the spectrum of the PPDA/γ-Fe_2O_3/25, due to difficulties with proper dispersion of rigid γ-Fe_2O_3 particles in the KBr pellets or low content of γ-Fe_2O_3 in the composite (≈7wt% according to TGA) to be estimated by infrared spectroscopy.

As the RB molecule includes several aromatic amine units, the FTIR spectrum of RB has some of spectral features resembling the spectrum of PPDA (Fig. 10). However, based on the bands at 1128 cm^{-1} and 1044 cm^{-1} assigned to the stretching vibration of C-O group and sulfonate ions respectively [58], it is possible to distinguish between both molecules. The band at 1044 cm^{-1} is slightly shifted to 1039 cm^{-1} after adsorption of RB onto PPDA, which suggests the interaction of dye with PPDA *via* the sulfonate groups.

Raman spectrum of PPDA at 514 nm (Fig. 11), showed the bands at 1600 cm^{-1} and 1535 cm^{-1} which are assigned to the C=C and C=N vibration in the quinoid rings respectively. The band at 1328 cm^{-1} reflects the stretching vibrations of C-N group in radical cations. The stretching vibration of C-N group connected to the benzenoid ring is linked to the band at 1238 cm^{-1}. The broad band connected to the vibrations n(C-N) and d(C-H) is located at 1191 cm^{-1} [56,57]. Similar to the FTIR spectra, the position and shape of the bands from the PPDA

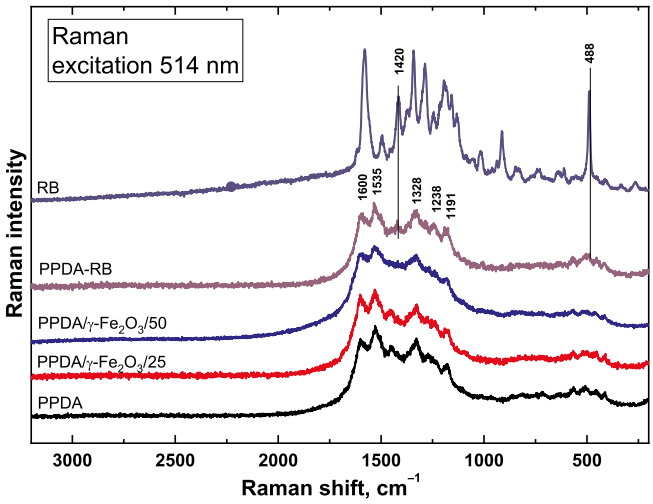

Fig. 11. Raman spectra at 514 nm of Reactive Black 5, poly(*p*-phenylenediamine), poly(*p*-phenylenediamine) with different concentrations of maghemite and poly(*p*-phenylenediamine)/Reactive Black 5.

spectrum remain unchanged in the spectra of the composites. In contrast to the FTIR spectrum of the PPDA/γ-Fe_2O_3/50, the spectral features of γ-Fe_2O_3 are not observed in the Raman spectrum and we can assume that the γ-Fe_2O_3 particles are fully covered by PPDA as the Raman spectroscopy is surface sensitive method.

Reactive Black 5 is in resonance with the green laser wavelength 514 nm; the Raman spectrum is intensive and the bands are relatively well separated. The strong band at 488 cm^{-1} linked to the CC deformation vibration in naphthalene ring is located in the region where the spectrum of PPDA is relatively featureless. The spectrum of the neat PPDA shows the band at 1422 cm^{-1}, assigned to the stretching vibrations of aromatic amines, and the shoulder at 488 cm^{-1} on the band at 505 cm^{-1} which could be assigned to RB [59].

4. Conclusions

Facile preparation of PPDA and its composites with different contents of γ-Fe_2O_3 was successfully achieved. TEM analysis, FTIR and Raman spectra proved the incorporation of γ-Fe_2O_3 nanoparticles into the PDDA matrix. The introduction of γ-Fe_2O_3 into the PPDA matrix was used to ease the material separation after adsorption of Reactive Black 5 dye and enhancing the adsorption capacity. The adsorption of RB onto PPDA and its composites follows Langmuir isotherm model with maximum adsorption monolayer capacities of 185.2, 233 and 123 mg g^{-1} for PPDA, PPDA/γ-Fe_2O_3/25 and PPDA/γ-Fe_2O_3/50, respectively. Separation factor (R_L) values and Freundlich constant (n) values suggest favourable adsorption processes of all the studied materials.

Acknowledgments

The authors wish to thank the Czech Science Foundation (18-04669S) for the financial support.

Declaration of Competing Interest

There are no conflicts to declare.

References

[1] R.P. Schwarzenbach, T. Egli, T.B. Hofstetter, U.V. Gunten, B. Wehrli, Global water pollution and human health, Annu. Rev. Env. Resour. 35 (2010) 109–136.
[2] S.K. Gunatilake, Methods of removing heavy metals from industrial wastewater, Methods 1 (2015) 14.
[3] V.K. Gupta, R. Jain, A. Nayak, S. Agarwal, M. Shrivastava, Removal of the

hazardous dye—tartrazine by photodegradation on titanium dioxide surface, Mat. Sci. Eng. C 31 (2011) 1062–1067.
[4] T.A. Saleh, V.K. Gupta, Photo-catalyzed degradation of hazardous dye methyl orange by use of a composite catalyst consisting of multi-walled carbon nanotubes and titanium dioxide, J. Colloid Interface Sci. 371 (2012) 101–106.
[5] R. Saravanan, E. Sacari, F. Gracia, M.M. Khan, E. Mosquera, V.K. Gupta, Conducting PANI stimulated ZnO system for visible light photocatalytic degradation of coloured dyes, J. Mol. Liq. 221 (2016) 1029–1033.
[6] R. Saravanan, S. Karthikeyan, V.K. Gupta, G. Sekaran, V. Narayanan, A.J.M.S. Stephen, Enhanced photocatalytic activity of ZnO/CuO nanocomposite for the degradation of textile dye on visible light illumination, Mat. Sci. Eng. C 33 (2013) 91–98.
[7] I. Ali, M. Asim, T.A. Khan, Low cost adsorbents for the removal of organic pollutants from wastewater, J. Environ. Manage. 113 (2012) 170–183.
[8] A. Mittal, J. Mittal, A. Malviya, V.K. Gupta, Removal and recovery of Chrysoidine Y from aqueous solutions by waste materials, J. Colloid Interface Sci. 344 (2010) 497–507.
[9] J. Zhang, J. Han, M. Wang, R. Guo, Fe_3O_4/PANI/MnO_2 core–shell hybrids as advanced adsorbents for heavy metal ions, J. Mater. Chem. A 5 (2017) 4058–4066.
[10] M.M. Ayad, W.A. Amer, S. Zaghlol, I.M. Minisy, P. Bober, J. Stejskal, Polypyrrole-coated cotton textile as adsorbent of methylene blue dye, Chem. Pap. 72 (2018) 1605–1618.
[11] K. Gong, S. Guo, Y. Zhao, Q. Hu, H. Liu, D. Sun, M. Li, B. Qiu, Z. Guo, Bacteria cell templated porous polyaniline facilitated detoxification and recovery of hexavalent chromium, J. Mater. Chem. A 6 (2018) 16824–16832.
[12] A. Almasian, M. Giahi, G.C. Fard, S.A. Dehdast, L. Maleknia, Removal of heavy metal ions by modified PAN/PANI-nylon core-shell nanofibers membrane: Filtration performance, antifouling and regeneration behavior, Chem. Eng. J. 351 (2018) 1166–1178.
[13] N. Jian, L. Qian, C. Wang, R. Li, Q. Xu, J. Li, Novel nanofibers mat as an efficient, fast and reusable adsorbent for solid phase extraction of non-steroidal anti-inflammatory drugs in environmental water, J. Hazard. Mater. 363 (2019) 81–89.
[14] I.M. Minisy, N.A. Salahuddin, M.M. Ayad, Chitosan/polyaniline hybrid for the removal of cationic and anionic dyes from aqueous solutions, J. App. Polym. Sci. 136 (2019) 47056.
[15] S. Yang, D. Liu, F. Liao, T. Guo, Z. Wu, T. Zhang, Synthesis, characterization, morphology control of poly(*p*-phenylenediamine)-Fe_3O_4 magnetic micro-composite and their application for the removal of $Cr_2O_7^{2-}$ from water, Synth. Met. 162 (2012) 2329–2336.
[16] L. Mdlalose, M. Balogun, K. Setshedi, M. Tukulula, L. Chimuka, A. Chetty, Synthesis, characterization and optimization of poly(*p*-phenylenediamine)-based organoclay composite for Cr(VI) remediation, Appl. Clay Sci. 139 (2017) 72–80.
[17] Y.-L. Min, T. Wang, Y.-G. Zhang, Y.-C. Chen, The synthesis of poly(*p*-phenylenediamine) microstructures without oxidant and their effective adsorption of lead ions, J. Mater. Chem. 21 (2011) 6683–6689.
[18] K.Z. Elwakeel, A.S. Al-Bogami, Influence of Mo(VI) immobilization and temperature on As(V) sorption onto magnetic separable poly *p*-phenylenediamine-thiourea-formaldehyde polymer, J. Hazard. Mater. 342 (2018) 335–346.
[19] A. Targhoo, A. Amiri, M. Baghayeri, Magnetic nanoparticles coated with poly(*p*-phenylenediamine-co-thiophene) as a sorbent for preconcentration of organophosphorus pesticides, Microchim. Acta. 185 (2018) 15.
[20] Z. Mehrani, H. Ebrahimzadeh, A.A. Asgharinezhad, Synthesis and characterization of a poly(*p*-phenylenediamine)-based electrospun nanofiber for the micro-solid-phase extraction of organophosphorus pesticides from drinking water and lemon and orange juice samples, J. Sep. Sci. 41 (2018) 3477–3485.
[21] P. Magdziarz, P. Bober, M. Trchová, Z. Morávková, M. Bláha, J. Prokeš, J. Stejskal, Conducting composites prepared by the reduction of silver ions with poly(*p*-phenylenediamine), Poly. Int. 64 (2015) 496–504.
[22] J. Stejskal, Polymers of phenylenediamines, Prog. Polym. Sci. 41 (2015) 1–31.
[23] Z. Liu, H. Zhou, Z. Huang, W. Wang, F. Zeng, Y. Kuang, Graphene covalently functionalized with poly(*p*-phenylenediamine) as high performance electrode material for supercapacitors, J. Mater. Chem. A 1 (2013) 3454–3462.
[24] C. Hu, Y. Shi, C. Sun, S. Liang, S. Bao, M. Pang, Facile preparation of ion-doped poly (*p*-phenylenediamine) nanoparticles for photothermal therapy, Chem. Commun. 54 (2018) 4862–4865.
[25] M. Baghayeri, E.N. Zare, M.M. Lakouraj, A simple hydrogen peroxide biosensor based on a novel electro-magnetic poly(*p*-phenylenediamine)@Fe_3O_4 nanocomposite, Biosens. Bioelectron. 55 (2014) 259–265.
[26] P. Bober, B.A. Zasonska, P. Humpolíček, Z. Kuceková, M. Varga, D. Horák, V. Babayan, N. Kazantseva, J. Prokeš, J. Stejskal, Polyaniline-maghemite based dispersion: electrical, magnetic properties and their cytotoxicity, Synth. Met. 214 (2016) 23–29.
[27] B.A. Zasońska, P. Bober, P. Jošt, E. Petrovský, P. Boštík, D. Horák, Magnetoconductive maghemite core/polyaniline shell nanoparticles: Physico-chemical and biological assessment, Colloid. Surface. B 141 (2016) 382–389.
[28] B.A. Zasońska, U. Acharya, J. Pfleger, P. Humpolíček, J. Vajďák, J. Svoboda, E. Petrovsky, J. Hromádková, Z. Walterová, P. Bober, Multifunctional polypyrrole@maghemite@silver composites: synthesis, physico-chemical characterization and antibacterial properties, Chem. Pap. 72 (2018) 1789–1797.
[29] T. Plachy, M. Sedlacik, V. Pavlinek, Z. Morávková, M. Hajná, J. Stejskal, An effect of carbonization on the electrorheology of poly (*p*-phenylenediamine), Carbon 63 (2013) 187–195.
[30] X.G. Li, X.L. Ma, J. Sun, M.R. Huang, Powerful reactive sorption of silver (I) and mercury (II) onto poly (*o*-phenylenediamine) microparticles, Langmuir 25 (3) (2009) 1675–1684.
[31] K.Y. Foo, B.H. Hameed, Insights into the modelling of adsorption isotherm systems, Chem. Eng. J. 156 (2010) 2–10.
[32] T. Karthikeyan, S. Rajgopal, L.R. Miranda, Chromium (VI) adsorption from aqueous solution by Hevea Brasilinesis sawdust activated carbon, J. Hazard. Mater. 124 (2005) 192–199.
[33] M.M. Lakouraj, E.N. Zare, P.N. Moghadam, Synthesis of novel conductive poly (*p*-phenylenediamine)/Fe_3O_4 nanocomposite via emulsion polymerization and investigation of antioxidant activity, Adv. Polym. Tech. 33 (2014) 21385.
[34] J.J. Wang, J. Jiang, B. Hu, S.H. Yu, Uniformly shaped Poly (*p*-phenylenediamine) microparticles: Shape-controlled synthesis and their potential application for the removal of lead ions from water, Adv. Funct. Mater. 18 (7) (2008) 1105–1111.
[35] X.G. Li, W. Duan, M.R. Huang, Y.L. Yang, D.Y. Zhao, Preparation and solubility of a partial ladder copolymer from *p*-phenylenediamine and *o*-phenetidine, Polymer 44 (20) (2003) 6273–6285.
[36] X.G. Li, M.R. Huang, R.F. Chen, Y. Jin, Y.L. Yang, Preparation and characterization of poly (p-phenylenediamine-co-xylidine), J. Appl. Polym. Sci. 81 (13) (2001) 3107–3116.
[37] Y. Khambhaty, K. Mody, S. Basha, B. Jha, Kinetics, equilibrium and thermodynamic studies on biosorption of hexavalent chromium by dead fungal biomass of marine Aspergillus niger, Chem. Eng. J. 145 (2009) 489–495.
[38] J. Li, J. Feng, W. Yan, Excellent adsorption and desorption characteristics of polypyrrole/TiO2 composite for Methylene Blue, Appl. Surf. Sci. 279 (2013) 400–408.
[39] H.N.M.E. Mahmud, A.O. Huq, R. binti Yahya, The removal of heavy metal ions from wastewater/aqueous solution using polypyrrole-based adsorbents: a review, RSC Adv. 6 (18) (2016) 14778–14791.
[40] E.N. Zare, A. Motahari, M. Sillanpää, Nanoadsorbents based on conducting polymer nanocomposites with main focus on polyaniline and its derivatives for removal of heavy metal ions/dyes: a review, Environ. Res. 162 (2018) 173–195.
[41] D. Mahanta, G. Madras, S. Radhakrishnan, S. Patil, Adsorption of sulfonated dyes by polyaniline emeraldine salt and its kinetics, J. Phys. Chem. B 112 (33) (2008) 10153–10157.
[42] B.K. Farahani, M. Hamzehloo, R. Rostamian, Adsorption behaviour of Reactive Black dye 5 by magnetically separable nano-adsorbent, Phys. Chem. Res. 7 (2019) 475–490.
[43] M. Bhaumik, R.I. McCrindle, A. Maity, S. Agarwal, V.K. Gupta, Polyaniline nanofibers as highly effective re-usable adsorbent for removal of Reactive Black 5 from aqueous solutions, J. Colloid Interf. Sci. 466 (2016) 442–451.
[44] R. Tang, Q. Li, L. Ding, H. Cui, J. Zhai, Reactive sorption of mercury (II) on to poly (m-phenylenediamine) microparticles, Environ. Technol. 33 (3) (2012) 341–348.
[45] M.R. Huang, Q.Y. Peng, X.G. Li, Rapid and effective adsorption of lead ions on fine poly (phenylenediamine) microparticles, Chem-Eur. J. 12 (16) (2006) 4341–4350.
[46] W. Wang, K. Cai, X. Wu, X. Shao, X. Yang, A novel poly (*m*-phenylenediamine)/reduced graphene oxide/nickel ferrite magnetic adsorbent with excellent removal ability of dyes and Cr (VI), J. Alloy. Compd. 722 (2017) 532–543.
[47] Z. Eren, F.N. Acar, Adsorption of Reactive Black 5 from an aqueous solution: equilibrium and kinetic studies, Desalination 194 (2006) 1–10.
[48] A.W.M. Ip, J.P. Barford, G.A. McKay, Comparative study on the kinetics and mechanisms of removal of Reactive Black 5 by adsorption onto activated carbons and bone char, Chem. Eng. J. 157 (2010) 434–442.
[49] H. Deng, M. Zhang, Y. Cao, Y. Lin, Decolorization of Reactive Black 5 by mesoporous Al_2O_3@TiO_2 nanocomposites, Environ. Prog. Sustain. 38 (2019) S230–S242.
[50] B. Heibati, S. Rodriguez-Couto, A. Amrane, M. Rafatullah, A. Hawari, M.A. Al-Ghouti, Uptake of Reactive Black 5 by pumice and walnut activated carbon: chemistry and adsorption mechanisms, J. Ind. Eng. Chem. 20 (2014) 2939–2947.
[51] M. Shirzad-Siboni, S.J. Jafari, O. Giahi, I. Kim, S. Lee, J. Yang, Removal of acid blue 113 and Reactive Black 5 dye from aqueous solutions by activated red mud, J. Ind. Eng. Chem. 20 (2014) 1432–1437.
[52] Z. Li, L. Sellaoui, G.L. Dotto, A.B. Lamine, A. Bonilla-Petriciolet, H. Hanafy, A. Erto, Interpretation of the adsorption mechanism of Reactive Black 5 and Ponceau 4R dyes on chitosan/polyamide nanofibers via advanced statistical physics model, J. Mol. Liq. 285 (2019) 165–170.
[53] M.M. Galangash, A. Ghavidast, Z. Bozorgpanah, Adsorption of Acid Red 114 and Reactive Black 5 in aqueous solutions on dendrimer-conjugated magnetic nanoparticles, J. Chin. Chem. Soc. 66 (2019) 62–74.
[54] M.T. Samadi, H. Zolghadrnasab, K. Godini, A. Poormohammadi, M. Ahmadian, S. Shanesaz, Kinetic and adsorption studies of Reactive Black 5 removal using multi-walled carbon nanotubes from aqueous solution, Der. Pharma Chem. 7 (2015) 267–274.
[55] Z.M. Khoshhesab, K. Gonbadi, G.R. Behbehani, Removal of Reactive Black 8 dye from aqueous solutions using zinc oxide nanoparticles: investigation of adsorption parameters, Desalin. Water Treat. 56 (2015) 1558–1565.
[56] R.H. Sestrem, D.C. Ferreira, R. Landers, M.L.A. Temperini, G.M. do Nascimento, Structure of chemically prepared poly-(*para*-phenylenediamine) investigated by spectroscopic techniques, Polymer 50 (2009) 6043–6048.
[57] M. Bláha, M. Trchová, Z. Morávková, P. Humpolíček, J. Stejskal, Semiconducting materials from oxidative coupling of phenylenediamines under various acidic conditions, Mater. Chem. Phys. 205 (2018) 423–435.
[58] G. Socrates, Infrared and Raman characteristic group frequencies, Wiley & Sons Ltd, Chichester UK, 2001.
[59] T. Aguayo, C. Garrido, R.E. Clavijo, J.S. Gómez-Jeria, M.C. Araya, M. Icaza, M.F. Espinoza, V.M.M. Campos, Raman and surface enhanced Raman scattering of a black dyed silk, J. Raman Spectrosc. 44 (2013) 1238–1245.

Appendix 8

Conducting polymer composite aerogel with magnetic properties for organic dye removal

Synthetic Metals 260 (2020) 116266

Contents lists available at ScienceDirect

Synthetic Metals

journal homepage: www.elsevier.com/locate/synmet

Conducting polymer composite aerogel with magnetic properties for organic dye removal

Patrycja Bober[a,*], Islam M. Minisy[a], Udit Acharya[a], Jiří Pfleger[a], Vladimir Babayan[b], Natalia Kazantseva[b], Jiří Hodan[a], Jaroslav Stejskal[a]

[a] Institute of Macromolecular Chemistry, Academy of Sciences of the Czech Republic, 162 06 Prague 6, Czech Republic
[b] Centre of Polymer Systems, Tomas Bata University in Zlin, 760 01 Zlin, Czech Republic

ARTICLE INFO

Keywords:
Polyaniline
Aerogel
Magnetic properties
Composites
Conductivity
Dye removal

ABSTRACT

Multifunctional conducting polyaniline/hexaferrite aerogels supported by poly(vinyl alcohol) have been prepared by simple one-step procedure. The incorporation of magnetic particles into aerogel matrix was successfully proven with scanning electron microscopy and by examination of magnetic properties. Such novel hybrid aerogels showed better resistance against elastic deformation when stress is applied, increased conductivity compared to neat polyaniline/poly(vinyl alcohol) cryogels, and also enhanced coercive force compared with neat hexaferrite due to increased effective magnetic anisotropy by magnetostriction. Moreover, the efficient adsorption of Reactive Black 5 dye by aerogel has been illustrated. Therefore, this work offers new type of macroporous dye adsorbents which can be efficiently separated from the aqueous medium and thus used for wastewater treatment.

1. Introduction

Electric and magnetic stimuli-responsive systems have attracted considerable attention during recent years due to a large array of applications including biosensors [1,2], magnetic-resonance-imaging contrast agents [3], supercapacitors [4,5], fuel cells [6,7], radio- and microwave absorbers [8] and electromagnetic-interference shielding materials [9–11]. Such materials contain, *e.g.*, magnetic particles (different types of ferrites, iron oxides, carbonyl iron, *etc.*) incorporated in conducting polymer matrix [12–20]. Besides, hybrid composites based on conducting polymers and magnetic particles can be employed in various water-treatment methods for the capture, transfer, and removal of organic dyes and heavy-metal ions from wastewater [21–27]. It is established, that the adsorbent capacity depends on its specific surface area and chemical nature of surface, as well as on adsorbent dosage, contact time, pollutant concentration, *etc*. The main advantage of magnetic adsorbents is that they can be rapidly and easily separated from water using a magnetic field.

Nowadays, with increased demand of textile products in human daily life, the reuse of wastewater containing dyes or heavy-metal ions in industry has become a worldwide environmental issue. Dyes and heavy-metals residues in wastewater are usually toxic, carcinogenic, mutagenic and inhibit the growth of aquatic biota. There are several treatment methods of their removal, like chemical oxidation, photocatalytic decomposition, filtration or adsorption. The preparation of new adsorbent materials with good selectivity, chemical and thermal stability, which could be easily and effectively separated using a low-cost technology, is the biggest challenge.

Conducting polymers, such as polyaniline or polypyrrole, have recently been investigated as materials for dye removal [28,29] by adsorption or photocatalytic decompostion. However, due to the poor processability and poor mechanical properties, their practical use is still limited. To overcome this problem, a new class of conducting composite materials represented by macroporous polyaniline cryogels and aerogels has recently been studied [30–33]. For most of the conducting polymer composites, the adsorption process is classified as physical sorption, hydrogen bonding, electrostatic or π–π interactions, *etc.* [34].

In the present work, we report the simple, one-step procedure for the preparation of polyaniline/poly(vinyl alcohol) composite aerogels containing hexaferrite particles. Such conducting and magnetic composites are macroporous and have good mechanical properties, they can be easily handled and prepared in desired shape. The ability of this new composite aerogel to remove organic dye from wastewater was also illustrated on example of anionic Reactive Black 5 dye. Moreover, we demonstrate the possibility to manipulate aerogel using static magnetic field as a proof-of-concept for effective removal of adsorbent from fluidic system (Fig. 1).

* Corresponding author.
E-mail address: bober@imc.cas.cz (P. Bober).

https://doi.org/10.1016/j.synthmet.2019.116266
Received 27 September 2019; Received in revised form 3 December 2019; Accepted 6 December 2019

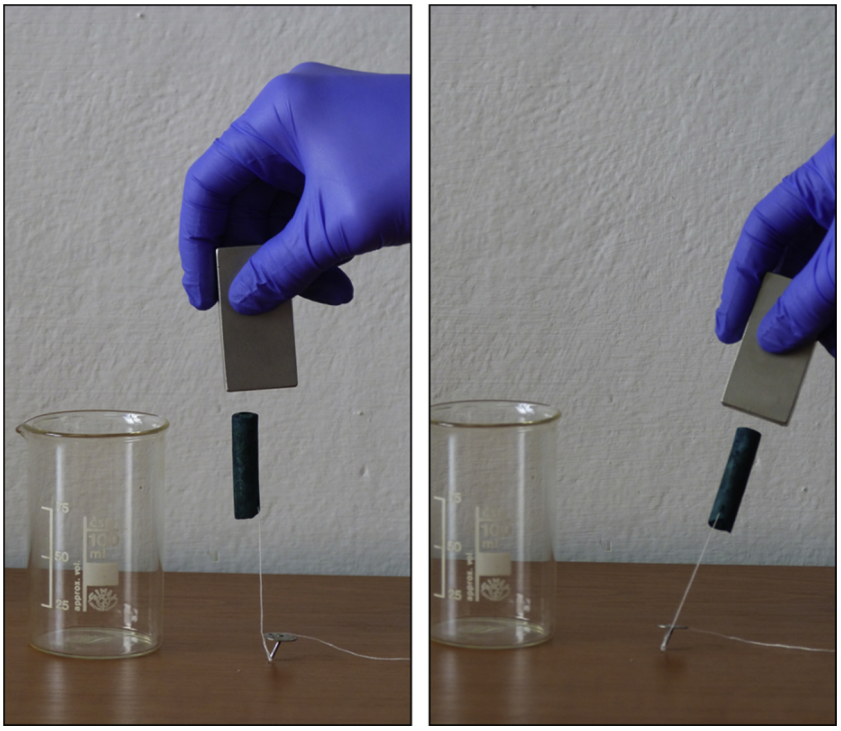

Fig. 1. Attraction of the polyaniline/poly(vinyl alcohol)/hexaferrite aerogel to permanent magnet.

2. Experimental

2.1. Preparation of aerogels

Polyaniline/poly(vinyl alcohol)/hexaferrite (PANI/PVAL/F) cryogels were prepared by oxidation of aniline hydrochloride (0.2 M; Penta, Czech Republic) with ammonium peroxydisulfate (0.25 M; Lach-ner, Czech Republic) in the presence of 5 wt.% of poly(vinyl alcohol) (Mowiol 10–98, Sigma-Aldrich; molecular weight 61,000) in aqueous suspension of hexaferrite particles (Ni_2SrCr_xW hexaferrite, Ferrite Domen Co., St. Petersburg, Russian Federation, 1 or 2 wt.%), at 25 °C. The mixture was sucked into a plastic syringe, quickly frozen in solid carbon dioxide/ethanol suspension, and then left in a freezer at −24 °C for 5 days to polymerize [30]. After thawing at room temperature, cryogels were removed from the syringe and immersed in excess of water to extract any residual reactants and by-products. Then PANI/PVAL/F aerogel was obtained by freeze-drying of corresponding cryogels.

2.2. Removal of organic dye

Dye adsorption capability of PANI/PVAL/F was examined by using Reactive Black 5 (Sigma-Aldrich) as a model anionic dye molecule. Reactive Black 5 is a water soluble dye with a characteristic optical absorption maximum at 598 nm. The experiment was carried out using 50 mL of 55 mg L^{-1} Reactive Black 5 solution in which 50 mg of adsorbent was added, without any adjustment of the pH. The mixture was kept under stirring for 4 h at room temperature to attain equilibrium.

2.3. Characterization

Morphology was assessed by JEOL 6400 electron scanning microscope. DC conductivity was obtained by a van der Pauw method on freeze-dried materials compressed to pellets 13 mm in diameter at 70 kN using a hydraulic press Trystom H-62. A Keithley 230 Programmable Voltage Source in serial connection with a Keithley 196 System DMM was used for current measurement and the potential difference was measured with a Keithley 181 Nanovoltmeter. Measurements were carried out under stable ambient conditions at 23 °C and relative humidity 35 ± 5 %. The conductivity was obtained as an average from the measurements in two perpendicular directions. Static mechanical properties of hydrogels were determined on electromechanical testing machine Instron 6025/5800R equipped with a 10 N load cell at room temperature and with a cross-head speed of 10 mm min^{-1}. Measurement of cylindrical specimens with diameter 4.5 mm and length 60 mm was made on samples immersed in deionized water. Reported values are the averages of at least three measurements. The magnetization curves of neat hexaferrite powder and hexaferrite-filled aerogels were measured on a VSM 7407 Vibrating Sample Magnetometer (Lake Shore, USA) in magnetic fields up to 10 kOe. The measurements were carried out at room temperature in air. The amplitude and the frequency of vibration were 1.5 mm and 82 Hz, respectively. The UV–vis spectra were recorded with Lambda 950 spectrometer (Perkin Elmer, UK).

3. Results and discussion

3.1. Morphology

Scanning electron microscopy shows uniform, macroporous structure of neat PANI/PVAL aerogel (Fig. 2a). Hexaferrite particles have a size close to 5 μm (Fig. 2b). They were incorporated inside the aerogel during the preparation procedure in two fractions, 1 and 2 wt.% relative to swollen hydrogel (PANI/PVAL/1%F and PANI/PVAL/2%F) (Fig. 2c, d). The polyaniline content is ≈2 wt.%, [30] *i.e.* comparable with the last hexaferrite fraction, PVAL contribution amounts to 5 wt.%. The remaining part is represented by aqueous phase. Due to large difference in density, however, the volume fraction of hexaferrite is considerably lower than that of polymer part (Fig. 2c, d). To make particles visible, the electron micrographs were taken using back-scattered electrons (Fig. 2c, d). They are present in the PANI/PVAL/1%F and PANI/PVAL/2%F areogels as the white spots (Fig. 2c, d). They are separated from each other and rather randomly distributed inside the composite aerogels. The shape and size of the hexaferrite particles did

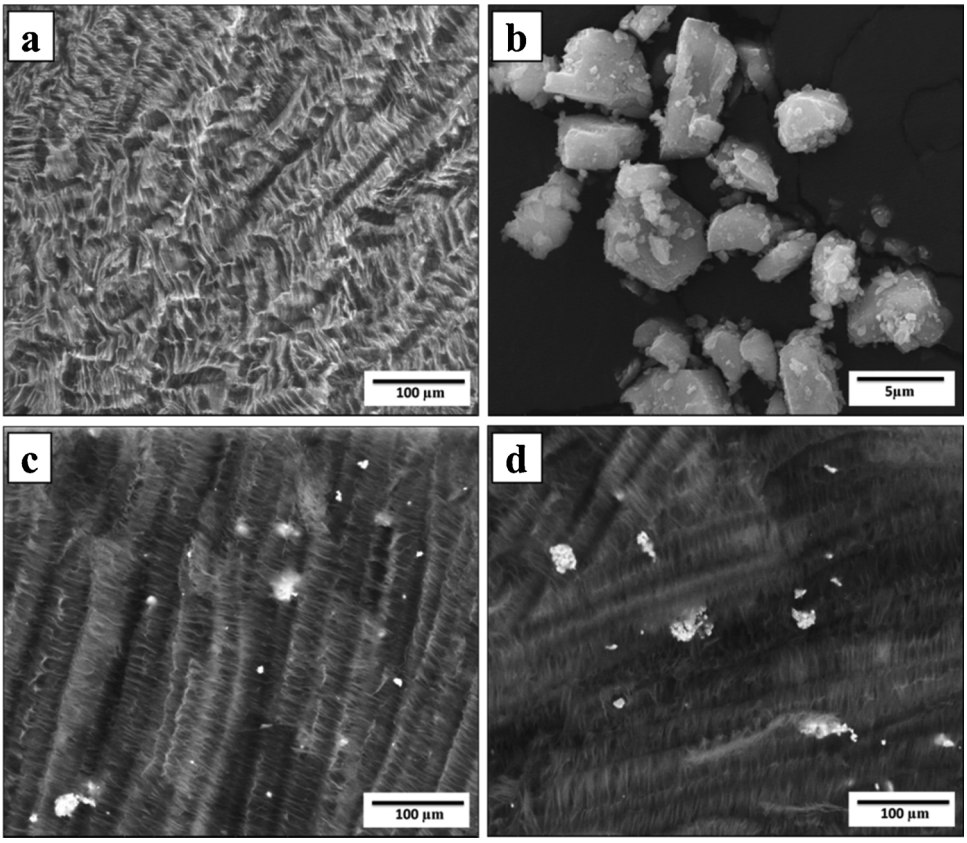

Fig. 2. Scanning electron micrographs of polyaniline/poly(vinyl alcohol) aerogel (a), hexaferrite particles (b), polyaniline/poly(vinyl alcohol) aerogel with 1 wt.% and 2 wt.% of hexaferrite (c) and (d), respectively.

not change during the preparation of composite aerogels.

The pore size in aerogels prepared in the presence and in the absence of hexaferrite is substantially different; the pores are smaller in the latter case. The structure of pores is associated with the ice crystals that serve as templates for the polymerization of aniline. We can speculate that the hexaferrite particles act as crystallization nuclei that subsequently affect the structure of ice, and consequently also the microstructure of polymer phase.

3.2. Mechanical properties

The mechanical properties were investigated on gels swollen with water, due to the possible application of such magnetic aerogels in wastewater purification. Neat PANI/PVAL gels possess good mechanical properties [30]. The addition of hexaferrite particles to cryogel causes a decrease in strain-at-break and in tensile strength (Table 1). At the same time the Young modulus increased from 47 kPa to ≈110 kPa. Generally, PANI/PVAL/1%F and PANI/PVAL/2%F composite gels show better resistance to elastic deformation when stress is applied compared to the neat PANI/PVAL gels.

3.3. Conductivity

Conductivity of composites was determined after the compression of aerogels to a pellet. The conductivity of aerogels prepared in the presence of hexaferrite particles is one order of magnitude higher compared with those prepared in their absence (Table 1). The contribution of the hexaferrite to the conductivity of the composite can be neglected, the conducting PANI content is the same in all the composites under study and neither its chemical composition nor the doping level is assumed to be different. The increase in conductivity probably reflects the difference in morphology. As evidenced by Fig. 2 the PANI/PVAL/F composites have more dense s tructure with smaller pores. Such material will assure better connectivity of the conducting PANI phase, which improves the transport of charges in the PANI/PVAL/F composite compared to PANI/PVAL aerogel without hexaferrite.

3.4. Magnetic properties

The room-temperature magnetization curves of neat hexaferrite and PANI/PVAL/F aerogel composites are shown in Fig. 3. The saturation magnetization for aerogel composites is significantly lower, 7.7–12.5 emu g^{-1} compared with hexaferrite particles alone, 40.6 emu g^{-1} that is result of low concentration of magnetic phase in the

Table 1
Mechanical properties and conductivity of aerogels.

Sample name	Strain-at-break, %	Tensile strength, kPa	Young modulus, kPa	Conductivity, S cm^{-1}
PANI/PVAL	133[a]	12.2[a]	47[a]	0.07
PANI/PVAL/1%F	63	9.2	113	0.22
PANI/PVAL/2%F	59	9	104	0.32

[a] The data taken from Ref. [30].

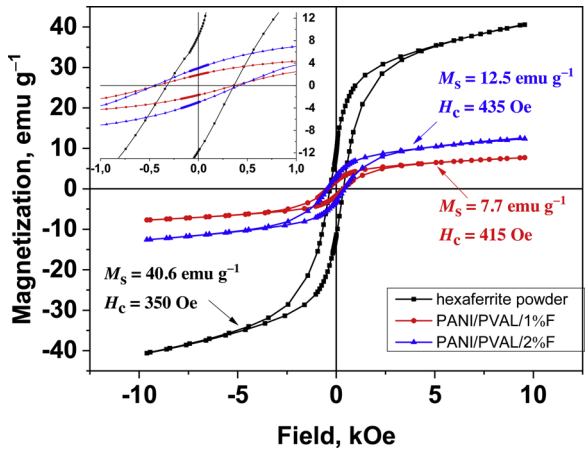

Fig. 3. Magnetization curve of PANI/PVAL aerogel without and with hexaferrite particles. The inset shows an enlarged view of the magnetization curves showing a coercive force for all three samples.

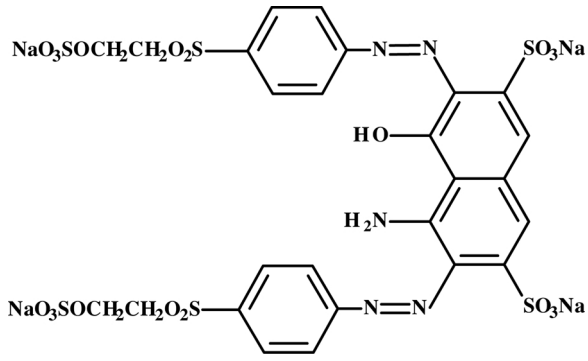

Fig. 4. The formula of Reactive Black 5.

composite (Fig. 3). The remanent magnetization was similarly reduced, 12.5–15 emu g^{-1}, compared with 35 emu g^{-1} for hexaferrite powder. However, a clearly detectable increase in coercive force from 350 Oe to 415–435 Oe has been observed for aerogels (Fig. 3). High value of coercivity of hexaferrite-contained aerogels guarantees easy removal from wastewater by external magnetic field.

The coercive force enhancement can be explained by increase in

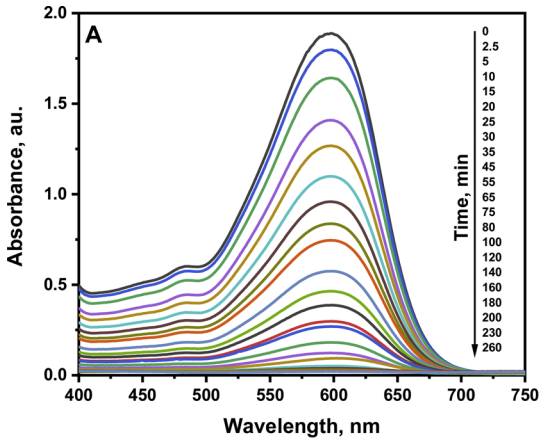

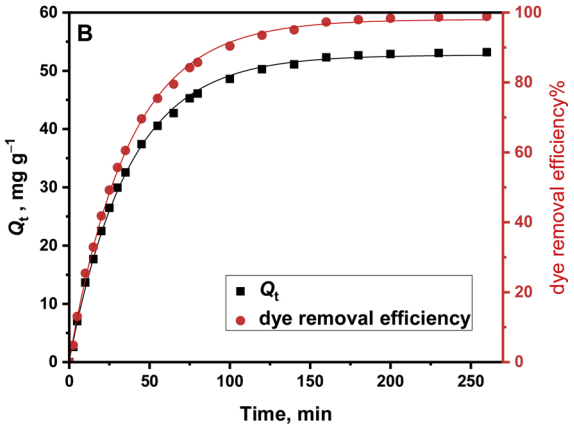

Fig. 6. The change in the optical absorbance of aqueous solution of Reactive Black 5 after introduction of a magnetic PANI/PVAL/2%F aerogel (A), effect of the contact time on the adsorption capacity (Q_t) and dye removal efficiency (B). Initial concentration of dye is 55 mg L^{-1}; dosage of PANI/PVAL/2%F aerogel is 50 mg.

effective magnetic anisotropy owing to magnetostriction. This assumption has been made on the basis of theoretical and experimental works on the deformation of ferrogels in a uniform magnetic field [35,36]. To understand the occurrence of magnetostriction in PANI/

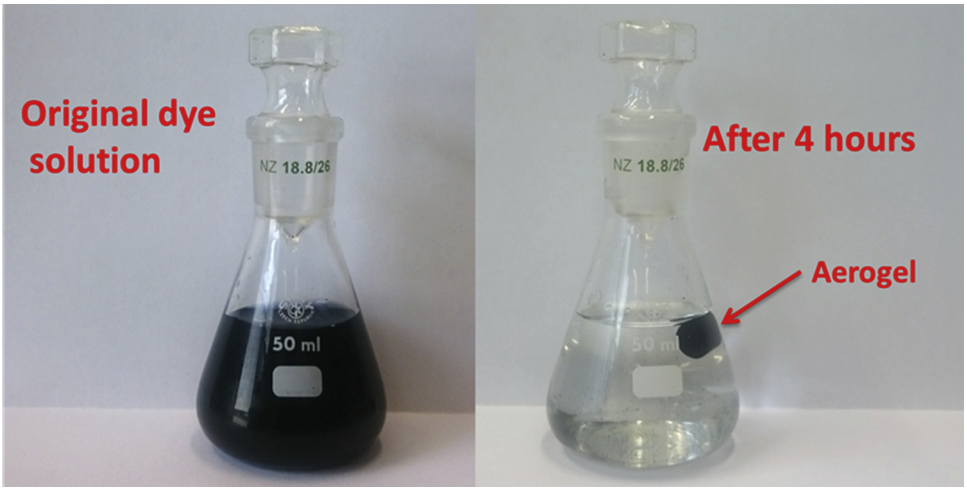

Fig. 5. The aqueous solution of Reactive Black 5 becomes colourless after immersion of a magnetic PANI/PVAL/2%F aerogel for 4 h.

PVAL/F aerogel composites requires additional investigation, namely polymer–magnetic particles interaction determining the network architecture of aerogels.

3.5. Removal of organic dye by the magnetic aerogel

The materials combining conducting polymers and magnetic component have been used in the design of electromagnetic interference shielding [10,11] and in environmental issues, such as water-pollution treatment as dye adsorbents [37–40] and as catalysts in photoactalytic degradation of dyes [41–44].

It has been established in the literature that conducting polymers adsorb many organic dyes [28,29] that are rated as frequent pollutants. The incorporation of a magnetic component allows for an easy separation of adsorbent from the treated medium. Novel materials reported in the present communication, the macroporous aerogels, can well host the hexaferrite particles and, simultaneously, they are efficient dye adsorbers or decomposition photocatalysts. It is not the purpose of this study to provide the detailed study on the extent and mechanism of dye adsorption but rather to illustrate the feasibility of its application in water-pollution treatment on an example of an anionic dye, Reactive Black 5 (Fig. 4).

When the small piece of an aerogel (about ≈ 50 mg) was added to the aqueous solution of a Reactive Black 5 dye (50 mg L^{-1}, 50 mL), the intensive dark blue coloration of the dye solution was substantially reduced after 4 h (Fig. 5). By spectroscopic assay (Fig. 6), the removal of dye was 99 % after 4 h.

4. Conclusions

The conducting poylaniline/poly(vinyl alcohol) cryogels have been prepared by the oxidation of aniline in frozen poly(vinyl alcohol) aqueous solution. The presence of Ni_2SrCr_xW hexaferrite affected the microstructure of hydrogels when the pore size became smaller; the presence of a hexaferrite obviously affected the formation of ice crystals that serve as a template for polyaniline deposition. The macroporous aerogels have been obtained after freeze-drying. After the compression to pellets, they display the conductivity higher by one orders of magnitude compared with a material prepared in the absence of hexaferrite. This is also the consequence of the smaller pore size and resulting better connectivity of the conducting phase. The aerogel has been illustrated to adsorb the organic dye, Reactive Black 5, 99 % after 4 h, and thus be useful in water-pollution treatment. The hexaferrite particles with high value of coercive force allow for the easy separation of adsorbent from aqueous medium. The conductivity and redox properties of polyaniline have not been directly exploited but could be used for the controlled adsorption/desorption by electrochemical switching between the leucoemeraldine, emeraldine, and pernigraniline oxidation states.

CRediT authorship contribution statement

Patrycja Bober: Conceptualization, Methodology, Visualization, Project administration, Supervision, Writing - original draft, Writing - review & editing, Funding acquisition. **Islam M. Minisy:** Investigation, Visualization, Writing - review & editing. **Udit Acharya:** Investigation, Writing - review & editing. **Jiří Pfleger:** Writing - review & editing. **Vladimir Babayan:** Investigation, Writing - review & editing. **Natalia Kazantseva:** Investigation, Writing - review & editing. **Jiří Hodan:** Investigation. **Jaroslav Stejskal:** Writing - review & editing.

Declaration of Competing Interest

There are no conflicts to declare.

Acknowledgment

The authors wish to thank the Czech Science Foundation (18-04669S) for the financial support.

References

[1] H. Ben Fredj, S. Helali, C. Esseghaier, L. Vonna, L. Vidal, A. Abdelghani, Labeled magnetic nanoparticles assembly on polypyrrole film for biosensor applications, Talanta 75 (2008) 740–747.
[2] Z. Shahnavaz, F. Lorestani, Y. Alias, P.M. Woi, Polypyrrole-$ZnFe_2O_4$ magnetic nanocomposite with core-shell structure for glucose sensing, Appl. Surf. Sci. 317 (2014) 622–629.
[3] K.G.B. Alves, C.A.S. Andrade, S.L. Campello, R.E. de Souza, C.P. de Melo, Magnetite/polypyrrole hybrid nanocomposites as a promising magnetic resonance imaging contrast material, J. Appl. Polym. Sci. 128 (2013) 3170–3176.
[4] M. Mallouki, F. Tran-Van, C. Sarrazin, P. Simon, B. Daffos, A. De, C. Chevrot, J. Fauvarque, Polypyrrole-Fe_2O_3 nanohybrid materials for electrochemical storage, J. Solid State Electrochem. 11 (2007) 398–406.
[5] M. Mallouki, F. Tran-Van, C. Sarrazin, C. Chevrot, J.F. Fauvarque, Electrochemical storage of polypyrrole-Fe_2O_3 nanocomposites in ionic liquids, Electrochim. Acta 54 (2009) 2992–2997.
[6] K. Mohanraju, V. Sreejith, R. Ananth, L. Cindrella, Enhanced electrocatalytic activity of PANI and $CoFe_2O_4$/PANI composite supported on graphene for fuel cell applications, J. Power Sources 284 (2015) 383–391.
[7] S. Khilari, S. Pandit, J.L. Varanasi, D. Das, D. Pradhan, Bifunctional manganese ferrite/polyaniline hybrid as electrode material for enhanced energy recovery in microbial fuel cell, ACS Appl. Mater. Interfaces 7 (2015) 20657–20666.
[8] R. Peymanfar, A. Javidan, S. Javanshir, Preparation and investigation of structural, magnetic, and microwave absorption properties of aluminum-doped strontium ferrite/MWCNT/polyaniline nanocomposite at KU-band frequency, J. Appl. Polym. Sci. 134 (2017) 45135.
[9] W. Wang, S.P. Gumfekar, Q. Jiao, B. Zhao, Ferrite-grafted polyaniline nanofibers as electromagnetic shielding materials, J. Mater. Chem. C 1 (2013) 2851–2859.
[10] B.J. Madhu, M. Gurusiddesh, T. Kiran, B. Shruthi, H.S. Jayanna, Structural, dielectric, ac conductivity and electromagnetic shielding properties of polyaniline/$Ni_{0.5}Zn_{0.5}Fe_2O_4$ composites, J. Mater. Sci.-Mater. Electron. 27 (2016) 7760–7766.
[11] M. Abdullah Dar, K. Majid, M. Hanief Najar, R.K. Kotnala, J. Shah, S.K. Dhawan, M. Farukh, Surfactant-assisted synthesis of polythiophene/$Ni_{0.5}Zn_{0.5}Fe_2$-$xCexO_4$ ferrite composites: study of structural, dielectric and magnetic properties for EMI-shielding applications, Phys. Chem. Chem. Phys. 19 (2017) 10629–10643.
[12] K. Singh, A. Ohlan, V.H. Pham, R. Balasubramaniyan, S. Varshney, J. Jang, S.H. Hur, W.M. Choi, M. Kumar, S.K. Dhawan, B.-S. Kong, J.S. Chung, Nanostructured graphene/Fe_3O_4 incorporated polyaniline as a high performance shield against electromagnetic pollution, Nanoscale 5 (2013) 2411–2420.
[13] V. Babayan, N.E. Kazantseva, I. Sapurina, R. Moučka, J. Stejskal, P. Sáha, Increasing the high-frequency magnetic permeability of MnZn ferrite in polyaniline composites by incorporating silver, J. Magn. Magn. Mater. 333 (2013) 30–38.
[14] N.E. Kazantseva, et al., Magnetic particle-filled polymer microcomposites, in: S. Thomas (Ed.), Polymer Composites, vol. 1, Willey-VCH, Weinheim, 2012, pp. 613–669.
[15] R. Suresh, K. Giribabu, R. Manigandan, A. Stephen, V. Narayanan, Fe_2O_3@polyaniline nanocomposite: characterization and unusual sensing property, Mater. Lett. 12 (2014) 8369–8372.
[16] D.E. Park, H.S. Chae, H.J. Choi, A. Maity, Magnetite-polypyrrole core-shell structured microspheres and their dual stimuli-response under electric and magnetic fields, J. Mater. Chem. C 3 (2015) 3150–3158.
[17] P. Bober, B.A. Zasońska, P. Humpolíček, Z. Kuceková, M. Varga, D. Horák, V. Babayan, N. Kazantseva, J. Prokeš, J. Stejskal, Polyaniline-maghemite based dispersion: electrical, magnetic properties and their cytotoxicity, Synth. Met. 214 (2016) 23–29.
[18] B.A. Zasońska, P. Bober, P. Jošt, E. Petrovský, P. Boštík, D. Horák, Magnetoconductive maghemite core/polyaniline shell nanoparticles: physico-chemical and biological assessment, Colloid Surf. B-Biointerfaces 141 (2016) 382–389.
[19] H. Gu, H. Zhang, C. Ma, S. Lyu, F. Yao, C. Liang, X. Yang, J. Guo, Z. Guo, J. Gu, Polyaniline assisted uniform dispersion for magnetic ultrafine barium ferrite nanorods reinforced epoxy metacomposites with tailorable negative permittivity, J. Phys. Chem. C 121 (2017) 13265–13273.
[20] B.A. Zasońska, U. Acharya, J. Pfleger, P. Humpolíček, J. Vajďák, J. Svoboda, E. Petrovsky, J. Hromádková, Z. Walterová, P. Bober, Multifunctional polypyrrole@maghemite@silver composites: synthesis, physico-chemical characterization and antibacterial properties, Chem. Pap. 72 (2018) 1789–1797.
[21] A.A. Farghali, M. Moussa, M.H. Khedr, Synthesis and characterization of novel conductive and magnetic nano-composites, J. Alloys Compd. 499 (2010) 98–103.
[22] D. Mehta, S. Mazumdar, S.K. Singh, Magnetic adsorbents for the treatment of water/wastewater-a review, J. Water Process Eng. 7 (2015) 244–265.
[23] B. Mu, A. Wang, One-pot fabrication of multifunctional superparamagnetic attapulgite/Fe_3O_4/polyaniline nanocomposites served as an adsorbent and catalyst support, J. Mater. Chem. A 2 (2015) 281–289.
[24] A.R. Sadrolhosseini, M. Naseri, S.A. Rashid, Polypyrrole-chitosan/nickel-ferrite nanoparticle composite layer for detecting heavy metal ions using surface plasmon resonance technique, Opt. Laser Technol. 93 (2017) 216–223.
[25] M.S. Zoromba, M.I.M. Ismail, M. Bassyouni, M.H. Abdel-Aziz, N. Salah, A. Alshahrie, A. Memic, Fabrication and characterization of poly (aniline-*co*-o-

anthranilic acid)/magnetite nanocomposites and their application in wastewater treatment, Colloid Surf. A: Physicochem. Eng. Aspects 520 (2017) 121–130.
[26] U.O. Aigbe, R. Das, W.H. Ho, V. Srinivasu, A. Maity, A novel method for removal of Cr(VI) using polypyrrole magnetic nanocomposite in the presence of unsteady magnetic fields, Sep. Purif. Technol. 194 (2018) 377–387.
[27] E.N. Zare, A. Motahari, M. Sillanpaa, Nanoadsorbents based on conducting polymer nanocomposites with main focus on polyaniline and its derivatives for removal of heavy metal ions/dyes: a review, Environ. Res. 162 (2018) 173–195.
[28] B. Yan, Z.H. Chen, L. Cai, Z.M. Chen, J.W. Fu, Q. Xu, Fabrication of polyaniline hydrogel: synthesis, characterization and adsorption of methylene blue, Appl. Surf. Sci. 356 (2015) 39–47.
[29] M.M. Ayad, W.A. Amer, S. Zaghlol, I.M. Minisy, P. Bober, J. Stejskal, Polypyrrole-coated cotton textile as adsorbent of methylene blue dye, Chem. Pap. 72 (2018) 1605–1618.
[30] J. Stejskal, P. Bober, M. Trchová, A. Kovalcik, J. Hodan, J. Hromádková, J. Prokeš, Polyaniline cryogels supported with poly(vinyl alcohol): soft and conducting, Macromolecules 50 (2017) 972–978.
[31] P. Bober, M. Trchová, J. Kovářová, U. Acharya, J. Hromádková, J. Stejskal, Reduction of silver ions to silver with polyaniline/poly(vinyl alcohol) cryogels and aerogels, Chem. Pap. 72 (2018) 1619–1628.
[32] J. Stejskal, P. Bober, Conducting polymer colloids, hydrogels, and cryogels: common start to various destinations, Colloid Polym. Sci. 296 (2018) 989–994.
[33] P. Bober, J. Pfleger, I.A. Pašti, N.M. Gavrilov, S.K. Filippov, D. Klepac, M. Trchová, H. Hlídková, J. Stejskal, Carbogels: carbonized conducting polyaniline/poly(vinyl alcohol) aerogels derived from cryogels for electrochemical capacitors, J. Mater. Chem. A 7 (2019) 1785–1796.
[34] Y. Huang, J. Li, X. Chen, X. Wang, Applications of conjugated polymer based composites in wastewater purification, RSC Adv. 4 (2014) 62160–62178.
[35] P.A. Sanchez, O.V. Stolbov, S.S. Kantorovich, Y.L. Raikher, Modeling the magnetostriction effect in elastomers with magnetically soft and hard particles, Soft Matter 15 (2019) 7145–7158.
[36] P. Ilg, Stimuli-responsive hydrogels by magnetic nanoparticles, Soft Matter 9 (2013) 3465–3468.
[37] M. Bhaumik, H.J. Choi, R.I. McCrindle, A. Maity, Composite nanofibers prepared from metallic iron nanoparticles and polyaniline: high performance for water treatment applications, J. Colloid Interface Sci. 425 (2014) 75–82.
[38] W.L. Guo, F.F. Hao, X.X. Yue, Z.H. Liu, Q.Y. Zhang, X.H. Li, J. Wei, Rhodamine B removal using polyaniline-supported zero-valent iron powder in the presence of dissolved oxygen, Environ. Prog. Suistain. Energy 35 (2016) 48–55.
[39] H.F. Xie, M. Yan, Q. Zhang, H.X. Qu, J.M. Kong, Hemin-based biomimetic synthesis of PANI@iron oxide and its adsorption of dyes, Desalin. Water Treat. 67 (2017) 346–356.
[40] B. Mu, J. Tang, L. Zhang, A.Q. Wang, Facile fabrication of superparamagnetic graphene/polyaniline/Fe_3O_4 nanocomposites for fast magnetic separation and efficient removal of dye, Sci. Rep. 7 (2017) 5347.
[41] A. Pant, R. Tanwar, B. Kaur, U.K. Mandal, A magnetically recyclable photocatalyst with commendable dye degradation activity at ambient conditions, Sci. Rep. 8 (2018) 14700.
[42] S. Zeng, J. Yang, X.Y. Qiu, Z.Y. Liang, Y.M. Zhang, Magnetically recyclable $MnFe_2O_4$/polyaniline compositewith enhanced visible light photocatalytic activity for rhodamine B degradation, J. Ceram. Soc. Japan 124 (2016) 1152–1156.
[43] M.R. Abukhadra, M. Shaban, M.A. Abd El Samad, Enhanced photocatalytic removal of Safranin-T dye under sunlight within minute time intervals using heulandite/polyaniline@ nickel oxide composite as a novel photocatalyst, Ecotoxicol. Environ. Saf. 162 (2018) 261–271.
[44] R. Tanwar, U.K. Mandal, Photocatalytic activity of $Ni_{0.5}Zn_{0.5}Fe_2O_4$@ polyaniline decorated BiOCl for azo dye degradation under visible light - integrated role and degradation kinetics interpretation, RSC Adv. 9 (2019) 8977–8993.

I.M. Minisy is a PhD student at the Faculty of Science, Charles University, Prague, Czech Republic.

U. Acharya is a PhD student at the Faculty of Mathematics and Physics, Charles University, Prague, Czech Republic.